IMAGE RECONSTRUCTION FROM PROJECTIONS

A thesis presented for the degree of
Doctor of Philosophy in Electrical Engineering
in the University of Canterbury,
Christchurch, New Zealand.

by

T.M. PETERS B.E. (Hons)

1973

And, as in uffish thought he stood,

The Jabberwock, with eyes of flame,

Came whiffling through the tulgey wood,

And burbled as it came!

- Lewis Carroll

ABSTRACT

The problem of reconstructing cross-sections from their projections, using Fourier transform processing, is considered in detail and is related to problems in medical tomography. A number of equations relating cross-sections to their projections are derived, and are used as the bases for algorithms which enable cross-sections to be reconstructed from a finite number of projections. Results of computations on analytically derived and radiographically measured projections demonstrate the usefulness of these techniques.

A proposal for a new type of transverse tomographic system is described. It is demonstrated that images of cross-sections may be restored from tomograms produced using this system, by the use of both optical and digital processing techniques.

Image reconstruction techniques using Fourier transforms are shown to be of use for reconstructing three-dimensional radio-isotope distributions, from scintigraphic projections measured with a gamma camera.

ACKNOWLEDGEMENTS

I am especially grateful to my supervisor, Dr R.H.T. Bates, for his guidance and encouragement during the course of the project. I also wish to thank Dr P.R. Smith for his assistance.

I am indebted to the staff members of Christchurch and Princess Margaret Hospitals, the New Zealand Radiation Laboratory, and the Non-destructive Testing unit of the New Zealand National Airways Corporation for their assistance and cooperation. I wish to thank Mr A. Vernon of the Electrical Engineering Department's technical staff for his valuable assistance.

I also wish to thank my wife Leigh for her patience and encouragement.

The financial assistance of the University Grants Committee is gratefully acknowledged.

TABLE OF CONTENTS

GLOSSARY

Unless indicated otherwise, symbols used in this thesis have the meanings given below.

a	Radius of circle enclosing cross-section
A_m, B_m, a_m, b_m	Fourier coefficients of order m

Convolution theorem: $\mathfrak{F}(A*B) = \mathfrak{F}(A).\mathfrak{F}(B)$

DRR	Diverging Ray Reconstruction
DSR	Density Space Reconstruction
db	decibel
ε_n	Neumann factor. $\varepsilon_n = 1; \quad n = 0$ $= 2; \quad n \neq 0$
$e(\xi,\phi)$	Projected density measured with diverging radiation
$f(\xi,\phi)$	Projected density
$f_\gamma(\xi,\phi)$	Scintigraphic projected density
$\mathfrak{F}\{\cdot\}$	Forward Fourier Transform

$$\mathfrak{F}\{f(\xi)\} = F(\rho) = \int_{-\infty}^{\infty} f(x)\exp(j2\pi\rho\xi)\,d\xi$$

$\mathfrak{F}^{-1}\{\cdot\}$	Inverse Fourier Transform

$$\mathfrak{F}^{-1}\{F(\rho)\} = f(\xi) = \int_{-\infty}^{\infty} F(\rho)\exp(-j2\pi\rho\xi)\,d\rho$$

FFT	Fast Fourier Transform
FT	Fourier transform
FTR	Fourier Transform Reconstruction
$g(r,\theta)$	Polar coordinate representation of layergram
$G(\rho,\phi)$	Fourier transform of $g(r,\theta)$
$h(x,y)$	Cartesian coordinate representation of layergram

$H(\alpha,\beta)$	Fourier transform of $h(x,y)$
$\mathcal{H}\{\cdot\}$	Hilbert transform
	$\mathcal{H}\{f(x)\} = f(x) * \frac{-1}{\pi x}$
$I_{N,\phi}$	Interpolation operator
$I(\phi)$	Interpolation kernel
$J_n(x)$	Bessel function of first kind of order n and argument x
$\mathcal{K}(\sigma,\theta)$	Position varying weighting factor
LHS	Left hand side (of equation)
$O(x)$	of the order of x
r	radius coordinate in density space
R	Distance of X-ray source from film
R'	R - a
RDL	Rho-filtered Discrete Layergram
RFL	Rho-filtered Layergram
RHS	Right hand side (of equation)
rect(x)	$= 1; \quad \lvert x\rvert \leq .5$
	$= 0; \quad \lvert x\rvert > .5$
S(x,y,z)	selectivity function
sinc(x)	$\frac{\sin(\pi x)}{\pi x}$
sgn(x)	$= 1, \quad x \geq 0$
	$= -1, \quad x < 0$
w.r.t	with respect to
x,y,z	Cartesian coordinates in density space
α,β	Cartesian coordinates in Fourier transform space
$\Gamma(x,y)$	Distribution of radio-isotope
$\delta(\cdot)$	Dirac delta function

ξ,η	Cartesian coordinates in density space rotated by ϕ from x,y
θ	angular coordinate in density space
$\lambda(r,\theta)$	density distribution expressed in polar coordinates
$\Lambda(\rho,\phi)$	Fourier transform of density expressed in polar coordinates
ρ	radial coordinate in transform space
$\hat{\rho}$	cut-off spatial frequency
σ	R/(R-a)
ϕ	angular coordinate in transform space, and angle at which projection is measured
ψ	divergence of X-ray beam
Φ	angle of central ray in transverse tomographic system from horizontal
$\omega(x,y)$	density distribution expressed in Cartesian coordinates
$\Omega(\alpha,\beta)$	Fourier transform of density expressed in rectangular coordinates
* (superscript)	complex conjugate. If $W = \alpha+j\beta$ then $W^* = \alpha-j\beta$.
* (in line)	$f(x) * g(x) = \int_{-\infty}^{\infty} f(u)g(u-x)du$
~	'is equivalent to'
→	'followed by'
< (≤)	is less than (or equal to)
> (≥)	is greater than (or equal to)
≈	is approximately equal to
{•}	notation for a set
∈	is a member of (a set)
∀	for all values of

CHAPTER 1

INTRODUCTION

The Fourier transform has long been considered an important mathematical tool. It forms the basis of such diverse subjects as X-ray crystallography, radio-astronomy, optics, spectroscopy, X-ray metallography, antenna theory, information theory, signal processing and image processing. The recent general use of digital computers and the fast Fourier transform (FFT) algorithm has enabled the Fourier transform to play an increasing part in the numerical solution of problems in the areas cited above.

In this thesis, the use of Fourier transforms is extended into the field of medical imaging. The most common method of viewing the internal structure of the human body is by means of radiographic projections. While the radiograph is able to impart a great deal of information to the trained clinician, it displays many cross-sections superimposed on one another, thus tending to obscure important features. The need for accurately imaging three-dimensional structure in general and individual two-dimensional sections in particular in certain instances (particularly in radiotherapy treatment planning), was recognised early in the development of radiography. A number of methods, grouped together under the name of tomography, was developed to enable radiographic images of single planes within the object, to be imaged with greater fidelity than other planes. Since conventional tomograms suffer from the disadvantage that they generally display blurred images, various ways are examined in this thesis to improve this situation.

Two approaches to this problem are considered, both of which relate the information present in radiographic projections to the information in an image of a particular cross-section of the human anatomy being studied. Since the problem of imaging a three-dimensional object may be reduced to that of reconstructing a series of serial sections, techniques presented in this thesis relate only to the reconstruction of a single section from its projections. The first approach is concerned with using the information, contained in a number of one-dimensional projections of a particular section, to numerically reconstruct an image of the section itself. The second approach is to modify a conventional tomographic apparatus to allow the cross-section to be computed from an effectively continuous range of projections around the body. The central theme of this thesis is the efficient computation and use of Fourier transforms as part of these reconstruction procedures.

New material is included in chapters 3-9, which discuss the theoretical bases of a number of techniques for reconstructing images from their projections. Computational methods are discussed, experimental results are presented, and the design of a new type of tomographic device is described. The clinical implications of the work are discussed.

Chapter 2 describes the development of tomography from its inception. Early methods are discussed in some detail in order to establish the principals upon which conventional tomography is based. Many recent improvements which have attempted to provide two- and three-dimensional images both in medicine and in other disciplines are also considered, leading to a general

discussion of the numerical methods which have come into use since the advent of electronic digital computers.

Chapter 3 presents formal derivations of a number of 'radiation transforms, so called since they unambiguously relate the density of a section of an object to its radiographic projections. Radiation transforms are formulated for both the ideal situation when the imaging X-rays are parallel and for the more general case when the radiation is emitted from a point source and impinges upon the object in a diverging beam. All of the radiation transforms presented here depend either explicitly or implicitly upon Fourier transforms.

Chapter 4 describes methods of using these radiation transforms to reconstruct images from a finite number of projections. To enable a set of measured projections to be operated upon by the radiation transform procedures, the given data must be interpolated in some manner. This step enables the projections to be represented as if they had been measured continuously in angle. Various interpolation schemes are discussed for performing this procedure, and the relationships between each are examined. Also discussed in this chapter is an iterative procedure (from the literature) for reconstructing images from a small number of projections.

In chapter 5, the consequences of measuring the data at discrete angular and radial points, rather than in a continuous fashion, is discussed. This is shown to be particularly important when related to the use of the FFT algorithm. The use of one particular class of interpolation scheme is shown to give rise to an a posteriori estimate of the noise level on the data. A further result of using interpolations in this

class is that an image may be computed which contains the maximum amount of non-ambiguous information allowed by the use of a finite number of projections. A discussion of the important question of the maximum attainable resolution in the reconstructed image concludes chapter 5.

Chapter 6 presents numerous computational examples to illustrate the reconstruction techniques discussed in previous chapters. Examples of reconstructions on both ideal (analytically computed) and radiographically measured projections are given. Results using Fourier transform reconstruction methods are compared with the results of using one of the iterative schemes from the literature.

Chapter 7 deals with a different approach to the reconstruction problem. Instead of measuring a number of discrete projections of the object, the technique of conventional transverse tomography is modified to allow projections of a single cross-section to be recorded continuously in angle. The intermediate image that is recorded using this procedure is shown to be visually similar to a transverse tomogram acquired in the conventional manner, but also to have the property of being representable in terms of a linear blurring operation on the ideal image. This property is exploited by the use of optical and digital image deblurring methods to restore the intermediate image to a more accurate representation of the object. An experimental, modified, transverse tomographic apparatus is described, and results obtained using this device are presented.

A further branch of medicine where a recent interest has been shown in the use of tomography, is the field of radionuclide imaging. Chapter 8 considers the adaptation of

class is that an image may be computed which contains the maximum amount of non-ambiguous information allowed by the use of a finite number of projections. A discussion of the important question of the maximum attainable resolution in the reconstructed image concludes chapter 5.

Chapter 6 presents numerous computational examples to illustrate the reconstruction techniques discussed in previous chapters. Examples of reconstructions on both ideal (analytically computed) and radiographically measured projections are given. Results using Fourier transform reconstruction methods are compared with the results of using one of the iterative schemes from the literature.

Chapter 7 deals with a different approach to the reconstruction problem. Instead of measuring a number of discrete projections of the object, the technique of conventional transverse tomography is modified to allow projections of a single cross-section to be recorded continuously in angle. The intermediate image that is recorded using this procedure is shown to be visually similar to a transverse tomogram acquired in the conventional manner, but also to have the property of being representable in terms of a linear blurring operation on the ideal image. This property is exploited by the use of optical and digital image deblurring methods to restore the intermediate image to a more accurate representation of the object. An experimental, modified, transverse tomographic apparatus is described, and results obtained using this device are presented.

A further branch of medicine where a recent interest has been shown in the use of tomography, is the field of radionuclide imaging. Chapter 8 considers the adaptation of

reconstruction techniques described in earlier chapters to the problem of reconstructing two- and three-dimensional isotope distributions within the human body. It is shown that this problem differs from its radiographic counterpart since the projections that are measured are due to radiation being emitted from within the body, rather than from outside. This is shown to complicate the analysis of the problem considerably. However, it is demonstrated that satisfactory qualitative reconstructions may be obtained by applying reconstruction techniques based on radiation transforms, so long as the photon attenuation of the medium, in which the isotope distribution is located, is not too great. A practical example using an isotope-filled phantom illustrates the usefulness of the technique for reconstructing a three-dimensional radionuclide distribution, by combining the versatility of a gamma camera with the computational power of a small digital computer.

Essential to the success of the reconstruction techniques described in this thesis are two algorithms relating to Fourier transforms and interpolation. These algorithms, and other computational techniques relevant to the implementation of the procedures discussed in this thesis, are developed in chapter 9.

Chapter 10 gives concluding remarks and suggestions for further research and development of topics relevant to those presented in this thesis.

The Appendices, in addition to miscellaneous mathematical analyses pertinent to the body of the thesis, include a detailed discussion of digital image input and output devices which were specifically developed for this project.

Papers published, or submitted for publication, to date on topics relevant to the material presented in this thesis are as follows:

Bates, R.H.T. and Peters, T.M. 1971 Towards improvements in tomography. N.Z. J. Sci. 14. 883-896.

Peters, T.M. 1972 Improvements to transverse body-section radiography using computer processing. Proc. 5th Hawaii Internat. Conf. on System Sciences. HICSS-5, Jan. 12-14 1972. 238-240.

Smith, P.R., Peters, T.M. and Bates, R.H.T. 1973 Image reconstruction from finite numbers of projections. J. Phys. A.6. 361-382.

Peters, T.M., Smith, P.R. and Gibson, R.D. 1973 Computer aided transverse body-section radiography. Brit. J. Radiol. 46, 314-317.

Peters, T.M. 1973 Spatial filtering to improve transverse tomography. Submitted for publication in IEEE Trans. Biomed. Eng.

Peters, T.M., Rogers, T.G.H. and Glasgow, G.M. 1973 Fourier transforms in gamma camera tomography. Submitted for publication in Phys. Med. Biol.

Kennedy, W.K. and Peters, T.M. 1973 High quality image recording and display using a small hybrid computer. Submitted for publication in Aust. Computer J.

CHAPTER 2

HISTORY OF BODY-SECTION IMAGING METHODS

2.1 Introduction

This chapter briefly traces the development of techniques which enable the internal structure of objects to be determined using penetrating radiation. The discussion of such techniques is confined to radiation which undergoes negligible refraction or diffraction (e.g. X-radiation, or gamma radiation) when transmitted through an object.

Sections 2.2-2.4 describe how early attempts to construct a lens to focus X-rays, and so obtain depth information, evolved into the technique which is now termed 'tomography'. Initially the methods were aimed at providing images of longitudinal sections of the human anatomy, and later these techniques were modified to provide images of transverse sections. In section 2.5, extensions to the basic tomographic principles which enable a number of planes to be imaged simultaneously are described.

One of the disadvantages of conventional tomography is that it produces images which are distorted by blurring effects. Section 2.6 outlines methods which have been proposed to overcome this problem. In section 2.7 there is a discussion of the various methods which have been suggested to reconstruct the entire three-dimensional volume of the object from a series of radiographs, both by simple optical methods, and by using holography. Section 2.8 describes a variety of new imaging methods which were made possibly by the advent of the digital computer. Their use originated in the fields of radio-astronomy and electron microscopy, and have recently been

adapted to aid medical diagnosis (section 2.9). Methods of this type form the basis of a large part of this thesis. Finally, various methods which have been suggested to present three-dimensional images to the observer are discussed in section 2.10.

2.2 Body Section Imaging

In 1890 Röntgen discovered a new type of radiation which was able to penetrate matter, could be used to expose photographic film, and could cause certain substances to emit light. Almost immediately, these Röntgen rays (or X-rays) were put to use in the field of medical diagnosis. Physicians were then able to observe projections of the anatomical structure of the body, with a resulting increase in their diagnostic ability. Because some of the properties of X-rays were the same as those of light, the next step was to attempt to focus an X-ray beam so that sections of the body could be imaged selectively in much the same way as a microscope can be made to focus on a particular plane of a specimen being observed. However, despite much effort on the part of numerous early workers in the field (c.f. Etter 1965, ch.2), no such focusing action could be observed with X-rays. To overcome this limitation, the focusing ability of light was simulated (very imperfectly of course) by moving the X-ray source and the recording film relative to the body.

Since 1921, many such methods of body-section imaging using X-rays have been proposed. These methods have been variously named by their proponents as laminagraphy, planigraphy, stratigraphy, layergraphy and tomography. They were proposed by a number of authors during the period 1921-

1923. In this thesis, the term tomography is used when referring to any conventional method of body-section radiography which results in an image (tomogram) of the plane being studied. The term layergram is used to denote the image obtained in a recently proposed method of body-section imaging (Peters 1973, Smith et al. 1973) which is also developed in chapters 3 and 7 of this thesis. There are two distinct types of tomography; those methods which image sections parallel to the patient's longitudinal axis, and those which produce tomograms of planes perpendicular to this axis. These methods are known as longitudinal and transverse tomography respectively.

2.3 Longitudinal Tomography

The first reference to any method of radiographic body-section imaging was in a French patent application by Bocage (1922). The three methods he proposed at that time for imaging planes parallel to the patient's longitudinal axis (c.f. Andrews 1936) are shown diagrammatically in fig. 2.1. These are called methods A, B and C respectively. All of these approaches to tomography are essentially the same and differ only in minor details. Bocage's method A is described below in detail, to illustrate the basic principle of tomography.

2.3.1 Principle of Linear Tomography

Longitudinal tomography may be again broken down into sub-classes, namely linear, circular and areal tomography (Edholm 1960), which refer to techniques using linear, circular, or more complicated tube-film motions respectively. However, the underlying principle of all three methods may be illustrated by considering the linear motion used in Bocage's method A.

Consider a body for which a linear tomogram is to be made of a particular plane. For simplicity, the example is reduced to the case of obtaining a one-dimensional tomogram from a two-dimensional object. In fig. 2.1a the line aa denotes the plane to be imaged within the body cccc. A second plane below aa is denoted by bb. The X-ray source lies in the line DD, while the tomogram appears on a photographic plate in the plane ee, which is parallel to aa. The point S_0 is at the mid-point of the line DD, and A lies in both aa and cccc. The points S_0, A, B and P_0 lie on the same straight line.

When making a conventional radiograph of the object, the source is fixed at a particular point, say S_0. The X-ray beam passing through A and B impinges on the photographic plate at the point P_0, so that the X-ray exposure of the plates is affected by the X-ray absorptivities of all of the points along the line S_0P_0, and there is no means of determining the relative vertical placements of points A and B within the object.

To make a linear tomogram, the source S traverses DD while the photographic plate is moved in the opposite direction in such a way that the X-ray beam S P_A passing through A always strikes the same point on the film. Since the line S P_A effectively rotates about a fulcrum A in the tomographic plane aa, the section of the body being imaged is often called the fulcrum plane. The relative motion of S and the film plate ensures that there is a one-to-one correspondence between points on the film plate and points on aa. However the X-ray beam S P_B passing through B strikes different parts of the plate as S traverses DD. Thus in contradistinction to the conventional radiograph or shadowgram, the tomogram is a

selective image of the fulcrum plane, although the image is heavily blurred since the X-ray beam must pass through all other planes in the body parallel to aa.

2.3.2 Development of Longitudinal Tomographic Techniques

Bocage's method B (fig. 2.1b) is similar to his method A, except that the source-film motion may be varied to describe circles, crosses or spirals. In his method C (fig. 2.1c), the source and the film describe arcs about a centre of rotation in the fulcrum plane with the film remaining horizontal.

About the same time as Bocage described these methods, a second French patent was filed by Portes and Chausse (c.f. Edholm 1960), which suggested the use of Bocage's method B as a means of concentrating the radiation depth dose in radiotherapy. Thus, early in its history, tomography began to be associated with the treatment of cancer tumours as well as in their diagnosis.

The first practical medical application of the tomographic principle was due to Vallebona (1930). His was a simple technique whereby the X-ray tube and film remained stationary, while the patient was rotated about an axis in the plane to be imaged (fig. 2.2). He later published a modification to this method whereby the patient remained stationary while the tube and the film were mounted at opposite ends of a pendulum-like arm, which was pivoted about a point in the fulcrum plane of the patient.

Ziedses des Plantes (1932, 1971) described a 'planigraphic' apparatus which he developed in 1921. In his method, the patient remained stationary while the tube-film system was moved with the central ray from the source passing through a point in the fulcrum plane at all times. Ziedses des Plantes'

system allowed freedom of tube-film movement, and he suggested that a spiral motion was the most satisfactory for blurring the images of parts of the body outside the tomographic plane. His apparatus is shown diagrammatically in fig. 2.3. This is the same in concept as a device proposed by Kieffer (1938).

The simplest, and until recently the most widely used, apparatus for longitudinal body-section radiography was proposed by Grossman (1935). The name 'tomography' which he gave to his method has now become a term which is synonymous with any method of body-section imaging. His method (fig. 2.4) used an X-ray tube which was fixed to a pendulous arm pivoted in the fulcrum plane. The film, at the remote end of the arm, was made to remain horizontal at all times during the motion of the pendulum, which was constrained to swing in a single plane. Thus, while capable only of linear blurring (as distinct from the multi-directional blurring of Ziedses des Plantes' apparatus), it had the advantage of being inexpensive to produce because of its mechanical simplicity.

Grossman considered the use of obscuring motions other than the linear variety. Andrews (1936) reproduced the results of a study made by Grossman who compared the distortions caused by a number of different obscuring motions. Grossman concluded that the disturbing shadows were diminished more by spiral obscuring motions than by circular motions, but that these shadows were effectively removed by the pendulous motion, provided that the angular excursion of the pendulum was sufficiently large.

Andrews and Stava (1937) studied mathematically each of the methods described above, from the points of view of the accuracy with which a particular fulcrum plane may be imaged

and the degree of blurring of the unwanted planes. They showed that Vallebona's methods result in only a single line within the fulcrum plane being imaged sharply under conditions of linear tube-film motion, and that only a single point was imaged clearly when multi-directional motion is used. In this same study, Andrews and Stava showed that the devices of Ziedses des Plantes and Grossman yielded identical results under conditions of linear tube-film motion. In both of these cases the fulcrum plane was imaged without the distortion encountered by Vallebona's method, and that the only essential difference between the two methods was the more versatile nature of the former in being able to execute non-linear obscuring motions.

In later years both of these techniques have been further developed and Grossman's method is often implemented by making a simple modification to existing X-ray units enabling them to be used to produce linear tomograms. Specialized units capable of many obscuring motions are also currently manufactured.

There has recently been a revived interest in the analysis of tomographic systems in order to determine the nature of the obscuring motion which is best suited for imaging sections of a particular organ. Edholm (1960) has published an extensive study of the information contained in tomograms of a number of simple objects, made with many different obscuring motions, and Stieve (1972) has extended this work. Reichmann (1972a) proposed a modified theory which more accurately describes the formation of the tomographic image in the presence of noise and film non-linearities. He also studied the spurious contours which can occur in tomograms

of spherical and cylindrical objects (Reichmann, 1972b).

2.4 Transverse Tomography

So far, only methods of imaging sections parallel to the longitudinal axis of the body have been considered. However, in many applications, it is of interest to image a transverse body section (that is, one which is perpendicular to the patient's longitudinal axis). This is of particular relevance in the diagnosis and treatment of cancer, where the position of the malignant tumour must be accurately located prior to radio-therapy, in order that only the selected tissue is destroyed. Obviously, to enable transverse cross-sections of the neck, thorax, or abdomen to be imaged, tomographic procedures different from those described above are required. The application of conventional techniques to these situations would require the X-ray beam to traverse the entire length of the body. This would mean in turn that both the energy of the radiation would need to be increased to ensure adequate penetration, and the exposure time would have to be lengthened, greatly increasing the danger to the patient. While several early experiments along these lines have been reported (Vallebona 1955, Amisano 1955), the method never found practical application because of its inherent disadvantages.

In the tomographic methods developed up to this time, the radiation impinged on the film almost perpendicularly. The undesirable features of requiring the rays to travel through the body longitudinally in order to image a transverse section, were circumvented by passing the rays transversely across the body and allowing them to fall obliquely onto the film. Experimental work carried out in the period 1938-1947

by Kieffer, Amisano, Frain and Lacroix, and Vallebona was described by Vallebona (1955). The first practical demonstration of axial transverse tomography was given by Vallebona (1947), who used the method which is still principally in use today.

2.4.1 Principle of Transverse Tomography

Apart from the change in the angle of incidence of radiation onto the film, the transverse tomograph operates on essentially the same principle as the longitudinal tomographs previously discussed. The system used for transverse tomography is shown diagrammatically in fig. 2.5. Here the angle Φ (from the horizontal) of the line joining the source and the mid-point of the image plane is decreased relative to that used in longitudinal tomography and the linear motions of the X-ray tube and the film plane are replaced by synchronous rotation of the object and film plate. In a manner analogous to that described for linear tomography, only a single plane within the object is imaged sharply on the film, while all other planes give rise only to blurred images. Note that the obscuring motion in transverse tomography, is the same as that present when circular motion is used in longitudinal tomography. In some cases, X-ray tomographic units have been designed to be used for both applications (Amisano 1955). By decreasing the angle Φ in fig. 2.5 towards zero, the effect of blurring due to planes other than that being studied is minimised (effectively reducing the thickness of the section being imaged). Some blurring of the tomogram still persists. The explicit nature of this residual blurring is further considered in chapter 7.

2.5 Extensions to Basic Techniques

It was shown geometrically by Andrews and Stava (1937) that to change the section being imaged in any tomographic system, all that was required was to move the film to another plane parallel to the original. This led to the technique of multi-section radiography both in longitudinal and transverse tomography (c.f. "Solidography"; Takahashi 1965). When using these methods, a cassette loaded with a number of parallel film plates, appropriately spaced, is exposed by the transmitted radiation during the period of obscuring motion (fig. 2.6). In this way, a number of planes of the body are selectively imaged simultaneously, rather than the single plane of the previously described methods. The set of film plates, when viewed together on development, provide a three-dimensional representation of the irradiated volume. In longitudinal tomography, intensifying screens and films of varying sensitivity are used to ensure that the photographic effect on the lowest plate is equivalent to that on the uppermost film. In transverse tomography, because of the obliquity of the rays striking the film, and hence the increased attenuation caused by the intensifying screens, it was found (Takahashi 1965) that best results are achieved using non-screen films.

Transverse body-section radiography has assumed greatest importance in the field of radiotherapy treatment planning, along with the related technique of radiotherapy similation. These techniques are used to determine the shape of the effective area of therapeutic radiation within the body during radiotherapy. Having determined the position of the tumour, and the appropriate shape of the radiation beam, therapy may be carried out without undue damage to healthy tissue.

While the earlier transverse tomographs produced tomograms while the patient was rotated in an upright position, most of the more modern machines enable the patient to lie stationary and horizontal. This type of apparatus ensures that the organs of the patient remain in the same position for both transverse tomography and radiotherapy treatment, but in turn requires the use of a more complicated device than that used previously. Instead of the X-ray tube remaining stationary, it must be able to move around the patient in a planetary motion, remaining in opposition to the film plate which is rotating about an axis.

The techniques of transverse tomography have also found industrial applications. In the non-destructive testing of multi-layer printed circuit boards, it is desirable to be able to image individual layers which may only be .1 mm apart. Semler and Moler (1967) have developed a precision transverse tomograph for this purpose, and are able to image layers as thin as .05 mm.

2.6 Elimination of Blur

While loss of detail, due to blurring, is known to be present in all the tomographic methods cited, little effort has been made to reduce or eliminate it. In some instances circular or hypocycloidal obscuring motions may be used to reduce the effect of blurring, but this is seldom practical economically in view of the complexity and cost of areal tomographic systems. With this in mind, Edholm and Quiding (1970) describe a method of approximately "deblurring" linear tomograms. A preliminary tomogram is made in the conventional

way while a second is made from the first by a contact printing process. By moving the original tomogram linearly in the direction of the blur while the copying process takes place, the detail of the fulcrum plane is obscured, while the original blurring remains virtually unchanged. Thus the two images, one of the fulcrum plane plus linear blur, and the other of the approximate linear blur only, may be photographically or electronically subtracted to render a sharper image of the required plane. They also describe a similar result achieved using conventional closed circuit television combined with linear electrical filtering methods. Enhancement of the tomogram is effected in this case by applying a high pass filter to the image, causing the fine structure to be accentuated, while the average background level of the image is reduced.

The new method of transverse tomography which is described by Peters (1973) and also in chapter 7 of this thesis, eliminates shadows of the unwanted planes by irradiating only the cross-section to be imaged. Since the remaining blur in the image can in this case be expressed in terms of a linear blurring operation on the original cross-section, an inverse filter may be applied to the tomogram to restore the desired image.

2.7 Related Body-Section Imaging Techniques

Stereoscopic radiography has played its part in providing the radiologist with some degree of three-dimensional information from conventionally formed radiographs. Two X-ray images are made from slightly different angles, and the result, when one picture is viewed with each eye, is an image which

provides the viewer with the illusion of depth. The result is similar to conventional photographic stereoscopy. While this method is of definite advantage to the radiologist in some situations, he is limited by the lack of true three-dimensional information, as the image cannot exhibit parallax on movement of the viewer's head.

This difficulty may be overcome using a television fluoroscopy system (Stauffer et al. 1962). Two X-ray sources each produce fluoroscopic images which are relayed to television monitors, one of which is viewed with each eye. Here a real-time stereoscopic image is made available to the radiologist, and by varying the angle of view of the X-ray sources and television cameras, he may effectively 'look around' a particular feature. However, it is not possible with such a system to obtain a hard-copy image of a particular plane or planes within the object.

A variety of techniques has been suggested to overcome this objection and to make arbitrary views of the object more accessible. These methods combine a number of distinct projections in order to reconstruct a three-dimensional image volume. Most of these methods are based on holography.

In optics, holography has provided a means of efficient storage and retrieval of three-dimensional images, but these techniques have not yet been extended into the field of radiography directly, since neither a coherent X-ray source of sufficient power, nor a suitable recording medium is feasible at present. However, the properties of holograms made with coherent light may be simulated by combining a number of radiographic projections of the object onto a single high

resolution film using optical holography. When this 'pseudo-hologram' is illuminated with coherent light, three-dimensional real and virtual images are formed in space. While these images exhibit perspective, they do not appear continuous, but rather jump discontinuously as the reconstructed volume is observed from angles corresponding to those at which the original projections were formed.

Holographic methods of this type have been described by Redman et al. (1968), Baily et al. (1971), Groh and Kock (1970) and Chau (1971). An alternative method ('Tomosynthesis') which reconstructs the three-dimensional volume directly without the need to form an intermediate hologram, was described by Grant (1972). In this case the individual shadowgrams (typically 20) are projected optically into an image volume of a size comparable to that of the original object.

Other authors have suggested different methods of producing tomograms from a number of individual views of the body. These include techniques which optically or photographically superimpose up to eight individual projections to obtain a tomogram of any desired longitudinal plane within the body (c.f. Miller et al. 1971), and which record information relating to a number of different radiographic views of the object onto a single film by means of a lenticular lens (Shechter et al. 1971). In the latter case, a three-dimensional virtual image is observed when the film is viewed through a similar lens.

2.8 Mathematical Methods

Many other disciplines besides radiography have encountered the problem of reconstructing two-dimensional or three-dimensional distributions from a series of one-dimensional or two-dimensional projections. Ever since electronic digital computers have been in general use, mathematical techniques have received considerable attention in such diverse fields as radio astronomy and molecular biology. These methods differ from those considered in the previous part of this chapter in that the observed data is processed numerically in order to produce the desired cross-sectional or volumetric image.

Mathematically, the problem is that of reconstructing a three-dimensional function from its two-dimensional projections. The problem may be simplified to some extent by considering the volume to be composed of a number of stacked planes and then reconstructing each of these planes from its one-dimensional projections. In this form, the measured data and the required image are related by an integral transform, which is discussed in detail in chapter 3.

The earliest reference to the problem appears to be by Radon (1917) when discussing the representation of a function in terms of its plane integrals. Later John (1955, p.13) extended this method to express a function of n variables, in terms of its integrals over (n-1) dimensional hyperplanes. The earliest practical application of these techniques was in radio astronomy by Bracewell (1956), who described methods of reconstructing two-dimensional intensity distributions of celestial objects by making one-dimensional measurements with a radio telescope. He was among the first to use Fourier

transforms explicitly to evaluate two-dimensional distributions from one-dimensional data, using a theorem which relates the one-dimensional Fourier transforms of projections of a two-dimensional function, to the Fourier transform of the two-dimensional function itself. Bracewell and Riddle (1967) published a variation of this technique which operates on the measured data directly rather than on the Fourier transforms of the data.

In recent years, reconstruction techniques have assumed importance in the field of electron microscopy. The considerable attention which has been devoted to the study of reconstruction methods in this area was initiated by De Rosier and Klug (1968). Much subsequent work has been undertaken by their group (c.f. Crowther et al. (1970), Crowther (1971), Klug and Crowther (1972) and Gilbert (1972a,b)), who use Fourier methods similar to that proposed by Bracewell (1956). Their application of this approach appears to be an extension of earlier work by some of the group in the field of X-ray crystallography. A statement of the Fourier transform solution to the problem may also be found in literature relating to this subject (c.f. Klug et al. 1958).

A second group, also concerned with the reconstruction of electron micrograph images, has proposed an iterative method ('ART') for reconstructing cross-sections from a small number of views (Gordon et al. 1970, Gordon and Herman 1971). The relative merits of 'ART' and the Fourier techniques have recently been the subject of some controversy (Bellman et al. 1971, Crowther and Klug 1971). Further comments on 'ART' are made in chapters 4 and 6.

Vainshtein (1971a,b) has also proposed methods of reconstructing images from electron micrographs. He suggests further numerical methods for manipulating the micrograph data to form two-dimensional cross-sections.

While much of the emphasis placed on these reconstruction techniques arises from the desire to reconstruct three-dimensional structures from electron micrographs, it is interesting to note that all of the methods proposed by the electron microscopists (in spite of some claims made to the contrary by Gordon et al. 1970), require data to be collected from views of the object spaced throughout 180 degrees. However, with presently available equipment, it is impossible to view a single sample on a tilt stage of an electron microscope over an angular range of more than about 15 or 20 degrees. In spite of this severe limitation, Crowther et al. (1970) have shown that their methods are powerful for reconstructing objects for which certain symmetries exist or may be assumed. Also, if a large number of samples of the specimen being imaged can be viewed (their relative orientations must be known or assumed a priori) then the projections from a number of samples may be combined to give an image which is representative of that particular class of object. Various mathematical techniques for dealing with data of this sort are described by Crowther et al. (1970) and De Rosier and Moore (1970).

The problem of reconstructing binary digital patterns (i.e. patterns whose elements take on only the values 0 or 1) from their projections has also been studied from the point of view of data compression. If a digitized image could be represented unambiguously by a small number of projections, then the computer storage required to represent the image would be reduced. Chang (1971) gave the conditions under which a binary pattern may be reconstructed from two projections,

and also gave algorithms for reconstructing such patterns from multiple views (Chang and Shelton 1971). Gordon and Herman (1971) also suggested data compression (or bandwidth reduction) as a possible application of their algorithms.

2.9 Computational Reconstruction Techniques in Medicine

Cormack (1963,1964) recognised a radiological application of the reconstruction problem. He considered an anatomical structure to be scanned with a pencil beam of gamma rays which were detected by a scintillation counter placed in opposition to the radiation source. The attenuation of the beam as the body is scanned, may be directly related to the integral of the gamma ray absorptivity in the path of the ray. By making such measurements of the object from a number of directions, and curve-fitting the data with suitable functions, he was able to express the data in terms of polynomial coefficients. Reconstruction of an image of the object was effected by making a transformation on the polynomials, so that the required cross-section is also expressed in terms of the previously determined coefficients.

Fourier transform techniques for image reconstruction in medicine were suggested by Tretiak et al. (1968), and Bates and Peters (1971). Various computational examples have been given by Peters et al. (1973) and Smith et al. (1973) who also describe an extension to Cormack's work. Ramachandran and Lacshminarayanan (1971a,b) proposed a technique similar to the method of Bracewell and Riddle (1967) for the reconstruction of images from radiographic projections.

Goitein (1972) has developed algorithms using iterative relaxation techniques to solve the reconstruction problem in

radiography, and a commercial device recently marketed by EMI Ltd (1972) was developed by Hounsfield (1972). This machine is designed to image accurate cross-sections of the brain. It uses a scanning method similar to that proposed by Cormack (1964) and processes the data in a computer using an iterative algorithm similar to 'ART' (Gordon et al. 1970) to reconstruct the images. Chang and Chow (1973) have presented a method for reconstructing the boundaries of specialised two-dimensional objects from a pair of orthogonal projections.

A further novel approach to the problem has been suggested by Farmer and Collins (1971). They used a pencil beam of gamma rays to scan a section of the body, but instead of detecting the transmitted beam, the energy of photons scattered by the Compton effect was measured. The energy of these photons may be related to the scattering angle, and hence to the distance along the beam from which the scattering occurred. The amount of radiation scattered from each point in the section, and thus the density distribution of the section itself, may be measured in this manner.

Nuclear medicine is a field which is particularly amenable to computer processing of data, as it is becoming common practice to have radioisotope scanners and scintillation cameras (also known as 'Anger-' or 'gamma' cameras) interfaced to small computers. In this field, instead of measuring the total attenuation of a beam traversing the object, one observes the emitted radiation from an isotope within the body. It is the spatial distribution of this isotope, rather than the density of the object itself, which is of interest. Techniques for reconstructing three-dimensional isotope distributions from scintigraphic projections have been

proposed by Kuhl and Edwards (1968,1970),Kuhl et al. (1972) and Muehllehner and Wetzel (1970). Other systems which simulate conventional radiographic tomography include those suggested by Freedman (1972) and Rider et al. (1972) who use rotating collimators attached to the gamma camera, and by Anger (1968) who employs a scanning pinhole collimator and a series of optical systems to image a number of tomographic layers simultaneously.

2.10 Viewing of Three-Dimensional Images

When viewing a three-dimensional image of anatomical structure, there arises the conceptual problem of unambiguously displaying all of the information relating to the volume. This situation does not normally arise when considering conventional optics or holography, as one is generally dealing with images of only the surfaces of physical objects. However, with three-dimensional images of internal body-structure, one would like to see not only the boundaries of the organs, but also their interiors, especially if the position of a tumour or cyst is being sought.

This problem may be overcome to some extent by forming a real image in space, and by observing selected planes by interposing an opaque screen (as in 'Tomosynthesis'; Grant 1972), and so forming an image of a particular section. The section being viewed may then be altered simply by moving the screen to another part of the image volume. As previously pointed out, this image still suffers from distortions similar to tomographic blur.

Some of the imaging methods already described produce a series of two-dimensional sections of the object rather than the three-dimensional volume per se. The normal method of deriving the three-dimensional information from the serial sections is to view each in turn and form a mental picture of the volume.

The cross-sectional pictures may be printed on transparent slides and physically stacked to build up the required image (Baum and Greenwood 1961). While providing some useful information, this method suffers from difficulties in viewing through the edges of the slides, and the opacity of the information bearing areas.

Another approach is to display the images sequentially on the face of a cathode ray tube, and to reflect these pictures to the observer by means of a vibrating varifocal mirror (Rawson 1969). A varifocal mirror is a concave mirror whose focal length may be varied electronically. In this manner the observer is presented with an image which appears to possess the required three-dimensional qualities.

If the sequence of reconstructed sections is in digital form, then the various planes of the three-dimensional volume may be computed and displayed using the techniques described by Robinson (1972). He presents procedures for interpolating between the various sections using a digital computer in order to provide images of arbitrary cuts through the volume. The interpolated plane is then displayed on the face of an oscilloscope in the normal manner.

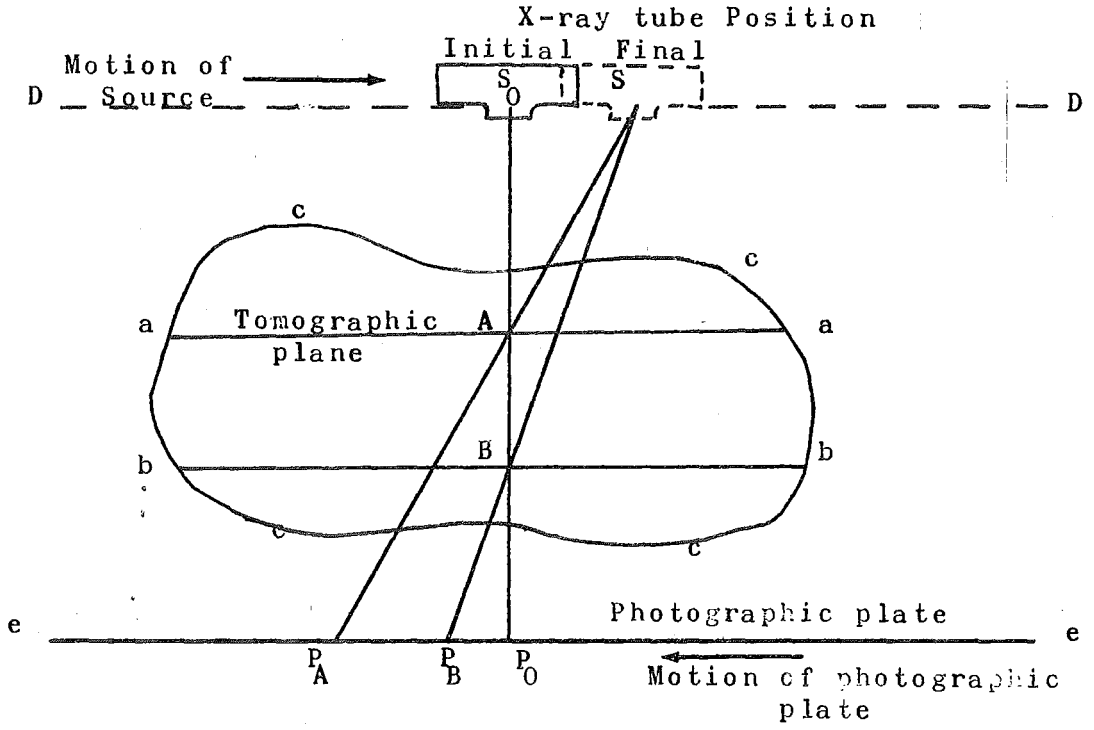

Fig. 2.1. Bocages tomographic methods.

a) Method A. The X-ray film and source move in opposite directions in parallel planes. The X-ray tube S remains horizontal throughout the imaging procedure. The central ray from the source remains perpendicular to the film.

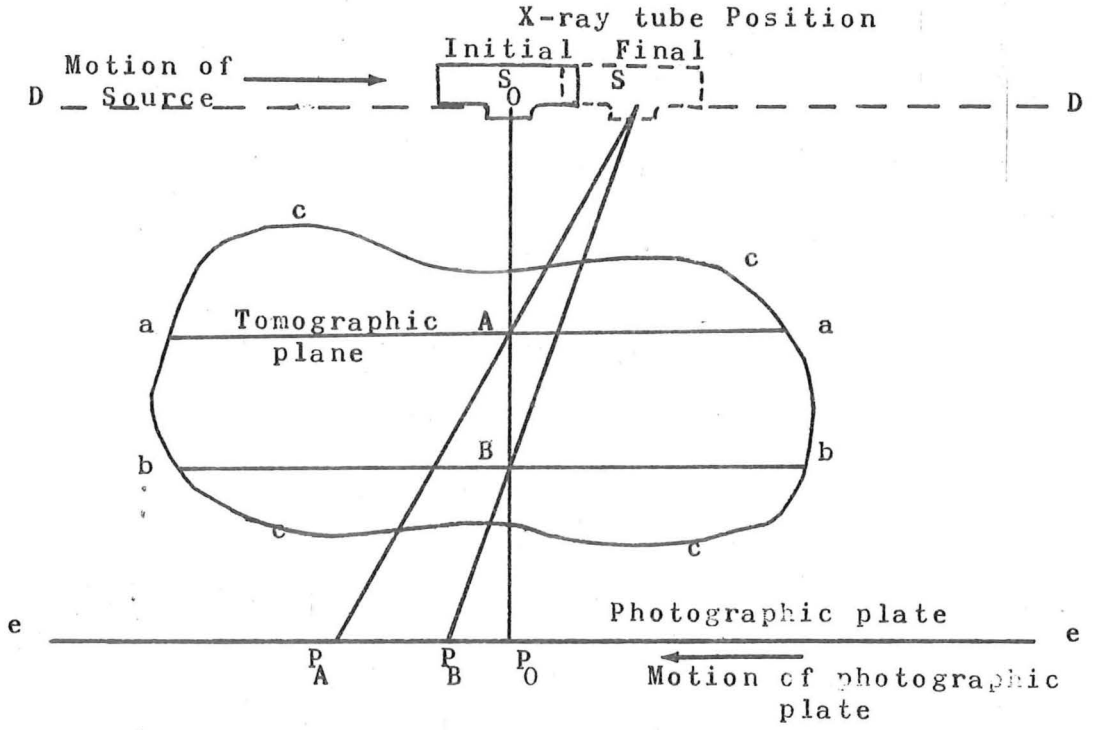

Fig. 2.1. Bocages tomographic methods.

a) Method A. The X-ray film and source move in opposite directions in parallel planes. The X-ray tube S remains horizontal throughout the imaging procedure. The central ray from the source remains perpendicular to the film.

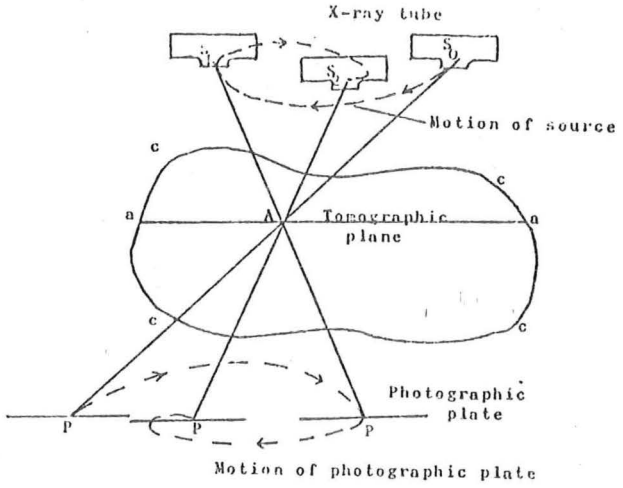

b)

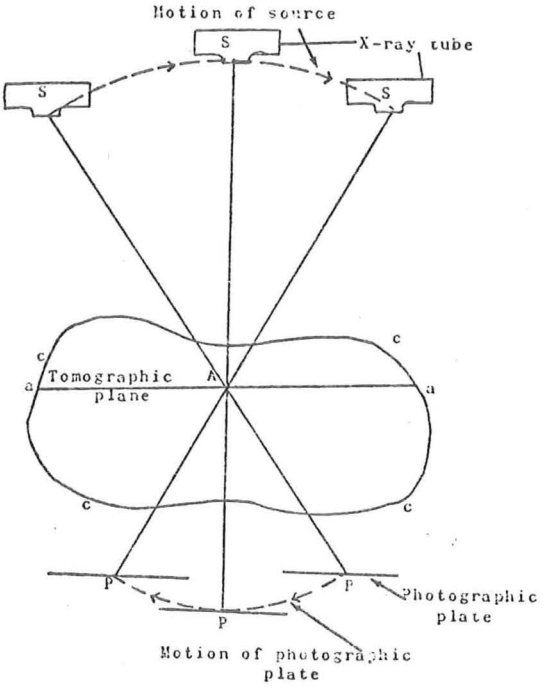

c)

b) Method B. The tube and film remain in parallel planes as in method A, but describe more general obscuring motions, e.g. circles, spirals, or crosses.

c) Method C. The X-ray source and film describe arcs about a point in the tomographic plane. The source moves in the arc s-s-s, while the photographic film moves in the arc P-P-P.

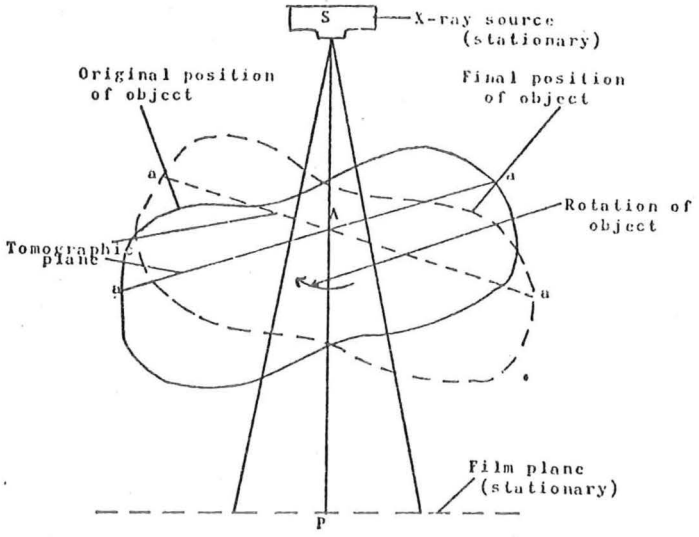

Fig. 2.2. Vallebona's tomographic method.
X-ray tube and film remain stationary while the object is rotated through a small arc about a point A in the tomographic plane.

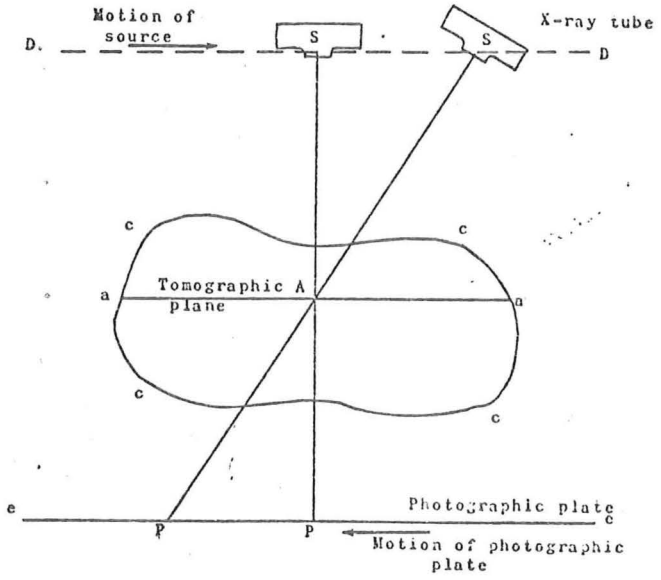

Fig. 2.3. Zeidses des Plantes' tomographic method.
X-ray tube moves along the line D-D while the film moves along e-e. Tube is always tilted during imaging motion so that the central ray always passes through a particular point in the tomographic plane. System is capable of single or multi-directional obscuring motion.

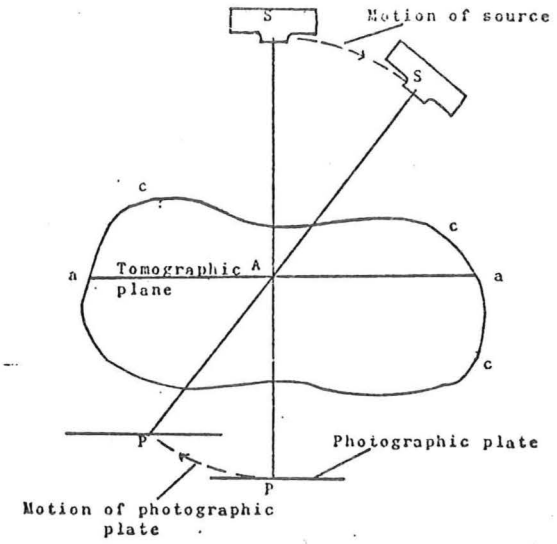

Fig. 2.4. Grossman's tomographic method.
X-ray source and film describe arcs about a point in the tomographic plane. The tube is tilted so that the central ray always passes through a single point in the tomographic plane, while the film remains horizontal.

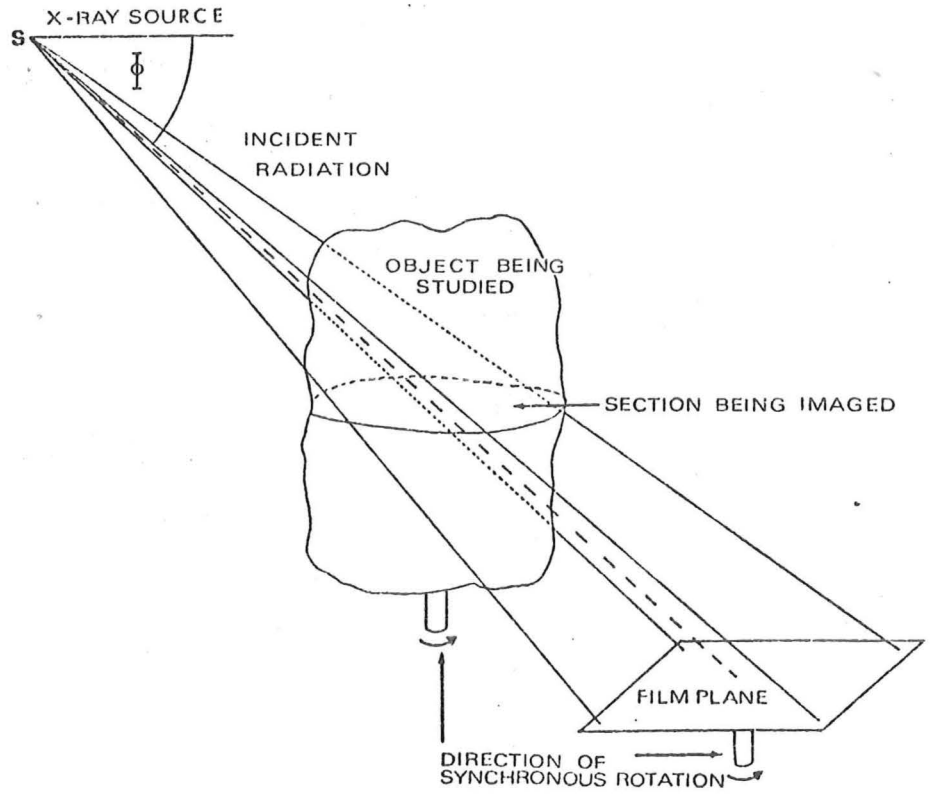

Fig. 2.5. Transverse tomography.
Incident radiation originating from point S is transmitted through the object and impinges on the film plane. Obscuring motion is provided by the synchronous rotation of both the object and film.

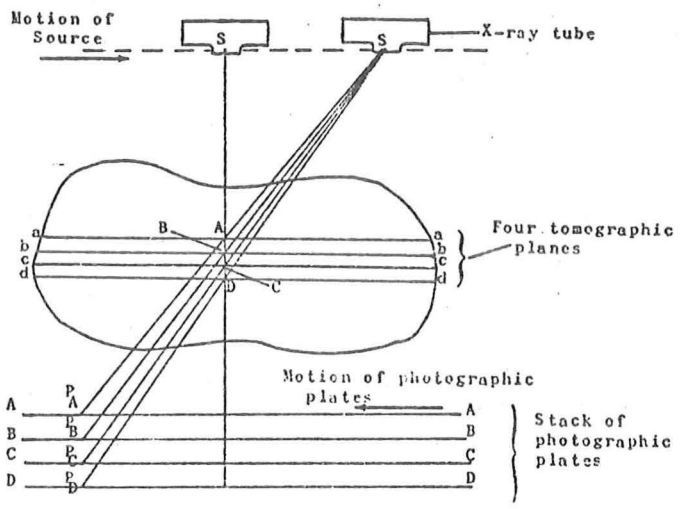

Fig. 2.6. Multi-plane tomography.

The system shown here is based on Bocage's method A, but other methods may be used also. Since different planes within the body come to 'focus' at different planes below the body, separate films may be used to provide a number of tomograms simultaneously.

CHAPTER 3

RADIATION TRANSFORMS

3.1 Introduction

This chapter is concerned with a number of formulae relating to the reconstruction of images from radiographic data. Because of their association with radiography, these formulae have previously (Bates and Peters 1971) been given the name 'radiation transforms', and are concerned with imaging one or a number of planes of an object, using knowledge of the (radiographic) projections of these planes. In practice the intensity of the transmitted radiation is recorded by some device, typically a photographic plate. The optical density (D) of the developed plate is related to the exposure (E) by

$$D = -\gamma \log_{10} E \tag{3.1}$$

where γ is the slope of the linear part of the Hurther and Driffield curve for the particular film (James and Higgins, 1948), and the exposure is defined as the intensity of the transmitted radiation multiplied by the exposure time. The intensity I of the radiation after it has been transmitted through the object, is related to the intensity I_0 of the incident radiation by

$$I = I_0 \exp\left(-\int_{-\infty}^{\infty} \omega(x)\,dx\right) \tag{3.2}$$

where $\omega(x)$ is the radiation absorption coefficient (in the x direction) peculiar to the object being imaged. The value of $\omega(x)$ depends upon the nature of the radiation being used. By combining eqns (3.1) and (3.2) the quantity

$$\int_{-\infty}^{\infty} \omega(x)\,dx$$

may be inferred directly from a measurement of the optical density D of the developed film.

Section 3.2 deals with necessary definitions to establish notation, while section 3.3 outlines the derivations of four distinct radiation transform formulae. Three of these formulae assume that the projections are formed by a parallel beam of radiation passing through the object, while the fourth shows how an image of a plane may be reconstructed when the radiation is diverging through the object.

The first radiation transform formula relates the image of a plane of an object to its projections, through the use of one-dimensional and two-dimensional Fourier transform operations. Image reconstruction procedures based on this formula are called Fourier Transform Reconstruction (FTR) methods. The second radiation transform formula is a variation of the FTR formulation. It suggests a reconstruction procedure which is most easily described in terms of linear system theory. This procedure is called the Rho-Filtered Layergram (RFL) reconstruction method. While both the FTR and RFL methods depend upon the explicit use of Fourier transforms, it is possible to develop a formula, relating an image to its projections, which does not require the computation of Fourier transforms. Image reconstruction procedures based on this third radiation transform formula are called Density Space Reconstruction (DSR) methods. The fourth radiation transform formula applies when the rays diverge through the object. Image reconstruction procedures based on this fourth formula are called Diverging Ray Reconstruction (DRR) methods.

They are closely related to the FTR and RFL methods.

Section 3.4 examines the relationships existing between the radiation transform formulae.

3.2 Definitions

Both the geometrical term cross-section and the medical term section are used when referring to the plane of an object under study. The density of the two-dimensional cross-section of an object is denoted by $\omega(x,y)$ in Cartesian coordinates, and $\lambda(r,\theta)$ in polar coordinates (fig. 3.1a). The descriptive term density, as used here, is synonymous with X-ray absorptivity. The mass μ associated with the density is

$$\mu = \int_{-\infty}^{\infty}\int \omega(x,y)\,dxdy = \int_{-\infty}^{\infty}\int \omega(x,y)\,d\xi d\eta = \int_{0}^{a}\int_{0}^{2\pi} \lambda(r,\theta)\,rdrd\theta \qquad (3.3)$$

where the infinite limits on the first two double integrals imply that μ is the total mass. The Cartesian coordinate system (ξ,η) is rotated from (x,y) by an angle ϕ (fig. 3.1a). The finite radial limit on the third integral indicates that the extent of the cross-section under study is normalised by requiring that it is completely enclosed by a circle of radius a (fig. 3.1a).

Unless otherwise stated, the radiation passes through a particular cross-section in parallel straight lines. The variation of density throughout this cross-section is $\omega(x,y)$. The intensity of each ray of the radiation, having passed through the cross-section, is attenuated by a factor dependent upon the integrated density along the ray. It is from sets of measured values of this attenuation that an image of the cross-section is reconstructed. It is perhaps worth noting

that whereas images formed by wave fields are usually in planes perpendicular to radiation beams, in this case the image is parallel to the radiation beam.

For a particular value of ϕ (fig. 3.1a), the integrated density along lines perpendicular to the ξ axis is called a projection or shadowgram, and is denoted by $f(\xi,\phi)$. The set of all projections, for $0 \leq \phi < \pi$, is termed the projected density. So, in terms of the density, $f(\xi,\phi)$ is given by

$$f(\xi,\phi) = \int_{-\infty}^{\infty} \omega(x,y)\,d\eta = \int_{-\infty}^{\infty} \lambda(r,\theta)\,d\eta \qquad (3.4)$$

Note, from (3.3) and (3.4) that

$$\int_{-\infty}^{\infty} f(\xi,\phi)\,d\xi = \mu \qquad (3.5)$$

The two-dimensional Fourier transform of the density distribution $\omega(x,y)$ is denoted by $\Omega(\alpha,\beta)$ in Cartesian coordinates, and $\Lambda(\rho,\phi)$ in polar coordinates (fig. 3.1b) where

$$\Omega(\alpha,\beta) = \Lambda(\rho,\phi) = \int\int_{-\infty}^{\infty} \omega(x,y)\ \exp(j2\pi[\alpha x+\beta y])\,dxdy \qquad (3.6)$$

$$= \int_0^a \int_0^{2\pi} \lambda(r,\theta)\ \exp(j2\pi\rho r\cos(\theta-\phi))\,rd\theta dr \qquad (3.7)$$

The Fourier inverses of eqns (3.6) and (3.7) are

$$\omega(x,y) = \lambda(r,\theta)$$

$$= \int_{-\infty}^{\infty}\int \Omega(\alpha,\beta)\ \exp(-j2\pi[\alpha x+\beta y])\,d\alpha d\beta \qquad (3.8)$$

$$= \int_{0}^{\infty}\int_{0}^{2\pi} \Lambda(\rho,\phi)\ \exp[-j2\pi\rho r\cos(\theta-\phi)]\,\rho\,d\phi d\rho \qquad (3.9)$$

Upper and lower case versions of a particular symbol are used to denote a Fourier transform pair.

The notation $\mathfrak{F}_{(n)}\{\cdot\}$ is used to denote an n-dimensional Fourier transform, of the function enclosed by the brackets, from the real plane to the transform plane (fig. 3.1a,b). $\mathfrak{F}_{(n)}^{-1}\{\cdot\}$ is used for the inverse n-dimensional transform. For a one-dimensional transform of a function which depends explicitly on more than one variable, it is necessary to specify the variable with respect to which the transform is taken, (i.e. which variable becomes the variable of integration in the Fourier integral.) This is done for the variable ξ by writing $\mathfrak{F}_{(1)\xi}\{\cdot\}$.

3.3 Radiation Transform Derivations

3.3.1 Fourier Transform Reconstruction (FTR)

The relationship between the projected density and the cross-section from which the projected density is obtained may be derived by rewriting eqn (3.4) with $\omega(x,y)$ expressed in terms of its Fourier transform $\Omega(\alpha,\beta)$:

$$f(\xi,\phi) = \int_{-\infty}^{\infty}\int\int \Omega(\alpha,\beta)\ \exp(-j2\pi[\alpha x+\beta y])\,d\alpha d\beta d\eta \qquad (3.10)$$

By expressing x and y in terms of the rotated coordinates (ξ,η), and using $\delta(\xi)$ to denote the Dirac delta function of argument ξ, the projected density may be written as

$$f(\xi,\phi) = \int_{-\infty}^{\infty}\iiint \Omega(\alpha,\beta)\exp(-j2\pi[(\alpha\cos\phi + \beta\sin\phi)\xi - (\alpha\sin\phi - \beta\cos\phi)\eta])d\eta d\alpha d\beta \quad (3.11)$$

$$= \int_{-\infty}^{\infty}\iint \Omega(\alpha,\beta)\exp(-j2\pi[\alpha\cos\phi + \beta\sin\phi]\xi)\,\delta(\alpha\sin\phi - \beta\cos\phi)\,d\alpha d\beta \quad (3.12)$$

$$= \sec\phi \int_{-\infty}^{\infty} \Omega(\alpha,\alpha\tan\phi)\exp(-j2\pi\xi\alpha\sec\phi)\,d\alpha. \quad (3.13)$$

$$= \int_{-\infty}^{\infty} \Omega(\rho\cos\phi,\rho\sin\phi)\exp(-j2\pi\rho\xi)\,d\rho;\ \rho = \alpha\sec\phi \quad (3.14)$$

$$= \int_{-\infty}^{\infty} \Lambda(\rho,\phi)\exp(-j2\pi\rho\xi)\,d\rho. \quad (3.15)$$

The Fourier inverse of eqn (3.15) is

$$\Lambda(\rho,\phi) = \int_{-\infty}^{\infty} f(\xi,\phi)\ \exp(j2\pi\rho\xi)\,d\xi \quad (3.16)$$

so that the FTR radiation transform formula may be written as

$$\lambda(r,\theta) = \omega(x,y) = \mathfrak{F}^{-1}_{(2)}\{\mathfrak{F}_{(1)\xi}\{f(\xi,\phi)\}\} \quad (3.17)$$

The FTR formula forms the basis of the reconstruction techniques proposed by Bracewell (1956), Tretiak et al. (1969) and Crowther et al. (1970).

3.3.2 Rho-Filtered Layergram (RFL)

An image which is related to the actual cross-section is obtained by replacing each point in the cross-section by the integral of all possible projections through that point. This image, denoted by $h(x,y)$ in Cartesian coordinates or $g(r,\theta)$ in polar coordinates, is called a layergram (after Bates and Peters 1971), and is defined in the following manner, where the variables in eqn (3.18) relate to fig. 3.2 .

$$h(x,y) = g(r,\theta) = \int_0^{\infty}\int_0^{2\pi} \lambda(r',\theta')\,d\tau\,dX. \qquad (3.18)$$

In fig. 3.2 the point P has coordinates (r,θ) whilst the point P' has coordinates (r',θ'). By writing $\lambda(r,\theta)$ in terms of its Fourier transform, the layergram may be expressed as

$$g(r,\theta) = \int_0^{\infty}\int_0^{2\pi}\int_0^{\infty}\int_0^{2\pi} \Lambda(\rho,\phi)\,\exp(-j2\pi\rho r'\cos(\theta'-\phi))\,\rho\,d\phi\,d\rho\,d\chi\,d\tau \qquad (3.19)$$

$$= \int_0^{\infty}\int_0^{2\pi}\int_0^{\infty}\int_0^{2\pi} \Lambda(\rho,\phi)\,\exp[-j2\pi\rho r\cos(\phi-\theta)]$$

$$.\exp[-j2\pi\rho\tau\cos(\phi-\chi)]\,\rho\,d\phi\,d\rho\,d\chi\,d\tau \qquad (3.20)$$

by inspection of fig. 3.2 . By expanding the second exponential function in terms of a Bessel function series (Abramowitz and Stegun 1965, formulae 9.1.44, 9.1.45) and integrating with respect to χ, the following is obtained.

$$g(r,\theta) = 2\pi \int_0^{\infty}\int_0^{2\pi} \Lambda(\rho,\phi)\exp(-j2\pi\rho r\cos(\phi-\theta))J_0(2\pi\rho\tau)\rho d\phi d\rho d\tau \tag{3.21}$$

$$= \int_0^{\infty}\int_0^{2\pi} \Lambda(\rho,\phi)\ \exp(-j2\pi\rho r\ \cos(\phi-\theta))d\phi d\rho \tag{3.22}$$

using formula 11.4.17 of Abramowitz and Stegun (1965). The Fourier inverse of eqn (3.22) is

$$\rho^{-1}\Lambda(\rho,\phi) = \int_0^{\infty}\int_0^{2\pi} g(r,\theta)\exp(j2\pi\rho r\ \cos(\theta-\phi))rd\theta dr. \tag{3.23}$$

Multiplying both sides of eqn (3.23) by ρ and taking the Fourier inverse gives the RFL radiation transform formula:

$$\lambda(r,\theta) = \mathfrak{F}_{(2)}^{-1}\{\rho\mathfrak{F}_{(2)}\{g(r,\theta)\}\}. \tag{3.24}$$

It is the presence of the factor ρ by which the Fourier transform of $g(r,\theta)$ is weighted that gives rise to the expression 'rho-filtered layergram', describing an image that has been reconstructed in this way (Bates and Peters 1971, Peters 1973). Rho-filtered layergrams are discussed in more detail in chapters 4 and 7.

Applying the convolution theorem for Fourier transforms (Bracewell 1965, ch.6) to eqn (3.23), the layergram may be expressed in terms of the density as

$$g(r,\theta) = \lambda(r,\theta) * \mathfrak{F}_{(2)}^{-1}\{\rho^{-1}\}, \tag{3.25}$$

where the in-line asterisk denotes convolution. Now,

$$\mathfrak{F}_{(2)}^{-1}\{\rho^{-1}\} = 2\pi \int_0^{\infty} \rho^{-1}\ J_0(2\pi\rho r)\rho d\rho \tag{3.26}$$

$$= r^{-1} \tag{3.27}$$

as can be shown by making use of formula 11.4.17 of Abramowitz and Stegun (1965). So the layergram can be written as

$$g(r,\theta) = \lambda(r,\theta) * r^{-1} \tag{3.28}$$

Note that since r^{-1} is a two-dimensional function, the simple pole that it possesses at $r = 0$ is integrable, and so the convolution integral exists. $\lambda(r,\theta)$ may be considered as the input to an imaging system, and $g(r,\theta)$ as the output. The output is said to be related to the input by a convolution of the input with the point-spread function of the system (i.e. r^{-1} in eqn 3.28). The convolution relationship expressed by eqn (3.28) may be derived in a different manner without the use of Fourier transforms. Consider the original definition of the layergram as given by eqn (3.18):

$$g(r,\theta) = \int_0^{\infty}\int_0^{2\pi} \lambda(r',\theta')\,d\tau\,d\chi. \tag{3.29}$$

From the geometry of fig. 3.2, eqn (3.29) may be re-expressed as

$$g(r,\theta) = \int_0^{\infty}\int_0^{2\pi} \frac{\lambda(r',\theta')\,\tau\,d\tau\,d\chi}{((x'-x)^2+(y'-y)^2)^{\frac{1}{2}}} \tag{3.30a}$$

By changing the variables of integration from polar to Cartesian, eqn (3.30) becomes:

$$h(x,y) = \int_{-\infty}^{\infty}\int \frac{\omega(x',y')\,dx'\,dy'}{((x'-x)^2+(y'-y)^2)^{\frac{1}{2}}} \tag{3.30b}$$

$$= \omega(x,y) * (x^2+y^2)^{-\frac{1}{2}} \tag{3.31}$$

or alternatively

$$g(r,\theta) = \lambda(r,\theta) * r^{-1} \tag{3.32}$$

as derived previously in eqn (3.28).

It is also convenient to express the layergram explicitly in terms of the projected density. Writing the RHS of eqn (3.32) in terms of its Fourier transform, gives

$$g(r,\theta) = \int_0^{2\pi}\int_0^{\infty} \rho^{-1}\Lambda(\rho,\phi)\ \exp(-j2\pi\rho r\ \cos(\theta-\phi))\rho d\rho d\phi \tag{3.33}$$

$$= \int_0^{\pi}\int_{-\infty}^{\infty} \Lambda(\rho,\phi)\ \exp(-j2\pi\rho r\ \cos(\theta-\phi))d\rho d\phi \tag{3.34}$$

The change in the limits of integration is justified since $\Lambda(\rho,\phi)$ may be written as $\Lambda(-\rho,\phi+\pi)$. If eqn (3.15) is substituted into eqn (3.34), the expression for the layergram becomes

$$g(r,\theta) = \int_0^{\pi} f(r\ \cos(\theta-\phi),\phi)d\phi. \tag{3.35}$$

Expressed in this way, the projections are said to be 'back-projected' (Gilbert 1972a) onto the (r,θ) plane to form the layergram.

An alternative version of the RFL radiation transform formula can be derived by writing $\lambda(r,\theta)$ in terms of its Fourier Transform (eqn 3.9), and again changing the limits of integration, so that

$$\lambda(r,\theta) = \int_{-\infty}^{\infty}\int_0^{\pi} |\rho|\Lambda(\rho,\phi)\ \exp[-j2\pi\rho r\ \cos(\theta-\phi)]d\phi d\rho \tag{3.36}$$

Now define $\hat{f}(\xi,\phi)$ to be the inverse Fourier transform, with respect to ρ, of $|\rho|\Lambda(\rho,\phi)$. This gives

$$\lambda(r,\theta) = \int_0^{\pi} \hat{f}(r\cos(\theta-\phi),\phi)d\phi. \qquad (3.37)$$

It is useful to think of $\hat{f}(\xi,\phi)$ as being the projected density modified by a one-dimensional rho-filtering operation, since eqns (3.36) and (3.37) give

$$\hat{f}(\xi,\phi) = \mathfrak{F}^{-1}_{(1)\rho}\{|\rho|\,\mathfrak{F}_{(1)\xi}\{f(\xi,\phi)\}\}. \qquad (3.38)$$

Expressions in forms similar to eqns (3.37) and (3.38) have been presented previously by Bracewell and Riddle (1967), Gilbert (1972a) and Ramachandran and Lakshminarayanan (1971a,b). In each case the authors suggest modifying the projected density by a convolution, rather than by taking the Fourier transform of the data and rho-filtering before computing the inverse transform.

3.3.3 Density Space Reconstruction (DSR)

A formula which does not require the explicit evaluation of Fourier transforms for reconstructing the cross-section from its projected density, is considered below. Substitution of eqn (3.16) into eqn (3.9) gives

$$\lambda(r,\theta) = \int_0^{\infty}\int_0^{2\pi}\int_{-a}^{a} f(\xi,\phi)\exp(j2\pi\rho\xi)\exp(-j2\pi\rho r\cos(\phi-\theta))|\rho|\,d\rho d\phi d\xi \qquad (3.39)$$

where the limits of the ξ integral are changed from $(-\infty,\infty)$ to $(-a,a)$ since $f(\xi,\phi)$ is of extent $2a$. It is convenient to use the same change in the integration limits as is used in eqn

(3.34), giving,

$$\lambda(r,\theta) = \int_{-\infty}^{\infty}\int_{0}^{\pi}\int_{-a}^{a} f(\xi,\phi)\exp(-j2\pi\rho(r\cos(\phi-\theta)-\xi))|\rho|\,d\rho\,d\phi\,d\xi \tag{3.40}$$

$$= 2\int_{0}^{\infty}\int_{0}^{\pi}\int_{-a}^{a} f(\xi,\phi)\cos[2\pi\rho(r\cos(\phi-\theta)-\xi)]\rho\,d\rho\,d\phi\,d\xi. \tag{3.41}$$

Integrating by parts with respect to ξ gives

$$\lambda(r,\theta) = -\frac{1}{\pi}\int_{0}^{\infty}\int_{0}^{\pi}\left\{\left[f(\xi,\phi)\sin 2\pi\rho(r\cos(\phi-\theta)-\xi)\right]_{-a}^{a} - \int_{-a}^{a}\frac{\partial f(\xi,\phi)}{\partial\xi}\sin 2\pi\rho(r\cos(\phi-\theta)-\xi)\,d\xi\right\}d\phi\,d\rho \tag{3.42}$$

As long as the value of $f(\xi,\phi)$ approaches zero smoothly as $|\xi|$ approaches a, the first part of the RHS of eqn (3.42) vanishes. Integrating the second part of the RHS of eqn (3.42) with respect to ρ leads to

$$\lambda(r,\theta) = \frac{1}{2\pi^2}\int_{0}^{\pi}\int_{-\infty}^{\infty}\frac{\partial f(\xi,\phi)}{\partial\xi}\left[\frac{\cos 2\pi\rho(r\cos(\phi-\theta)-\xi)}{r\cos(\phi-\theta)-\xi}\right]_{0}^{\infty} d\xi\,d\phi \tag{3.43}$$

$$= -\frac{1}{2\pi^2}\int_{0}^{\pi}\int_{-\infty}^{\infty}\frac{\partial f(\xi,\phi)}{\partial\xi}\frac{d\xi\,d\phi}{(r\cos(\theta-\phi)-\xi)} + \frac{1}{2\pi^2}\int_{0}^{\pi}\int_{-\infty}^{\infty}\frac{\partial f(\xi,\phi)}{\partial\xi}\frac{\cos 2\pi T(r\cos(\phi-\theta)-\xi)}{(r\cos(\phi-\theta)-\xi)}\,d\xi\,d\phi \quad \lim T\to\infty \tag{3.44}$$

$$= -\frac{1}{2\pi^2}\int_{0}^{\pi}\int_{-\infty}^{\infty}\frac{\partial f(\xi,\phi)}{\partial\xi}\frac{d\xi\,d\phi}{(r\cos(\phi-\theta)-\xi)}. \tag{3.45}$$

An expression similar to eqn (3.45) was derived by Berry and Gibbs (1970), and is also a limiting case of the expression presented by John (1955, p.13).

Now the Hilbert transform with respect to x, of a function f(x,y) is defined as

$$\mathcal{H}_x\{f(x,y)\} = -\frac{1}{\pi}\int_{-\infty}^{\infty}\frac{f(\alpha,y)}{(\alpha-x)}\,d\alpha \qquad (3.46a)$$

$$= f(x,y) * (-\frac{1}{\pi x}). \qquad (3.46b)$$

By defining a function $\bar{f}(\xi,\phi)$ in the following manner;

$$\bar{f}(\xi,\phi) = \frac{1}{2\pi}\mathcal{H}_\xi\left\{\frac{\partial f(\xi,\phi)}{\partial \xi}\right\} \qquad (3.47a)$$

eqn (3.45) may be re-expressed in the form

$$\lambda(r,\theta) = \int_0^{\pi}\bar{f}(r\cos(\phi-\theta),\phi)\,d\phi \qquad (3.47b)$$

Note the equivalence of the rho-filtering operation indicated by eqn (3.36) to the combination Hilbert transformation/partial differentiation/back-projection operations of eqns (3.47a,b).

When the object exhibits circular symmetry, the projected density is a function of ξ only. In this case eqn (3.45) reduces to (Whittaker and Watson, 1952, p.229)

$$\lambda(r) = -\frac{1}{\pi}\int_r^{\infty}\frac{\partial f(\xi)}{\partial \xi}\,\frac{d\xi}{(\xi^2-r^2)^{\frac{1}{2}}}\,. \qquad (3.48a)$$

and $f(\xi)$ is known as the Abel transform of $\lambda(r)$. The Abel inverse of eqn (3.48a) is

$$f(\xi) = 2\int_\xi^{\infty}\frac{\lambda(r)\,rdr}{(r^2-\xi^2)^{\frac{1}{2}}}\,. \qquad (3.48b)$$

3.3.4 Diverging Ray Reconstruction (DRR)

3.3.4.1 Formulation Based on FTR Formula

The three radiation transforms described above assume that the radiation passes through the object in parallel rays. In practice, the x-ray source may be close to the object, in which case this assumption is invalid. When the ray divergence is significant, the geometry of the system is given by fig. 3.3 , which shows an arbitrary ray in the beam diverging with an angle ψ from the central ray. The projected density is measured as a function of ξ as previously, but in this instance the measured projection for any ξ is due to the integrated density along the line $v = 0$, rather than along a line parallel to the η axis.

The (x,y) coordinates of points lying on the line $v = 0$ may be written as

$$\begin{aligned} x\big|_{v=0} &= u \sin\psi \cos\phi + (R-a)\sin\phi - u \cos\psi \sin\phi \\ &= u \sin(\psi-\phi) + R' \sin\phi \\ y\big|_{v=0} &= u \sin\psi \sin\phi - (R-a)\cos\phi + u \cos\psi \cos\phi \\ &= u \cos(\psi-\phi) - R' \cos\phi \end{aligned} \qquad (3.49)$$

where $R' = R-a$. Using the relationship

$$\xi = R' \tan\psi, \qquad (3.50)$$

the measured projection at a distance ξ along the ξ axis, of an object with an arbitrary orientation ϕ with respect to the x axis, is denoted by $e(R' \tan\psi, \phi)$. This quantity may be expressed in terms of the density by

$$e(R' \tan \psi, \phi) = \int_{-\infty}^{\infty} \omega(x,y)\Big|_{v=0} du. \tag{3.51}$$

By writing $\omega(x,y)$ as a Fourier transform, eqn (3.51) becomes

$$e(R'\tan\psi,\phi) = \iiint_{-\infty}^{\infty} \Omega(\alpha,\beta)\exp(-j2\pi(\alpha x+\beta y))\,d\alpha d\beta du \tag{3.52}$$

$$= \iiint_{-\infty}^{\infty} \Omega(\alpha,\beta)\exp(-j2\pi[(u\sin(\psi-\phi)+R'\sin\phi)\alpha + (u\cos(\psi-\phi)-R'\cos\phi)\beta])\,d\alpha d\beta du \tag{3.53}$$

by substitution of eqn (3.49) into eqn (3.52). Integrating with respect to u gives a delta function:

$$e(R'\tan\psi,\phi) = \iint_{-\infty}^{\infty} \Omega(\alpha,\beta)\exp(-j2\pi R'[\alpha\sin\phi - \beta\cos\phi])\,\delta(\alpha\sin(\psi-\phi) + \beta\cos(\psi-\phi))\,d\alpha d\beta. \tag{3.54}$$

Integrating this expression with respect to β gives

$$e(R'\tan\psi,\phi) = \sec(\psi-\phi)\int_{-\infty}^{\infty} \Omega(\alpha,\alpha\tan(\phi-\psi))\exp(-j2\pi R'\alpha\sin\psi\sec(\phi-\psi))\,d\alpha \tag{3.55}$$

$$= \int_{-\infty}^{\infty} \Omega(\alpha\cos(\phi-\psi),\alpha\sin(\phi-\psi))\exp(-j2\pi R'\alpha\sin\psi)\,d\alpha. \tag{3.56}$$

Replacing $\phi-\psi$ by Φ and taking the Fourier inverse of eqn (3.56) leads to

$$\Omega(\alpha\cos\Phi,\alpha\sin\Phi) = \Lambda(\rho,\Phi)$$

$$= \int_{-\infty}^{\infty} e(R'\tan\psi,\Phi+\psi)\exp(j2\pi R'\rho\sin\psi)\,d(R'\sin\psi). \tag{3.57}$$

Therefore the first DRR radiation transform formula may be written as

$$\lambda(r,\theta) = \mathfrak{F}^{-1}_{(2)}\left\{\mathfrak{F}_{(1)R'\sin\psi}\{e(R'\tan\psi, \phi+\psi)\}\right\}, \qquad (3.58)$$

where the standard notation (ϕ) for both the angular orientation of the object, and the angular Fourier transform coordinate, is restored.

3.3.4.2 Formulation Based on RFL Formula

The DRR radiation transform formula derived above is an extension of the FTR formula. It might also be expected that the RFL formula could be extended to allow objects to be reconstructed from projections formed by diverging radiation. In this regard, it is of interest to consider the form of a layergram which has been computed from 'diverging-ray' projections. Instead of back-projecting the data along parallel lines as suggested by eqn (3.35), the projections may be projected along sets of lines which match the paths of the imaging rays, fig. 3.3 . The point-spread function of the system may then be computed by considering the layergram of a single point $P(r,\theta)$ within the cross-section.

In fig. 3.3, the line SP represents both the ray passing through the point $P(r,\theta)$, and the back-projection of the projection of this point, when the object is oriented at an angle ϕ from some datum. The ray SP is diverging from the central ray with an angle ψ. The line Su formed by back-projecting the projection of $P(r,\theta)$ is described by the function $L(r',\theta')$ where

$$L(r',\theta') = C\,\delta(r' \sin(\gamma-\theta')). \qquad (3.59)$$

(r',θ') is a polar coordinate system centred on $P(r,\theta)$, θ' is measured from the line OP, and C is a constant of proportionality having dimensions [density].[length]^2. Let $\tilde{g}(r',\theta')$ denote the 'diverging-ray' layergram of the point $P(r,\theta)$. This layergram may be computed by integrating the effect of the line $L(r',\theta')$ as ϕ increases uniformly in the range $(0,\pi)$, i.e.

$$\tilde{g}(r',\theta') = C \int_0^{\pi} \delta(r'\sin(\gamma-\theta'))d\phi. \tag{3.60}$$

The following relationships between angles may be established from fig. 3.3.

$$\sigma = \frac{r}{R-a} = \frac{\sin\psi}{\sin\gamma} \tag{3.61}$$

and

$$\frac{\pi}{2} + (\theta-\phi) = \gamma+\psi. \tag{3.62}$$

By eliminating ψ between eqns (3.61) and (3.62), the following relation is obtained

$$\sin(\phi-\theta) = \sigma\sin^2\gamma - \cos\gamma\,(1-\sigma^2\sin^2\gamma)^{\frac{1}{2}}. \tag{3.63}$$

Differentiating eqn (3.63) gives

$$\frac{\partial\phi}{\partial\gamma} = -\mathcal{K}(\sigma,\gamma)$$

$$= -\frac{\sigma\sin 2\gamma + \sin\gamma\,(1-\sigma^2\sin^2\gamma)^{\frac{1}{2}} + \frac{\sigma^2}{4}(1-\sigma^2\sin^2\gamma)^{-\frac{1}{2}}\sin 3\gamma}{[1-\{\sigma\sin^2\gamma - \cos\gamma\,(1-\sigma^2\sin^2\gamma)^{\frac{1}{2}}\}^2]^{\frac{1}{2}}} \tag{3.64}$$

Using eqn (3.64), eqn (3.60) may be re-expressed, with γ as the variable of integration, as

$$\tilde{g}(r',\theta') = C\int_0^{\pi} \delta(r'\sin(\gamma-\theta'))\,\mathcal{K}(\sigma,\gamma)\,d\gamma \qquad (3.65)$$

$$= C(r')^{-1}\mathcal{K}(\sigma,\theta'). \qquad (3.66)$$

From eqn (3.66) it is evident that the point-spread function associated with a 'diverging-ray' layergram is r^{-1} (c.f. the conventional layergram, eqn 3.28) weighted by a factor $\mathcal{K}(\sigma,\theta')$ which varies with the position of the point $P(r,\theta)$. At the centre of the (r,θ) plane (i.e. when $\sigma = 0$), $\mathcal{K}(\sigma,\theta')$ is unity, so at the origin of coordinates the point-spread functions are identical for both the 'diverging-ray' and 'parallel-ray' layergrams.

The fact that the point-spread function for the 'diverging-ray' layergram is a function of position means that such layergrams cannot be restored exactly by rho-filtering, and so the DRR/RFL radiation transform formula is not exact. However, provided that the function $\mathcal{K}(\sigma,\theta')$ does not deviate too far from unity, it would be expected that rho-filtering might furnish a satisfactory approximation to the ideal reconstructed image. $\mathcal{K}(\sigma,\theta')$ is plotted in fig. (3.4) as a function of θ', for several values of σ. For small values of σ, the deviation of $\mathcal{K}(\sigma,\theta')$ from unity is approximately equal to σ. Since σ is proportional to radius (c.f. eqn 3.61), the image is reconstructed more accurately towards the centre of the (r,θ) plane than it is near the periphery.

3.4 Relationships Between Radiation Transform Formulae

The manner in which each of the first three formulae are interrelated is conveniently illustrated by a flow graph (fig. 3.5). Four paths are evident between nodes 1 and 9 corresponding to the sequence of operations necessary to reconstruct the density $\lambda(r,\theta)$ from its projected density $f(\xi,\phi)$. From the graph it is seen that in addition to the cascaded operations along any path between nodes 1 and 9 being equivalent, there are several sets of shorter sequences of operations which are also equivalent (the numbers in brackets indicate the paths in fig. 3.5 being referred to).

Using the symbols $\longrightarrow$ and $\sim$ as defined in the glossary:

1. Back projection $\longrightarrow$ two-dimensional Fourier transformation $\longrightarrow$ multiplication by ρ $\sim$ one-dimensional Fourier transformation w.r.t. ξ. (1 - 2 - 3 - 5 $\sim$ 1 - 4 - 5).
2. One-dimensional Fourier transformation $\longrightarrow$ multiplication by ρ $\longrightarrow$ one-dimensional inverse Fourier transformation $\sim$ partial differentiation w.r.t. ξ $\longrightarrow$ Hilbert transformation w.r.t. ξ (1 - 4 - 7 - 8 $\sim$ 1 - 6 - 8).
3. Two-dimensional Fourier inverse transformation $\sim$ multiplication by ρ $\longrightarrow$ one-dimensional Fourier inverse transformation w.r.t. ρ $\longrightarrow$ back projection (4 - 5 - 9 $\sim$ 4 - 7 - 8 - 9).

While the above demonstrates that certain sequences of operations are mathematically equivalent, it is shown in following chapters of this thesis that some are more convenient to use computationally than others.

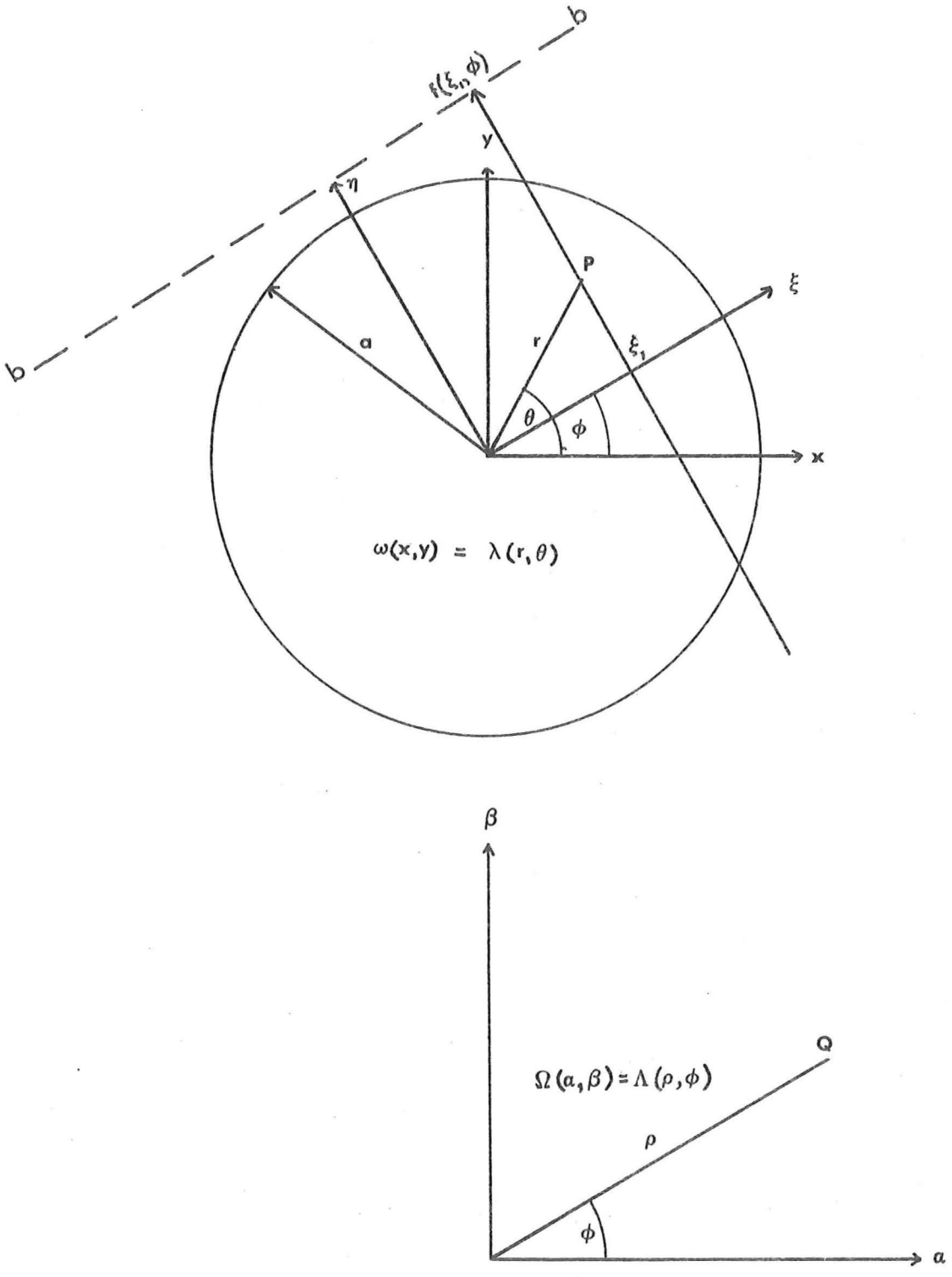

Fig. 3.1 Geometry for computing projections.

a) Density space. Coordinates of arbitrary point P: (x,y) Cartesian, (r,θ) polar. The coordinates (ξ,η) are Cartesian and rotated with respect to (x,y) by an angle ϕ. Imaging radiation is parallel to the η axis. Density of object is assumed to be zero outside the circle of radius a.

b) Fourier transform plane. Coordinates of point Q: (α,β) Cartesian, (ρ,ϕ) polar. The Fourier transform with respect to ξ of $f(\xi,\phi)$ corresponds to $\Lambda(\rho,\phi)$ in the Fourier transform plane.

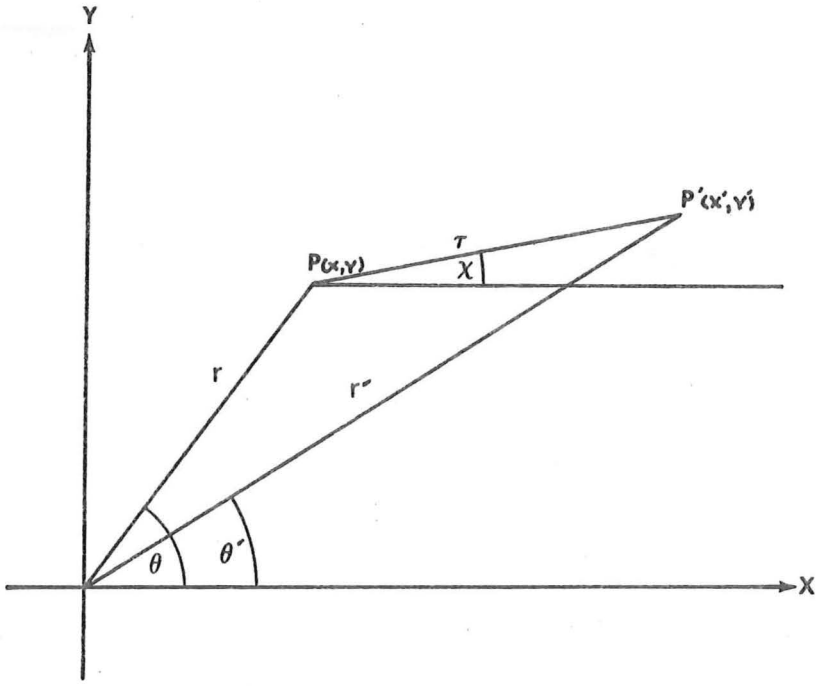

Fig. 3.2 Geometry for computing layergram.
Coordinates of P are (x,y) Cartesian, (r, θ) polar.
A second point P' a distance τ from P has coordinates (x', y') or (r', θ'). The line joining P P' makes an angle χ with the x axis.

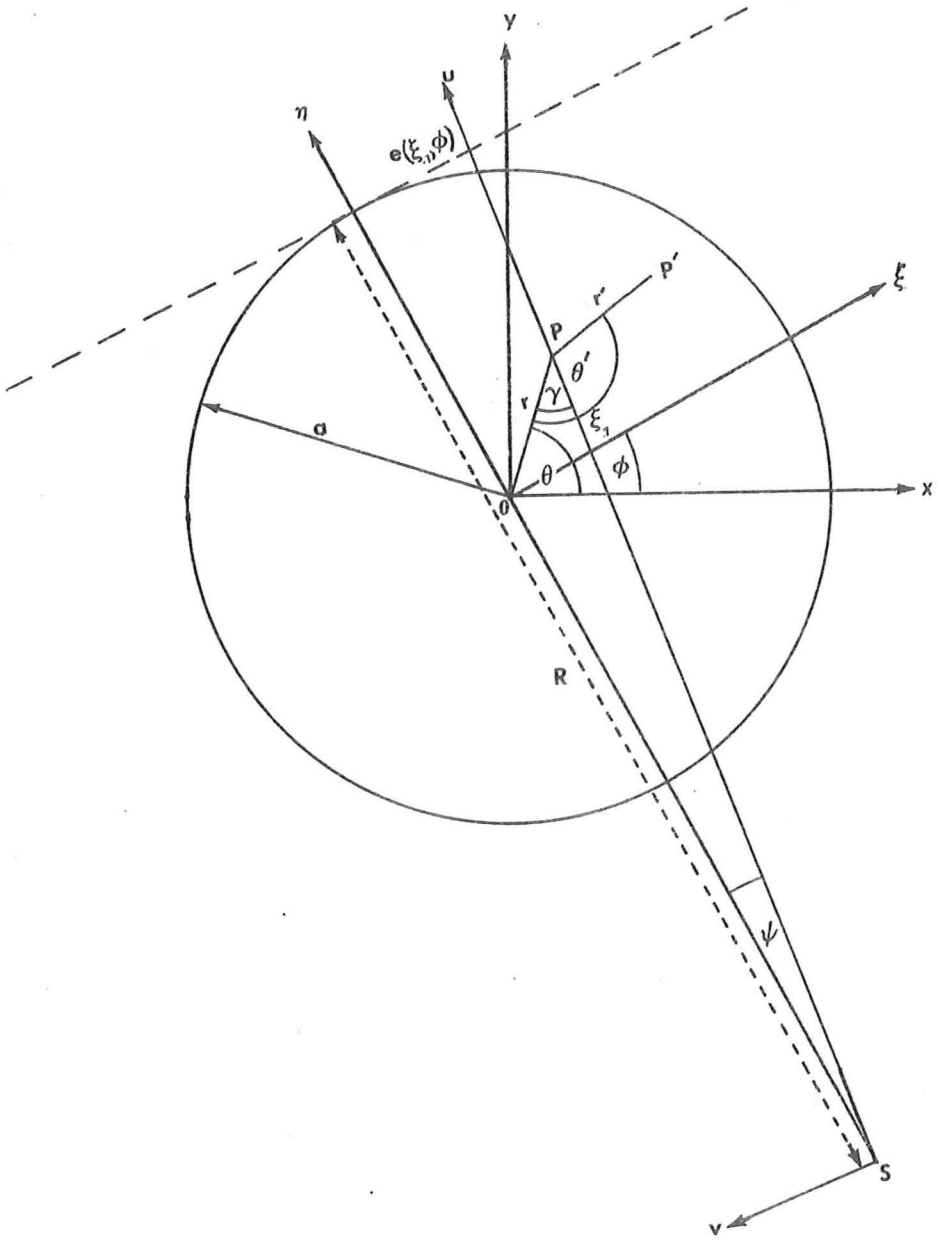

Fig 3.3 Geometry for computing 'Diverging-ray' projections and 'Diverging-ray' layergrams.

The incident radiation originates from the point S. The object density $\lambda(r,\theta) = \omega(x,y)$ lies within the circle of radius a. The (ξ,η) coordinate system is rotated by an angle ϕ from the (x,y) system. An arbitrary ray S u is shown diverging from the central ray S η with an angle ψ. The projection of point $P(r,\theta)$ is given by $e(\xi,\phi)$. The (r',θ') coordinate system is centred on the point P, with θ' being measured from the radius vector 0 P. The angle between 0 P and the ray S u is γ.

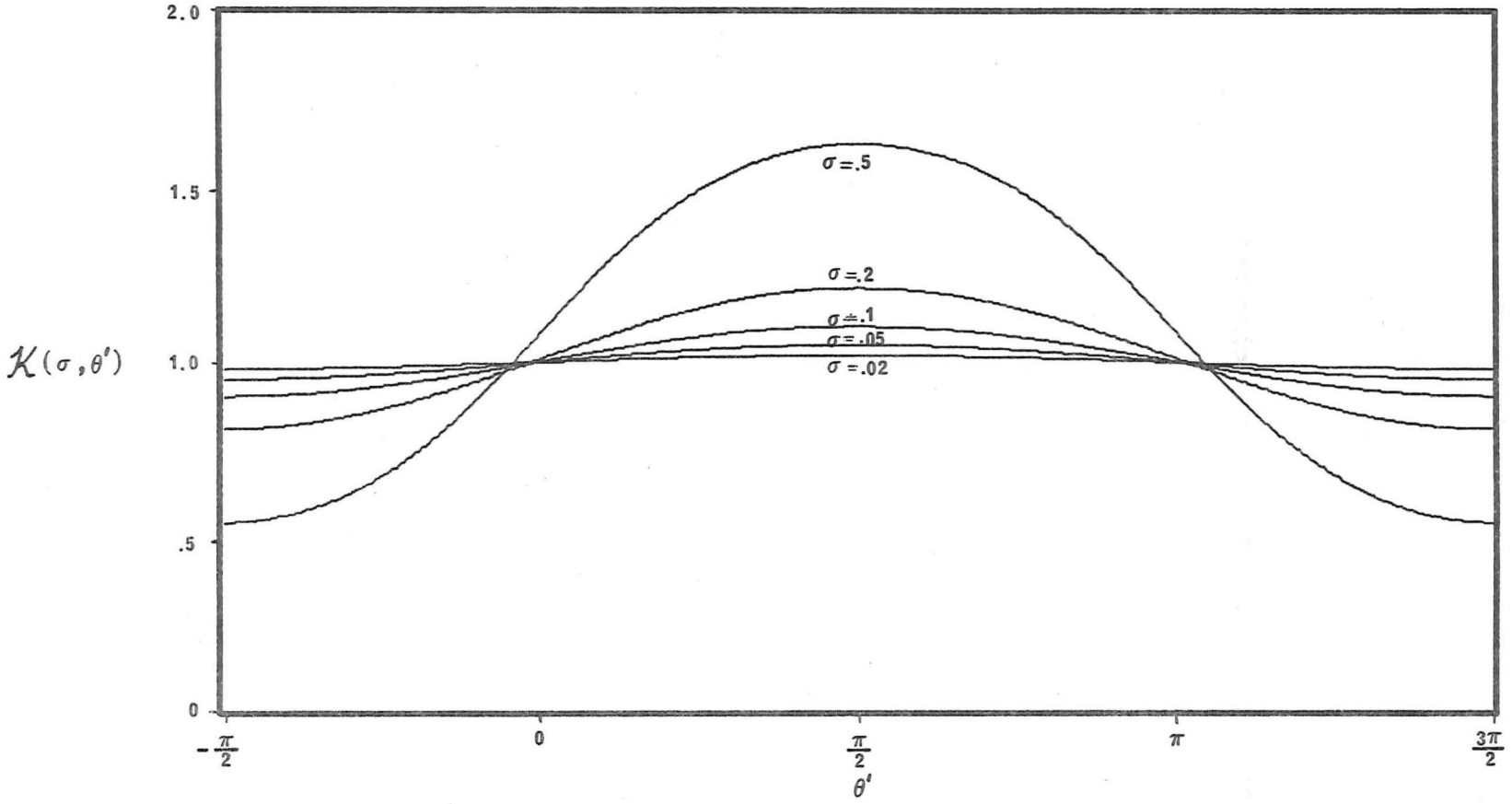

Fig. 3.4. The weighting factor $\mathcal{K}(\sigma,\theta')$ plotted against θ' for several values of σ.

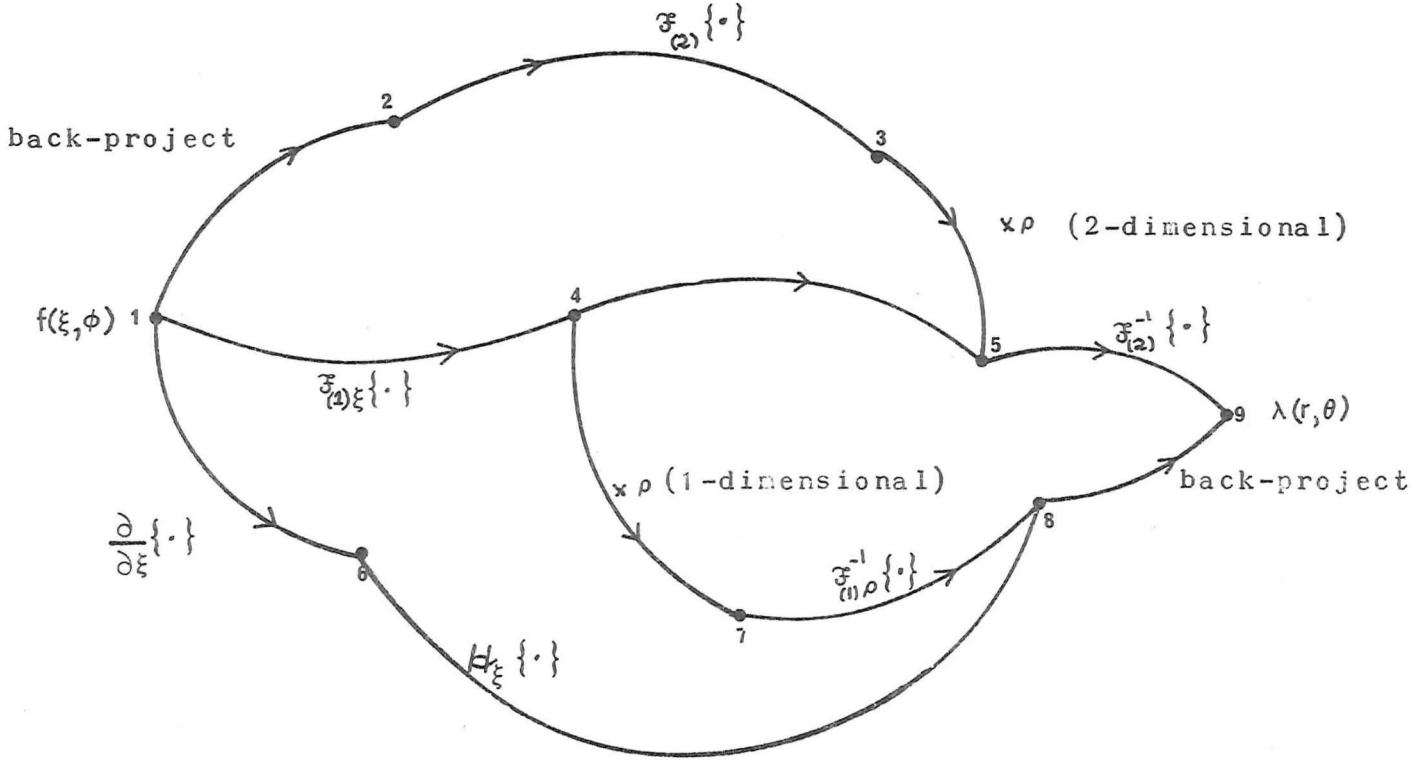

Fig. 3.5. Flow chart showing the relationships between the various radiation transform expressions.

CHAPTER 4

IMAGE RECONSTRUCTION FROM A FINITE NUMBER OF PROJECTIONS

4.1 Introduction

In this chapter, the radiation transform formulae developed in chapter 3 are modified so that they become useful in practical situations in which only a finite number of projections is measured. The first to be considered (section 4.2) is the discrete layergram formula which describes how an image is formed by back-projecting the measured projections onto a plane. The use of this formula to reconstruct a cross-section from a set of measured projections results in an image similar to the transverse tomogram discussed in chapter 2. Section 4.3 gives a formula for computing the rho-filtered discrete layergram (RDL).

The relationship between the rho-filtered discrete layergram and the work of other authors is also discussed here. To enable images to be reconstructed from a finite number of projections using the FTR formula, the data must be interpolated in some manner. Section 4.4 outlines four suitable methods, two of which are simple and approximate, and two of which are more complicated but can be justified rigorously. The implications of using Fourier transform techniques for reconstructing images from a set of 'diverging-ray' projections (the DRR radiation transforms described in chapter 3) are discussed in section 4.5. Finally, section 4.6 discusses iterative techniques which have been recently proposed as solutions to the reconstruction problem. One of the algorithms which has received considerable attention in the literature is considered in detail.

4.1.1 Extended Notation

Since this chapter is concerned with formulae for reconstructing cross-sections from a finite number of projections, it is convenient to introduce an extended notation which allows the formulae presented here to be identified with 'discrete' rather than with 'continuous' reconstruction procedures. The symbols $f_N(\xi,\phi)$ and $\Lambda_N(\rho,\phi)$ indicated that $f(\xi,\phi)$ and $\Lambda(\rho,\phi)$ are available only for angles which are members of the set $\{\phi_n\}$. Unless otherwise stated, it is assumed that the N angles ϕ_n at which the projections are measured are equally spaced in the range $(0,\pi)$, i.e.

$$\phi_n = \frac{n\pi}{N} . \tag{4.1}$$

A super-bar (e.g. $\bar{\Lambda}_N(\rho,\phi)$) is used to denote an estimate of a particular quantity resulting from the application of an interpolation scheme, or image-reconstruction procedure, to the N discrete projections.

The function $\mathrm{Star}_N(\rho,\phi)$ which resembles 2N equally spaced spokes radiating from a central point, is defined by

$$\mathrm{Star}_N(\rho,\phi) = \frac{\pi}{N\rho} \sum_{n=1}^{N} \{\delta(\phi-\phi_n) + \delta(\phi-\phi_n+\pi)\} \tag{4.2}$$

$$= \mathfrak{F}_{(2)}\{\mathrm{Star}_N(r,\theta+\tfrac{\pi}{2})\}. \tag{4.3}$$

Note that since $\mathrm{Star}_N(\rho,\phi)$ exhibits two-fold symmetry, it is convenient to take N to be even so that

$$\mathrm{Star}_N(\rho,\phi) = \mathfrak{F}_{(2)}\{\mathrm{Star}_N(r,\theta)\}. \tag{4.4}$$

4.2 Discrete Layergrams

Because the available knowledge of the projected density is incomplete when only a finite number of projections is measured, all that may be inferred directly from eqn (3.35) is the discrete layergram $\bar{g}_N(r,\theta)$ of the object, where

$$\bar{g}_N(r,\theta) = \frac{\pi}{N} \sum_{n=1}^{N} f(r\cos(\theta-\phi_n),\phi_n). \tag{4.5}$$

By using eqn (3.15), the RHS of eqn (4.5) may be expressed in terms of the Fourier transform of $f(r\cos(\theta-\phi_n),\phi_n)$ as

$$\bar{g}_N(r,\theta) = \frac{\pi}{N} \sum_{n=1}^{N} \int_{-\infty}^{\infty} \Lambda(\rho,\phi_n) \exp(-j2\pi\rho r\cos(\theta-\phi_n))d\rho \tag{4.6}$$

$$= \frac{\pi}{N} \sum_{n=1}^{N} \int_{0}^{\infty}\int_{0}^{2\pi} \rho^{-1}\Lambda(\rho,\phi)[\delta(\phi-\phi_n) + \delta(\phi-\phi_n+\pi)]$$

$$.\exp(-j2\pi\rho r\cos(\theta-\phi))\rho d\rho d\phi \tag{4.7}$$

$$= \mathfrak{F}_{(2)}^{-1}\{\Lambda(\rho,\phi)\ \mathrm{Star}_N(\rho,\phi)\}. \tag{4.8}$$

So, using the convolution theorem for Fourier transforms (see glossary), eqn (4.8) may be re-expressed as

$$\bar{g}_N(r,\theta) = \lambda(r,\theta) * \mathrm{Star}_N(r,\theta). \tag{4.9}$$

Eqn (4.8) shows that the Fourier transform of the discrete layergram corresponds to the Fourier transform of the cross-section along the spokes of $\mathrm{Star}_N(\rho,\theta)$ and is zero elsewhere, i.e.

$$\bar{G}_N(\rho,\phi) = \Lambda(\rho,\phi)\ \mathrm{Star}_N(\rho,\phi). \tag{4.10}$$

Although the cross-section, and hence the projections, are defined in section 3.2 to be of maximum extent 2a, it may be deduced from eqn (4.5) that the discrete layergram is unbounded in certain directions. If, in eqn (4.5), θ approaches $\phi_n+\frac{\pi}{2}$ it is seen that $\bar{g}_N(r,\theta)$ has a finite value no matter how large r is made. The discrete layergram therefore exhibits clutter outside the region occupied by the cross-section.

A number of authors have considered ways of reconstructing images by using discrete layergrams. Vainshtein (1971a,b) suggests that, given a set of equally spaced projections $\{f(\xi,\phi_n);\ n = 1,N\}$, a discrete layergram be computed in the manner described by eqn (4.4). Vainshtein then proposes two procedures to improve this image. Although the extent of the discrete layergram as described by eqn (4.4) is unbounded, knowledge of the extent of each projection allows a 2N-sided polygon bounding the object to be reconstructed in the image plane. While this enables clutter outside the area of the object to be removed, the high background level in the remaining image masks the detail of the object.

In the following, C is a constant whose dimension is that of $[\text{length}]^{-1}$. It allows the reconstructed density $\bar{\lambda}_N(r,\theta)$ to be expressed in the appropriate units. In eqn (4.11) below, $\bar{g}_N(r,\theta)$ is that part of the discrete layergram lying within the 2N-sided polygon discussed above. The second procedure suggested by Vainshtein for improving the discrete layergram is given by

$$\bar{\lambda}_N(r,\theta) = C\{\bar{g}_N(r,\theta) - \frac{(N-1)}{\pi N}\int_{-\infty}^{\infty} f(\xi,\phi_n)d\xi\} \qquad (4.11)$$

$$= C\{\bar{g}_N(r,\theta) - \frac{(N-1)}{\pi N}\mu\}, \qquad (4.12)$$

using eqn (3.3). Note that μ may be computed by integrating any one of the projections in the set $\{f(\xi,\phi_n);\ n = 1,N\}$. However, the procedure described by eqn (4.11) removes only the background level in the layergram, while the details of the image remain unchanged.

Herman (1972) also describes this method of reconstructing images, and compares it with an iterative method ('ART', Gordon et al. 1970). He concludes that although Vainshtein's methods are simple and lead to reasonable reconstructed images, they are inferior to 'ART' in most applications.

Crowther et al. (1970) consider the discrete layergram approach as a possible method of reconstructing a field of point objects (e.g. molecules) from their projections. They conclude that even in this case, the discrete layergram may contain undesirable artefacts which could be mistaken for additional objects.

4.3 Rho Filtered Discrete Layergrams

The RFL radiation transform formulae which are derived in chapter 3 (eqns (3.24) and (3.37)) are used here as the basis of formulae for reconstructing a cross-section from a finite number of projections. In practice it is more efficient computationally to use the formula described by eqn (3.37), since only one-dimensional Fourier transforms need to be evaluated. Since $f(\xi,\phi)$ is known only for $\phi = \phi_n$; $1 \leqslant n \leqslant N$, eqn (3.38) becomes

$$\hat{f}(\xi,\phi_n) = \mathfrak{F}^{-1}_{(1)\rho}\{|\rho|\ \mathfrak{F}_{(1)\xi}\{f(\xi,\phi_n)\}\} \qquad (4.13)$$

and eqn (3.37) may be written as

$$\bar{\lambda}_N(r,\theta) = \frac{\pi}{N} \sum_{n=1}^{N} \hat{f}(r \cos(\theta-\phi_n),\phi_n) \qquad (4.14)$$

Thus the N projections may each be one-dimensionally rho-filtered before computing the rho-filtered discrete layergram by back-projection. Equation 4.14 describes the Rho-filtered Discrete Layergram (RDL) procedure. The back-projection procedure required to reconstruct the rho-filtered discrete layergram is shown diagrammatically in fig. 4.1a.

4.3.1 Band-limitedness of Data

It is known (c.f. Bracewell 1965, ch.10) that a function of finite extent has a Fourier transform whose extent is infinite. If the Fourier transform of a function is set to zero in some region, e.g. for spatial frequencies greater than some value, the function which is recovered on inverting the transform is only an approximation to the original function. In practice, the spatial frequency spectra of most physical objects are negligible outside some radius, which is denoted here by $\hat{\rho}$, in the spatial frequency domain. The Fourier transform of an object may therefore be set to zero for spatial frequencies greater than $\hat{\rho}$, without appreciably affecting the image of the object. A function is said to be essentially band-limited (c.f. Temes et al. 1973) if it is such that it possesses negligibly small Fourier components for spatial frequencies greater than $\hat{\rho}$.

It follows from eqn (3.17) (which describes how the Fourier transforms of the projections are related to the Fourier transform of the object), that an object which is band-limited to $\hat{\rho}$ has a set of projections which also have negligible Fourier transforms for spatial frequencies greater than $\hat{\rho}$ at most. It is therefore expedient to introduce a cut-off in

Fourier space at $\hat{\rho}$, since it is probable that any significant Fourier transform values for $\rho > \hat{\rho}$ are due to noise. Define

$$P(\rho) = \begin{cases} |\rho| & ; \quad |\rho| \leqslant \hat{\rho} \\ 0 & ; \quad |\rho| > \hat{\rho} \end{cases} \tag{4.15}$$

Hence eqn (4.14) may be rewritten, to accommodate the spatial frequency cut-off at $\hat{\rho}$, as

$$f(\xi,\phi_n) = \mathfrak{F}^{-1}_{(1)\rho}\{P(\rho)\ \mathfrak{F}_{(1)\xi}\{f(\xi,\phi_n)\}\}. \tag{4.16}$$

So long as $\hat{\rho}$ is chosen such that the quantity $\rho\mathfrak{F}_{(1)\xi}\{f(\xi,\phi_n)\}$ is negligible for $\rho \geqslant \hat{\rho}$, the sharp cut-off of $P(\rho)$ at $\hat{\rho}$ does not adversely affect the rho-filtered projection $\hat{f}(\xi,\phi)$, (see the discussion on data windows, chapter 9).

4.3.2 Modifying Projections using Convolution

Denoting the Fourier transform of $P(\rho)$ by $p(\xi)$ and using the convolution theorem, eqn (4.16) may be written as

$$\hat{f}(\xi,\phi_n) = p(\xi) * f(\xi,\phi_n). \tag{4.17}$$

Using the definition of $P(\rho)$ given by eqn (4.15), the following expression for $p(\xi)$ is obtained;

$$p(\xi) = \int_{-\infty}^{\infty} P(\rho)\ \exp(-j2\pi\rho\xi)d\rho \tag{4.18}$$

$$= 2\int_{0}^{\hat{\rho}} \rho\ \cos(2\pi\rho\xi)d\rho \tag{4.19}$$

$$= \frac{\hat{\rho}}{\pi\xi}\sin(2\pi\hat{\rho}\xi) - \frac{1}{2(\pi\xi)^2}[1 - \cos(2\pi\hat{\rho}\xi)]. \tag{4.20}$$

Eqn (4.20) is derived from eqn (4.19) by integrating by parts.

Expressions similar to eqn (4.20) have been suggested by a number of authors as a means of modifying projections by convolution prior to back-projecting the projections to form an image. Bracewell and Riddle (1967) form the modified set of projections by

$$\hat{f}(\xi,\phi_n) = f(\xi,\phi_n) * \{\delta(\xi) - \hat{\rho}\ \mathrm{sinc}^2(\hat{\rho}\xi)\} \qquad (4.21)$$

which is equivalent to eqn (4.20), if $f(\xi,\phi_n)$ is band-limited to $\hat{\rho}$.

Ramachandran and Lakshminarayanan (1971a,b) require that the projections $f(\xi,\phi_n)$ be measured at evenly spaced points in ξ. Their convolution function is expressed as a sequence of numbers corresponding to the local maxima and zeros of $p(\xi)$.

Gilbert (1972a) derives his expression for the modified projections in the manner outlined below. It may be shown (Bracewell 1965, p.117,365) that

$$\mathfrak{F}_{(1)\xi}\left\{\frac{\partial}{\partial\xi}\{f(\xi,\phi_n)\}\right\} = -j2\pi\rho\Lambda(\rho,\phi_n), \qquad (4.22)$$

and that

$$\mathfrak{F}_{(1)}\{\xi^{-1}\} = -j\pi\ \mathrm{sgn}(\rho). \qquad (4.23)$$

$P(\rho)$ has the form

$$P(\rho) = |\rho| = \rho\ \mathrm{sgn}\ (\rho) \qquad (4.24)$$

so that by combining eqns (4.22) and (4.23) and using the convolution theorem it may be shown that

$$\hat{f}(\xi,\phi_n) = \mathcal{F}^{-1}_{(1)}\{\mathrm{sgn}(\rho)\} * \mathcal{F}^{-1}_{(1)\rho}\{\rho\Lambda(\rho,\phi_n)\} \tag{4.25}$$

$$= -\frac{1}{2\pi^2}\frac{\partial}{\partial\xi}\{f(\xi,\phi_n)\} * \xi^{-1}. \tag{4.26}$$

It will be noted that eqns (4.26) and (4.14) may be combined to give an expression for the DSR radiation transform derived in chapter 3 (eqn 3.45) when the continuous angular variable ϕ is replaced by the members of the set $\{\phi_n\}$, and the angular integral is replaced by a summation over n.

4.4 Image Reconstruction Using Data Interpolation

Here various formulae are considered which take the Fourier transforms of the given discrete set of projections, and interpolate from these a two-dimensional function which is effectively continuous in angle. The basis for these formulae is the FTR radiation transform which is derived in chapter 3.

It is convenient to introduce an interpolation operator which describes the way in which the transformed projections $\Lambda_N(\rho,\phi_n)$ are related to any arbitrary point (ρ,ϕ) in the Fourier transform plane. $I_{N,\phi}\{\cdot\}$ is defined to be any operator that provides a continuous estimate $\bar{\Lambda}_N(\rho,\phi)$ of the Fourier transform of the object by the operation

$$\bar{\Lambda}_N(\rho,\phi) = I_{N,\phi}\{\Lambda_N(\rho,\phi_n)\}, \tag{4.27}$$

and computes $\bar{\Lambda}_N(\rho,\phi)$ such that

$$\bar{\Lambda}_N(\rho,\phi_n) = \Lambda_N(\rho,\phi_n), \tag{4.28}$$

so that the given data is undistorted. The condition implied by eqn (4.28) ensures that the projections of the

reconstructed object made at angles $\phi \in \{\phi_n\}$ are consistent with the projections $f(\xi,\phi_n)$. An interpolation scheme which exhibits this property is said to give a consistent interpolation of the given data.

Using the interpolation operator, the analogue of the FTR equation for reconstructing an image from N projections $f(\xi,\phi_n)$ may be written as

$$\bar{\lambda}_N(r,\theta) = \mathfrak{F}^{-1}_{(2)}\{I_{N,\phi}\{\mathfrak{F}_{(1)\xi}\{f(\xi,\phi_n)\}\}\}. \tag{4.29}$$

The interpolation operation is expressed as a convolution of an interpolation kernel $I(\phi)$ with the measured projections, i.e.

$$I_{N,\phi}\{f(\xi,\phi_n)\} = \sum_{n=1}^{N} I(\phi-\phi_n)\ f(\xi,\phi_n) \tag{4.30}$$

where the maximum value of $I(\phi)$ is unity for $\phi = 0$. When applying the interpolation operator to the projections, it is seen that

$$I_{N,\phi}\{\mathfrak{F}_{(1)\xi}\{f(\xi,\phi_n)\}\}$$

$$= \sum_{n=1}^{N} I(\phi-\phi_n)\int_{-\infty}^{\infty} f(\xi,\phi_n)\exp(-j2\pi\rho\xi)d\xi \tag{4.31}$$

$$= \int_{-\infty}^{\infty} \sum_{n=1}^{N} [I(\phi-\phi_n)f(\xi,\phi_n)]\exp(-j2\pi\rho\xi)d\xi. \tag{4.32}$$

Eqns (4.33) and (4.34) indicate that a particular interpolation operator may be applied to either the projections $f(\xi,\phi_n)$, or to the one-dimensional Fourier transforms of the projections $\Lambda(\rho,\phi_n)$. Computational algorithms may be devised which perform the interpolation either before (eqn 4.32) or

after (eqn 4.31) Fourier transforming the projections.

Four interpolation schemes are listed below.

4.4.1 Spread Interpolation

The interpolation operator $\text{spread}_N\{\cdot\}$ is defined by the following operation on a function $H_N(r,\theta)$ which is known only on the spokes of $\text{Star}_N(r,\theta)$.

$$\text{Spread}_N\{H_N(r,\theta)\} = H(r,\theta_n); \quad \frac{\theta_n+\theta_{n-1}}{2} \leq \theta < \frac{\theta_{n+1}+\theta_n}{2} \tag{4.33}$$

When this interpolation scheme is applied to the FTR method, the reconstructed density is related to the projections by

$$\bar{\lambda}_N(r,\theta) = \mathfrak{F}^{-1}_{(2)}\{\text{spread}_N\{\Lambda_N(\rho,\phi)\}\} \tag{4.34}$$

The spread interpolation scheme gives an estimate of the Fourier transform of the object by spreading the known values of $\Lambda(\rho,\phi)$ (on the spokes of $\text{Star}_N(\rho,\phi)$) onto contiguous sectors in the Fourier transform plane.

4.4.2 Linear Interpolation

A linear interpolation operator $\text{lin}_N\{\cdot\}$ is defined by the following operation on $H_N(r,\theta)$:

$$\text{lin}\{H_N(r,\theta)\} = [(\theta-\theta_n)H(r,\theta_{n+1}) + (\theta_{n+1}-\theta)H(r,\theta_n)]/(\theta_{n+1}-\theta_n);$$

$$\theta_n \leq \theta \leq \theta_{n+1} \tag{4.35}$$

Using this, the estimate of the density is given by

$$\bar{\lambda}_N(r,\theta) = \mathfrak{F}^{-1}_{(2)}\{\text{lin}_N\{\Lambda_N(\rho,\phi)\}\} \tag{4.36}$$

4.4.3 Fourier Transform Fourier Series Interpolation (FTFSI)

The Fourier transform of an object of finite extent is an entire function (c.f. Goodman 1968, p.133). It is therefore desirable to seek an interpolation scheme which gives an estimate of the Fourier transform that has the properties of an entire function. Such an estimate may be obtained by expressing the Fourier transform of the object as an angular Fourier series;

$$\Lambda(\rho,\phi) = \sum_{n=-N}^{N} a_n(\rho)\, \exp(jn\phi), \tag{4.37}$$

where the set of coefficients $\{a_n(\rho)\}$ is computed from

$$a_n(\rho) = \frac{1}{2N+1} \sum_{m=-N}^{N} \Lambda(\rho,\phi_m)\, \exp(-jn\phi_m). \tag{4.38}$$

The interpolation kernel associated with this expansion is evaluated by substituting eqn (4.38) into (4.37) to give

$$I_{(fsi)}(\phi) = \sum_{n=-N}^{N} \exp(jn\phi) = \frac{\sin[(N+\tfrac{1}{2})\phi]}{(2N+1)\sin(\phi/2)}. \tag{4.39}$$

$I_{(fsi)}(\phi)$ is sometimes known as the Fourier series kernel (Papoulas 1962, p.44). Therefore the continuous estimate of the Fourier transform of the object is computed from the transforms of the projections by

$$\bar{\Lambda}_N(\rho,\phi) = \sum_{n=-N}^{N} \Lambda(\rho,\phi_n)\, \frac{\sin(N+\tfrac{1}{2})(\phi-\phi_n)}{(2N+1)\sin[(\phi-\phi_n)/2]}, \tag{4.40}$$

and the estimate of the density is obtained by computing the inverse two-dimensional Fourier transform of $\bar{\Lambda}_N(\rho,\phi)$.

4.4.4 Density Space Fourier Series Interpolation (FSI)

An alternative Fourier series interpolation scheme interpolates the projected density itself, rather than the Fourier transform of the density, using a Fourier series expansion. It is convenient to introduce a modified projected density (c.f. Smith et al. 1973), defined by

$$\begin{aligned} F(\xi,\phi) &= f(\xi,\phi), \quad \xi \geq 0 \\ & \qquad\qquad ; \qquad 0 \leq \phi \leq \pi \\ F(-\xi,\phi+\pi) &= f(\xi,\phi), \quad \xi \leq 0 \end{aligned} \tag{4.41}$$

which implies that $F(\xi,\phi)$ exists in $0 \leq \xi \leq a$, $0 \leq \phi \leq 2\pi$, whereas $f(\xi,\phi)$ exists in $-a \leq \xi \leq a$, $0 \leq \phi < \pi$. If $f_N(\xi,\phi)$ and $F_N(\xi,\phi)$ denote the parts of the projected density that are known, then

$$\begin{aligned} F_N(\xi,\phi) &= F(\xi,\phi_n); \qquad 1 \leq n \leq 2N, \\ &= f_N(\xi,\phi); \qquad 0 \leq \phi < \pi, \\ &= f_N(-\xi,\phi); \qquad \pi \leq \phi < 2\pi. \end{aligned} \tag{4.42}$$

It is convenient to use a trigonometric Fourier series expansion (following the approach of Smith et al. 1973), rather than a complex exponential expansion, for the following analysis.

The modified projected density $F(\xi,\phi)$ is interpolated from the given $F_N(\xi,\phi)$ by

$$\bar{F}_N(\xi,\phi) = \sum_{m=0}^{N} A_m(\xi) \cos(m\phi) + \sum_{m=1}^{N-1} B_m(\xi) \sin(m\phi) \tag{4.43}$$

where the $A_m(\xi)$ and $B_m(\xi)$ are computed such that $\bar{F}_N(\xi,\phi)$ is a consistent interpolation of $F_N(\xi,\phi)$, as defined at the beginning of section 4.4.

The Fourier coefficients $A_m(\xi)$ and $B_m(\xi)$ are defined within the interval $0 \leq \xi \leq a$ by

$$\begin{matrix} A_{2m}(\xi) \\ B_{2m}(\xi) \end{matrix} = \sum_{p=0}^{L} \begin{matrix} \alpha_{2m,p} \\ \beta_{2m,p} \end{matrix} \cos((2p+1) \arcsin(\xi/a)) \qquad (4.44)$$

$$\begin{matrix} A_{2m+1}(\xi) \\ B_{2m+1}(\xi) \end{matrix} = \sum_{p=1}^{L} \begin{matrix} \alpha_{2m+1,p} \\ \beta_{2m+1,p} \end{matrix} \sin(2p \arcsin(\xi/a)). \qquad (4.45)$$

The integer L is sufficiently large to include all computationally significant $\alpha_{m,p}$ and $\beta_{m,p}$, which may be computed in a standard fashion from the A_m, B_m (Hildebrand 1958, ch.9). By analytically computing both the one-dimensional Fourier transform of $\bar{F}_N(\xi,\phi)$ with respect to ξ, and the two-dimensional inverse transform of the result, the required density may be expressed in terms of the $\alpha_{m,p}$ and $\beta_{m,p}$. This analysis is given in detail by Smith et al. (1973) and is an extension of that proposed by Cormack (1964,1965).

As a consequence of eqns (4.31) and (4.32), both the FTFSI and the FSI methods are equivalent and lead to similar results when all of the $\{a_m(\rho)\}$ in the former case, and the $\{\alpha_{m,p},\beta_{m,p}\}$ in the latter case, are used in the reconstruction procedure. It is found that while the FTFSI approach is the more convenient computationally, both the FSI and FTFSI techniques have useful features that may be exploited in some circumstances. These features are discussed in section 5.4 of chapter 5, which deals with consistency conditions.

4.5 Discrete Diverging Ray Reconstruction

4.5.1 Fourier Transform Approach

The DRR radiation transform formula derived in chapter 3, deals specifically with situations where the divergence of the X-ray beam is significant. The equation which expresses the Fourier transform of the reconstructed image in terms of the measured projections, when only a finite number of views of the cross-section are available, is given by the following variation of eqn (3.57):

$$\bar{\Lambda}_N(\rho,\phi_n) = \int_{-\infty}^{\infty} e(R'\tan\psi,\phi_n+\psi)\ \exp(j2\pi\rho R'\sin\psi)\,d(R'\sin\psi) \tag{4.46}$$

$$= \int_{-\infty}^{\infty} e\left(\frac{R't}{(R'^2-t^2)^{\frac{1}{2}}},\phi_n+\psi\right)\ \exp(j2\pi\rho t)\,dt \tag{4.47}$$

where t is written in place of R'sin ψ.

By measuring only a finite number of projections of the cross-section, only certain parts of the function $f(\xi,\phi)$ can be determined. When the imaging rays are parallel, these parts are the radial lines shown in fig. 4.2a. However, when the rays form a diverging beam, as in fig. 3.3, the projected density $f(\xi,\phi)$ is only known along the contours shown in fig. 4.2b.

To reconstruct an image from projections of this sort using the FTR method, the data may be treated differently depending on whether the linear, spread or FTFSI interpolations are used, or whether the FSI scheme is employed. In the first three cases, the interpolation schemes require that $f(\xi,\phi)$ be known along the radial lines which are shown in fig. 4.2a. Therefore the data must be interpolated from the contours of fig. 4.2b onto the straight

lines of fig. 4.2a. In addition to this angular interpolation, the ordinate ξ must undergo a non-linear change in scale, since, while the projections are normally measured in equal increments of ξ (i.e. equal increments in $\tan \psi$), the Fourier transforms of the projections must be computed with respect to equal increments in $\sin \psi$. As there is rarely any technical problem in sampling the projections as finely as one pleases in ξ, the radial interpolation may be performed using a simple linear interpolation scheme. However, the angular interpolation is much more difficult. To make effective use of the available data it is preferable to use an angular Fourier series interpolation scheme.

Now the samples of $f(\xi,\phi)$ encountered at any radius ξ in fig. 4.2b are not equally spaced in angle throughout the range $0 \leqslant \phi \leqslant 2\pi$, so that it is necessary to perform a matrix inversion to compute the angular Fourier coefficients of these samples. This can be inconvenient computationally and it may be circumvented by changing the manner in which the projections are measured. The projections are normally measured over the following ranges of ξ and ϕ:

$$\begin{aligned} -a \leqslant \xi \leqslant a \\ 0 \leqslant \phi < \pi \end{aligned} \tag{4.48}$$

However, if the projections are measured in the ranges

$$\begin{aligned} 0 \leqslant \xi \leqslant a \\ -\pi < \phi \leqslant \pi \end{aligned} \tag{4.49}$$

the parts of the projected density that are determined are those shown in fig. 4.2c. Notice that samples at any radius become equi-spaced in angle and so it is a simple matter to

determine the angular Fourier coefficients of the data, in order to interpolate onto the radial lines of fig. 4.2a. To measure the projections in this manner, the object just be rotated through 2π radians, compared to the π radians required for all of the previously described methods. In the limit as the angle of ray divergence approaches zero, the contours shown in figs 4.2b and 4.2c degenerate into the radial lines shown in fig. 4.2a.

From fig. 3.3, it may be deduced that the angular shift at any radius ξ through which the projections must be interpolated from the contours of fig. 4.2c, to those shown in fig. 4.2a, is ψ, where

$$\psi = \arcsin(\xi/R). \tag{4.50}$$

To perform the angular interpolation, a set of radially dependent angular Fourier coefficients $\{c_m(\xi)\}$ is determined by

$$c_m(\xi) = \frac{1}{2N+1} \sum_{n=-N}^{N} e(\xi,\phi_n) \exp(jm[\phi_n + \arcsin(\xi/R)]) \tag{4.51}$$

$$= \frac{1}{2N+1} \exp(jm \arcsin(\xi/R)) \sum_{n=-N}^{N} e(\xi,\phi_n) \exp(jm\phi_n) \tag{4.52}$$

The values of $e(\xi,\phi)$, along the lines given by $\phi = \phi_n+\psi$, are then computed from

$$e(\xi,\phi_n+\psi) = \sum_{n=-N}^{N} c_m(\xi) \exp(-jm\phi_n). \tag{4.53}$$

Now, from eqn (4.47) and the Fourier transform of eqn (4.29), the functions $e(\xi,\phi_n)$ and $f(\xi,\phi_n)$ are related by

$$f(\xi,\phi_n) = e\left[\frac{R'\xi}{(R'^2-\xi^2)^{\frac{1}{2}}}, \phi_n+\psi\right]. \qquad (4.54)$$

So, provided $e(\xi,\phi)$ is properly interpolated in ϕ, and is sampled sufficiently finely in ξ, $f(\xi,\phi_n)$ may be computed from $e(\xi,\phi_n+\psi)$ using linear interpolation to perform the ordinate scale change indicated by eqn (4.54).

Having pre-processed the data in this way, the cross-section may be reconstructed by using any one of the FTFSI, linear or spread interpolation formulae.

If the FSI approach is employed to reconstruct the cross-section from its 'diverging-ray' projections, the angular and radial interpolations described above need not be performed explicitly, but may be built-in to the FSI algorithm. Since the $\{c_m(\xi)\}$ computed by eqn (4.52) is analogous to the $\{A_m(\xi),B_m(\xi)\}$ computed for the FSI scheme by eqn (4.45), this latter set of coefficients may still be computed accurately even though the samples of the projected density lie on curved contours (fig. 4.2c), rather than on straight lines (fig. 4.2a). Similarly, since a radial interpolation is necessary with the FSI scheme to effectively sample the projected density at equal increments with respect to $\arcsin(\xi/a)$, this step may be modified to incorporate the further non-linear scale change specified by eqn (4.54).

4.5.2 Rho-filtered Discrete Layergram Approach

A cross-section may also be reconstructed from its 'diverging-ray' projections using the rho-filtered discrete layergram approach which is based on the second DRR formula introduced in section 3.3.4.2.

From the geometry of fig. 3.3 it is seen that a point $P(r,\theta)$ casts a shadow on $e(\xi,\phi)$ when ξ has the value

$$\xi = \frac{Rr\cos(\theta-\phi)}{R' - r\sin(\theta-\phi)} \tag{4.55}$$

Therefore the back-projection procedure by which a discrete layergram $\bar{g}_N(r,\theta)$ is formed from the set $\{e(\xi,\phi_n)\}$ of measured projections is described by

$$\bar{g}_N(r,\theta) = \frac{\pi}{N}\sum_{n=1}^{N} e\left(\frac{Rr\cos(\theta-\phi_n)}{R' - r\sin(\theta-\phi_n)},\ \phi_n\right). \tag{4.56}$$

Similarly, the diverging ray rho-filtered discrete layergram is evaluated by computing a set of modified projections $\{\hat{e}(\xi,\phi_n)\}$ from

$$\hat{e}(\xi,\phi_n) = \mathfrak{F}^{-1}_{(1)\rho}\left\{|\rho|\{\mathfrak{F}_{(1)\xi}e(\xi,\phi_n)\}\right\} \tag{4.57}$$

which leads to the approximate reconstructed cross-section

$$\bar{\lambda}_N(r,\theta) = \frac{\pi}{N}\sum_{n=1}^{N} \hat{e}\left(\frac{Rr\cos(\theta-\phi_n)}{R' - r\sin(\theta-\phi_n)},\ \phi_n\right). \tag{4.58}$$

The back-projection by eqn (4.58) is shown in fig. 4.1b for two typical 'diverging-ray' projections $\hat{e}(\xi,\phi_1)$ and $\hat{e}(\xi,\phi_2)$.

4.6 Iterative Reconstruction Techniques

In addition to the Fourier methods discussed in sections 4.2-4.5, there are a number of algorithms which rely on iterative methods to reconstruct cross-sections from their projections. Many different approaches have been proposed by Gordon et al. (1970), Gordon and Herman (1971), Gilbert (1972b), Muehllehner and Wetzel (1970), Goitein (1972), Ambrose and Hounsfield (1973) and Kuhl et al. (1972). All of these methods regard the cross-section as being composed of a grid-like structure of cells, having a constant density within each

cell. This structure is represented numerically as a matrix, and each projection is considered to consist of a summation of matrix elements. A ray is defined as the area between two parallel lines which are spaced by the width of one cell and which overlay the matrix. A pseudo-projection (after Gilbert 1972b) is a projection computed by summing the matrix elements lying within contiguous rays. Sampled projections are assumed to be equivalent to pseudo-projections, and so a set of linear simultaneous equations may be written to express the matrix representing the reconstructed image in terms of the given projections. In principle, it is possible to solve this set of equations to obtain a reconstructed cross-section.

The use of conventional matrix inversion methods is impracticable when dealing with arrays of the size required to reconstruct useful images. Another difficulty, which precludes the use of conventional equation solving techniques, is that the set of equations is usually grossly underdetermined, and even if the number of observations is equal to the number of unknowns, the resulting matrix is still likely to be ill-conditioned (c.f. Crowther et al. 1970). To overcome this difficulty, the authors cited above have devised iterative algorithms for solving the reconstruction problem.

In most of the iterative schemes, the image is initially set to some average-density value at each of the grid points. The values of these densities are iteratively changed so that pseudo-projections computed from the image agree with the actual projections used as data. When the agreement is to within some pre-determined value for all given projections, the image is considered to have converged to a 'best estimate' of the cross-section.

The initial approach of Gordon et al. (1970) was to use Monte-Carlo methods to perturb randomly each image element in turn, until the pseudo-projections of the reconstructed image agreed with the data. They found that, while the reconstructed image was appreciably contaminated with noise, a satisfactory result could usually be arrived at by averaging several images obtained by successive applications of the algorithm.

A subsequent algorithm (the Arithmetic Reconstruction Technique or 'ART') proposed by Gordon et al. (1970) has received much publicity (Gordon et al. 1970, Herman and Rowland 1971, Herman 1972, Rowland 1972) and some of the claims made by its authors have been the subject of controversy (Bellman et al. 1971, Crowther and Klug 1971). The basis of the 'ART' algorithm is given below.

The density of the cross-section is described by the M x M point matrix $\omega_{i,j}$. The total density, μ, of the cross-section can be deduced approximately from the samples of the projections $f(\xi,\phi_n)$ for any angle ϕ_n. Initially all the $\omega_{i,j}$ are assigned values equal to the mean density of the cross-section:

$$\omega^{o}_{i,j} = \mu/M \; ; \qquad 1 \leqslant i \leqslant M, \quad i \leqslant j \leqslant M. \tag{4.59}$$

The pseudo-projection $R(k,\phi_n)$ is the sum of the elements $\omega_{i,j}$ which lie within the k^{th} ray at angle ϕ_n. The k^{th} sample of the projection at angle ϕ_n is given by $f(\xi_k,\phi_n)$. The problem is to determine all the $\omega_{i,j}$ from samples of the given projections $f(\xi_k,\phi_n)$.

In the following discussion $N(k,\phi_n)$ is the number of matrix elements $\omega_{i,j}$ within the pseudo-projection $R(k,\phi_n)$, and the superscript q refers to the value of a particular symbol

at the q^{th} iteration. At the q^{th} iteration, the pseudo-projections are given by:

$$R^q(k,\phi_n) = \sum_{(i,j) \in \text{ray}(\xi_k,\phi_n)} \omega_{i,j} \quad . \tag{4.60}$$

The original set of values $\{\omega_{i,j}\}$ is iteratively refined by either one of two different procedures, i.e.

$$\omega_{i,j}^{q+1} = \max[\omega_{i,j}^q + (f(\xi_k,\phi_n) - R^q(k,\phi_n))/N(k,\phi_n), 0], \tag{4.61}$$

or

$$\omega_{i,j}^{q+1} = \frac{f(\xi_k,\phi_n)}{R^q(k,\phi_n)} \omega_{i,j}^q \quad . \tag{4.62}$$

Eqn (4.61) describes the additive 'ART' algorithm, while eqn (4.62) describes the multiplicative 'ART' algorithm. Either of these formulae is applied to the projections $f(\xi_k,\phi_n)$ for each ϕ_n in turn. The sequence is repeated for as many times as is necessary to allow the $\omega_{i,j}$ to converge numerically. The degree of convergence is determined by comparing the pseudo-projections of the reconstructed image with the measured projections.

Gilbert (1972b) points out some deficiencies in the ART algorithm which could tend to make the procedure become unstable. He shows that while satisfactory results are obtained using pseudo-projections as data, analytically computed (or measured) projections give rise to erroneous reconstructed images. Gilbert proposes a Simultaneous Iterative Reconstruction Technique ('SIRT'), in which, at each iteration, the densities are changed by using data from all of the projections

simultaneously, in contrast to 'ART' where densities are altered using data from one projection at a time. The additive 'SIRT' algorithm is (Gilbert 1972b),

$$\omega_{i,j}^{q+1} = \max\left[\omega_{i,j}^{q} + \frac{\Sigma f(\xi_k,\phi_n)}{\Sigma L(k,\phi_n)} - \frac{\Sigma R^q(k,\phi_n)}{\Sigma N(k,\phi_n)} , 0\right], \qquad (4.63)$$

where $L(k,\phi_n)$ is the length of the k^{th} ray at angle ϕ_n. The multiplicative 'SIRT' algorithm is

$$\omega_{i,j}^{q+1} = \frac{\Sigma f(\xi_k,\phi_n)}{\Sigma L(k,\phi_n)} \cdot \frac{\Sigma N(k,\phi_n)}{\Sigma R^q(k,\phi_n)} \omega_{i,j}^{q} . \qquad (4.64)$$

In eqns (4.63) and (4.64) the summations are over all the projection samples $f(\xi_k,\phi_n)$ to which the matrix element $\omega_{i,j}$ contributes. Gilbert demonstrates that these algorithms are stable when measured data is used as input, and that reconstructed images obtained using 'SIRT' are similar in quality to images produced using Fourier transform methods.

While the 'SIRT' algorithm has not been programmed by the author, it is more complete than 'ART' and therefore it is expected that the computational time required for its execution would be longer than that required for 'ART'. A comparison of execution times of 'ART', and the reconstruction methods based on Fourier transforms, is given in chapter 6.

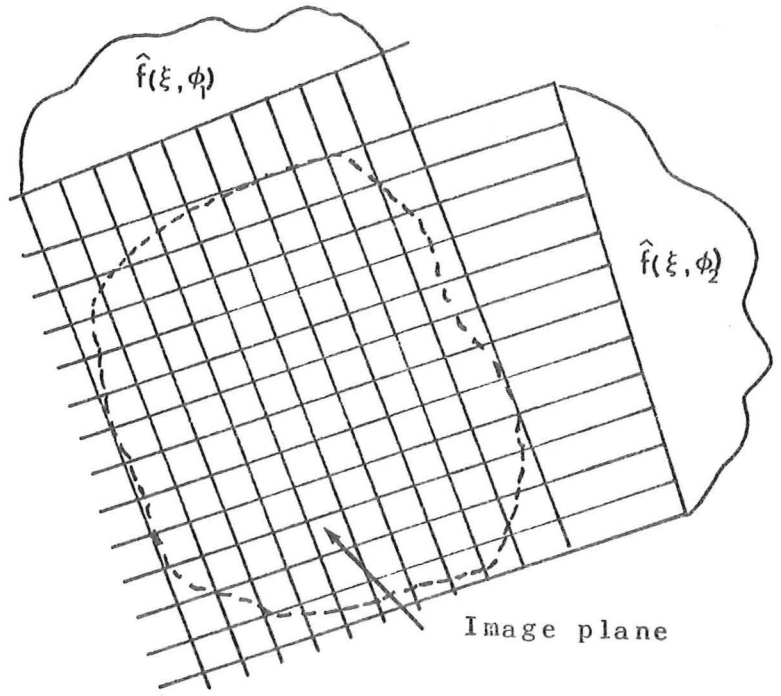

a)

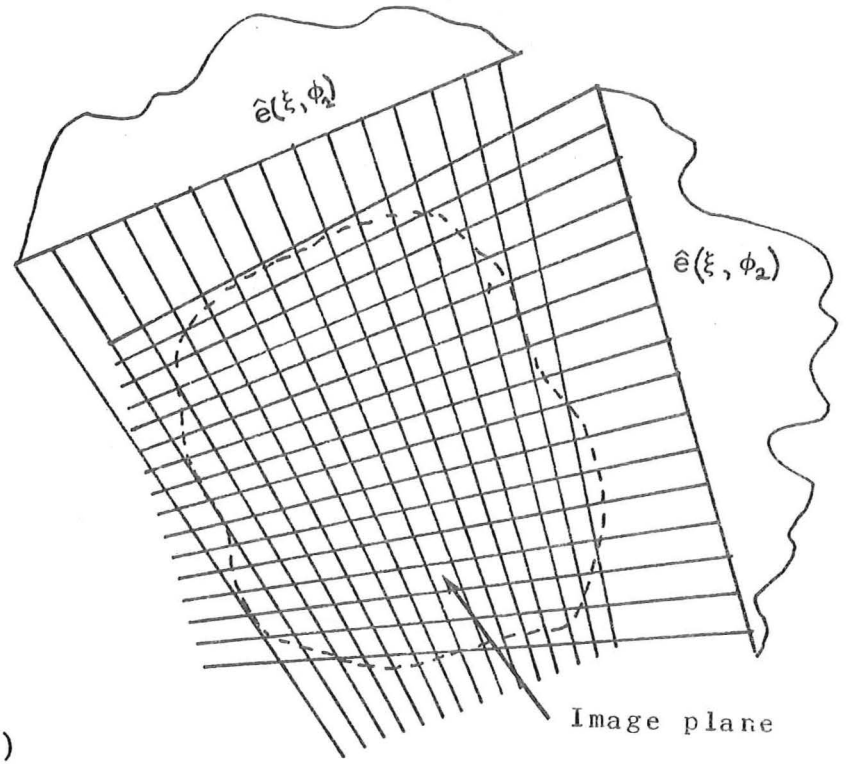

b)

Fig. 4.1. Back-projection of rho-filtered projections.

a) Back-projection of the rho-filtered projections $\hat{f}(\xi,\phi_1)$ and $\hat{f}(\xi,\phi_2)$. The original projections are obtained using parallel rays.

b) Back-projection of the rho-filtered projections $\hat{e}(\xi,\phi_1)$ and $\hat{e}(\xi,\phi_2)$. The original projections are obtained using diverging radiation.

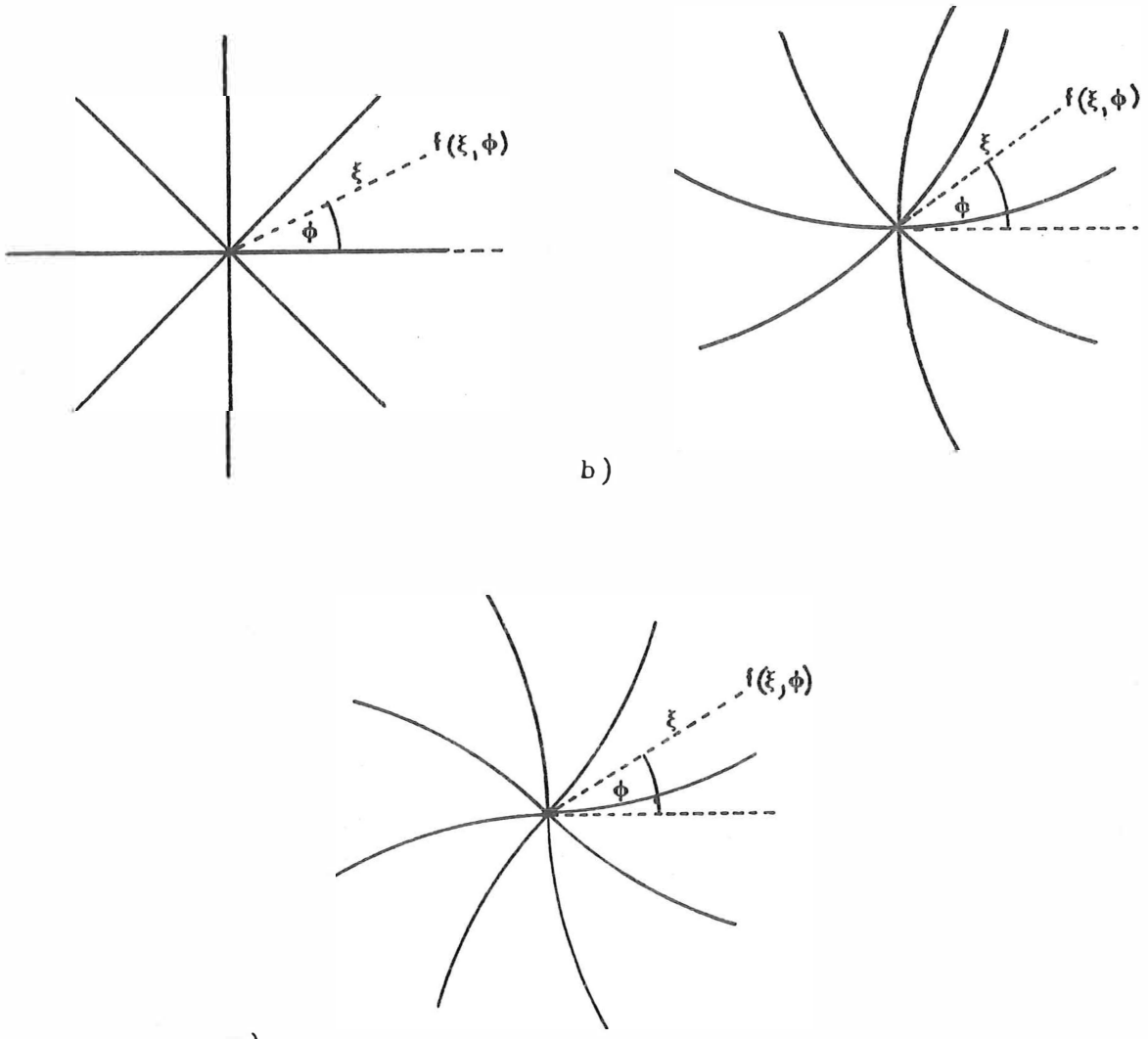

Fig. 4.2. Regions of $f(\xi,\phi)$ space which are known when using various data collection methods.

a) When projections are measured using parallel rays the parts of $f(\xi,\phi)$ space which are avaliable lie on radial lines.

b) Using diverging radiation to measure the projections with the parameters ξ, ϕ in the ranges $(-\infty,\infty)$ and (ϵ,π) respectively, $f(\xi,\phi)$ is able to be determined on the arcs passing through the origin. Note that for any radius ξ, angular samples are unequally spaced over 2π radians.

c) As for 4.2b but with ξ and ϕ in the ranges $(0,\infty)$ and $(0,2\pi)$.

CHAPTER 5

CONSEQUENCES OF USING DISCRETE DATA

5.1 Introduction

All of the radiation transform formulae which are developed in chapter 3 express the cross-section uniquely in terms of the projected density. Since the projected density $f(\xi,\phi)$ is continuous in both the variables ξ and ϕ, it follows that an image which is reconstructed from samples of $f(\xi,\phi)$ is bound to suffer from degradations of some sort. In chapter 4 various interpolation schemes are developed for treating the data, and in the present chapter the effects of implementing such schemes are investigated. The constraints imposed on the reconstruction procedures by the use of Fourier transforms are considered in section 5.2, while section 5.3 considers the effects of interpolating the data in both radius and angle. A feature of the FSI and FTFSI interpolation schemes is that they both lead to consistency checks which, in principle, allow the noise level in the measured projections to be estimated. The 'consistency condition' of the Fourier series interpolation schemes is discussed in section 5.4. Since the input data to any of the reconstruction schemes is composed of samples of $f(\xi,\phi)$ at discrete values of ϕ, it follows that there may be parts of the projected density, or its Fourier transform, which are not sampled sufficiently rapidly in ϕ for the complete function to be accurately recovered from its samples. The result is that high angular spatial frequency components in $f(\xi,\phi)$ are interpreted as low spatial frequency components. This effect is known as angular aliasing and is analysed in section 5.5.

In some situations, besides being only available at discrete values of ϕ, the data is confined to a restricted range of ϕ. If it is desired to use the information available from such a limited range of measurements, extrapolation or analytic continuation techniques must be used. Section 5.6 examines the feasibility of employing these methods when dealing with such situations. The final section of this chapter considers the important question of resolution which arises when images are reconstructed from a finite number of projections.

5.2 Constraints Due to Use of the Fast Fourier Transform

The fast Fourier transform algorithm (FFT) described by Cooley and Tukey (1965) and Bergland (1969), has turned the previously laborious machine computation of Fourier transforms into a relatively fast operation. The time required for the FFT to evaluate the Fourier transform of an N-point data record is proportional to $N \log_2 N$, while direct evaluation of the Fourier integral using a simple trapezoidal integration rule requires a computation time proportional to N^2. This saving in time is achieved by efficient factoring, of the array to be transformed, into a number of shorter length sequences. It is significant when a large number of data points is to be transformed. The efficiency of the FFT algorithm is the reason that so much attention is given in this thesis to reconstruction methods which require the evaluation of Fourier transforms.

The FFT algorithm computes the discrete Fourier transform, denoted by $a_{k,\ell}$, of a two-dimensional sampled record $X_{m,n}$ consisting of N^2 points, according to the formula

$$a_{k,\ell} = \sum_{m=0}^{N-1} \sum_{n=0}^{N-1} X_{m,n} W^{(km+\ell n)} . \qquad (5.1)$$

The $X_{m,n}$ are recovered from the $a_{k,\ell}$ by

$$X_{m,n} = \frac{1}{N^2} \sum_{\ell=0}^{N-1} \sum_{k=0}^{N-1} a_{k,\ell} W_N^{-(km+\ell n)} , \qquad (5.2)$$

where $W_N = \exp(j2\pi/N)$.

The main factor which must be considered when using the FFT, is that the data points, and computed coefficients, must be equally spaced throughout the density and spatial frequency domains, (the domains of the sets $\{X_{m,n}\}$ and $\{a_{k,\ell}\}$ respectively), at points lying on rectangular grids. It is this factor which dictates the use of interpolation schemes if the power of the FFT is to be fully utilised in image reconstruction procedures. Note that, if the FFT allowed two-dimensional data to be represented in polar rather than rectangular coordinates, the one-dimensional Fourier transforms of the projections would lie on the correct points in transform space, and since the inverse transform could then be evaluated directly, no interpolation procedure would be necessary. However, a computationally efficient algorithm does not exist for evaluating Fourier transforms of data represented in polar coordinates, for which time consuming Hankel transforms must be employed, requiring the repeated evaluation of Bessel functions (c.f. Crowther et al. 1970).

Fig. 5.1 shows how the one-dimensional transforms of the projections are related to the two-dimensional transform grid. The values of $\Lambda(\rho,\phi_n)$ at the crosses on the radial lines, are the Fourier transform samples computed by one-dimensional transformation of the individual projections. These are the values which must be related to the rectangular Fourier

transform grid by interpolation. Note that interpolation in both radial and angular directions is required.

5.3 The Effect of Interpolation

5.3.1 Radial Interpolation

Having computed the discrete Fourier transforms of the sampled projections, the transform values are available at a set of uniformly spaced points $\{\rho_n\}$ in the spatial frequency domain, where

$$\rho_{n+1} - \rho_n = \Delta\rho = (2a)^{-1} \tag{5.3}$$

and 2a is the extent of the data $f(\xi,\phi_n)$ in the ξ direction prior to transformation (c.f. Bergland 1969). If the projections are sampled according to the sampling theorem†, the continuous Fourier transform as a function of ρ may be evaluated by convolving the frequency domain samples at the set of points $\{\rho_n\}$ with the function

$$S(\rho) = \frac{\mathrm{Sin}(\pi\rho/2a)}{\pi\rho} = (2a)^{-1}\,\mathrm{sinc}(\rho/2a). \tag{5.4}$$

When the one-dimensional transforms of the projections are interpolated onto the two-dimensional transform grid, points which lie at a particular radius ρ from the coordinate origin of the grid, must be related to the values of the one-dimensional transforms at this same radius. Points in the two-

† The sampling theorem states that if a function is sampled at a rate equal to at least twice its highest frequency component, then the function may be restored unambiguously from knowledge of the samples, (Bracewell 1965, p.194).

dimensional transform plane may be specified by the coordinates (α,β) (see fig. 3.1b), and samples of the discrete Fourier transform by the coordinates (α_i,β_k), where

$$\alpha_k = \beta_k = k(2a)^{-1}. \tag{5.5a}$$

and i and k are integers. A sample at the point (α_i,β_k) may also be assigned the polar coordinates (ρ,ϕ) where

$$\rho = (\alpha_i^2+\beta_k^2)^{\frac{1}{2}},$$

and

$$\phi = \arctan(\beta_k/\alpha_i). \tag{5.5b}$$

In general, the radial coordinate ρ of any grid point does not correspond to one of the members of the set $\{\rho_m\}$, at which the transforms of the projections are computed. In order to determine the value of $\Lambda(\rho,\phi_n)$ at an arbitrary radius ρ, from the samples at $\{\rho_m\}$, the sampled values $\Lambda(\rho_m,\phi_n)$ must be convolved with $S(\rho)$.

If this operation is performed each time the radial value of a grid point ρ does not correspond to one of the members of $\{\rho_n\}$, then the computer time required to perform the $S(\rho)$ convolution increases to such an extent that any initial advantage gained by use of the FFT is lost.

It is of interest therefore to examine the effect of a simple linear interpolation in radius, as a substitute for the above time consuming, rigorous interpolation scheme. Now the radial coordinate ρ of the grid point (α_i,β_k) is such that

$$\rho_n \leqslant \rho \leqslant \rho_{n+1} \tag{5.6}$$

for some integer value of n. Let ρ be written as

$$\rho = \rho_n + \varepsilon\Delta\rho \tag{5.7}$$

where ε takes on different values between 0 and 1 for different grid points (α_i,β_k). However, it is instructive to consider a situation where ε is a constant, as described in the example below.

Since the Fourier transform of a real function is conjugate symmetric (Bracewell 1965, p.16), only half of the Fourier transform domain need be considered when performing interpolation operations, as the values on the other half of the domain are determined implicitly (see the discussion in chapter 9 of the Fourier transform algorithm 'R2FORT' which uses this property). Consider a real function $f(\xi)$ of extent 2a to have a Fourier transform $F(\rho)$ which is sampled at a set of points $\{\rho_n\}$. It is required to interpolate these samples onto a different set of points also spaced by $\Delta\rho$, but shifted laterally from the first set by an amount $\varepsilon\Delta\rho$, where $0 \leqslant \varepsilon \leqslant 1$. Fig. 5.2 illustrates the situation, showing the original samples of $F(\rho)$ (solid arrows), and the points $\rho_n+\varepsilon\Delta\rho$ onto which the $F(\rho_n)$ are to be linearly interpolated (broken arrows). The new function interpolated from the values at the sample points ρ_n is denoted by $\overline{F}(\rho_n+\varepsilon\Delta\rho)$. The points lying to the right of the origin are those which are actually interpolated, while those to the left of the origin are interpolated implicitly through the conjugate symmetry of $F(\rho)$. The linearly interpolated values at the points

$$\rho = \rho_n + \varepsilon\Delta\rho; \quad \rho \geqslant 0 \tag{5.8}$$

are related to the values of $F(\rho_n)$ by;

$$\bar{F}(\rho_n+\varepsilon\Delta\rho) = F(\rho_n)(1-\varepsilon) + \varepsilon F(\rho_{n+1}) \tag{5.9}$$

$$= F(\rho_n) * [(1-\varepsilon)\delta(\rho-\varepsilon\Delta\rho) + \varepsilon\delta(\rho+(1-\varepsilon)\Delta\rho)]. \tag{5.10}$$

By evaluating the Fourier transform of eqn (5.10), noting that the equivalent expression for $\rho < 0$ is the complex conjugate of eqn (5.10) and using the convolution theorem for Fourier transforms, the inverse Fourier transform $\bar{f}(\xi)$ of $\bar{F}(\rho)$ is shown to be

$$\bar{f}(\xi) = \underset{(1)}{f(\xi)[(1-\varepsilon)\cos\pi\varepsilon\xi/a + \varepsilon\cos\pi(1-\varepsilon)\xi/a]} + \underset{(2)}{\{f(\xi)[(1-\varepsilon)\sin\pi\varepsilon\xi/a - \varepsilon\sin\pi(1-\varepsilon)\xi/a]\}} * \frac{1}{\pi\xi} \tag{5.11}$$

So by interpolating the Fourier transform of a function in the manner illustrated by fig. 5.2, the function itself is modified as shown by eqn (5.11). By increasing the radius a of the circumscribing circle in fig. 3.1a to some value $\hat{a}$ (so that a is replaced by $\hat{a}$ in eqn 5.11), and computing the Fourier transforms of $f(\xi)$ for $-\hat{a} < \xi < \hat{a}$, part (1) of the RHS of eqn (5.11) may be made arbitrarily close to $f(\xi)$ while part (2) of the RHS of eqn (5.11) may be made negligible. For example, if $\hat{a} = 2a$, then part (1) of the RHS of eqn (5.11) has a maximum value at $\varepsilon = .5$ of

$$f(\xi)[(1-\varepsilon)\cos\pi\varepsilon\xi/\hat{a} + \varepsilon\cos\pi(1-\varepsilon)\xi/\hat{a}]\Big|_{\varepsilon=.5} = f(\xi)\cos\pi\xi/4a. \tag{5.12}$$

Recalling that the extent of $f(\xi)$ is a, the maximum value of the expression within square brackets of part (2) of the RHS of eqn 5.11, when a is replaced by 2a, is approximately .06

for $\varepsilon \approx .25$ and $\xi = a$.

The value of ε is not fixed for the actual problem being considered here but varies arbitrarily between 0 and 1, and so eqns (5.9-5.12) can only give an intuitive idea of the effect of interpolating from sample points on radial lines to points on a uniform rectangular grid. Since ε is not fixed, it would be expected that the effect of such an interpolation would be less than that suggested by part (1) of the RHS of eqn (5.11), and that part (2) of the RHS of eqn (5.11) would be negligible for all practical purposes.

Information loss and compensation in linear interpolation has been treated in some depth by Shapiro (1972) for meteorology. He considers the problem of linearly interpolating a function from a regular grid-system onto an irregular grid-system and discusses the effects of this interpolation on the spatial frequency of the interpolated function. To provide some compensation for these effects, he derives some approximate restoration operators which may be applied to the data prior to interpolation. Similar procedures could possibly be applied when radial interpolation is being performed in the Fourier transform domain, if it were found that the uncompensated linear interpolation described above did not lead to sufficiently accurate results.

5.3.2 Angular Interpolation

The task of interpolating the Fourier transforms of the given projections from radial lines onto two-dimensional grid-points, requires angular as well as radial interpolation. Assuming that the radial interpolation procedure discussed in section 5.3.1 is satisfactory, the effects of angular interpolation may be examined in isolation.

Using the notation introduced in chapter 4, the estimate of the Fourier transform which is obtained by interpolating the transforms of the measured projections, may be expressed as follows;

$$\bar{\Lambda}_N(\rho,\phi) = \sum_{n=-N}^{N} \Lambda_N(\rho,\phi_n)\ I(\phi-\phi_n). \tag{5.13}$$

It is convenient to express $I(\phi)$ as the angular Fourier series

$$I(\phi) = \frac{1}{2N+1} \sum_{m=-N}^{N} K_m \exp(jm\phi) \tag{5.14a}$$

where

$$K_m = \int_{-\pi}^{\pi} I(\phi) \exp(-jm\phi)\ d\phi. \tag{5.14b}$$

Substitution of eqn (5.14a) into the Fourier inverse of (5.13) gives

$$\bar{\lambda}_N(r,\theta) = \frac{1}{2N+1} \sum_{n=-N}^{N} \sum_{m=-N}^{N} \int_0^{2\pi}\int_0^{\infty} \Lambda_N(\rho,\phi_n) K_m \exp(jm\phi)$$

$$.\exp(-jm\phi_n)\ \exp(-j2\pi\rho r\cos(\theta-\phi))\rho d\rho d\phi. \tag{5.15}$$

Writing ϕ_n as $\frac{n\pi}{N}$, eqn (5.15) may be re-expressed as

$$\bar{\lambda}_N(r,\theta) = \frac{1}{2N+1} \sum_{n=-N}^{N} \sum_{m=-N}^{N} \int_0^{2\pi}\int_0^{\infty} [\Lambda_N(\rho,\tfrac{n\pi}{N})\ \exp(-j2\pi mn/2N)]$$

$$.\exp(jm\phi) K_m\ \exp(-j2\pi\rho r\ \cos(\theta-\phi))\rho d\rho d\phi. \tag{5.16}$$

The contents of the square brackets, associated with the summation over n, is clearly the decomposition of $\Lambda_N(\rho,\frac{n\pi}{N})$

into its set of angular Fourier coefficients $\{a_m(\rho)\}$, so that

$$\bar{\lambda}_N(r,\theta) = \frac{1}{2N+1} \sum_{m=-N}^{N} \int_0^{2\pi} \int_0^{\infty} a_m(\rho) K_m \exp(jm\phi)$$

$$.\exp(-j2\pi\rho r \cos(\theta-\phi))\rho d\rho d\phi . \qquad (5.17)$$

$$= \frac{2\pi}{2N+1} \sum_{m=-N}^{N} K_m \exp(-jm\theta)(-j)^m \int_0^{\infty} a_m(\rho)\, J_m(2\pi\rho r)\rho d\rho \qquad (5.18)$$

where formula (9.1.21) of Abramowitz and Stegun (1965) is used to obtain eqn (5.18) from eqn (5.17).

To determine the effects of implementing the angular interpolation schemes discussed in chapter 4, the members of $\{K_m\}$ are computed for each of the Spread, Linear and FSI/FTFSI schemes as follows. The subscripts (sp), (lin) and (fsi) on $I(\phi)$ and K_m below, refer to the $I(\phi)$ and K_m appropriate to the Spread, Linear and FSI/FTFSI interpolation schemes respectively.

5.3.2.1 Spread Interpolation

$$I_{(sp)}(\phi) = \begin{cases} 1 ; & |\phi| \leq \pi/2N \\ 0 ; & |\phi| > \pi/2N . \end{cases} \qquad (5.19)$$

$$\therefore \quad K_{(sp)_m} = \frac{N}{\pi} \int_{-\pi/2N}^{\pi/2N} \exp(-jm\phi)\, d\phi \qquad (5.20)$$

$$= \frac{2N}{m\pi} \sin(m\pi/2N) \qquad (5.21)$$

5.3.2.2 Linear Interpolation

$$I_{(lin)}(\phi) = \begin{cases} 1 - N\phi/\pi ; & |\phi| \leq \frac{\pi}{N} \\ 0 ; & |\phi| > \frac{\pi}{N} . \end{cases} \qquad (5.22)$$

$$\therefore \quad K_{(lin)_m} = \int_{-\pi/N}^{\pi/N} (1-|N\phi/\pi|)\, \exp(-jm\phi)\, d\phi, \tag{5.23}$$

$$= \left(\frac{2N}{m\pi}\right)^2 \sin^2\left(\frac{m\pi}{2N}\right), \tag{5.24}$$

which may either be obtained by integrating (5.23) by parts, or by observing that

$$I_{lin}(\phi) = I_{sp}(\phi) * I_{sp}(\phi) \tag{5.25}$$

and using the convolution theorem for Fourier transforms.

5.3.2.3 Fourier Series Interpolation

Note that this analysis applies also to the FTFSI scheme.

$$I_{(fsi)}(\phi) = \frac{1}{2N+1} \frac{\sin(N+\frac{1}{2})\phi}{\sin(\frac{\phi}{2})} = \sum_{n=-N}^{N} \exp(jn\phi) \tag{5.26}$$

$$\therefore \quad K_{(fsi)_m} = \frac{1}{2N+1} \int_{-\pi}^{\pi} \sum_{n=-N}^{N} \exp(jn\phi)\, \exp(-jm\phi)\, d\phi. \tag{5.27}$$

$$= 1, \quad \text{for all } m. \tag{5.28}$$

5.3.3 Relationships Between Interpolation Schemes

From the above analysis, it is seen that each of the interpolation schemes modifies the Fourier transform of the reconstructed image in a different way. The manner in which the transforms are altered is expressed by eqn (5.18). Each of the angular Fourier coefficients $a_m(\rho)$ of the Fourier transform of the cross-section is weighted by a value K_m appropriate to the particular interpolation scheme used. In the cases of linear and spread interpolation, the K_m decrease in value with an increase in $|m|$, so that the effect of the higher order Bessel functions in the reconstructed image is lessened. It is interesting to note that the members of $\{K_{(sp)_m}\}$ fall away

less rapidly with increasing $|m|$ than do the members of $\{K_{(lin)_m}\}$, which suggests that spread interpolation retains more information in the image than linear interpolation, since the former scheme affects the angular Fourier coefficients of the image the least.

However, for the third case, (Fourier series interpolation), $K_{(fsi)_m}$ is constant with increasing $|m|$, and so as long as the coefficients $a_m(\rho)$ for which $|m| > N$ are negligibly small, the Fourier series method is essentially exact.

5.4 Consistency Conditions

One interesting feature of the Fourier series interpolation schemes, is that they have their own 'built-in' consistency checks on the data. Using the argument previously introduced in section 4.3.1, the cross-section $\lambda(r,\theta)$ is assumed to be effectively band-limited to a spatial frequency $\hat{\rho}$. In this case, $\lambda(r,\theta)$ may be expanded as a finite Fourier series:

$$\lambda(r,\theta) = \sum_{m=-L}^{L} b_m(r)\, e^{jm\theta}. \qquad (5.29)$$

where the limits $\pm L$ of the summation are chosen such that the exclusion of the coefficients $b_m(r)$, $\forall\, |m| > L$, does not appreciably affect the recovery of the function $\lambda(r,\theta)$. The Fourier transform of eqn (5.29) is

$$\Lambda(\rho,\phi) = \sum_{m=-L}^{L} a_m(\rho)\, e^{jm\phi} \qquad (5.30)$$

where the members of $\{a_m\}$ and $\{b_m\}$ are related by (c.f. Papoulis 1968, chap. 5)

$$b_m(r) = 2\pi\ (-j)^m \int_0^\infty a_m(\rho)\ J_m(2\pi\rho r)\rho d\rho . \qquad (5.31)$$

5.4.1 Number of Projections Required for Uniformly Resolved Reconstructed Image

Since the function $\lambda(r,\theta)$ is effectively band-limited, it follows that the maximum spatial frequency which may occur at the periphery of the cross-section (i.e. for r = a), is $\hat{\rho}$. It is demonstrated in chapter 4 that the projected density exhibits the same band-limited behaviour as the cross-section, so that in order to preserve the spatial frequency component of $\hat{\rho}$ at the periphery of $f(\xi,\phi)$, sufficient angular samples of the projected density must be measured to satisfy the sampling condition at a radius $\xi = a$. Noting that N projections provide 2N angular samples of $f(\xi,\phi)$, the sampling condition is satisfied if

$$2N/2\pi\rho a \geq 2\hat{\rho} \qquad (5.32)$$

i.e.

$$N \geq 2\pi a\hat{\rho} \qquad (5.33)$$

This condition is also derived by Bracewell (1956) and Crowther et al. (1970).

Thus eqn (5.33) gives a measure of the number of projections which must be used by a reconstruction procedure to enable spatial frequency components up to a value $\hat{\rho}$ to be included in the reconstructed image of the cross-section. For example, a cross-section bounded by a circle 10 cm in diameter (i.e. a = 5 cm in fig. 3.1a), which is to be reconstructed such that all spatial frequencies up to

$$\hat{\rho} = .5 \text{ mm}^{-1} \tag{5.34}$$

are accurately represented would require

$$N = 50\pi \approx 157 \text{ projections.} \tag{5.35}$$

Now if each projection were completely independent of all others, it would be expected that M^2 independent samples of the projected density (i.e. M projections each of M samples) would be required to reconstruct M^2 independent samples of the density itself. However, eqn (5.33) shows that the number of projected density samples required to specify the object at M^2 independent points is $M^2\pi/2$, which demonstrates that the measured projections are not mutually independent. It is this interdependence of projections which gives rise to a consistency condition.

5.4.2 Derivation of Consistency Condition

Consider the expression for $\lambda(r,\theta)$ in terms of its angular Fourier components, (eqn 5.18 with K_m set to unity for all m).

$$\bar{\lambda}_N(r,\theta) = \frac{2\pi}{2N+1} \sum_{m=-N}^{N} \exp(-jm\theta)(-j)^m \int_0^\infty a_m(\rho) J_m(2\pi\rho r)\rho d\rho. \tag{5.36}$$

It is known that Bessel functions behave such that for $n > 5$ and $z > n$, $J_n(z)$ is an oscillatory function with a root mean squared value of approximately $(\pi z)^{-\frac{1}{2}}$. When

$$z < n-2, \tag{5.37}$$

$J_n(z)$ decreases sufficiently rapidly with z that it is negligible compared to $(\pi z)^{-\frac{1}{2}}$, for most practical purposes. Therefore, any of the $a_m(\rho)$ for which $m > 2\pi\rho a+2$, do not

contribute significantly to the reconstructed image of the cross-section for r < a. They would however contribute to parts of the image outside the circle r = a, but since this region is defined to be zero initially (eqn 3.3), these coefficients are defined as the insignificant coefficients. It follows that if any part of the reconstructed image lies outside the circle r = a, these coefficients must take on significant values indicating that the measured projections are in some way inconsistent. This means that they could not have been derived from accurate measurements of a physical cross-section, or that they have been contaminated by noise. If the members of $\{a_m(\rho)\}$ are normalised by dividing each by $a_0(0)$ to form a new set of coefficients $\{\bar{a}_m(\rho)\}$, then the condition that

$$\bar{a}_m(\rho) \approx 0 \quad \forall \ |m| > 2\pi\rho a+2 \tag{5.38}$$

is defined as a consistency condition on the given data for the FTFSI scheme.

A similar condition is introduced by Smith et al. (1973) for the FSI interpolation scheme which is described briefly in chapter 4. Recall that a set of coefficients $\{\alpha_{m,p}, \beta_{m,p}\}$, analogous to the set $\{a_m(\rho)\}$ discussed above, is computed for this scheme. It is found that a stronger consistency condition exists in the FSI case, namely,

$$\alpha_{m,p} = \beta_{m,p} \equiv 0, \qquad \forall_m \geq 2p+1; \quad 0 \leq p \leq L. \tag{5.39}$$

When using the FSI interpolation scheme, the set $\{\alpha_{m,p}, \beta_{m,p}\}$ for which the condition given by eqn (5.39) is satisfied, is termed the set of redundant coefficients. The set of

coefficients $\{\alpha_{m,p}, \beta_{m,p} | m < 2p, 0 \leqslant p \leqslant L\}$ is the set of significant coefficients.

Measured data is always imperfect so that the consistency conditions are bound to be violated in practice. For the FSI scheme, denote by σ_R and σ_S respectively the standard deviations of the redundant coefficients and the errors in the significant coefficients due to random errors of standard deviation σ in the data. Smith et al. (1973) give the relation between these errors as

$$\sigma_R \approx \sigma_S = O(\sigma). \tag{5.40}$$

The errors in the significant and insignificant coefficients are found to be similarly related to the errors in the data when using the FTFSI scheme.

5.5 Effects of Angular Aliasing

If $\Lambda(\rho,\phi)$ possesses no angular Fourier components $a_n(\rho)$ of order greater than N, then the RHS of eqn (5.30) is an exact representation of $\Lambda(\rho,\phi)$. In general, $\Lambda(\rho,\phi)$ does possess higher order Fourier components for at least some values of ρ, so that some of the members of $\{a_m(\rho)\}$ are incorrectly computed. When this occurs, high order coefficients $a_m(\rho)$, for $2N \geqslant m > N$, are 'folded back' about the coefficient $a_N(\rho)$ and become added to $a_{2N-m}(\rho)$ causing the coefficients $a_m(\rho)$ for $N > m \geqslant 0$, to be computed incorrectly. This effect is known as aliasing (e.g. Bergland 1969).

It was argued in section 5.4.1 that a reconstruction procedure leads to a uniformly resolved image that represents

accurately all spatial frequency components up to $\hat{\rho}$ if the number of projections used is such that

$$N \geq 2\pi a\hat{\rho}. \tag{5.41}$$

If N is less than the value specified by eqn (5.41), and an attempt is made to recover all spatial frequency components in the reconstructed image up to $\hat{\rho}$, then errors due to angular aliasing are displayed in the reconstructed image. It is of interest to consider the nature of these errors in images reconstructed by both the rho-filtered discrete layergram and FTFSI procedures. For both cases, a two-dimensional density distribution whose density profile is in the form of a Gaussian blob, is used as a test cross-section. The blob is centred at coordinates (r_0,θ_0) in the (r,θ) plane, and the cross-section is expressed by

$$\lambda(r,\theta) = \exp(-(r^2+r_0{}^2-2r\,r_0\cos(\theta-\theta_0))/2W^2) \tag{5.42a}$$

where W is the effective width of the blob.

5.5.1 Aliasing in Rho-filtered Discrete Layergram

Since the rho-filtering operation is position invariant, the Gaussian blob may be centred at the origin of the (r,θ) plane without any loss of generality. Thus

$$\lambda(r,\theta) = \exp(-r^2/2W^2). \tag{5.42b}$$

The projected density is independent of ϕ and is given by the Abel transform of $\lambda(r,\theta)$ (Bracewell 1965, p.264);

$$f(\xi,\phi) = (2\pi)^{\frac{1}{2}}\, W \exp(-\xi^2/2W^2). \tag{5.43}$$

The Fourier transform of the cross-section is

$$\Lambda(\rho,\phi) = 2\pi W^2 \exp(-2\pi^2 W^2 \rho^2) \tag{5.44}$$

and so the Fourier transform of the rho-filtered discrete layergram is (see eqn 4.10)

$$\bar{\Lambda}(\rho,\phi) = \rho\Lambda(\rho,\phi)\ \mathrm{Star}_N(\rho,\phi). \tag{5.45}$$

The rho-filtered discrete layergram is given by the Fourier inverse of eqn (5.45):

$$\bar{\lambda}_N(r,\theta) = \mathfrak{F}^{-1}_{(2)} \{\rho\Lambda(\rho,\phi)\ \mathrm{Star}_N(\rho,\phi)\}. \tag{5.46}$$

This expression may be manipulated as shown in Appendix A to give

$$\bar{\lambda}_N(r,\theta) = \lambda(r,\theta) + C(r,\theta), \tag{5.47}$$

where $C(r,\theta)$ is the error or <u>clutter</u> associated with angular aliasing. The function $C(r,\theta)$ is shown in Appendix A to have the form:

$$C(r,\theta) = \frac{\pi^{\frac{1}{2}} r}{2^{\frac{1}{2}} W} \exp(-r^2/4W^2) \sum_{m=1}^{\infty} \left[I_{mN-\frac{1}{2}}\left(\frac{r^2}{4W^2}\right) - I_{mN+\frac{1}{2}}\left(\frac{r^2}{4W^2}\right) \right] \cos 2mN\theta \tag{5.48}$$

which has its maximum magnitude when $\theta = \frac{n\pi}{2N}$, where n is any integer. This expression has been evaluated using Blanch's (1964) continued-fraction recurrence method to compute the modified Bessel functions. It is shown as a function of r/W and N in fig. 5.3. Fig. 5.4a shows the discrete layergram computed from the projected density given by eqn (5.43), and fig. 5.4b shows the rho-filtered discrete layergram computed

from the same projections. In both cases, 20 projections of the Gaussian blob are used in the reconstruction procedure. The extent of the reconstructed image in each direction is 50W. The unfiltered layergram is seen to be a distorted image of the Gaussian blob, while the rho-filtered discrete layergram displays the blob reconstructed accurately within the dashed circle. Fig. 5.3 shows that the reconstructed blob should possess negligible clutter for values of r/W and N lying to the left of the dashed line. For an image of the Gaussian blob reconstructed from 20 projections, fig. 5.3 shows that there should be negligible clutter within a circle of radius 8W from the centre of the blob. This conclusion is verified by fig. 5.4b, where the dashed circle has a radius of 8W.

5.5.2 Angular Aliasing in FTFSI Image

Unless a uniformly resolved image is computed by introducing a spatial frequency cut-off $\hat{\rho}$ as specified by eqn (5.33), any feature reconstructed using the FTFSI will be reconstructed differently depending upon its position within the cross-section. Hence the clutter associated with the reconstructed image varies as the Gaussian blob is moved about in the (r,θ) plane. A convenient method has not been found for describing analytically the clutter in the image of a Gaussian blob reconstructed with the FTFSI scheme. However, the clutter introduced into the image as the blob is placed at different positions in the (r,θ) plane is demonstrated in fig. 5.5. The maximum clutter occurs when the blob is near the edge of the (r,θ) plane, and decreases as the blob is moved towards the centre of the plane. The reconstructed images displayed

in fig. 5.5 are computed using 20 equally-spaced projections of the blob.

5.6 Image Reconstruction from Unequally Spaced Projections

In some cases it is not possible to measure projections at equal increments in ϕ. This situation often occurs in radio-astronomy where the directions at which measurements of objects on the celestial sphere may be made, are only partly under the control of the observer. In using radio-interferometry, the directions at which the measurements may be made are determined by the number and placements of available interferometer arrays, and the position of the object in the sky (Burns and Yao 1970). These authors consider the use of prolate spheroidal wavefunctions (Slepian and Pollak 1961) to estimate the parts, which cannot be measured directly, of the Fourier transform of a brightness-temperature distribution. Other authors have attempted to use the condition that brightness distributions are positive (e.g. Biraud 1969) or to reconstruct from the available data an image that has maximum entropy (Frieden 1972). These techniques are closely related to methods which attempt to use a priori knowledge of the nature of cross-sections, in order to increase the resolution in the reconstructed images, as discussed in section 5.6.

A further example which illustrates the constraints imposed upon the angles at which measurements may be made in radio-astronomy, is when the two-dimensional brightness temperature distribution of a radio-star is being determined from measurements made during a lunar occultation, (c.f. Scheuer 1962, Taylor 1967). 'Projections' in this case are

one-dimensional equivalent line-source distributions of the two-dimensional brightness temperature of the star. The projections are computed as the star becomes obscured by the moon (Scheuer 1962), so that the angles at which the projections are available depend entirely upon the motion of the star with respect to the lunar disk. Successive projections may only be measured at later dates when the moon and radio-star again come into conjunction.

In other situations, a number of equi-spaced projections may be available only from within a narrow cone of views. Such a situation is encountered in electron microscopy (Crowther et al. 1970), where physical constraints on the microscope tilt stage enable projections of an object to be made only within a range of approximately 20°. The proponents of 'ART' (Gordon et al. 1970) claim that their method provides satisfactory reconstructions from a set of projections from within an arbitrarily small angular range. However, in practice there are severe limitations on any method which attempts to compute a uniformly resolved reconstruction from such measurements.

5.6.1 Mathematical Basis

There is a mathematical basis for attempting to reconstruct images from data measured in either of the situations outlined above, and relies on the fact that the Fourier transform of a cross-section of finite extent is an entire function (c.f. Goodman 1968, p.133).

Let the Fourier transform of the cross-section be represented by an angular Fourier series expansion,

$$\Lambda(\rho,\phi) = \sum_{n=-N}^{N} a_n(\rho) \exp(jn\phi). \qquad (5.49)$$

The projections are measured at arbitrary angles ϕ_m in the range $0 < \phi < \pi$, so that 2N independent samples of $\Lambda(\rho,\phi)$ are obtained for a particular ρ. The samples of $\Lambda(\rho,\phi)$ may be related to the coefficients $a_n(\rho)$ through a matrix multiplication

$$[\Lambda(\rho)] = [E][a(\rho)], \qquad (5.50)$$

where the (m,n)th element of [E] is

$$E_{m,n} = \exp(j(n-N-1)\phi_m). \qquad (5.51)$$

So, provided [E] is not singular, the coefficients $a_n(\rho)$ are obtained by matrix inversion:

$$[a(\rho)] = [E]^{-1}[\Lambda(\rho)]. \qquad (5.52)$$

The $a_n(\rho)$ are then substituted into eqn (5.49) and the Fourier transform evaluated for all ϕ, as described in chapter 4, section 4.4.3. In principle, the above approach remains valid as the angular range of the set of angles $\{\phi_m\}$ approaches zero. It is emphasised however that the above formula applies only for that part of $\Lambda(\rho,\phi)$ which is accurately representable by an angular Fourier series of 2N+1 terms.

To demonstrate the limitations inherent in using the method described above, an example is given in which the restoration of a periodic function from its samples is attempted. The restoration is computed for the samples lying within progressively smaller fractions of 2π radians. Evaluation of the function and the inversion of the matrix are performed on a digital computer using double precision arithmetic.

The periodic function considered is

$$\Lambda(\theta) = \sin\theta + .5\cos 2\theta + \sin 4\theta, \qquad (5.53)$$

samples of which are obtained by multiplying it by $S(\varepsilon,\theta)$, where

$$S(\varepsilon,\theta) = \sum_{n=-7}^{8} \delta(\theta - \frac{n\varepsilon\pi}{8}). \qquad (5.54)$$

The intervals between the samples, and hence the range over which $\Lambda(\theta)$ is sampled, is determined by the value which ε takes within the range $0 < \varepsilon \leqslant 1$. The sampled values are then substituted into eqn (5.52) and the Fourier coefficients a_n computed by matrix inversion.

Fig. 5.6 shows how errors in the computed coefficients are magnified as ε is decreased. It is emphasised that the original samples are computed with the double-precision accuracy for the IBM 360/44 computer of 1 part in 10^{14}. If the samples are computed with an accuracy of only .01%, then the error level in the computed coefficients is magnified considerably as is shown in fig. 5.6. However, it is doubtful whether radiographic projections could be measured with even this precision, so that the extrapolation method described above is not feasible in practice.

Numerous authors have investigated similar problems under the headings of super-resolution (Toraldo di Francia 1955, Barnes 1966), analytic continuation (Harris 1964, Helstrom 1967) and non-uniform sampling in optics (Gori and Guattari 1971). Each concludes that the extrapolation of functions into regions outside those in which the functions are measured, while theoretically possible, is severely limited by the noise level in the measurements.

One may obtain an approximate reconstructed image from data collected from a restricted cone of views by using any of the FTR or DFL methods, simply by ignoring the missing data. If this is done, a sector of the Fourier transform plane is effectively set to zero, resulting in an image which is well resolved in certain directions but poorly resolved in others.

A further method of partially correcting the reconstructed image when it is computed from a set of unequally spaced projections is described by Bracewell and Riddle (1967). To reconstruct an image from projections measured at the set of arbitrary angles $\{\phi_n | a \leq \phi_n < \pi\}$, Bracewell and Riddle evaluate a set of coefficients $\{\chi_n\}$ where

$$\chi_n^{-1} = A \sum_{m=1}^{N} \exp(-N^2(\phi_m-\phi_n)^2/6) \tag{5.55}$$

and A is chosen such that

$$\frac{1}{N} \sum_{n=1}^{N} \chi_n = 1. \tag{5.56}$$

The members of $\{\chi_n\}$ are arbitrary measures of the numbers of projections per unit angle in the vicinity of each ϕ_n, (c.f. $\mathcal{K}(\sigma,\theta)$ introduced in eqn (3.64)). These values are then used to weight the rho-filtered projections measured at the various ϕ_n, prior to back-projection to form the image:

$$\bar{f}_N(r,\theta) = \frac{\pi}{N} \sum_{n=1}^{N} \chi_n \hat{f}(r\cos(\theta-\phi_n),\phi_n). \tag{5.57}$$

5.7 Resolution and Uncertainty

Given some number N of measured projections, one wishes to determine what fineness of detail can be attained in the reconstructed image. This is the question of resolution in which one asks how close two separate features of the image can be before they become indistinguishably merged (c.f. the Rayleigh resolution criterion, Lipson and Lipson (1969), p.213). It is difficult to find unambiguous answers because the attainable resolution is appreciably affected by the detailed shapes not only of the two features, but also of the neighbouring parts of the image (c.f. Toraldo de Francia 1955).

The density is zero for $|x| > a$ and $|y| > a$, so that from the sampling theorem, $\omega(x,y)$ is uniquely defined by the samples of its Fourier transform, $\Omega(m/a,n/a)$, where m and n are integers in the range $(-\infty,\infty)$. The given data can only be related directly to the values which $\Omega(\alpha,\beta)$ assumes on straight lines passing through the origin of the Fourier transform plane. So $\Omega(m/a,n/a)$ cannot be computed for all m and n from the given data unless $\Omega(\alpha,\beta) = \Lambda(\rho,\phi)$ is taken to be negligible for ρ greater than some finite value $\hat{\rho}$. This means effectively that $\Omega(\alpha,\beta)$ need only be known at a finite number of sample points. In practice, $\Lambda(\rho,\phi)$ is known at a finite number of discrete values of ρ, and at 2N values of ϕ, so that the required Fourier transform samples $\Omega(m/a,n/a)$ may be estimated by inverting finite-order matrices (Crowther et al. 1970). If suitable radial interpolation is performed on the known samples of $\Lambda(\rho,\phi)$ (as discussed in section 5.3) so that $\Lambda(\rho,\phi)$ is able to be determined continuously in radius, then an equivalent result can be achieved by using the FTFSI

scheme discussed in section 4.4.3. This approach is computationally more efficient than either the matrix inversion or Hankel transform methods which are discussed by Crowther et al. (1970).

If a reconstructed image is to be uniformly resolved for all spatial frequencies up to $\hat{\rho}$, then eqn (5.33) shows that the required number of projections is at least

$$N = 2\pi a\hat{\rho}. \tag{5.58}$$

However, by including some of the $a_m(\rho)$ in eqn (5.18), an image may be computed which, although it is not uniformly resolved, is nevertheless free from clutter, caused by angular aliasing. Consider again eqn (5.18):

$$\bar{\lambda}_N(r,\theta) = \frac{2\pi}{2N+1} \sum_{m=-N}^{N} \exp(-jm\theta)(-j)^m \int_0^\infty a_m(\rho)\, J_m(2\pi\rho r)\rho d\rho. \tag{5.59}$$

Note that since Fourier series interpolation is being used, the members of $\{K_m\}$ in eqn (5.18) are unity for $-N \leqslant m \leqslant N$. If the members of $\{a_m(\rho') \mid \hat{\rho} \leqslant \rho' \leqslant 2\hat{\rho}\}$ are included in the image, then from the discussion in section 5.5, the coefficients $a_{N+p}(\rho')$, where

$$p = [N(\frac{\rho'}{\hat{\rho}} - 1)], \tag{5.60}$$

are aliased with the coefficients $a_{N-p}(\rho')$. To avoid including coefficients which are subject to aliasing errors, the maximum radius r' in the object, within which the density may be reconstructed to a resolution of at least ρ', is given by

$$2\pi\rho' r' \leqslant N - p. \tag{5.61}$$

Rearranging this expression and substituting for p from eqn (5.60), it may be shown that

$$\rho' \leq \frac{N}{\pi(r'+a)} . \qquad (5.62)$$

This is equivalent to the condition given by Gilbert (1972b) and is also analogous to the 'Basic Image' concept discussed by Smith et al. (1973). The resolution criterion given by eqn (5.62) shows that the image may be reconstructed with spatial frequencies up to a value of

$$\rho' = \frac{N}{\pi a} \qquad (5.63)$$

at the centre of the object, and to half this value at the periphery, provided that the coefficients in the set $\{a_m(\rho)\}$, which are affected by aliasing, are not included in the reconstruction procedure. The set of coefficients $\{a_m(\rho)\}$ in the FTFSI scheme, and $\{\alpha_{m,p}, \beta_{m,p}\}$ in the FSI scheme, which are subjected to aliasing errors, are called the sets of ambiguous coefficients.

The foregoing reasoning applies only to images about which one has no pre-knowledge, apart from the radii of their circumscribing circles. If one knows a priori that the image possesses some special property, for example a particular symmetry, as is true of certain micro-biological specimens (Crowther et al. 1970), then this knowledge may be used to advantage to reduce the number of projections required to reconstruct an image. Crowther et al. (1970) and De Rosier and Moore (1970) describe procedures for reconstructing cross-sections of objects which exhibit icosahedral or helical symmetry.

The fact that the cross-section of the object is known to be real and positive has been suggested by a number of authors as a possible means of increasing the resolution in the reconstructed image (c.f. Gilbert 1972a,b, Klug and Crowther 1972, Gordon et al. 1970, Biraud 1969, Frieden 1972, and Frieden and Burke 1972). So far it appears that it is computationally expedient to make use of this constraint only in iterative schemes (Gilbert 1972a). However, the extent to which the application of the positivity constraint is of use in such techniques, remains to be determined.

When using a direct space iterative reconstruction scheme such as 'ART' (Gordon et al. 1970, Frieder and Herman 1971), care must be exercised not to make unwarranted assumptions regarding the topology of the cross-section. Such iterative methods require that the cross-section be considered as being composed of cells on a grid, with the density being constant but unknown within each cell. Bellman et al. (1971) use this argument to show that an image may be reconstructed exactly on an N x N point grid by using N projections each of N samples. In situations where one has an object with such a cellular topology, N^2 independent equations in N^2 unknowns may be formulated, and these may be solved by conventional matrix inversion or by 'ART'. However, as is shown in section 5.4, the projections of a cross-section which does not have this topology are not completely independent of each other, and so more than N projections are required to reconstruct N^2 independent points of the cross-section.

Gordon et al. (1970) argue further that their contention that only N projections are required to reconstruct the image, holds even when the sector within which the projections are

measured approaches zero. This same argument is extended in chapter 6 and in Appendix B to demonstrate the kind of dangers that are inherent in assuming that the cross-section being reconstructed has a grid-like structure. It is shown that such a cross-section may be reconstructed from a single projection, provided that the angle at which the projection is measured is suitably chosen. However, the same reconstruction technique, when applied to a single radiographic projection, is shown to lead to a meaningless image. Iterative techniques clearly have practical application, as shown by the results presented by Ambrose and Hounsfield (1973). However, it is felt that there is a need to investigate more fully the conditions under which satisfactory images may be obtained using these methods.

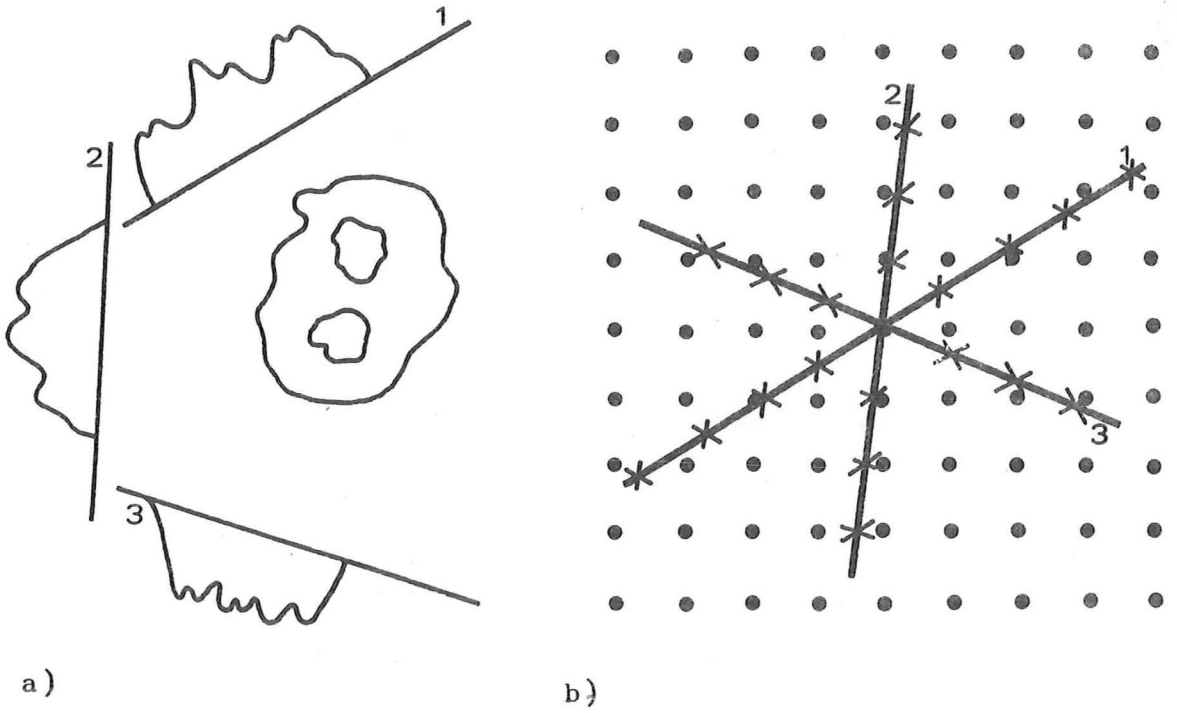

Fig. 5.1. Relationship of Fourier transforms of projections to two-dimensional transform grid.

a) Three typical projections of an object.

b) The Fourier transforms of these projections must be interpolated from radial lines onto the Fourier transform grid. The crosses indicate the samples of the projection transforms and the dots denote the points of the Fourier transform grid onto which values must be interpolated.

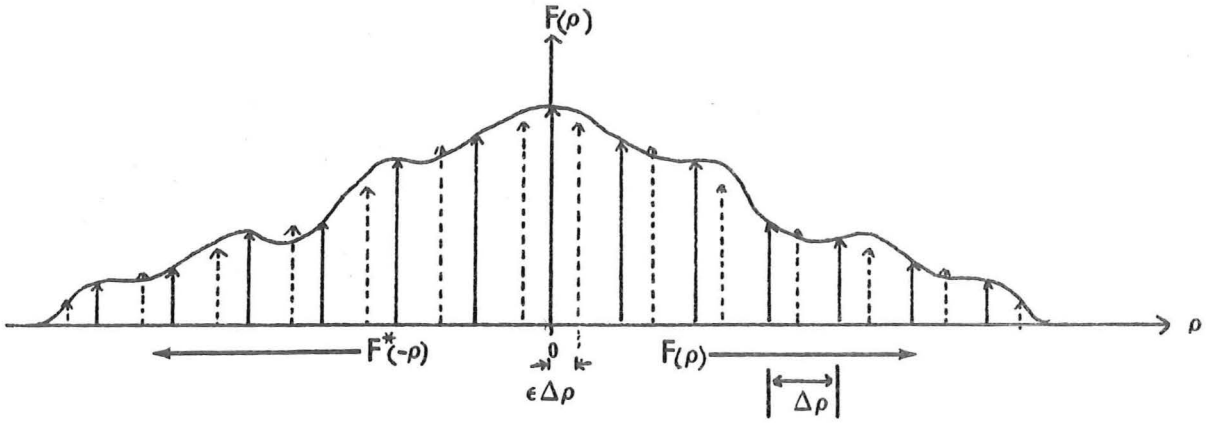

Fig.5.2. Linear interpolation between grid systems. Samples of $F(\rho)$ at the points ρ_n are shown by the solid arrows spaced by $\Delta\rho$. The broken arrows denote the values $\bar{F}(\rho_n+\epsilon\Delta\rho)$ which are linearly interpolated from the samples $F(\rho_n)$. The original and interpolated samples are conjugate symmetric about the origin.

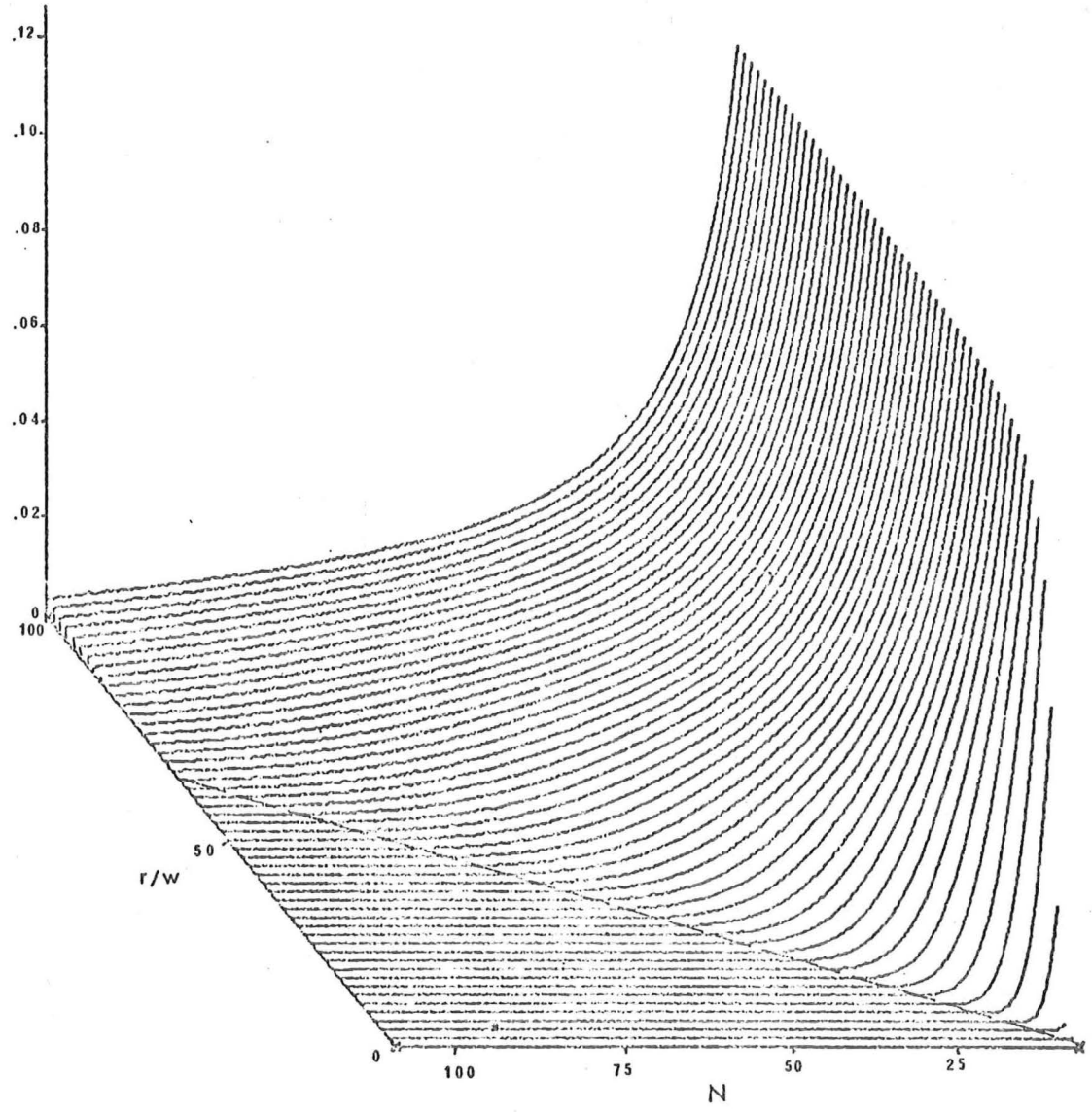

Fig.5.3. Maximum magnitude of clutter associated with the rho-filtered discrete layergram of a Gaussian blob, as a function of the number of projections (N) and the normalised distance from the centre of the blob (r/w).

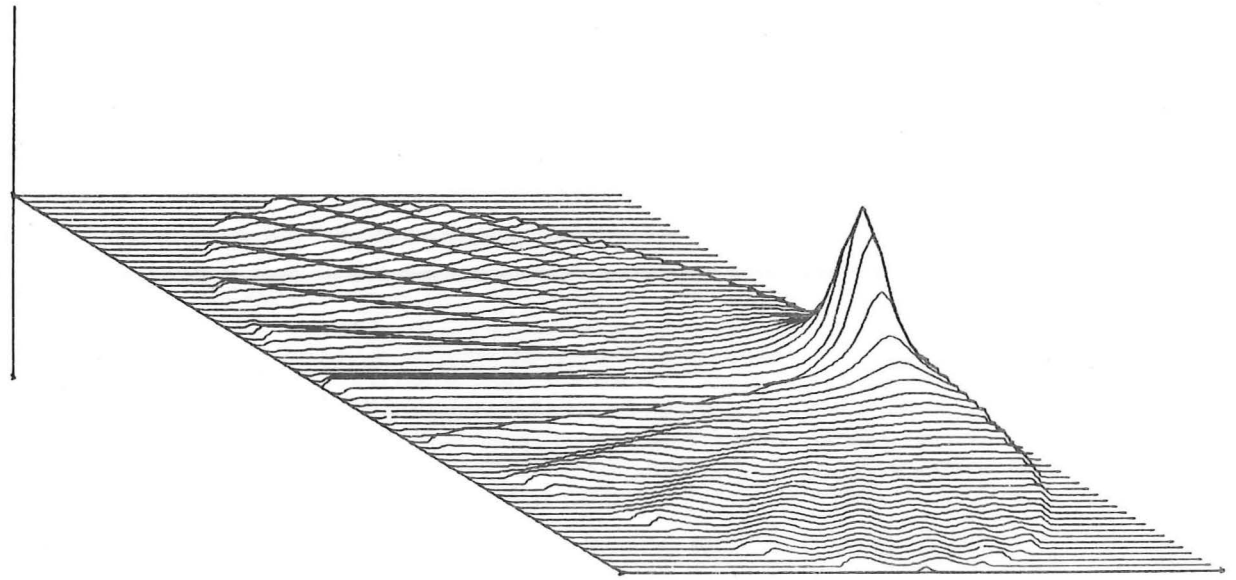

a)

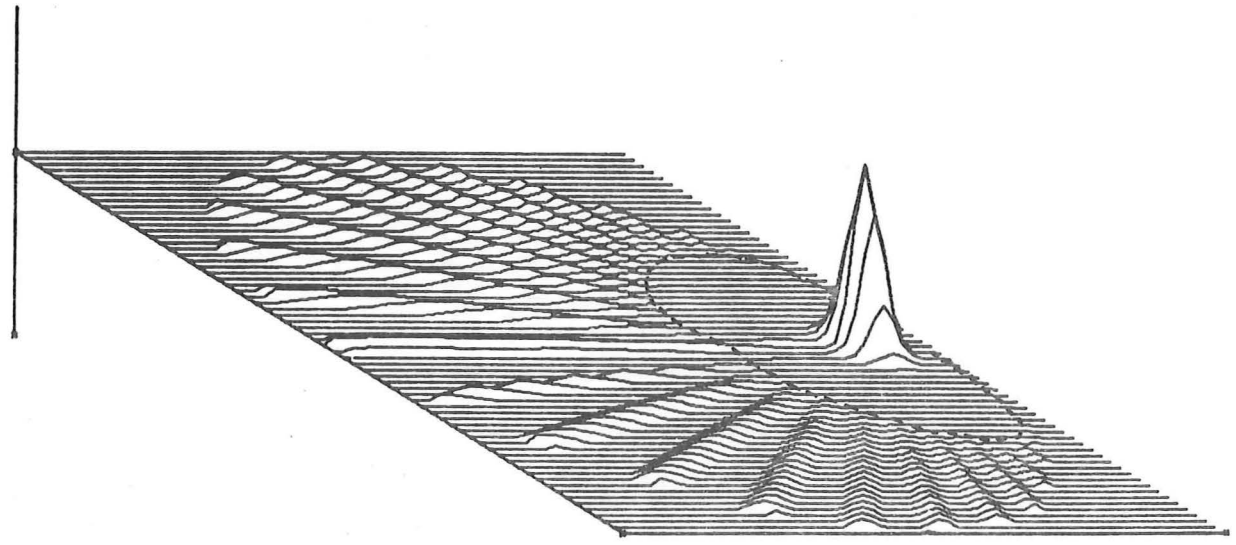

b)

Fig. 5.4. Reconstructed images of Gaussian blob showing clutter level.

a) Discrete layergram.

b) Rho-filtered discrete layergram.

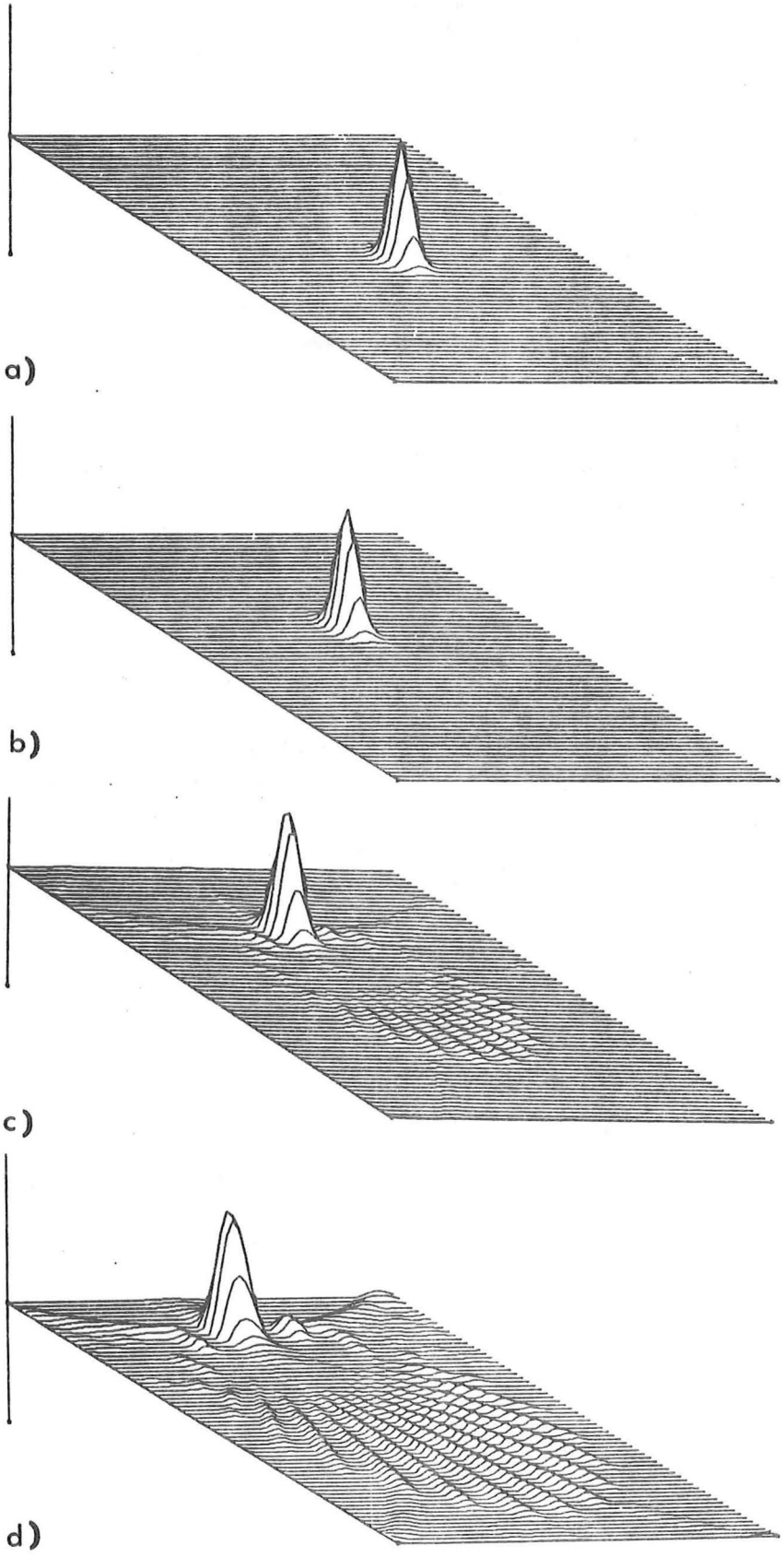

Fig. 5.5. Reconstructed images of Gaussian blob using FTFSI scheme showing clutter level.

Blob centred at r/w = a) 0.
= b) 6.4,
= c) 12.8,
= d) 19.2.

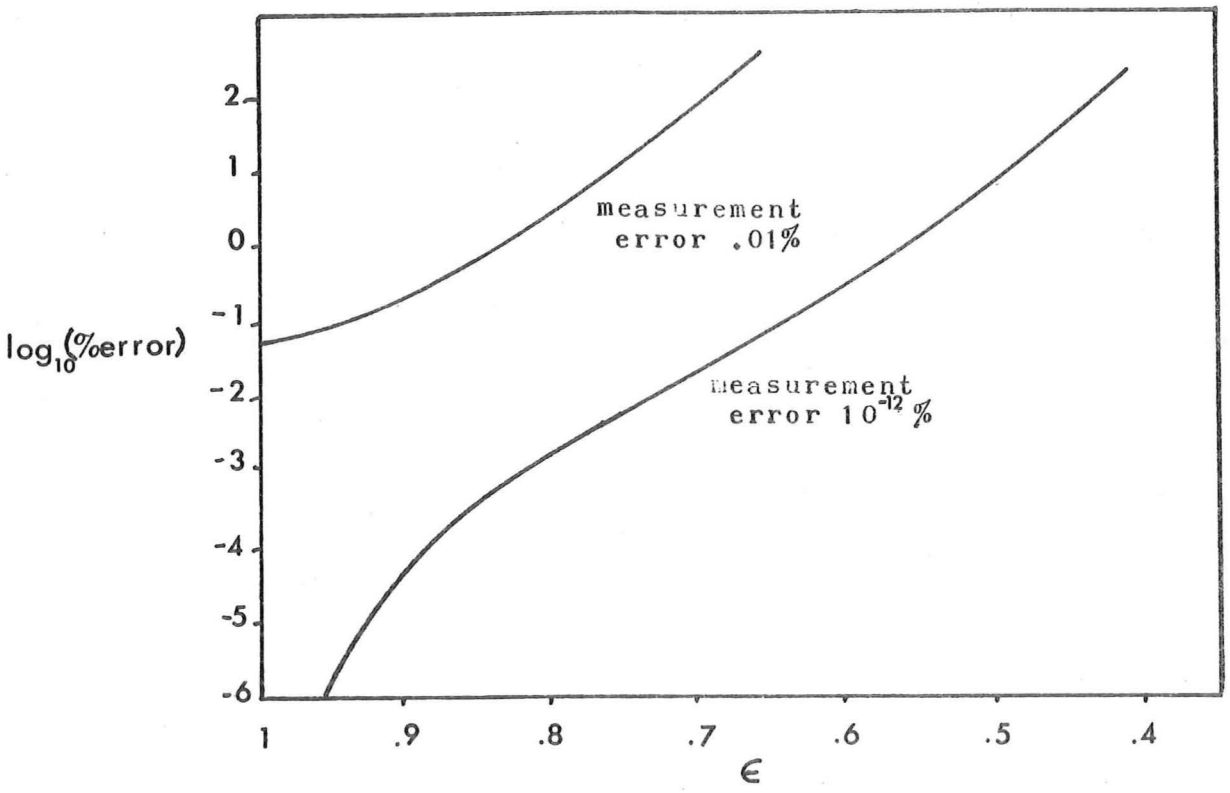

Fig. 5.6. Error in angular extrapolation of Fourier transforms. ϵ indicates the fraction of 2π radians within which a periodic function is sampled. Restoration of this function is attempted over the entire range $(0,2\pi)$ by matrix inversion. The lower curve shows how the rms error in the computed coefficients varies with ϵ when the initial samples are measured with double precision accuracy. The upper curve gives the rms error in the computed coefficients when the samples are accurate to .01%.

CHAPTER 6

COMPUTATIONAL RESULTS

This chapter is devoted to the presentation and discussion of computational results which illustrate the use of the various formulae presented in the preceeding chapters. Images displayed in figs 6.3, 6.4 and 6.7 are produced using the facsimile machine described in Appendix C.

6.1 Comparison of Reconstruction Methods

To compare the five main reconstruction methods considered previously, a set of 20 projections equally spaced in angle within the range $(0,\pi)$ is computed analytically for the annular cross-section shown in fig. 6.1a. While this is a simple test object, the sharp transitions in density at the edges represent crucial tests for the reconstruction procedures. Reconstructed images of this cross-section using the discrete layergram, rho-filtered discrete layergram, spread, linear and FTFSI reconstruction schemes are displayed by the contour plots of fig. 6.1b-6.1f. Adjacent contour lines are spaced at increments of 10% in density.

The first example (fig. 6.1b), illustrates the nature of the reconstructed image when the discrete layergram of the cross-section is computed. The lack of detail in this image is easily seen. This image is theoretically of infinite extent (c.f. chapter 4, section 4.2), although it is bounded in this instance by a circle of radius a since it is assumed *a priori* that no density exists for $\xi > a$. It is not obvious

that the image represents an object with a hole in its centre, as the reconstructed density in this region is approximately 80% of the maximum, and it is not possible to determine the positions of the edges of the annulus.

Fig. 6.1c shows the rho-filtered discrete layergram (RDL), of the same cross-section. When the Fourier transforms of the projections are evaluated prior to rho-filtering, 64 complex Fourier coefficients are computed for each projection. For this image, no data window is applied to the transformed projections, and so fig. 6.1c contains all 64 coefficients. Note that at most seven radial Fourier coefficients should be included in the reconstruction procedure to satisfy the resolution criterion of eqn (5.33). The following examples in this section all violate the resolution criterion of eqn (5.33) to this same extent. The clutter present in this image is due to angular aliasing, as discussed in section 5.5 of chapter 5. The reconstructed annulus is seen to be very sharply delineated with the reconstructed value at the centre of the annulus being zero. However, the clutter level, which is up to 25% of the maximum reconstructed density, detracts somewhat from this image.

Figs 6.1d-f show the reconstructed images of the annulus using the Spread, Lin and FTFSI schemes respectively. The three images are all alike and vary slightly only in the level and extent of the clutter which they exhibit. The image computed by the FSI scheme (Smith et al. 1973) is similar to the FTFSI image (fig. 6.1f) and so is not displayed separately. Each of the RDL, Lin, Spread and FTFSI reconstruction procedures lead to negative clutter whose magnitude is similar to that of the positive clutter. However, for clarity only

positive parts of the reconstructed images are displayed in the examples given in this chapter.

These results demonstrate that both the rho-filtered discrete layergram procedure and the procedures which interpolate the Fourier transform of the cross-section lead to images which are superior to the discrete layergram shown in fig. 6.1a. The RDL image is sharp but significantly contaminated by clutter, while the Lin, Spread, and FTFSI procedures produce images which are sharply resolved in radius, but poorly resolved in angle. However, while these images are not as sharp as the RDL image, they also exhibit much less clutter. From the results displayed in figs 6.1c-f, it is clear that useful images are obtained using each of the RDL, Lin, Spread and FTFSI reconstruction schemes, in spite of the small number (20) of projections used.

6.2 Images Reconstructed Using the FTFSI Scheme

The effects on the reconstructed images, of suppressing certain of the coefficients in the set $\{a_m(\rho)\}$ computed for the FTFSI scheme, are demonstrated by the perspective plots of figs 6.2 a-d. Again 20 projections are used, in the reconstruction of an ideal cross-section consisting of a disk of unit density whose extent is a/4 situated at the coordinates $(a/4,\pi)$ in the (r,θ) plane, as shown in fig. 6.2a. The image shown in fig. 6.2b is that which is computed using the resolution criterion derived in chapter 5, eqn (5.33). If 20 projections are to be used, the maximum frequency component that must be included in the image is shown by eqn 5.33 to be 7/2a cycles per unit length. To obtain the image shown in fig.

6.2b, all parts of the Fourier transform of the image for spatial frequencies greater than 7/2a cycles per unit length are set to zero. Since the Fourier transform is truncated abruptly at this spatial frequency, ripples due to Gibbs' phenomenon are generated in the region outside the reconstructed disk (c.f. Chapter 9, section 9.1.2).

Fig. 6.2c demonstrates the nature of the image that is obtained by setting to zero those members of the set $\{a_m(\rho)\}$ which are affected by aliasing errors. This is the non-uniformly resolved aliasing-free image that is discussed in chapter 5, section 5.7 . It is also analogous to the 'Basic Image' of Smith et al. 1973. This image is sharper than the previous one since more spatial frequency components are included. However, since the number of Fourier coefficients $a_m(\rho)$ that are included in the Fourier transform of the image varies linearly from 40 at $\rho = 7/2a$, to zero at $\rho = 7/a$, the spatial frequency cut-off is effectively more gradual than that present in fig. 6.2b. Hence the magnitude of the ripples present in fig. 6.2b is reduced in fig. 6.2c.

The image shown in fig. 6.2d is computed using the FTFSI scheme when all of the coefficients in the set $\{a_m(\rho)\}$ are included in the reconstruction procedure. It is seen that the addition of the angularly aliased coefficients in this image, while causing the disk to be reconstructed more sharply than in the previous two images, also causes the clutter level in the image to be increased.

It is emphasised that while the aliasing-free image shown in fig. 6.2c contains the maximum amount of unambiguous information that it is possible to extract from 20 projections, this image exhibits twice the resolution at the centre of the

(r,θ) plane than it does at the edge of this plane. However, the image shown in fig. 6.2b exhibits uniform resolution throughout the (r,θ) plane and so structure in the cross-section is reconstructed in a manner which is independent of its position in the plane.

6.3 Image Reconstruction from Projections Measured with Diverging Radiation

Two DRR schemes which are based on the FTR and RFL radiation transforms respectively, are presented in chapter 4. These schemes enable images to be reconstructed from finite numbers of projections which have been measured with diverging radiation. If projections of this sort are used with the FTFSI or RDL schemes directly, the reconstructed images that result from the application of these schemes are distorted. Figs. 6.3a,b demonstrate the nature of the reconstructed images that are obtained when the FTFSI and discrete RDL schemes respectively are applied to simulated projections computed using 'radiation' whose maximum angle of divergence is 24 degrees. By operating upon this data as if it were obtained with parallel radiation, the distortions shown in figs 6.3a,b are introduced into the reconstructed images. The actual cross-section from which the projections are derived is shown in fig. 6.1a.

By pre-processing the 'diverging-ray' projections as described for the first DRR scheme outlined in chapter 4, section 4.5.1, and then applying the FTFSI scheme to the new set of projections generated by the preprocessing operation, the reconstructed image shown in fig. 6.3c is obtained. The

distortions present in fig. 6.3a are absent and the annulus is reconstructed accurately. Similarly, by rho-filtering the set of 'diverging-ray' projections and back-projecting them along converging lines as described for the second DRR method in chapter 4, section 4.5.2, the image shown in fig. 6.3d is obtained. By back-projecting the 'diverging-ray' projections in this fashion, the distortions evident in fig. 6.3b are removed.

In order to compare the reconstructed images in figs 6.3a-d with those obtained by using projections measured with parallel radiation, images reconstructed from projections 'measured' with parallel rays using both FTFSI and RDL techniques are shown in figs 6.3e and 6.3f respectively. It is seen that the image reconstructed with the first DRR scheme is similar to that obtained with the FTFSI scheme. However, the image reconstructed with the second DRR scheme is slightly different to the RDL image shown in fig. 6.3f. This is to be expected since, as pointed out in chapter 4, section 4.5.2, the derivation of the second DRR method is approximate.

In previous treatments of the problem of reconstructing cross-sections from radiographs, the difficulty caused by beam divergence has been either neglected (e.g. Berry and Gibbs 1970), overcome by using a scanning pencil-beam (Ambrose and Hounsfield 1973, Cormack 1963), or considered to limit the resolution in the reconstructed image (Tretiak et al. 1969). However, it has been demonstrated by the examples displayed in fig. 6.3 that provided appropriate computational steps are taken when dealing with projections measured with diverging radiation, satisfactory images may still be reconstructed.

6.4 Images Reconstructed Using 'ART'

The iterative reconstruction technique 'ART' presented by Gordon et al. (1970) and described in chapter 4, section 4.6, is used here to reconstruct the annular cross-section shown in fig. 6.1a. Reconstructed images are shown using 'ART' for projections computed in two different ways. For the first reconstructed image shown here (fig. 6.4a) a set of pseudo-projections of the cross-section is used as data. To compute the pseudo-projections, the cross-section shown in fig. 6.1a is superimposed onto a rectangular grid. Points lying within the region of the cross-section which possesses density are set to zero. The pseudo-projections of this numerically represented cross-section are computed by the method described in chapter 4, section 4.6, i.e. sets of parallel lines separated by the grid spacing are placed over the grid at angles corresponding to the angles ϕ_n at which the pseudo projections are to be computed; the values on the grid-points lying within pairs of the parallel lines are summed to give the pseudo-projections, which are then used as data for the 'ART' algorithm. The grid on which the cross-section is reconstructed consists of 64 x 64 points. The image reconstructed using the additive 'ART' algorithm (fig. 6.4a) is a reasonable representation of the cross-section. The reconstructed density does not vary significantly within the walls of the annulus and there is no clutter surrounding the annulus.

However, a completely different image is obtained when an analytically computed set of projections is used as data. The same set of projections that were derived analytically from the cross-section shown in fig. 6.1a and used for the

reconstructed images of figs 6.1b-f, are used here as input to 'ART'. The resulting image which is shown in fig. 6.4b, is a distorted representation of the cross-section. Regions of the image that were reconstructed with a constant density in fig. 6.4a, now show variations of up to 50%. The outline of the annular cross-section is also indistinct.

Each of the images displayed in fig. 6.4 were obtained after allowing the 'ART' algorithm to run for two iterations. It was found that the images obtained after further iterations showed no significant improvement over those displayed in fig. 6.4. It is interesting to note that for each of these images, the values of the pseudo-projections of the reconstructed cross-section slowly approach the values of the pseudo-projections or projections used as data, as the number of iterations increases. However, the mean squared deviation between the reconstructed cross-section and the cross-section itself increases slowly with the number of iterations. It seems therefore that the criterion of requiring that the pseudo-projections of the reconstructed image converge numerically to the projections used as data, is not sufficient to ensure that the reconstructed image converges to the cross-section. These observations are supported by Gilbert (1972b).

Gordon et al. (1970) state that projections measured within an arbitrarily narrow angular range may be used to reconstruct cross-sections using 'ART'. However, they assume that the cross-section possesses a grid-like topology. Their argument may be taken a step further to the point where a ridiculous situation ensues.

The cross-section shown in fig. 6.7a is crudely digitized into three levels (0, .5, 1) and a single pseudo-projection is computed in the manner outlined in Appendix B. This pseudo-projection is shown in fig. 6.5a. The iterative procedure described in Appendix B is used to reconstruct the image shown in fig. 6.5b from the pseudo-projection of fig. 6.5a. This reconstructed image is identical to the digitized cross-section from which the pseudo-projection is computed. However, when an actual projection (fig. 6.5c) is used as data for this procedure, the image shown in fig. 6.5d is obtained. As expected, this image bears no resemblance to the cross-section shown in fig. 6.5b.

Such a reconstruction method would never be used in practice, since there is a continuous infinity of cross-sections that can lead to a single projection. However, the example serves to illustrate that misleading results may be obtained if unwarranted assumptions are made regarding the nature of the cross-section being reconstructed.

6.5 Images Reconstructed Using Radiographically Measured Projections

The device shown diagrammatically in fig. 6.6 was used to measure 20 radiographic projections of a section of a bovine shin-bone. The device uses a slit aperture in a lead plate to allow the X-ray beam to impinge upon only the section of interest. By both rotating the bone in a step-wise fashion, and shifting the film between each exposure, the 20 radiographic projections were recorded on a single film. A radiograph was also made of an aluminium step-wedge for calibration purposes. The divergence of the X-ray beam was sufficiently narrow to be considered negligible.

These radiographs were scanned with a microdensitometer and the resulting numerical data was used as input for a digital computer. The radiograph of the aluminium step-wedge was also scanned with the densitometer and the results were used to correct the projections of the bone cross-section for non-linearities. After rescaling the projections using the step-wedge data, various image reconstruction procedures were applied to the projections in order to obtain images of the cross-section. Having measured the set of projections, the cross-section which was examined, was excised and radiographed. This radiograph is shown in fig. 6.7a.

Fig. 6.7b shows the image obtained using the discrete layergram procedure (chapter 4, section 4.2). This image is similar to that which would be obtained using the conventional transverse tomographic apparatus that is described in chapter 2, section 2.4. This image is heavily blurred, and it is neither clear that there is a hole in the centre of the bone nor that the bone consists of two components. However, the rho-filtered discrete layergram procedure which is described in chapter 4, section 4.3, leads to an image (fig. 6.7c) that displays all of the main features of fig. 6.7a, but has a high clutter level.

The three images depicted in figs 6.7d-f are reconstructed from the projections using three variations of the FTFSI reconstruction scheme. The first of these (fig. 6.7d) is the aliasing-free image of the cross-section which is computed by setting the aliased coefficients in the set $\{a_m(\rho)\}$ to zero. This image is less sharp than the rho-filtered discrete layergram shown in fig. 6.7c, but also exhibits negligible

clutter as discussed earlier in section 6.2. Note that it is analogous to the 'Basic Image' discussed by Smith et al. (1973). The second variation of the FTFSI scheme computes an image (fig. 6.7e) that possesses no Fourier coefficient whose spatial frequency is greater than 7/2a cycles per unit length. Thus this image obeys the resolution criterion derived in Chapter 5, eqn 5.33. While this image is uniformly resolved, and does not contain any ambiguous information, it clearly conveys less useful information about the structure of the cross-section of the bone than does the rho-filtered discrete layergram (fig. 6.7c), or the non-uniformly resolved aliasing-free image (fig. 6.7d). The third variation of the FTFSI scheme computes an image (fig. 6.7f) that retains all of the Fourier coefficients in the set $\{a_m(\rho)\}$ in the Fourier transform of the reconstructed image. In spite of the fact that most of the coefficients $a_m(\rho)$ are computed incorrectly because of aliasing, the reconstructed image shown in fig. 6.7f is nevertheless the image which most closely resembles the cross-section itself. The images computed using the Lin, Spread and FSI reconstruction schemes are visually similar to the FTFSI image of fig. 6.7f, and so are not displayed separately.

The result displayed in fig. 6.7f demonstrates that useful images of cross-sections of physical objects may be obtained even when only 20 projections are measured. Since the image shown in fig. 6.7f is not uniformly resolved and contains errors due to the inclusion of aliased Fourier coefficients, it is not possible to make accurate quantitative judgements regarding the density at any point of the cross-section on the basis of this image. If it is required to reconstruct an image

that is meaningful quantitatively, then sufficient projections must be measured to enable the image to be reconstructed with a specified uniform resolution. The commercial device developed by Hounsfield (Ambrose and Hounsfield 1973) uses 180 projections to reconstruct the cross-section on an 80 x 80 point grid. Ambrose and Hounsfield claim that by using such a large number of projections, the density in their reconstructed image is accurate to better than 0.5%.

6.6 Efficiency of Reconstruction Techniques

A comparison of the efficiencies of the various image reconstruction procedures, as executed on the IBM 360/44 computer at the University of Canterbury Computer Centre, is given by the computation times quoted in table 6.1. The final entry in table 6.1 illustrates the time saving that may be achieved by using the FFT algorithm rather than a direct integration rule to evaluate the Fourier transforms.

The time given in table 6.1 for the diverging-ray FTFSI method is 27% greater than the time required for the FTFSI method, and the time for the diverging-ray rho-filtered discrete-layergram method is 45% greater than the time required to reconstruct an image using the rho-filtered discrete layergram procedure. Thus, the fact that projections are measured with diverging radiation, does not appreciably affect the efficiency of the reconstruction algorithms.

The iterative methods 'ART' and 'SIRT' are shown by table 6.1 to be much slower than the Fourier transform techniques. From the author's experience (section 6.4) and Gilbert's (1972b) observations, both 'ART' and 'SIRT' require at least

Table 6.1

Reconstruction Method	Approximate time in minutes to reconstruct an image from 20 projections of 128 samples, onto a 128 x 128 point grid
Discrete Layergram	1.9
Rho-filtered Discrete Layergram	2.2
Spread/Linear Interpolation	.8
Fourier Series Interpolation (FSI)	2.9
Fourier Transform Fourier Series Interpolation (FTFSI)	1.1
Diverging-ray Rho-filtered Discrete Layergram	3.2
Diverging-ray FTFSI	1.4
'ART'*	4I
'SIRT'**	>4I
FTFSI using direct Fourier transform***	(a) 280 (b) 4.5

* I is the number of iterations required for convergence. Its value depends on the nature of the data being used (Gilbert 1972b).

** Estimate only.

*** The times given are extrapolated from a smaller problem. The time (a) is required if no factoring of the dimensional transform is performed. Time (b) is required if transform is factored into 256 one-dimensional transforms (c.f. Hunt et al. 1970).

two iterations to reconstruct an image.

From the results presented in this chapter, it is clear that by employing image reconstruction methods based upon Fourier transforms, one is able to compute cross-sections form projections very efficiently if the FFT algorithm is used. It is also evident that simple interpolation schemes (i.e. Lin, Spread) lead to images that are visually similar to those computed using the more rigorous schemes (i.e. FSI, FTFSI) and so the simple schemes should be used, whenever possible, to minimise computer time.

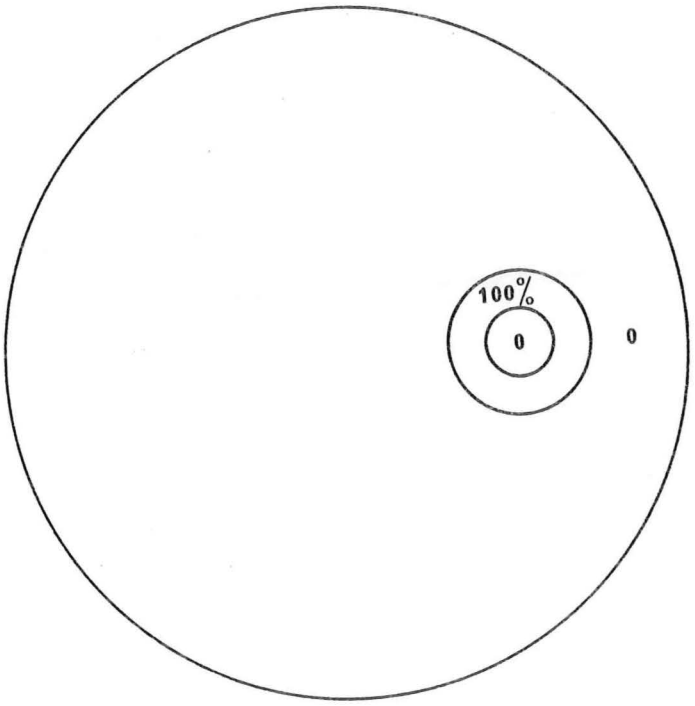

a)

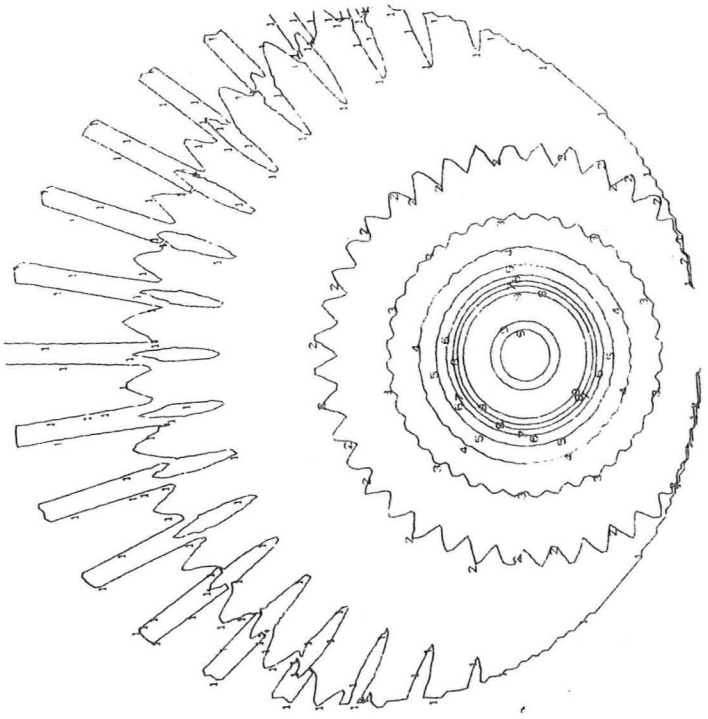

b)

Fig. 6.1....

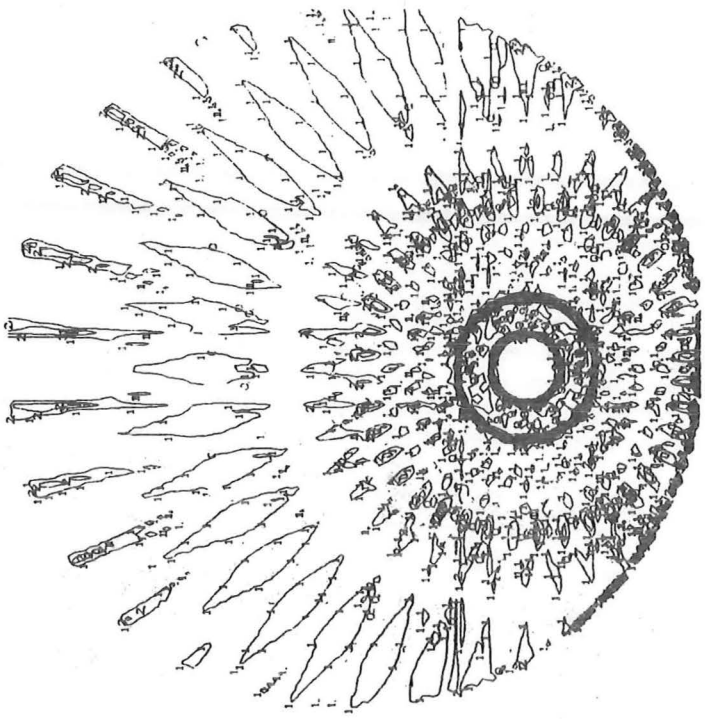

c)

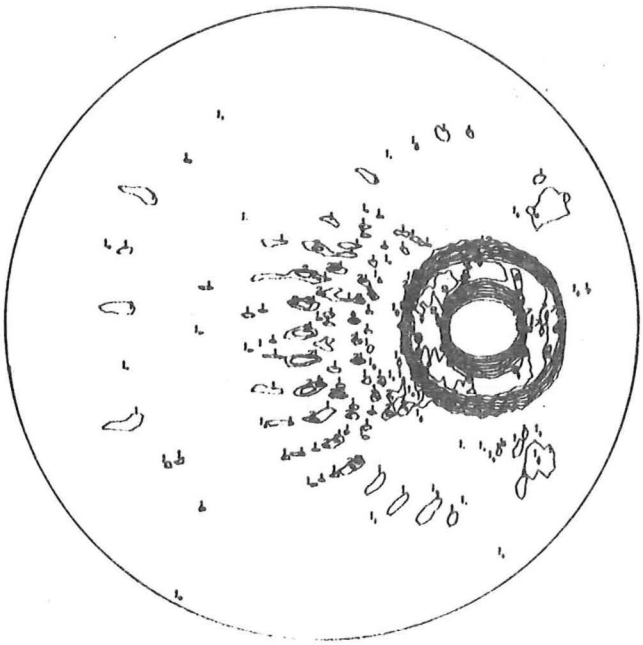

d)

Fig. 6.1....

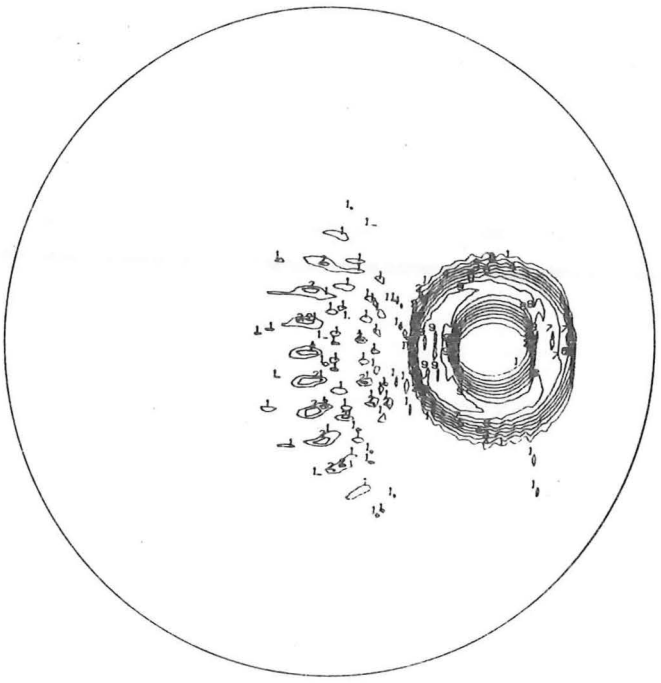

e)

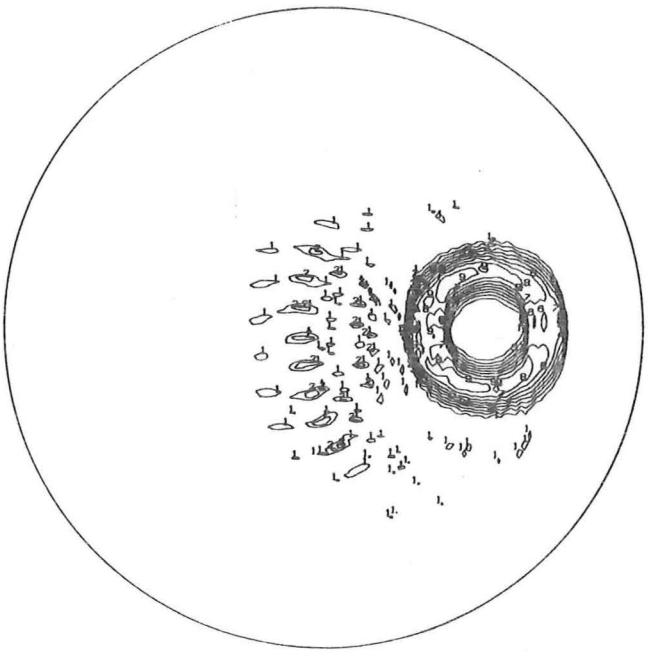

f)

Fig. 6.1. Results of reconstruction schemes on ideal data.

a) Ideal object.

b) Discrete layergram.

c) Rho-filtered discrete layergram.

d) Spread interpolation.

e) Linear interpolation.

f) FTFSI.

Images are contoured in steps corresponding to 10% of maximum reconstructed density.

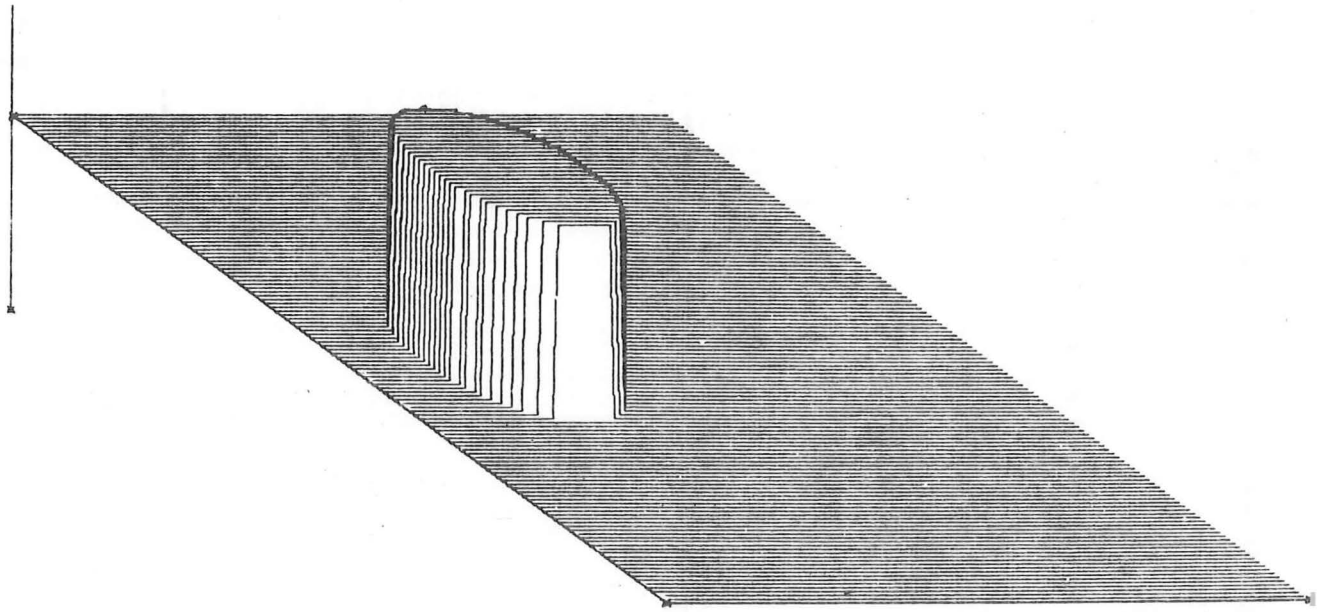

a)

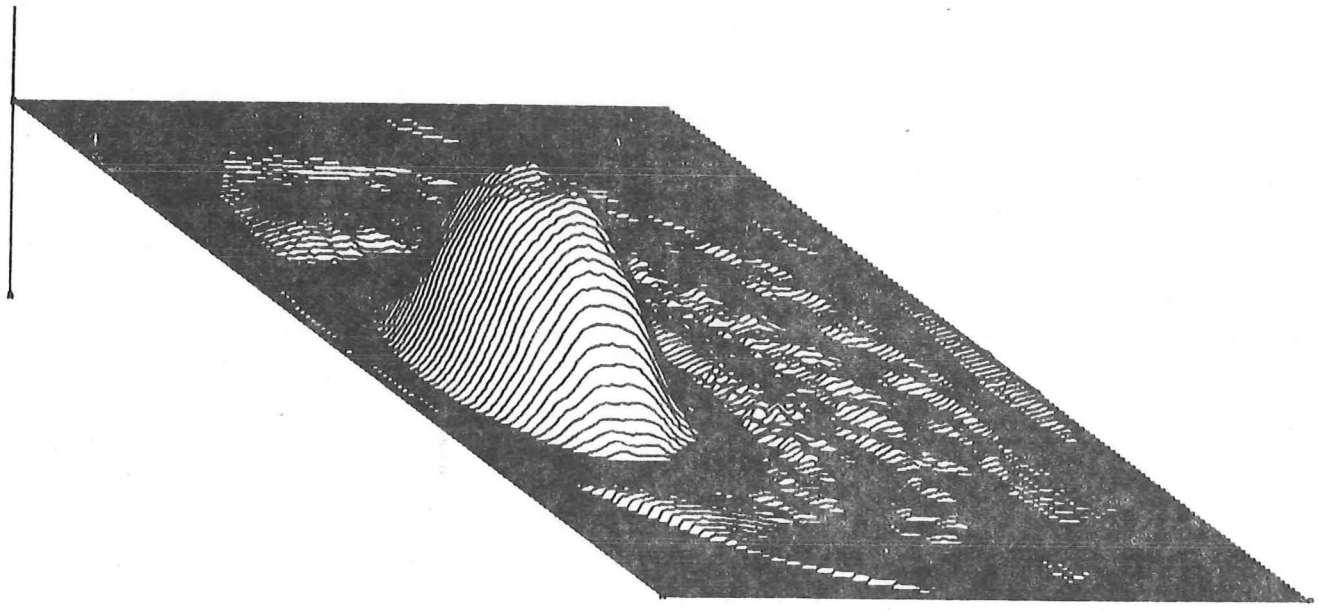

b)

Fig. 6.2....

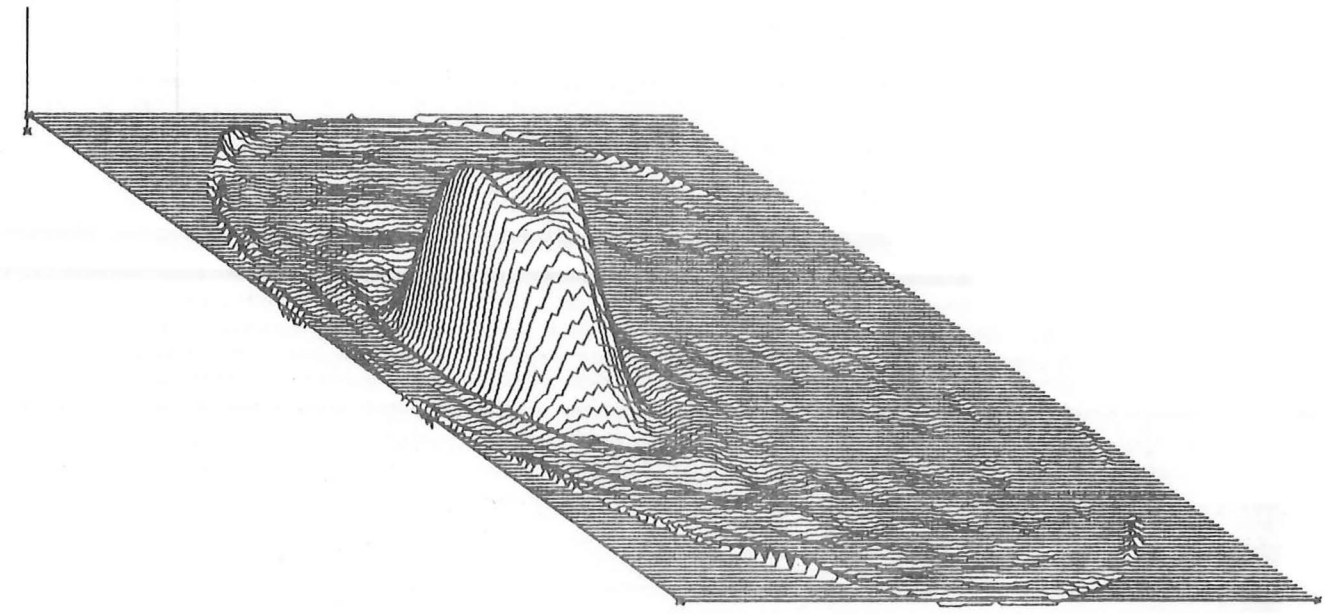

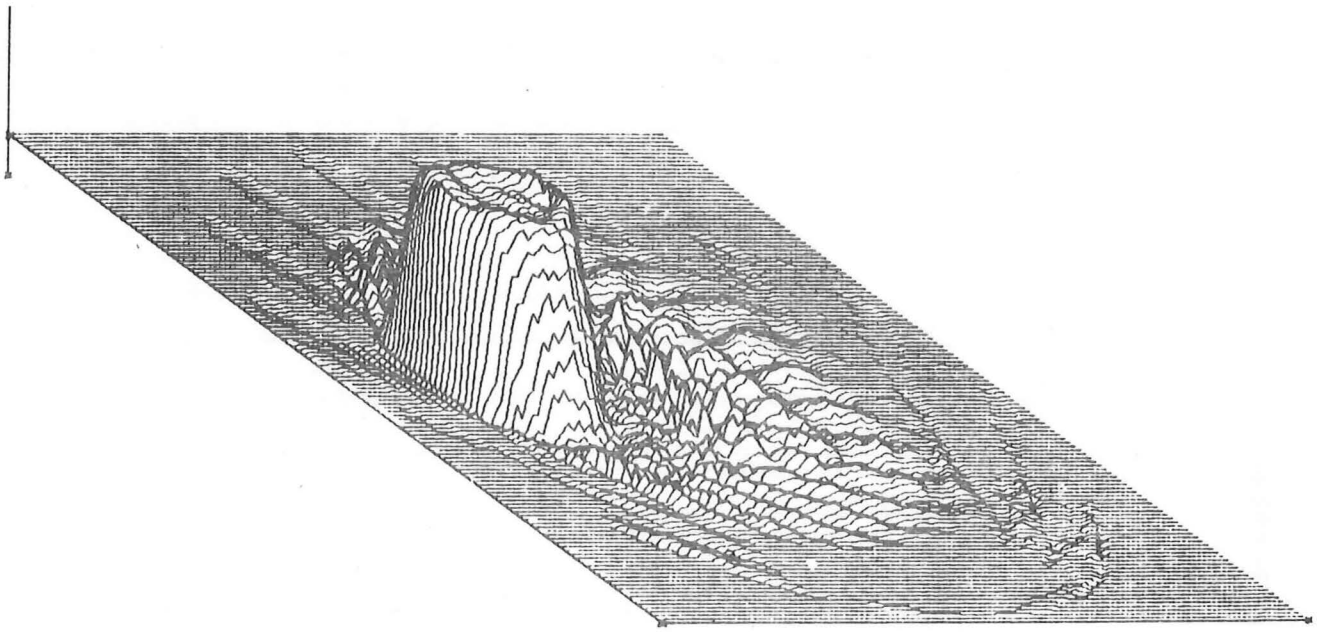

d)

Fig. 6.2. Reconstructed images using FTFSI scheme.
Apparent height is proportional to reconstructed density.
a) Ideal object.
b) Reconstructed image with frequency cut-off of 7/2a.
c) Aliasing-free reconstructed image.
d) Image obtained with all coefficients included in reconstruction procedure.

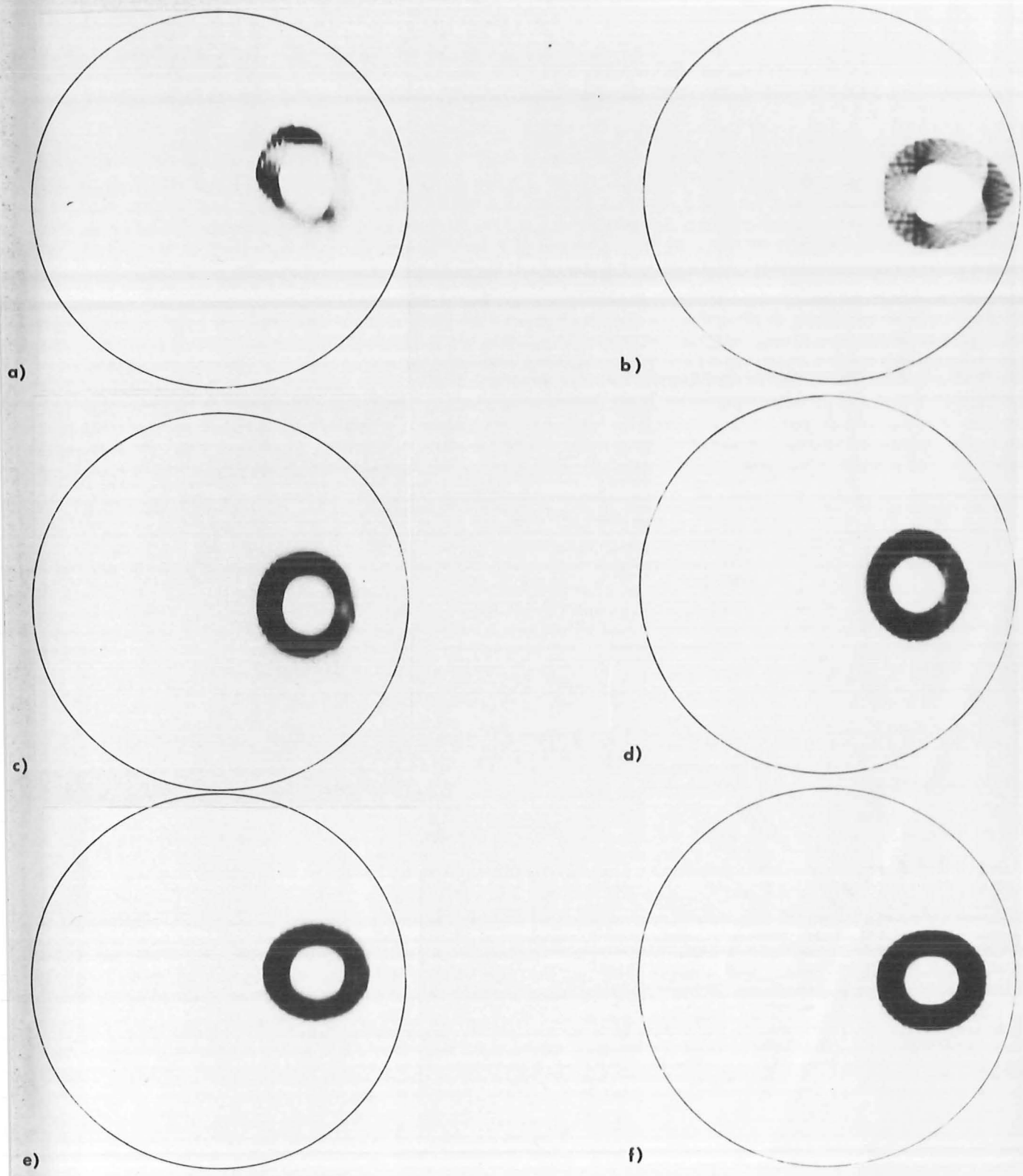

FIG. 6.3. IMAGES RECONSTRUCTED FROM 'DIVERGING-RAY' PROJECTIONS.

) NORMAL FTFSI IMAGE WITH 'DIVERGING-RAY' PROJECTIONS

) NORMAL RHO-FILTERED LAYERGRAM WITH 'DIVERGING-RAY' PROJECTIONS.

) FTFSI IMAGE WITH PRE-PROCESSING TO ACCOUNT FOR X-RAY DIVERGENCE.

) RHO-FILTERED LAYERGRAM WITH BACK-PROJECTION OF PROJECTIONS ALONG CONVERGING PATHS.

) IMAGE RECONSTRUCTED USING FTFSI PROCEDURE OPERATING ON IDEAL 'PARALLEL-RAY' PROJECTIONS.

) RHO-FILTERED LAYERGRAM USING IDEAL 'PARALLEL-RAY' PROJECTIONS.

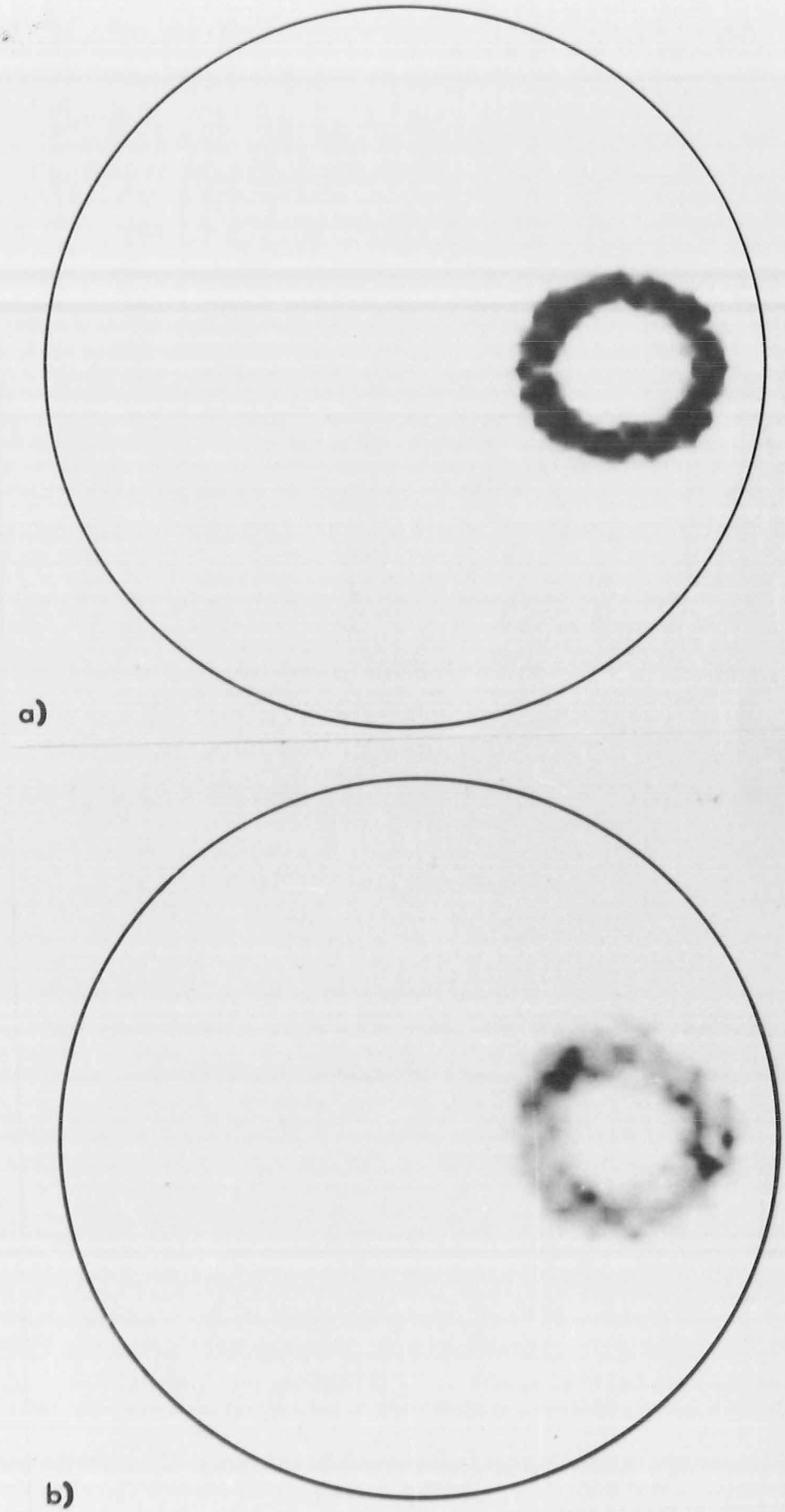

Fig. 6.4. Image reconstruction using the 'ART' algorithm.
a) Pseudo-projections used as data.
b) Analytically computed projections used as data.

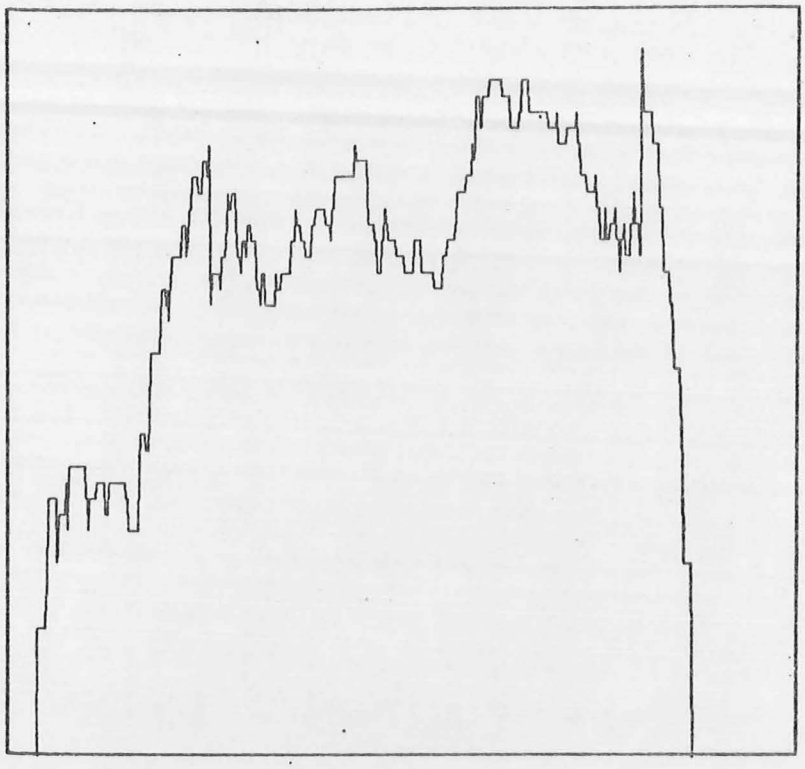

a

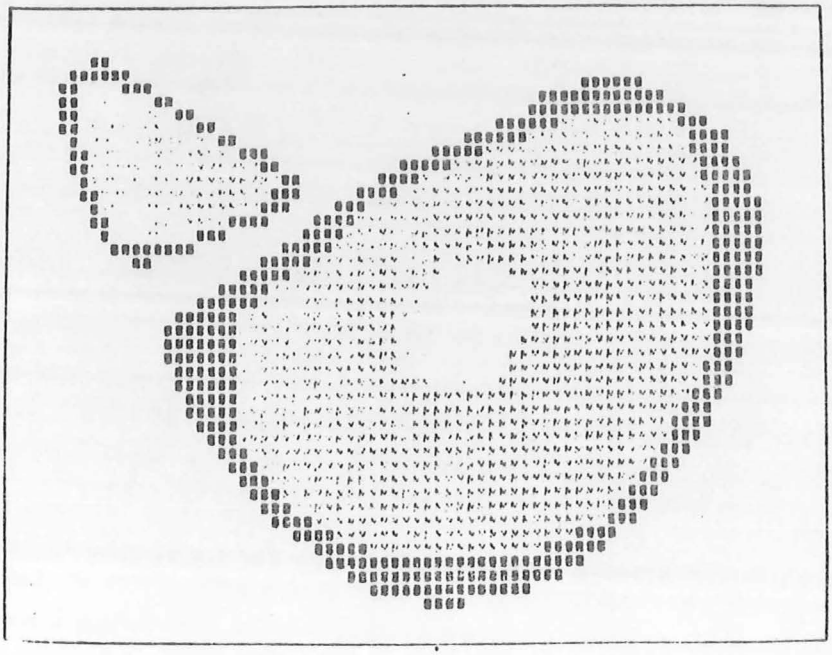

b

Fig.6.5....

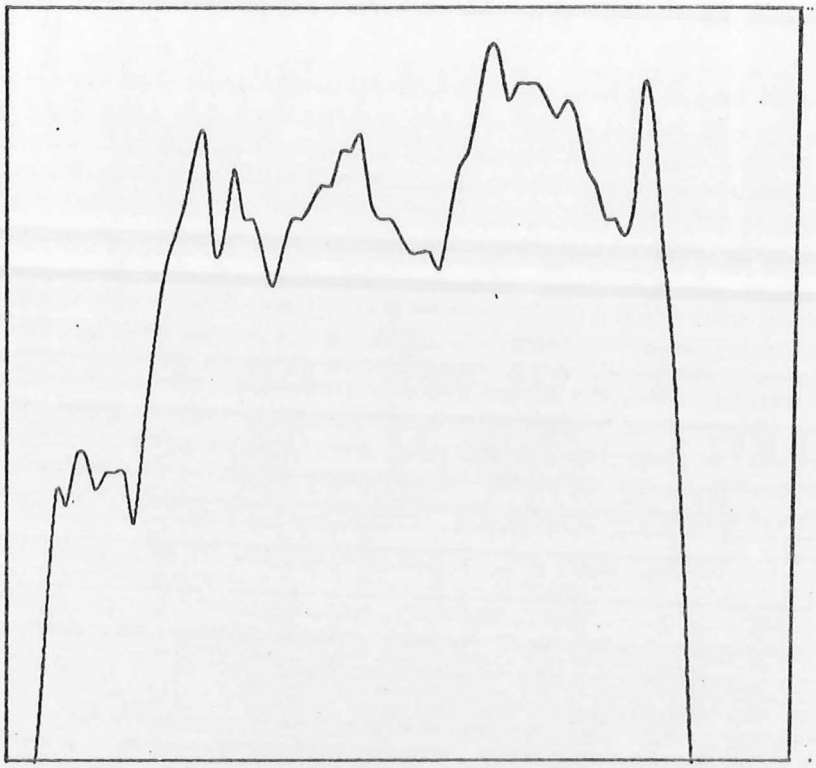

c)

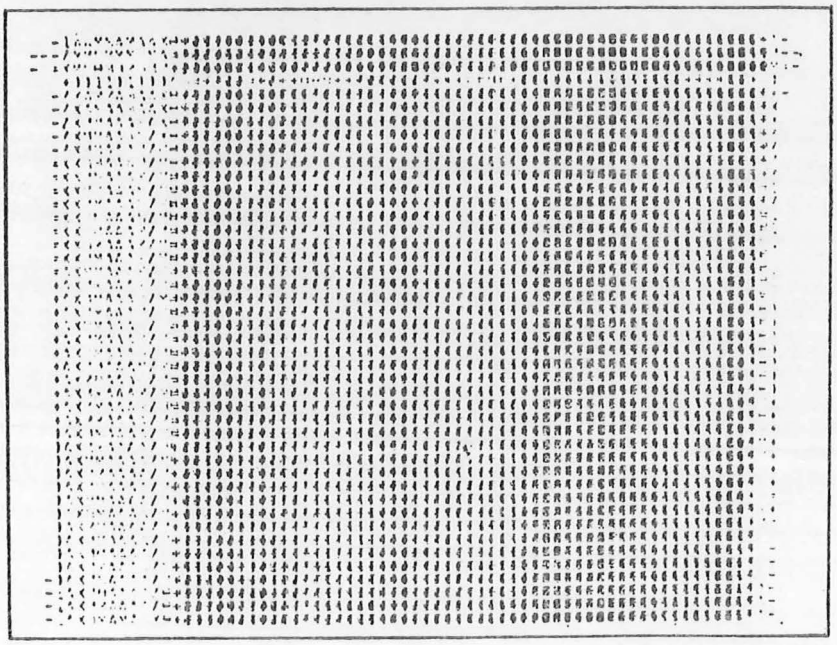

d)

Fig. 6.5. Image reconstruction from a single pseudo-projection.

a) Single pseudo-projection of the cross-section shown in fig. 6.7a.

b) Image reconstructed from this pseudo-projection.

c) Actual projection of the cross-section shown in fig.6.7a.

d) Image reconstructed from actual projection.

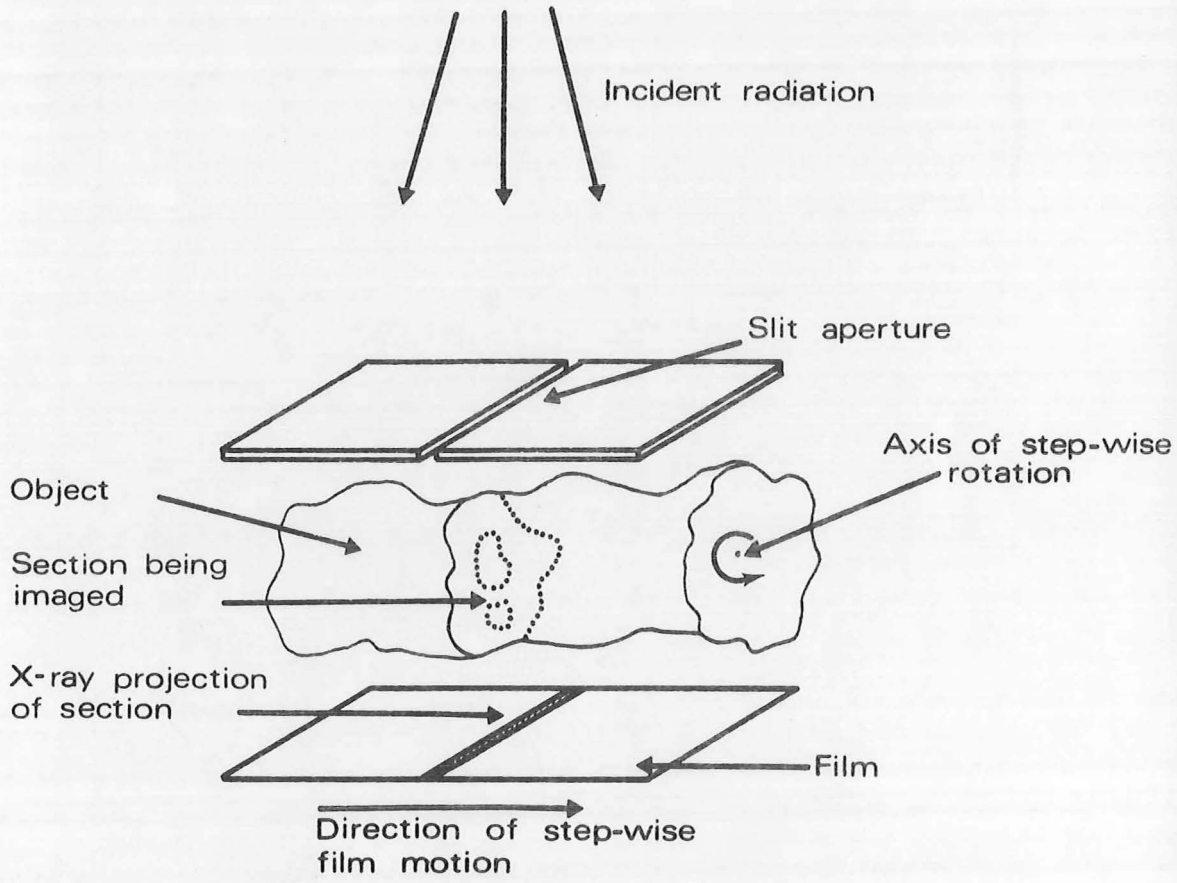

Fig. 6.6. Method used to measure radiographic projections.

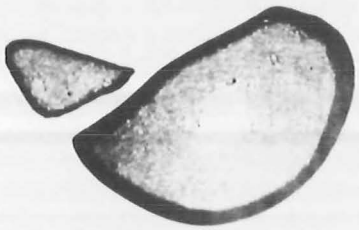

a)

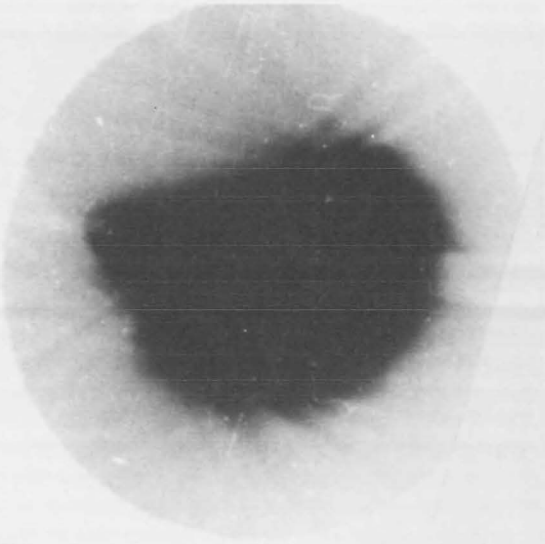

b)

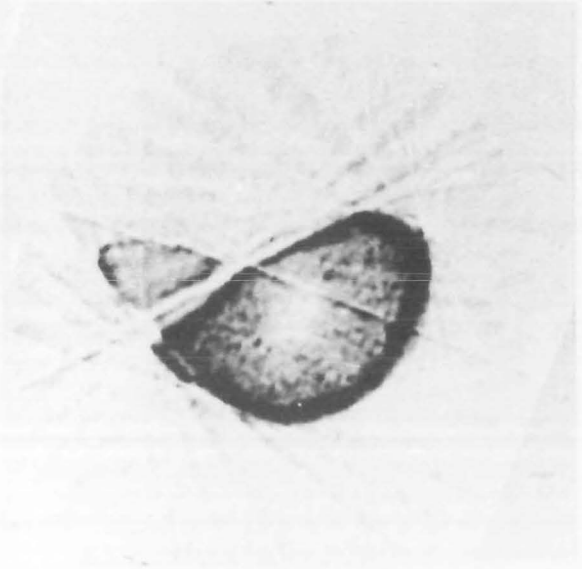

c)

d)

Fig. 6.7....

e)

f)

Fig. 6.7. Reconstructions of a section of bovine shin bone.

a) Radiograph of excised cross-section.

b) Discrete layergram.

c) Rho-filtered discrete layergram.

d) Aliasing-free reconstructed image using FTFSI.

e) FTFSI reconstructed image with a spatial frequency cut-off at 7/2a.

f) FTFSI reconstructed image with all computed coefficients used by reconstruction procedure.

CHAPTER 7

SPATIAL FILTERING TO IMPROVE TRANSVERSE TOMOGRAPHY

7.1 Introduction

In chapter 2, two methods of radiographic tomography (longitudinal and transverse) are considered in some detail. This chapter begins with a discussion of these two techniques from the point of view of linear systems theory. Using this approach, the tomogram is regarded as a superposition of images of all the planes within the object, with each section being reproduced with varying degrees of blurring. It is shown that no amount of processing may be applied to a conventional tomogram to 'focus' on any plane other than the fulcrum plane. However, it is shown that the systems theoretic approach may be usefully employed to improve the tomographic image, if certain modifications are made to the conventional tomographic apparatus. Section 7.3 outlines appropriate modifications which must be made to enable a layergram (c.f. chapter 3, eqn 3.18) of the tomographic plane to be obtained. While the layergram is similar in appearance to the conventional transverse tomogram, it has the special property that it is described by a linear blurring operation on the image of the cross-section. The construction of a practical device to produce such layergrams radiographically is also described in section 7.3.

Section 7.4. reintroduces the mathematical expressions (originally given in chapter 3), and derives an analytical expression for computing layergrams of a particular class of object.

The nature of the blurring in the layergram suggests simple optical and digital methods of restoring the original cross-section. Sections 7.5 and 7.6 describe both of these methods in detail.

Various approximations must be made in order to represent the practical radiographic layergram in terms of linear systems theory. Such approximations, and their effect on the reconstructed images, are described in section 7.7, while factors which limit the resolution of the system are discussed in section 7.8.

Experimental results using both optical and digital reconstruction methods are given in section 7.9, while the system as a whole is evaluated in section 7.10.

7.2 Tomography as a Linear Imaging System

As a prelude to the discussion of deblurring and image-enhancement methods as applied to tomography, it is useful to consider the tomographic imaging process in terms of linear systems theory. The following analysis applies to all tomographic systems which attempt to image a single plane of an object.

The three-dimensional object is represented in Cartesian coordinates as $\omega(x,y,z)$. The density distribution in the tomographic plane to be imaged is defined by $\omega(x,y,z_1)$ where the plane z_1 is chosen anywhere within the object perpendicular to the z axis. Consider $\omega(x,y,z_1)$ to be imaged using longitudinal tomography with both linear and circular obscuring motions, where for simplicity the X-rays are assumed to impinge upon the object in parallel beams. Figs 7.1

.a,b show the angular ranges through which a particular ray travels during the tomographic obscuring motion in each of these two cases. The angle Ψ is the maximum angular deviation of a particular ray from the centre-line in each instance. Note that the circular obscuring motion in longitudinal tomography is equivalent to that present in conventional transverse tomography.

The wedge-shaped volume in fig. 7.1a is that swept out by a laminar beam of rays during the imaging motion. Since obscuring motion occurs only in the x-direction, the linear tomographic system need only be analysed in two dimensions (i.e. the x-z plane). For circular tomography, obscuring motion occurs in both the x and y directions. Hence fig. 7.1b shows only the path of a single ray throughout the obscuring motion. It follows that the tomogram may be expressed as a convolution of the density distribution of the object with the function, termed the selectivity function S, describing the motion of the laminar beam in the case of linear tomography, or the single ray in the case of circular tomography.

From inspection of figs 7.1a,b, the selectivity functions for linear and circular tomography respectively, are seen to be

$$S_{lin}(x,z) = |z-z_1|^{-1} \text{rect}\left(\frac{x}{2|z-z_1|\tan\Psi}\right) \qquad (7.1)$$

and

$$S_{circ}(x,y,z) = (2\pi|z-z_1|)^{-1}\delta((x^2+y^2)^{\frac{1}{2}} - |z-z_1|\tan\Psi) \qquad (7.2)$$

Thus $S_{lin}(x,z)$ has the form of the solid double wedge shown in fig. 7.1a, while $S_{circ}(x,y,z)$ has the form of the surface of a double cone (fig. 7.1b). The apices of the wedge and cone respectively lie in the plane z_1. Let $h(x,y,z)$ denote the tomogram of a plane at any level z within the object. Using the selectivity function, this general tomogram may be written as

$$h(x,y,z) = \omega(x,y,z) * S. \tag{7.3}$$

Note that eqn (7.3) represents a convolution in two-dimensions for linear tomography and in three dimensions for circular tomography.

In the following analysis, C_n is used to denote a constant of proportionality whose dimensions are [density][length]^n. In order to determine the manner in which an arbitrary point within the cross-section is imaged in the tomogram, it is convenient to let the cross-section be represented as a single point with coordinates $(0,0,z_b)$, i.e.

$$\omega(x,y,z) = C_3\, \delta(x)\, \delta(y)\, \delta(z-z_b). \tag{7.4}$$

Since z_1 is the fulcrum plane in each tomographic system, the image of a point in any plane z_b becomes, for linear tomography,

$$h_{lin}(x,y,z_1) = C_3 \iint_{-\infty}^{\infty} \frac{\delta(x_a)\,\delta(y)\,\delta(z_a-z_b)}{|z_a-z_1|} \operatorname{rect}\left(\frac{x_a-x}{2|z_a-z_1|\tan\Psi}\right) .dx_a dz_a \tag{7.5a}$$

$$= C_3 |z_b-z_1|^{-1} \operatorname{rect}\left(\frac{x}{2|z_b-z_1|\tan\Psi}\right) \delta(y) \tag{7.5b}$$

which is a constant function along a line of extent $|z_b-z_1|\tan\Psi$, and of amplitude inversely proportional to the distance of the point $(0,0,z_b)$ from the tomographic plane z_1. Similarly the image of the point $(0,0,z_b)$ for circular obscuring motion, is

$$h_{circ}(x,y,z_1) = C_3\int_{-\infty}^{\infty}\int\int \frac{\delta(x_a)\delta(y_a)\delta(z_a-z_b)}{2\pi|z_b-z_1|}$$

$$.\delta\left[((x_a-x)^2+(y_a-y)^2)^{\frac{1}{2}} - |z_a-z_1|\tan\Psi\right]dx_a dy_a dz_a \qquad (7.6a)$$

$$= C_3(2\pi|z_b-z_1|)^{-1}\delta((x^2+y^2)^{\frac{1}{2}} - |z_b-z_1|\tan\Psi). \qquad (7.6b)$$

So, for the case of circular tomography, the image of a point lying in the plane $z = z_b$ is a function whose value is constant and proportional to $|z_b-z_1|^{-1}$ on a circle of radius $|z_b-z_1|\tan\Psi$, and zero elsewhere. Taking the limit as z_b approaches z_1 in eqn 7.5 (c.f. Bracewell 1965, p.70), i.e.

$$\lim_{z_b \to z_1} C_3|z_b-z_1|^{-1}\,\mathrm{rect}\left(\frac{x}{2|z_b-z_1|\tan\Psi}\right)\delta(y) = C_3\delta(x)\delta(y), \qquad (7.7)$$

shows that if the isolated point $(0,0,z_b)$ lies in the fulcrum plane, it is imaged perfectly as a single point in linear tomography. Similarly, by taking the limit as z_b approaches z_1 in eqn 7.6, it transpires that

$$\lim_{z_b \to z_1} C_3(2\pi|z_b-z_1|)^{-1}\delta((x^2+y^2)^{\frac{1}{2}} - |z_b-z_1|\tan\Psi) = C_3\frac{\delta(r)}{2\pi r}$$

$$= C_3\delta(x)\delta(y) \qquad (7.8a)$$

where

$$r = (x^2+y^2)^{\frac{1}{2}}. \qquad (7.8b)$$

For circular tomography then, points in the fulcrum plane are imaged perfectly in the absence of other structure within the volume $\omega(x,y,z)$.

The question now posed is, how this analysis might be used to improve the tomographic image. Since the tomogram contains information about all of the points within an object, albeit as blurred images for the most part, it is of interest to consider whether sections other than the tomographic plane may be enhanced.

It is shown by eqn (7.5) above, that a point located in the plane defined by $z = z_b$ (remote from the fulcrum plane z_1) is imaged as a line in the linear tomogram. In the absence of any density within the object other than in the plane z_1, the resulting tomogram is the same as an image that has been subjected to linear motion blurring. There are well established techniques for restoring such images to their undistorted form (e.g. Som (1971), Slepian (1967), NASA (1968)). These methods either explicitly or implicitly use some form of transform division to perform the inverse of the original blurring. For example, if an object contains density only in the plane z_b, so that its structure is described by $C_1\omega(x,y,a)\delta(z-z_b)$, then the tomogram produced using linear obscuring motion is

$$h(x,y,z_1) = C_1\omega(x,y,z)\delta(z-z_b) * \left[|z_b-z_1|^{-1} \operatorname{rect}\left(\frac{x}{2|z_b-z_1|\tan\Psi}\right)\right] \qquad (7.9)$$

Denoting the two-dimensional Fourier transforms with respect to x and y of $h(x,y,z)$ and $\omega(x,y,z)$ by $H(\alpha,\beta,z)$ and $\Omega(\alpha,\beta,z)$ respectively, the Fourier transform of eqn (7.9) is

$$H(\alpha,\beta,z_1) = 2C_1\Omega(\alpha,\beta,z_b)\tan\Psi\,\mathrm{sinc}(2\alpha|z_b-z_1|\tan\Psi) \qquad (7.10)$$

In order to restore the image to its unblurred form $\omega(x,y,z_1)$, one must divide $H(\alpha,\beta,z_1)$ by $2\tan\Psi\,\mathrm{sinc}(2\alpha|z_b-z_1|\tan\Psi)$, and invert the Fourier transform. However, if there is density in some other plane (say z_c), then eqn (7.10) becomes

$$H(\alpha,\beta,z_1) = 2C_1\tan\Psi\Big[\Omega(\alpha,\beta,z_b)\,\mathrm{sinc}\,(2\alpha|z_b-z_1|\tan\Psi) + \Omega(\alpha,\beta,z_c)\,\mathrm{sinc}\,(2\alpha|z_c-z_1|\tan\Psi)\Big] \qquad (7.11)$$

On division of both sides of eqn (7.11) by $2\tan\Psi\,\mathrm{sinc}(2\alpha|z_b-z_1|\tan\Psi)$, the first term of the RHS of eqn (7.11) gives $\Omega(\alpha,\beta,z_b)$ as previously. However, since the zeros of the denominator do not correspond with those of the numerator in the second part of the division, the expression is singular and cannot be evaluated. For this reason it is impossible to recover $\Omega(\alpha,\beta,z_b)$ (and hence $\omega(x,y,z_b)$) by classical image deblurring methods when more than a single plane within the object has significant density. A similar argument may be advanced for circular tomography.

However, the systems approach to tomography is useful in another area. Consider the form of the tomographic image when circular obscuring motion is used, and the object consists of a filament of density parallel to the z axis, i.e.

$$\omega(x,y,z) = C_2\,\delta(x)\,\delta(y). \qquad (7.12)$$

Substituting eqn (7.12) into eqn (7.3), and using the selectivity function S_{circ}, gives the tomogram of the density distribution described by eqn (7.12) as

$$h_{circ}(x,y,z_1) = C_2(x^2+y^2)^{-\frac{1}{2}} = C_2 r^{-1} \qquad (7.13)$$

and hence the point-spread function (see chapter 3, section 3.3.2) of the system is r^{-1}. So for any object with a density which varies arbitrarily in the x-y plane but does not vary in the z direction, the image produced by the circular tomograph is (c.f. section 2.4.1)

$$h(x,y,z_1) = \omega(x,y,z_1) * r^{-1} \qquad (7.14)$$

This is the function which is defined in chapter 3 as the layergram of $\omega(x,y,z_1)$. The rho-filtered layergram restoration method described in that chapter may therefore be used to recover the original cross-section.

Since objects of interest are unlikely in practice to be cylindrical, it is necessary to consider an appropriate modification to conventional transverse tomographic apparatus, to enable it to be used to produce layergrams. It was noted in chapter 2 that one method of attempting to remove the interfering effects of shadows, of density outside the tomographic plane, was to decrease the angle Φ (see fig. 2.5) of the central ray from the horizontal. There is however a limit, past which Φ cannot be further reduced, since radiation incident upon X-ray film has increasingly less photographic effect as the angle between the direction of the rays, and the film, approaches zero. To overcome this difficulty, the method of recording the image must be modified.

7.3 A New Layergraph

This section is concerned with a new tomographic device (called a layergraph) which allows the incident radiation to impinge upon the object normal to its longitudinal axis, and yet still enable the photographic film to be exposed satisfactorily.

The new tomographic system is shown in fig. 7.2. The essential differences between the new and the conventional systems may be seen by comparing figs 7.2 and 2.5. In the new system, the incident X-ray beam passes through a slit aperture in a lead plate so that only a thin section of the object is irradiated. On exit from the object, the radiation passes through a further such aperture, and falls on a fluorescent screen which registers the radiographic projection of any desired section of the object as a line of light. An optical system consisting of a cylindrical and a spherical lens images the line as a two-dimensional function on the photographic film. Denoting the intensity variation of the light along the line on the fluorescent screen as $f(\xi)$, and the two-dimensional distribution of light intensity at the film plane as $h(\xi,\eta)$, these two functions are related by

$$h(\xi,\eta) = f(\xi) \tag{7.15}$$

where (ξ,η) is a Cartesian coordinate system as defined by fig. 3.1a. By imaging the radiographic projection on film in this way, an optical equivalent of the digital 'back-projection' operation (c.f. eqn (3.35)) is performed. The effect of this is equivalent to that which would be obtained if a radiographic film could be exposed by the X-ray beam in conventional

tomography when the angle Φ in fig. 2.5 is zero. By synchronously rotating both the object and the photographic plate, a layergram of a cross-section of the object is built up on the film.

In the experimental design developed by the author (fig. 7.2), the one-dimensional 'optical' projection formed on the fluorescent screen is imaged onto the film by means of the optical system described above, and a mirror. The purpose of the mirror is to bend the optical path through 90^{o} to ensure that direct X-rays do not expose the film. The experimental layergraph is shown in fig. 7.3.

7.4 Closed-Form Expression for Layergram

From chapter 3, it will be recalled that the layergram is related to the projected density by

$$g(r,\theta) = \int_0^{\pi} f(r\cos(\theta-\phi),\phi)\,d\phi \qquad (7.16a)$$

$$= \mathfrak{F}_{(2)}^{-1}\{\rho^{-1}\mathfrak{F}_{(2)}\{\lambda(r,\theta)\}\} \qquad (7.16b)$$

and that the image is reconstructed by the rho-filtering operation

$$\lambda(r,\theta) = \mathfrak{F}_2^{-1}\{\rho\mathfrak{F}_2(g(r,\theta))\}. \qquad (7.17)$$

Before proceeding further with a discussion of image reconstruction methods, it is shown that layergrams of certain test objects may be computed in a closed form. The test object considered here is the same annulus (with inner and outer radii r_1 and r_2 respectively), which is used for demonstrating the results presented in chapter 6. It is

defined by

$$\begin{aligned} &= 0 \; ; \quad |r| < r_1 \\ \lambda(r,\theta) = \lambda(r) &= 1 \; ; \quad r_1 \leqslant |r| \leqslant r_2 \\ &= 0 \; ; \quad |r| > r_2. \end{aligned} \tag{7.18}$$

The projected density of this function is the Abel transform of $\lambda(r)$ (Bracewell 1965, p.264);

$$\begin{aligned} &= 2(r_2^2-\xi^2)^{\frac{1}{2}} - 2(r_1^2-\xi^2)^{\frac{1}{2}}; \quad |\xi| \leqslant r_1 \\ f(\xi,\phi) = f(\xi) &= 2(r_2^2-\xi^2)^{\frac{1}{2}} \; ; \quad r_2 > |\xi| > r_1 \\ &= 0 \qquad\qquad\quad ; \quad |\xi| \geqslant r_2. \end{aligned} \tag{7.19}$$

Since the projected density is circularly symmetric, so too is the layergram, so that eqn (7.15) may be rewritten as

$$g(r,\theta) = g(r) = \int_0^{\pi} f(r\cos\phi)\,d\phi = 2\int_0^{\pi/2} f(r\sin\phi)\,d\phi. \tag{7.20}$$

Substitution of eqn (7.19) into (7.20) gives

$$\begin{aligned} &= 4r_2\int_0^{\pi/2}(1-(r/r_2)^2\sin^2\phi)^{\frac{1}{2}}d\phi - 4r_1\int_0^{\pi/2}(1-(r/r_1)^2\sin^2\phi)^{\frac{1}{2}}d\phi; \\ &\qquad\qquad r \leqslant r_1 \\ g(r) &= 4r_2\int_0^{\pi/2}(1-(r/r_2)^2\sin^2\phi)^{\frac{1}{2}}d\phi - 4r_1\int_0^{\arcsin(r_1/r)}(1-(r/r_1)^2\sin^2\phi)^{\frac{1}{2}}d\phi; \\ &\qquad\qquad r_1 < r < r_2 \\ &= 4r_2\int_0^{\arcsin(r_2/r)}(1-(r/r_2)^2\sin^2\phi)^{\frac{1}{2}}d\phi \\ &\quad -4r_1\int_0^{\arcsin(r_1/r)}(1-(r/r_1)^2\sin^2\phi)^{\frac{1}{2}}d\phi; \quad r \geqslant r_2. \end{aligned} \tag{7.21}$$

Each integral on the RHS of eqn (7.21) is an elliptic integral. By making use of the reciprocal modulus transformation (Byrd and Friedman 1962), $g(r)$ can be expressed explicitly in terms

of combinations of complete elliptic integrals of the first and second kinds. This expression for the layergram was evaluated numerically using the standard library subprograms CEL1 and CEL2 (IBM 1968). The 'density' profile of the layergram of an annulus whose outer radius is twice the inner radius is shown in fig. 7.4, where it is seen that the layergram is a very blurred version of the object. Note that the profile shown is similar to that of the discrete layergram displayed in chapter 6 (fig. 6.1b). Edholm (1960) gives examples of measured and analytically computed transverse tomograms of circular cylinders. These tomograms closely resemble the layergram shown in fig. 7.4.

7.5 Optical Processing of Layergram

7.5.1 Optical Fourier Transformation

A standard result in coherent optics (Goodman 1968, ch.5) is that a lens may be used to compute the Fourier transform of the optical amplitude transmittance of a transparency. If a transparency is placed at one focal plane of a thin lens and is illuminated with a plane monochromatic light beam, then the Fourier transform of the transparency appears at the conjugate focal plane of the lens. Goodman shows that the optical system may be more general than this. For example, the transparency may be placed either in front of or behind the lens, and the illuminating beam need not be planar, but may be convergent or divergent. The effect of using such a general configuration is to introduce a scale change in the Fourier transform plane, or to multiply the Fourier transform by a quadratic phase factor, or to introduce a combination of these effects.

The input plane of an optical system is that in which a transparency is inserted, while the output plane is the plane in which the optical system forms an image of the transparency. If $t_0(x,y)$ is the amplitude transmittance of a transparency placed in the input plane of fig. 7.5, then the amplitude distribution $U(x_f,y_f)$ of the light at the effective focal plane a distance f from the lens, is related to $t_0(x,y)$ by (Goodman 1968, p.88),

$$U(x_f,y_f) = \frac{Af}{j\lambda d^2} \exp\left[j \frac{k}{2d} (x_f^2+y_f^2)\right] \cdot \int_{-\infty}^{\infty}\int t_0(x,y) P\left(\frac{xf}{d}, \frac{yf}{d}\right) \exp\left[\frac{-j2\pi}{\lambda d}(xx_f+yy_f)\right] dxdy \qquad (7.22)$$

where A is the amplitude of the incident light beam. The first term in eqn (7.22) is a quadratic phase factor across the effective focal plane, while the integral is the Fourier transform of $t_0(x,y)$. Since the Fourier transform of $t_0(x,y)$ is formed in the effective focal plane, this plane is often called the Fourier plane. Notice that the transmittance of the object is multiplied by the pupil function $P(\frac{xf}{d},\frac{yf}{d})$ of the lens, which is generally in the form of a circular aperture, whose size is a function of f/d. To prevent parts of the object being blocked by the pupil function during processing, the physical extent of $t_0(x,y)$ must be less than that of $P(\frac{xf}{d},\frac{yf}{d})$. From eqn (7.22), the variables equivalent to the normal Fourier transform variables (α,β) are $(\frac{x_f}{\lambda d},\frac{y_f}{\lambda d})$. Hence the scale of the Fourier transform appearing at the focal plane may be varied by shifting the position of the input plane containing the transparency along the axis of the optical system.

Eqn (7.22) is only valid for regions in the effective focal plane that are close to the optical axis of the system (Hildebrand 1962, Goodman 1968, p.80). An improved optical system consisting of a number of selected lenses, as described by von Bieren (1971), allows the Fourier transform relation to remain valid over a much greater area in the Fourier plane. However, economic considerations forced the author to use a single lens as the Fourier transforming element in his experiments.

It will be recalled from chapter 3 that the rho-filtering operation (eqn 3.24) requires that the Fourier transform of the layergram be weighted in proportion to the value of the radial spatial frequency coordinate ρ, before the inverse transform is computed. This procedure may be effected in an optical system, such as that shown in fig. 7.6, by placing the layergram in the input plane and inserting a suitably constructed filter in the focal plane. The Fourier transform of the transparency is modified by the filter whose optical amplitude transmittance profile is shown in fig. 7.7, and a second lens performs a further Fourier transforming operation in order to complete the reconstruction of the image from the layergram.

7.5.2 Fabrication of Optical Rho-filter

The form of the rho-filter is exceptionally simple when compared with filters commonly required to 'de-blur' images degraded by defocussing or by movement (Stroke 1973). The fabrication of such filters generally requires the use of sophisticated holographic techniques. In order to record the correct filter characteristic faithfully on film, the shape shown in fig. 7.8a is rotated and photographed to provide a

callibrated reference transparency. This image is then scanned with a microdensitometer to relate the grey levels produced by rotating the profile shown in fig. 7.8a, to the density steps in the transparency. Using this information, a second shape (fig. 7.8b) is computed such that the rho-filter characteristic is imaged on film when the shape is rotated and photographed.

It will be noted that the rho-filter profile shown in fig. 7.7 has a transmittance that increases linearly with radius, and then tapers smoothly to zero. Such a spatial frequency cut-off is incorporated in the rho-filter transparency to provide an upper spatial frequency value, beyond which no further filtering action takes place. Failure to use such a cut-off results in high frequency noise in the layergram being amplified by the rho-filter. A smooth, rather than a sharp cut-off is included since it is shown in chapter 9 that the use of a sharp cut-off results in an image that exhibits 'ringing' (or Gibbs' phenomenon).

7.5.3 Image Reconstruction

To reconstruct the cross-section, a photo-reduced layergram is placed in the input plane of the optical system and is illuminated with coherent monochromatic radiation (λ = 6328Å in the apparatus used by the author) from a laser (fig. 7.6). The rho-filter is inserted into the Fourier plane. To overcome phase distortions caused by variations in the thickness of the photographic emulsion in both the layergram and in the rho-filter, each is enclosed within a liquid gate which contains a refractive-index matching fluid between two parallel glass plates (c.f. Majkowski and Gara 1972). By moving the transparency of the layergram along the optical

bench between the lens L_1 and the Fourier plane, the scale of the Fourier transform is varied to arrive at the optimum cut-off frequency value $\hat{\rho}$. The distribution of light to the right of the rho-filter is the Fourier transform of the cross-section from which the layergram was made, and the second lens L_2 inverts this transform to restore the image.

7.6 Digital Processing

An alternative method of restoring an image of a cross-section from its layergram is to digitize the layergram and perform the rho-filtering operation numerically using a computer. With this approach, one has much greater control over the processing of the layergram than with the optical system, as the computer is effectively noise-free.

7.6.1 Fourier Processing

When using this method to process the layergram, the steps described in section 7.5.3 for the optical procedure are simulated in the computer. In order to represent the layergram by a two-dimensional array of numbers, it must first be digitized. In the author's investigations, this is effected using the computer-controlled image scanner desdribed in Appendix C. The output of the scanner is a 128 x 128 point array of samples which is transferred on paper tape to a high speed computer. The two-dimensional Fourier transform of the layergram is rapidly computed using the FFT algorithm in conjunction with the R2FORT algorithm that is described in chapter 9. To avoid undesirable amplification of high spatial frequency noise, a variable spatial frequency cut-off (analogous to that described in sections 7.5.2 and 7.5.3 for

the optical case) is incorporated in the rho-filtering procedure, by multiplying the transform after rho-filtering by a two-dimensional version of Tukey's 'interim' data window (c.f. chapter 9, section 9.1.2).

The Fourier transform of the layergram is stored in the computer as an array of complex numbers, representing samples of the transform, spaced at increments of $(2a)^{-1}$ in spatial frequency. The value of the transform at $\alpha = \beta = 0$ (i.e. the zero order term) is real and is a measure of the integrated 'volume' of the layergram. From the relationship (c.f. eqn 3.24)

$$\mathfrak{F}_{(2)}\{g(r,\theta)\} = \rho^{-1}\Lambda(\rho,\phi) \qquad (7.23)$$

it is seen that the zero-order term of the Fourier transform of an ideal layergram is infinite. However, when the layergram is digitized with the image scanner, only a finite area is scanned and so the integrated 'volume' of the layergram, and hence the zero order term, is finite. When the Fourier transform of the digitized layergram is multiplied by the rho-filter, the zero order term is set to zero. As a consequence, the integrated 'volume' of the reconstructed image is also zero (i.e. it has equal quantities of positive and negative density). In practice, it is found that satisfactory reconstructed cross-sections are obtained by applying the rho-filter to all of the Fourier transform samples except the zero-order term, and computing the inverse transform. The digital cross-section may be displayed on a line-printer (c.f. McLeod 1970) or punched onto cards for eventual display using a facsimile machine (Appendix C).

7.6.2 Convolution Processing

A result, equivalent to that obtained using the frequency domain processing described in the previous section, may be achieved using a convolution procedure. In chapter 4 (eqn 4.17) it is shown that individual projections may be modified, prior to back-projection, by convolution rather than by rho-filtering. If the cross-section is band-limited (c.f. chapter 4, section 4.3.1) to $\hat{\rho}$ there is an analogous convolution operation that may be performed on the layergram in order to retrieve the original cross-section.

It is convenient to define a two-dimensional function $P(\rho)$ having the form

$$\begin{aligned} P(\rho) &= \rho \; ; \quad \rho \leq \hat{\rho}, \\ &= 0 \; ; \quad \rho > \hat{\rho}. \end{aligned} \tag{7.24}$$

It follows that the Fourier transform of the reconstructed image may be written as

$$\Lambda(\rho,\phi) = P(\rho)\, G(\rho,\phi). \tag{7.25}$$

Using $p(r)$ to represent the two-dimensional Fourier transform of $P(\rho)$, taking the Fourier transform of both sides of eqn (7.25) and using the convolution theorem, the cross-section $\lambda(r,\theta)$ becomes

$$\lambda(r,\theta) = p(r) * g(r,\theta). \tag{7.26}$$

Since $p(r)$ is the two-dimensional Fourier transform of $P(\rho)$, its value may be computed as follows,

$$p(r) = 2\pi \int_0^{\infty} P(\rho)\ J_0(2\pi\rho r)\rho d\rho \qquad (7.27)$$

$$= 2\pi \int_0^{\hat{\rho}} \rho^2 J_0(2\pi\rho r)d\rho . \qquad (7.28)$$

Integrating by parts and writing γ in place of $2\pi\hat{\rho}r$ gives

$$p(r) = 2\pi\hat{\rho}^3 \left[\frac{J_1(\gamma)}{\gamma} + \frac{J_0(\gamma)}{\gamma^2} - \frac{1}{\gamma^3}\int_0^{\gamma} J_1(\gamma)d\gamma\right]. \qquad (7.29)$$

The function p(r) is plotted in fig. 7.9 for a $\hat{\rho} = 16/2a$.

7.6.3 Efficiency of Digital Fourier and Convolution Processing Techniques

In order to convolve an image (layergram), which is sampled at N^2 points, with a function (p(r)), which is sampled at M^2 points, it is necessary to centre p(r) on each of the samples of the layergram in turn, and perform M^2 multiplication and addition operations. For the complete convolution, a total of N^2M^2 of these operations is required.

The alternative frequency domain filtering method generally requires that fewer computer instructions be executed. Both forward and inverse Fourier transforms on the layergram each require $2N^2\log_2N^2$ multiplication and addition operations (Hartwell 1971), while the rho-filtering operation requires a maximum (depending in the radial extent of the data window applied to the rho-filtered transform) of N^2 multiplications. Therefore, the total number of computer operations required for rho-filtering using the FFT is $N^2(8\ \log_2N + 1)$ multiplications and $8N^2\log_2N$ additions. Comparing the numbers of operations required for each procedure, it is found that a break-even point is reached at approximately

$$M^2 = 8 \log_2 N \qquad (7.30)$$

so that convolution processing should be used if

$$M^2 < 8 \log_2 N \qquad (7.31)$$

and Fourier processing should be used if

$$M^2 > 8 \log_2 N. \qquad (7.32)$$

For a layergram sampled at 128 x 128 points, Fourier processing is more efficient for $M \geqslant 8$, corresponding to the case when the radius, within which p(r) is significant, is greater than a/8. Note that the p(r) shown in fig. (7.9) has significant value for $r > a/8$ when the value of $\hat{\rho}$ is chosen to be 16/2a and so Fourier processing is preferable when $\hat{\rho}$ has this value.

7.6.4 Analogue Convolution Processing

A further method of implementing the convolution approach is suggested here, although the author has not experimented with it. Schack and Swindell (1968) and Swindell (1970) describe a device which scans an image with an extended and spatially varying patch of light, rather than the small spot which is normally used when scanning an image (c.f. Appendix C). In order to convolve an image with a particular function (e.g. p(r)), photographic masks are fabricated which have transmittance characteristics proportional to the positive and negative parts of p(r) respectively, and each mask is used to modify the intensity distributions of two independent extended light beams which are made to scan the image. After being transmitted through the transparency of the image, each beam falls on a photodetector. The output from the photodetector which measures the 'negative' beam is subtracted from

the output of the photodetector, which measures the 'positive' beam, and the resulting electrical signal is used to control a lamp which scans an unexposed photographic film. This image on the film is the convolution of a transparency (i.e. the layergram) with p(r). It is possible that a similar result could be obtained by suitably modifying the image scanner described in Appendix C.

7.7 Departures From the Ideal System

7.7.1 Divergence of the X-ray Beam

In the foregoing analysis, it is assumed that the radiation is incident upon the object in parallel rays. In practice, however, the radiation originates from a small spot on the anode of the X-ray tube and impinges upon the object in a diverging beam. If the distance from the X-ray focal spot to the object is great enough relative to the diameter of the object under study, the assumption that the rays are parallel is justified. This was in fact the case for the experimental layergraph described in section 7.3. However, if the divergence of the beam is significant, the back-projection operation provided by the cylindrical lens is no longer suitable for forming the layergram on the film. It is shown in chapter 3 (eqn 3.66) that an approximate layergram may be obtained by back-projecting the 'diverging-ray' shadowgrams along converging lines, which match the divergence of the X-rays from the source. Fig. 4.1b, which shows such a back-projection procedure for discrete projections, also illustrates how the optical system within the layergraph must treat the optical representations of the projections, when a diverging

X-ray beam is used. The desired result may be obtained by replacing the cylindrical lens by a section of an axicon lens (McLeod 1954), which is often called a conical lens (Cutrona et al. 1966). In some situations it may be possible to simulate the effect of a conical lens by tilting the cylindrical and spherical lenses with respect to the optical axis of the layergraph (e.g. Offner, 1968). The approximate layergram obtained when using a conical lens in the optical system of the layergraph is the cross-section imaged with the position varying point spread function $K(\sigma,\theta)r^{-1}$, described by eqn (3.66). As suggested in chapter 3, and demonstrated for a discrete number of projections in chapter 6, rho-filtering of 'diverging-ray' layergrams made with apparatus such as that discussed above may be expected to yield useful images provided that the divergence of the X-ray beam is kept less than approximately 12^{o}.

7.7.2 Film Nonlinearity

In the discussion so far, it has been assumed that the photographic film used in the layergraph has the property that its optical amplitude transmittance is proportional to the integrated X-ray absorptivity of the cross-section in the path of the X-ray beam. For this relation to hold, the amplitude transmittance of the film must be proportional to a constant minus the logarithm of the exposure (c.f. eqn 3.2). While film does not normally possess these characteristics over a wide range, a suitable linear approximation may be obtained over a small range of exposures, as illustrated by fig. 7.10. In fig. 7.10 the transmittance of the developed film† is plotted against the integrated X-ray absorptivity

†Ilford FP4 cut-plate film, developed for 5 minutes at 20^{o}C in Agfa G170P developer.

expressed in terms of the equivalent thickness of aluminium in the path of the X-ray beam. The curve shows approximate linearity between points a and b. Since the film lacks linearity over a wide range, the mathematical analysis describing the linear formation of an ideal layergram, describes only approximately the formation of a practical layergram.

7.8 Resolution

In any radiographic system, the X-ray image is degraded by the fact that the radiation is emitted from the focal spot on the anode of the X-ray tube rather than from an ideal point source. The result is that any point in the object is imaged on the radiograph as a spot equal in size to the extent of the focal spot multiplied by the factor d_1/d_2, where d_1 and d_2 are the distances of the point within the object being radiographed from the fluorescent screen and the X-ray tube respectively. In the experimental layergraph, the object is positioned at approximately 2.5 cm from the screen, while the X-ray tube is 125 cm above the object. Hence the effective focal spot size at the film is only .02 mm x .02 mm, since the actual focal spot is approximately 1 mm x 1 mm in size.

The photographic film used by the author is capable of recording spatial frequency components in the incident light field of greater than 100 mm^{-1}, while the ZnS-CdS fluorescent screen used is only capable of resolving spatial frequencies below about 2 mm^{-1} (Hendee 1970, p.524).

The overall noise in the system (due to quantum effects, X-ray scatter and film granularity) also affects the maximum resolution that is attainable in the layergram. However, the

effects of noise could not be measured separately from the other factors which degrade resolution.

From the preceding discussion it is seen that the overall resolution of the system is limited primarily by the fluorescent screen.

It is common practice for the resolution capabilities of a radiographic system to be measured in terms of the modulation transfer function (MTF) of the system (c.f. Cartwright 1971). This function expresses the resolution of the system in terms of the transmittance variation in the X-ray film caused by exposing the film to a radiation field whose intensity varies with a particular spatial frequency. The MTF of the experimental layergraph in its rest state (i.e. with no motion of the object or the film), was measured using standard techniques (Rao 1971). The MTF for the experimental layergraph is shown in fig. 7.11. It is seen that the spatial frequency response of the system decreases to approximately 80% of its maximum value at a spatial frequency of 1 mm^{-1}, and falls rapidly after this value. The spatial frequency cut-off of the system is seen to be close to that quoted above for the fluorescent screen.

7.9 Experimental Results

7.9.1 Restoration of Layergraph Point-Spread Function by Optical System

The purpose of the optical system is to perform the inverse of the blurring introduced by the layergraph. The layergram of an isolated point within the object is proportional to the point-spread function (c.f. section 3.3.2.) of the layergraph, and so the performance of the optical system may

be evaluated by attempting to reconstruct a single point from its layergram. The layergram of a 1 mm diameter spot is shown in fig. 7.12a, and the reconstructed image of the spot after rho-filtering the layergram is shown in fig. 7.12b. Whereas the layergram of the spot is indistinct, the reconstructed image of the 1 mm diameter spot is a sharply defined disk. Fig. 7.12 demonstrates the noise amplification characterisfics of the rho-filtering operation. The relatively insignificant blemish (indicated by the arrow) in the layergram (fig. 7.12a) is imaged with increased contrast and shows a great deal of ringing in the reconstructed image obtained by rho-filtering the layergram.

7.9.2 Ideal Data

The ideal layergram which is computed by eqn (7.21) was imaged on film with the same method that was used to fabricate the rho-filter. This layergram is shown together with the results of both optical and digital processing in fig. 7.13. While the optically reconstructed image is slightly 'peppered' with the speckle noise characteristic of coherent optical systems, the digital procedure restores the original cross-section accurately.

7.9.3 Radiographically Measured Data

A layergram of a section of a sheep's shin bone was derived using the experimental layergraph described in section 7.3, and was subsequently processed by both the optical and digital reconstruction procedures. The distance between the X-ray source and the 2 cm diameter bone was 125 cm, so that the incident X-rays could be considered to be parallel.

Figs 7.14a,b show, respectively, the cross-section of the bone (excised after the experiment and radiographed) and

its layergram. Figs 7.14c,d display the reconstructed images obtained by the optical and digital procedures respectively. In both the reconstructed images (figs 7.14c,d), a smooth frequency cut-off (as shown in fig. 7.7) was introduced into the reconstruction procedures at a spatial frequency of

$$\hat{\rho} = 0.8 \text{ mm}^{-1}. \qquad (7.32)$$

Images reconstructed using a cut-off frequency in excess of this value were found to be severely degraded by noise.

The relatively poor quality of the optically reconstructed image is due to the following factors.

1. The optical system used by the author was unsophisticated, and the characteristics of some of the lenses and glass plates in the system were not ideal.
2. The layergram imaged by the layergraph must be photo-reduced from a 4" x 5" plate size to a 35 mm size to enable it to be inserted into the optical system. This procedure introduces further nonlinearities into the reduced transparency.
3. Difficulty was experienced in accurately positioning the rho-filter in the Fourier plane of the optical system.
4. The characteristics of the film used to construct the rho-filter were such that the dynamic range of transmittance values in the filter was limited to only 13 db (c.f. fig. 7.7).

However, while the images reconstructed by both the optical and digital systems are visually different, they both represent the cross-section shown in fig. 7.14a more accurately than does the layergram. It is not obvious that the layergram represents the bone cross-section shown in fig.

7.14a, and it certainly is not possible to estimate the thickness of the walls of the bone or its detailed shape from the layergram.

7.10 Discussion

A modified radiographic tomography apparatus based on the design described here would result in improved transverse section images of the human anatomy. However, it is emphasised that the device described is experimental and that considerable development is necessary before it could become clinically useful. The most pressing need appears to be for a photographic film which is sufficiently fast to enable the patient's X-ray dose to be kept to a minimum, while possessing the desired linear characteristic over a sufficiently wide range of exposures. From the results presented here it is obvious that a more sophisticated optical processing system than that used by the author is required, if results approaching the fidelity of those produced by computer processing are to be attained. While optical processing is virtually instantaneous in a properly adjusted optical system, it was found that considerable preparation of the layergram was required prior to the optical processing step. The layergram, as formed by the layergraph, must be photo-reduced, and carefully mounted in a liquid gate. On the other hand, while computer processing takes approximately 45 seconds of CPU time, and 10 minutes to scan the layergram and display the reconstructed image, prior preparation of the data is negligible.

Once a fluorescent screen/optical system/film combination was developed which enabled the radiation exposure to the

patient to be maintained within specified safety limits (e.g. Hendee chap. 24), it is possible that conventional transverse tomographic systems could be adapted to enable layergrams to be obtained. Alternatively the image processing methods described in this chapter could be applied to the enhancement of conventional transverse tomograms, for although they are distortions of true layergrams, they nevertheless resemble layergrams visually (c.f. Kotoulas and Sinis 1970). It is expected therefore that such tomograms may be usefully enhanced by rho-filtering.

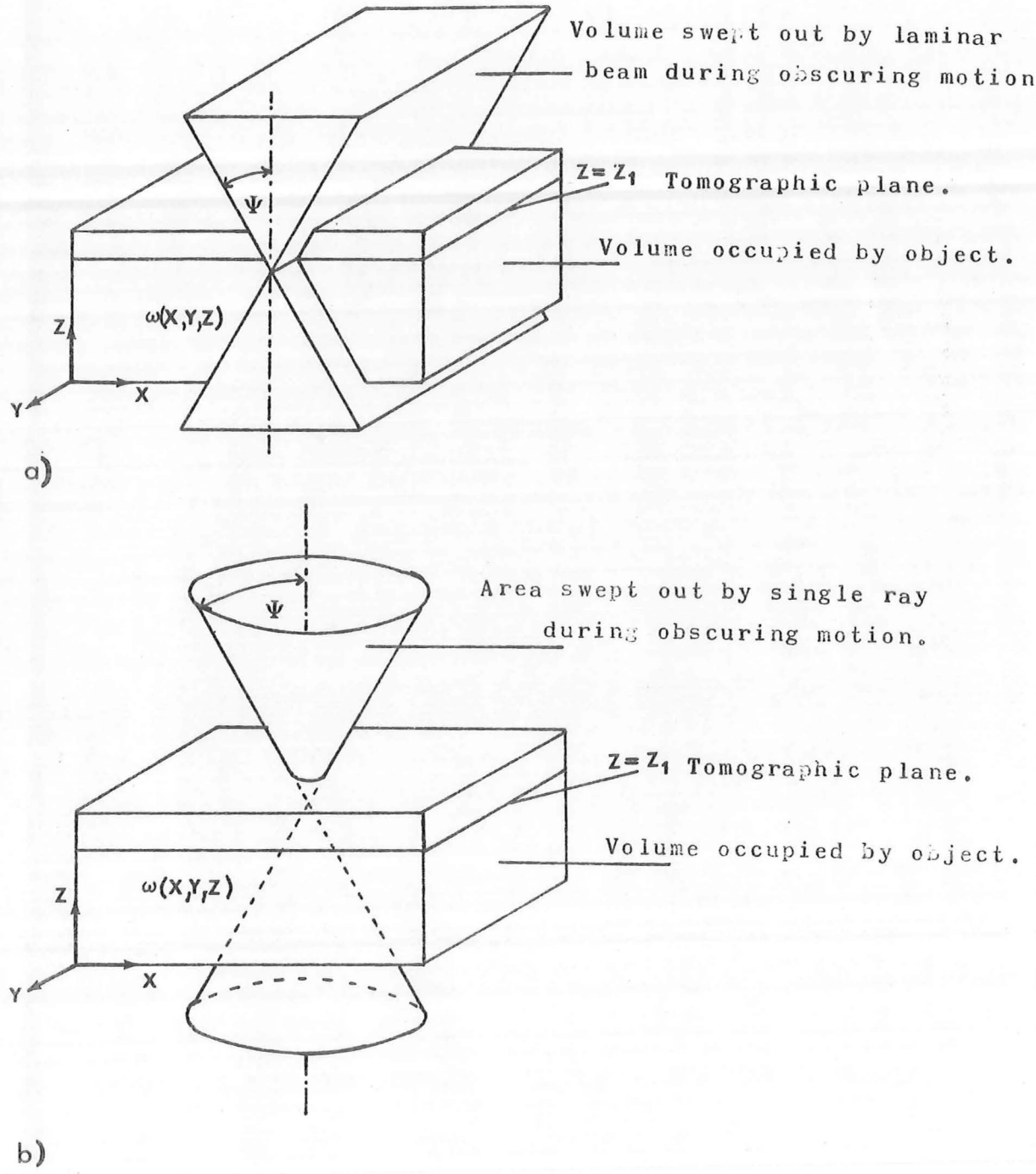

Fig.7.1. Ray paths in tomography.

a) Linear obscuring motion.

b) Circular obscuring motion.

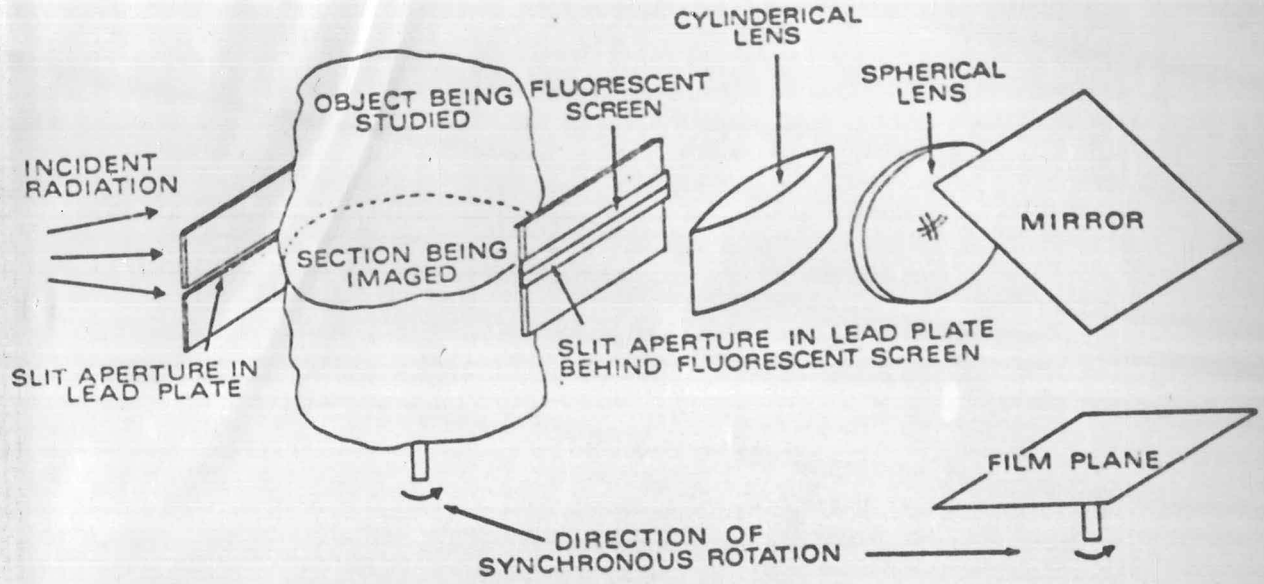

Fig. 7.2. Schematic of new layergraph.

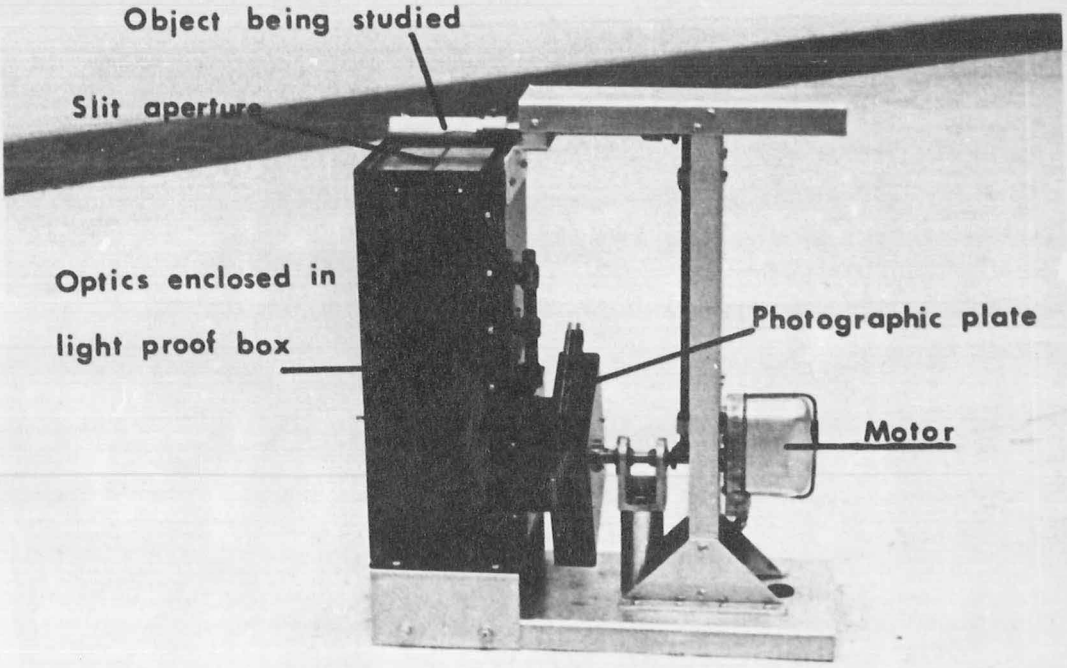

Fig. 7.3. Experimental layergraph.

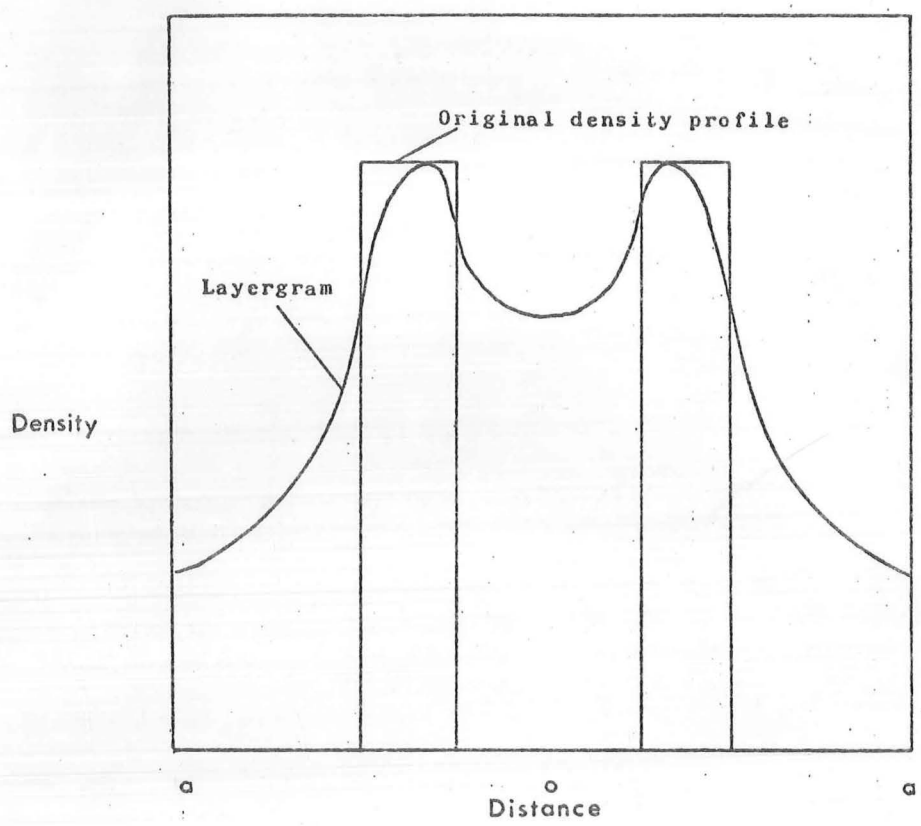

Fig. 7.4. Analytically computed layergram of annular density distribution.

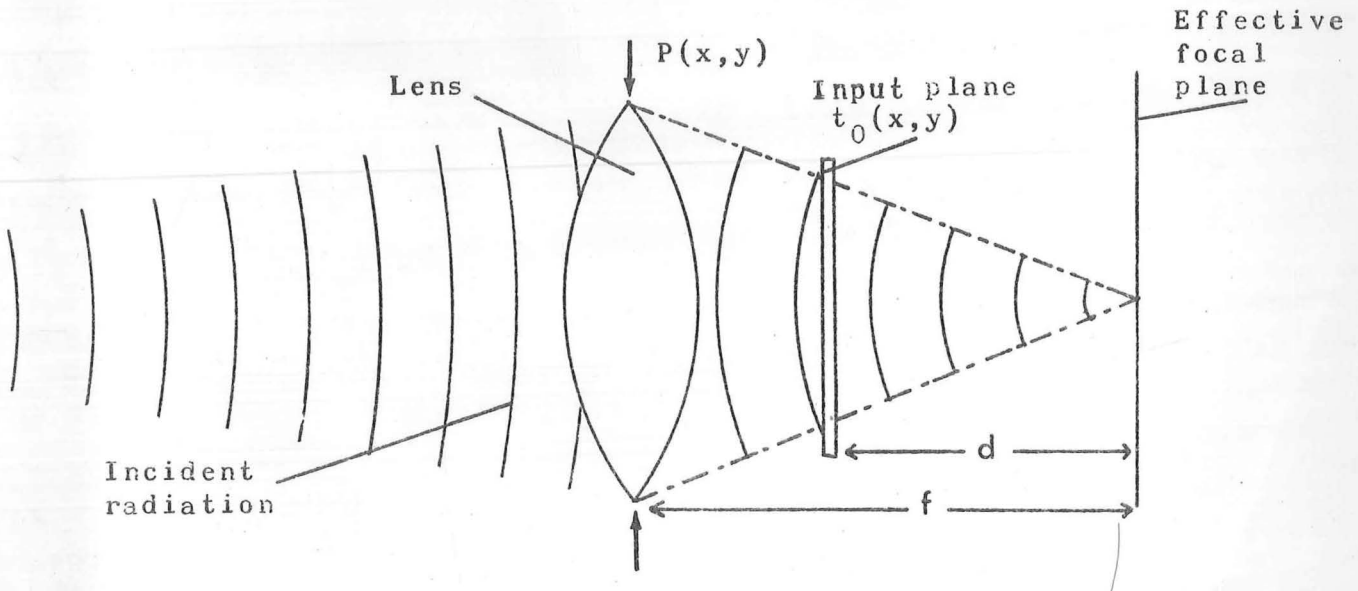

Fig. 7.5. Fourier transforming properties of lens

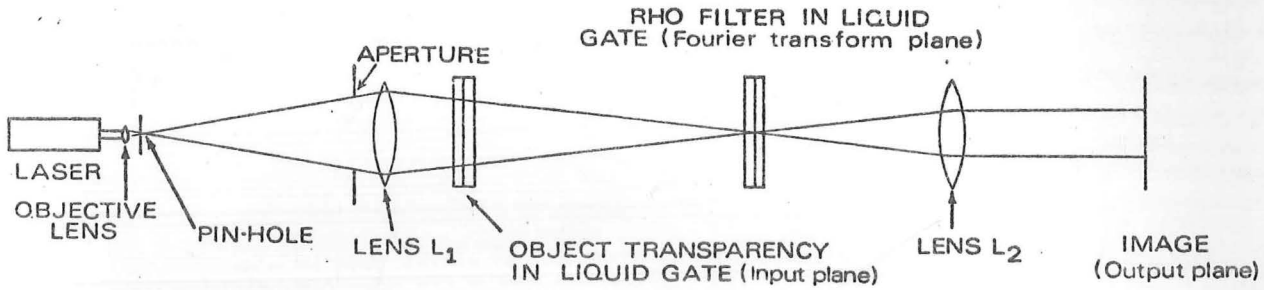

Fig. 7.6. Coherent optical system used to process layergram.

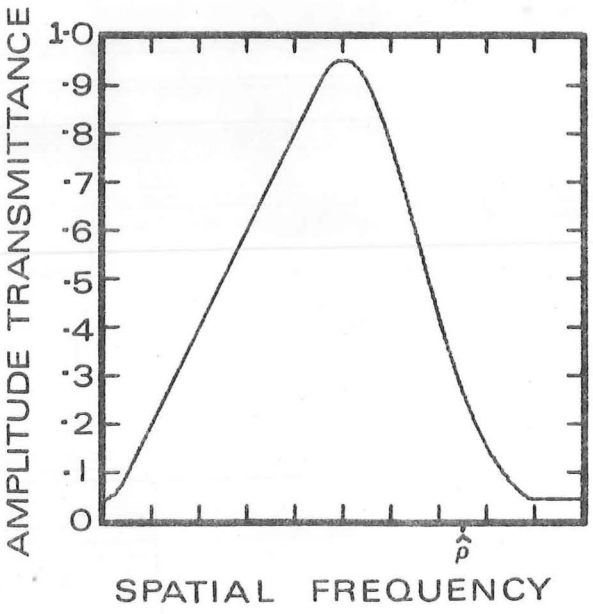

Fig. 7.7. Rho-filter characteristic.

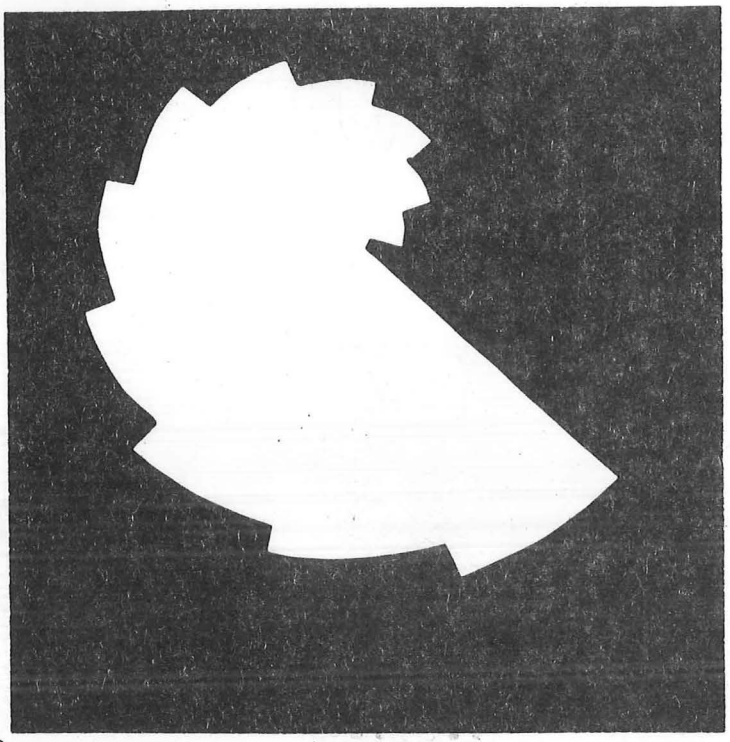

a)

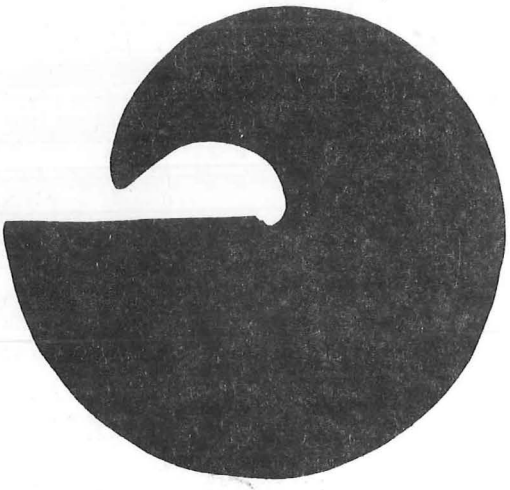

b)

Fig. 7.8. Fabrication of rho-filter. These shapes are rotated and photographed to give grey-level characteristic on film.

a) Calibration profile.

b) Rho-filter profile.

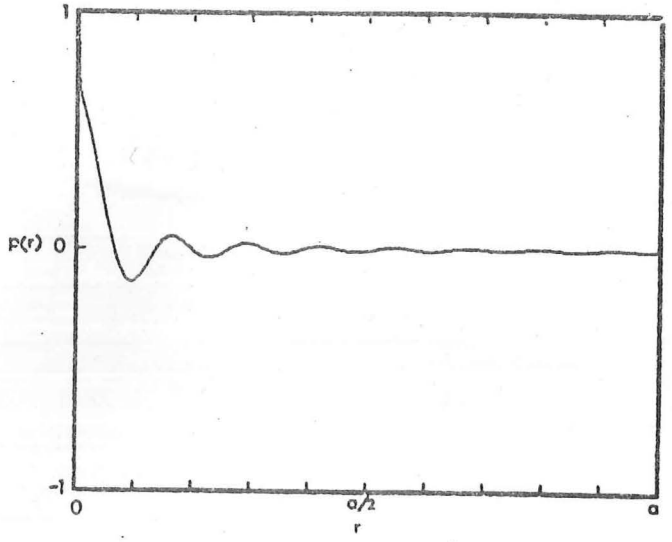

Fig. 7.9. The convolution function p(r).

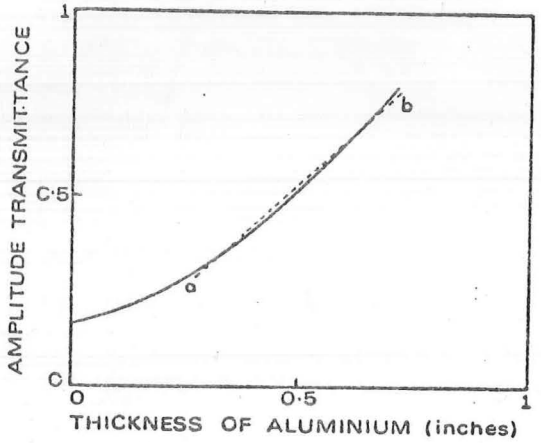

Fig. 7.10. Film linearity characteristic. Approximate linearity exists between the points a and b.

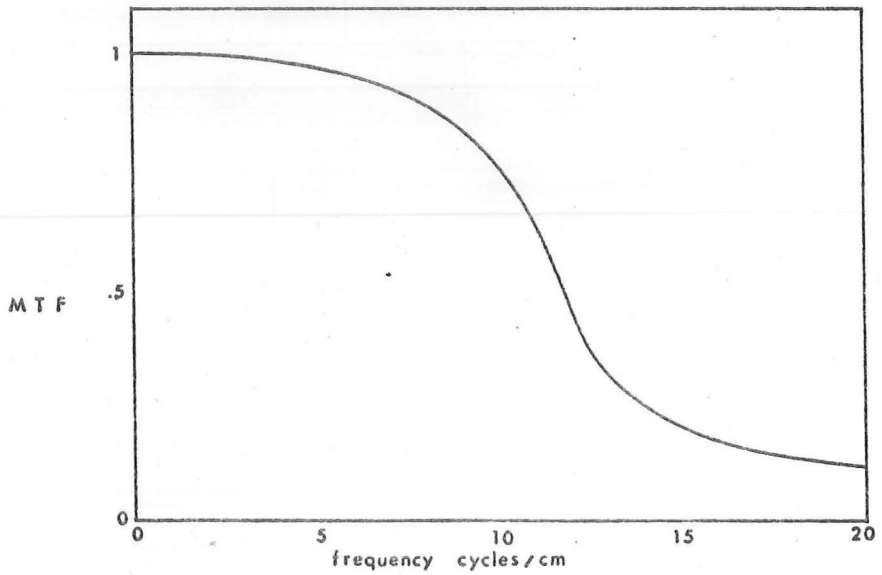

Fig. 7.11. Modulation transfer function of layergraph.

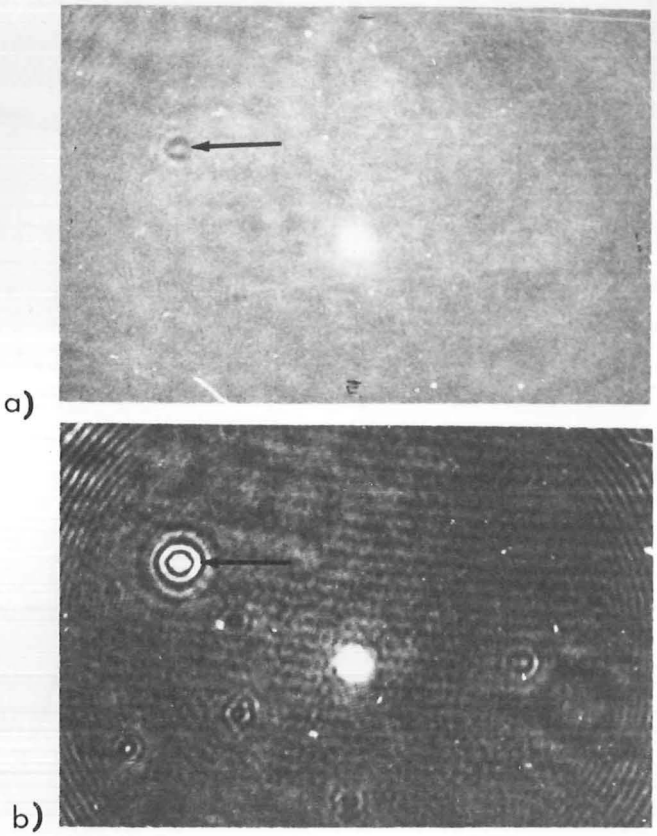

Fig. 7.12. Optical reconstruction of point spread function.
a) Point spread function of layergraph.
b) Optical reconstruction.
Arrows indicate noise in fig 7.12a which is amplified in fig 7.12b.

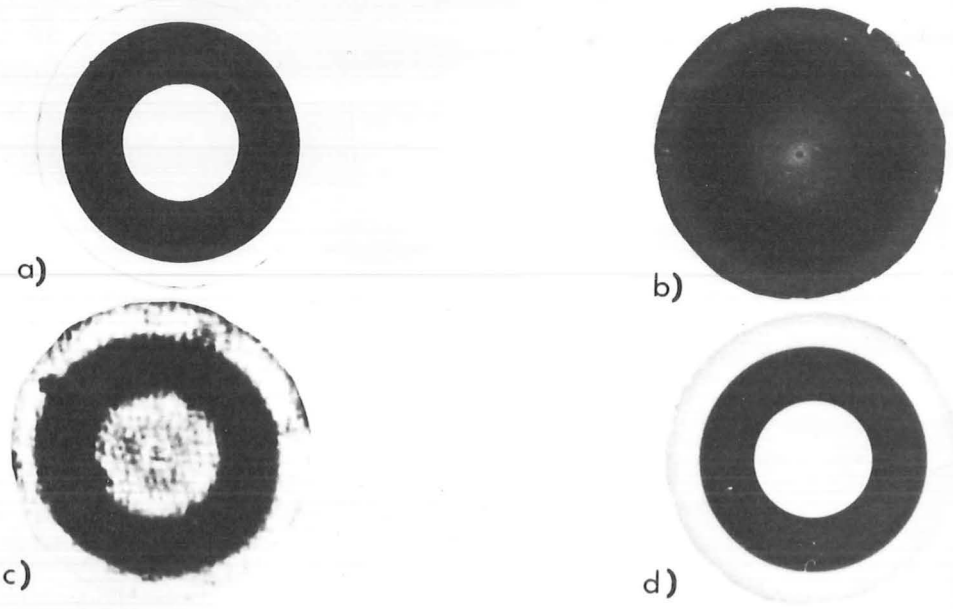

Fig. 7.13. Reconstructed images from ideal data.
a) Ideal object.
b) Analytically computed layergram of ideal object.
c) Optically reconstructed image.
d) Digitally reconstructed image.

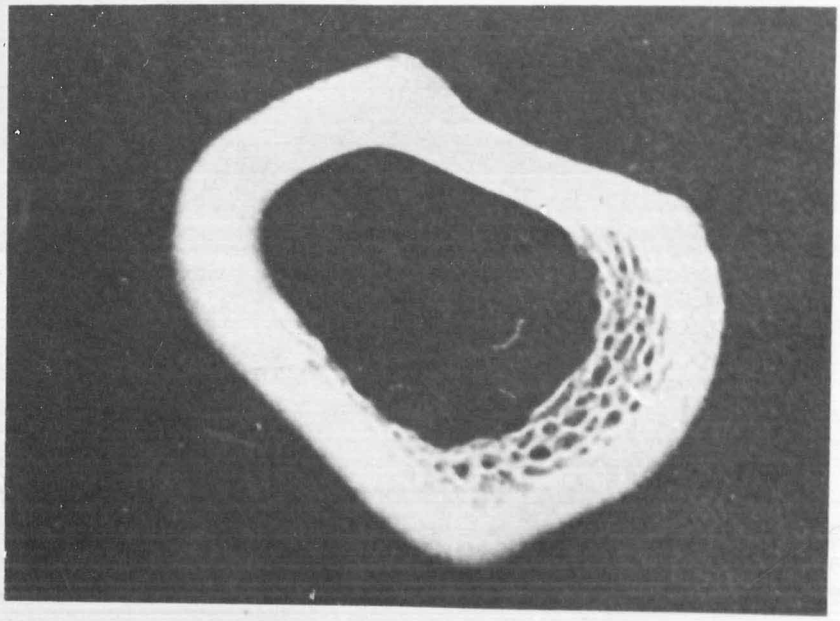

a)

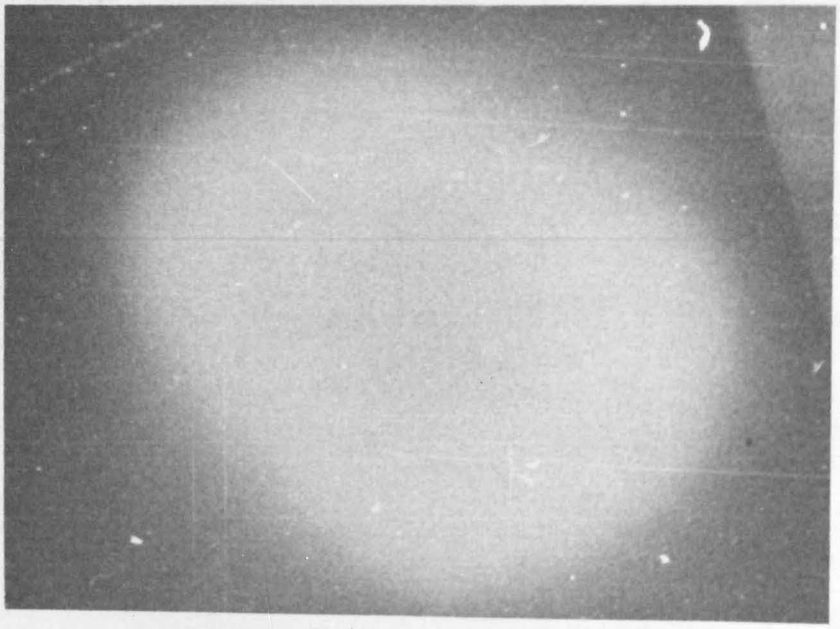

b)

Fig. 7.14....

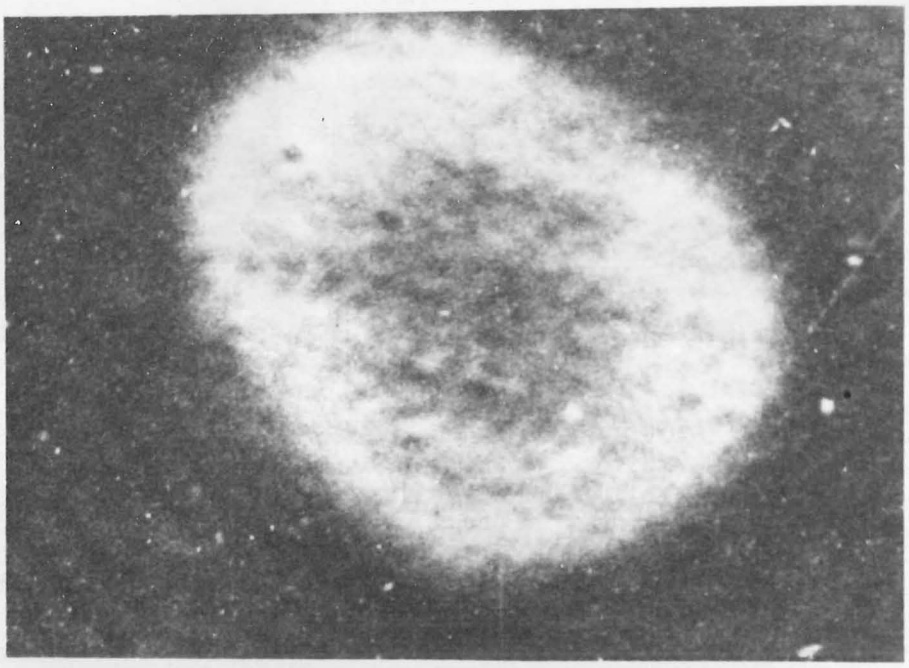

c)

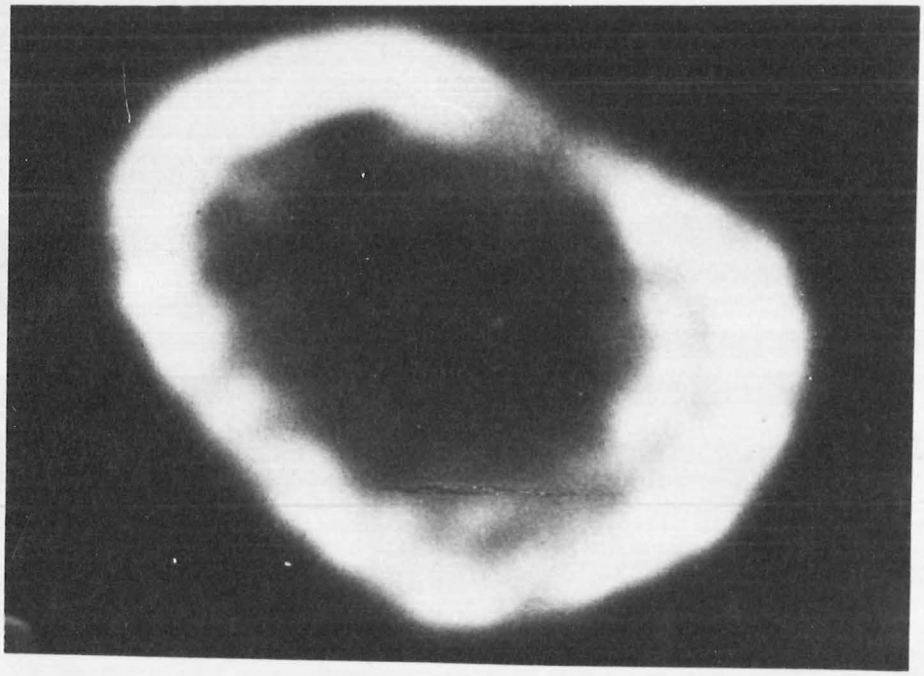

d)

Fig. 7.14. Images reconstructed from radiographic data.
a) Excised section of sheep's shin bone.
b) Layergram.
c) Optically reconstructed image.
d) Digitally reconstructed image.

CHAPTER 8

APPLICATION OF IMAGE RECONSTRUCTION IN GAMMA CAMERA TOMOGRAPHY

8.1 Introduction

The gamma camera (or Anger camera) has recently come into widespread use, replacing mechanical isotope scanners in a number of instances when projections of isotope distributions are required for diagnosing lesions of the liver, thyroid or brain. While some cameras have been equipped with rotating collimators in order to obtain longitudinal tomograms of the isotope distribution (Freedman 1972, Rider et al. 1972), they are expensive and unlikely to enjoy widespread use in the near future. Most gamma cameras in general use are designed specifically for imaging projections of isotope distributions rather than selectively viewing individual planes within the body.

Recently some authors have proposed methods for reconstructing three-dimensional isotope distributions by combining scintigraphic projections measured either by scanning (Kuhl and Edwards 1968, 1970; Kuhl et al. 1972) or by using a gamma camera (Anger et al. 1967, Muehllehner and Wetzel 1970).

As it is becoming common practice for nuclear medicine departments in hospitals to have a gamma camera interfaced to a small digital computer to perform a variety of tasks, it is of interest to investigate the possibility of using such a computer to reconstruct two- or three-dimensional distributions of radioactivity from a set of conventional scintigraphic projections.

Section 8.2 discusses the effect of photon absorption in the medium surrounding the isotope and shows that if the absorption coefficient is small, the scintigraphic projections are equivalent to radiographic projections and so the processing described in previous chapters may be used to reconstruct the distribution in this case. When the absorption coefficient is significant, such processing leads only to approximate reconstructions of the radioactivity distribution. Reconstructed images of a simulated lesion, embedded in a medium whose photon absorptivity may be varied, are displayed in section 8.3. It is shown that approximate but satisfactory images may be obtained when the photon absorptivity has values which are likely to be encountered in practice.

Section 8.4 discusses current gamma camera tomography techniques indicating how they relate to methods described in previous chapters of this thesis. An example showing the results of reconstructing the isotope distribution in a simple phantom from its scintigraphic projections is presented in section 8.5. The feasibility of implementing the proposed tomographic scheme in practice is discussed in section 8.6.

8.2 Effect of Absorption

There are four factors which affect the quality of an image which has been computed from its scintigraphic projections. These are

1. Absorption of emitted photons by the medium surrounding the isotope.
2. Scattering of emitted photons.
3. Influence of statistical variations in the number of counts detected.

4. Variation of camera resolution with the distance from the aperture.

A full discussion of all of these effects is beyond the scope of this thesis. However, the first effect listed above is usually the most significant (Muehllehner and Wetzel 1970) and is dealt with here in some detail.

It is useful to examine the expression which relates the scintigraphic projections $f_\gamma(\xi,\phi)$ of a two-dimensional isotope distribution, to the distribution itself. The symbols $\Gamma(x,y)$ and $\omega(x,y)$ are used to represent the distributions of radioactivity and photon absorptivity respectively within the object, while $f_\gamma(\xi,\phi)$ and $f(\xi,\phi)$ are used to denote the scintigraphic and radiographic projections of the object respectively. It is assumed that both $f_\gamma(\xi,\phi)$ and $f(\xi,\phi)$ are measured with radiation of the same energy. The geometry for recording the scintigraphic projections is the same as that shown for radiographic projections in fig. 3.1a.

The scintigraphic projection $f_\gamma(\xi,\phi)$ is defined by

$$f_\gamma(\xi,\phi) = \int_{-\infty}^{\infty} \Gamma(x,y)\, \exp\left(-\int_{\eta}^{\infty} \omega(x,y)\,d\eta\right) d\eta \qquad (8.1)$$

which may be redefined as the average of $f_\gamma(\xi,\phi)$ and $f_\gamma(\xi,\phi+\pi)$ to give

$$f_\gamma(\xi,\phi) = \tfrac{1}{2}\int_{-\infty}^{\infty} \Gamma(x,y)\left(\exp\left[-\int_{\eta}^{\infty} \omega(x,y)\,d\eta\right] + \exp\left[-\int_{-\infty}^{\eta} \omega(x,y)\,d\eta\right]\right) d\eta. \qquad (8.2)$$

Since the projections $f_\gamma(\xi,\phi)$ depend upon the gamma ray absorptivity $\omega(x,y)$ as well as on $\Gamma(x,y)$, two distinct sets

of measurements must be made to compute $\Gamma(x,y)$ accurately. A set of radiographic transmission measurements is required to determine $\omega(x,y)$, while a set of scintigraphic measurements is required to determine $f_\gamma(\xi,\phi)$. Only when both of these sets of data are available, one has sufficient information to solve eqn (8.1) for $\Gamma(x,y)$.

If the gamma-ray absorption coefficient $\omega(x,y)$ is sufficiently small, the exponentials in eqn (8.2) may be replaced by $(1 - \int_\eta^\infty \omega(x,y)d\eta)$ and $(1 - \int_{-\infty}^\eta \omega(x,y)d\eta)$ respectively, so that eqn (8.2) becomes

$$f_\gamma(\xi,\phi) = \tfrac{1}{2}\int_{-\infty}^{\infty} \Gamma(x,y)[2 - f(\xi,\phi)]d\eta \qquad (8.3)$$

A correction to the scintigraphic projections may then be made provided one knows the corresponding radiographic projections, i.e.

$$\frac{2f_\gamma(\xi,\phi)}{2-f(\xi,\phi)} = \int_{-\infty}^{\infty} \Gamma(x,y)d\eta. \qquad (8.4)$$

Eqn (8.4) now has the same form as eqn (3.4) and so may be solved for $\Gamma(x,y)$ using the FTR or RFL methods described in chapters 4, 5 and 6.

The necessary condition for replacing the exponentials in eqn (8.2) by a linear approximation such that

$$\left| \left| \exp - \int_\eta^\infty \omega(x,y)d\eta + \exp - \int_{-\infty}^\eta \omega(x,y)d\eta \right| - |2 - f(\xi,\phi)| \right| \leqslant .01 \quad (8.5a)$$

is that

$$\int_{-\infty}^{\infty} \omega(x,y)d\eta \leqslant .1. \qquad (8.5b)$$

Assuming that the largest linear dimension of the object being studied is 20 cm and that $\omega(x,y)$ is a constant, then $\omega(x,y)$ must be less than .005 cm^{-1} to satisfy the inequality (8.5b). The absorption coefficient of water (the major constituent of soft organs) to 140 Kev photons is .17 cm^{-1}, which is too large to allow eqn 8.4 to be used to obtain accurate reconstructions of the isotope distribution.

To reconstruct the radioactivity distribution quantitatively, it is necessary to measure $\omega(x,y)$ and $f_\gamma(\xi,\phi)$ accurately and then to obtain $\Gamma(x,y)$ by solving eqn (8.1). Although it would be possible in principle to formulate an iterative method of solving this equation (perhaps by using an algorithm similar to 'ART'-Gordon et al. 1970) such a procedure would be extremely time-consuming since it would require that integrals of the form

$$\exp\left(-\int_{\eta}^{\infty} \omega(x,y)d\eta\right)$$

be evaluated at each point in the image for each step of the iteration.

Since the value of .17cm^{-1} for ω is too large to allow the procedures discussed in chapters 3-5 to be used to reconstruct the isotope distribution exactly, it is of interest to examine the nature of the errors which are introduced into the reconstructed image by using these procedures, when the medium surrounding the isotope exhibits significant photon absorption.

8.3 Images Reconstructed from Simulated Scintigraphic Projections

The model used for this simulation is a 20 cm diameter disk of constant gamma-ray absorptivity ω, with a simulated circular 'hot' lesion of 2.5 cm diameter situated as shown in fig. 8.1. This model approximates a section of a human head containing a lesion of typical size (Kuhl 1968). Neglecting statistical effects, scattering and the effects of variable collimator resolution, but taking into account the absorption, the scintigraphic projections of this object may be computed in closed form for a number of different values of ω. Forty such projections have been computed for ϕ in the range $(0,2\pi)$ and opposing views have been averaged. The FTFSI technique described in chapter 4 has been used to obtain the reconstructed images which are shown in fig. 8.2. The images are displayed using successive character overprints on a line-printer (McLeod 1970). The scintigraphic projections are computed for the simulated lesion surrounded by a medium of gamma-ray absorptivity ω, whose value is varied between 0 and 3 cm^{-1}. For an absorption coefficient of .3 cm^{-1} (fig. 8.2b) the reconstructed image is not significantly worse than that obtained when ω is zero (fig. 8.2a). It is therefore expected that such processing would lead to satisfactory images of tumours within the brain where ω has a value of approximately .17 cm^{-1} for the 140 Kev photons emitted from the isotope ^{99m}Tc. As the value of ω is increased, the resolution in the reconstructed images becomes progressively worse along the radial direction, although even in the worst case (ω = 3 cm^{-1}) the most dense part of the reconstructed image still indicates the position of the simulated tumour (fig. 8.2d).

8.4 Existing Gamma Camera Tomography

There have been two main approaches to gamma camera tomography. That discussed by Freedman (1972) and Rudin and Hart (1972) uses a rotating collimator attached to the face of a conventional gamma-ray camera, and the method used to image sections is analogous to the conventional longitudinal radiographic tomography discussed in chapter 2. The alternative approach is to measure one-dimensional scintigraphic projections, and combine these using various optical or digital methods. Anger et al. (1967) and Kuhl and Edwards (1968) describe methods whereby layergrams and discrete layergrams respectively of individual sections are formed optically. Kuhl and Edwards (1968) also demonstrate that improved images could be obtained by computing the discrete layergram digitally. Kuhl et al. (1972) describe an iterative scheme for reconstructing the radioactivity distribution. While in all demonstrations of their technique the scintigraphic projections are measured using scanning scintillation detectors, Kuhl et al. suggest the use of a gamma camera as an imaging device in order to record information about several planes simultaneously. Muehllehner and Wetzel (1970) describe a further iterative method which is similar to 'ART' (Gordon et al. 1970).

The original digital transverse sectioning method of Kuhl and Edwards (1968) is that which most closely resembles the methods described in this thesis. They describe two methods of reconstructing images similar to layergrams. The first, called single sector addition (SSA), is effected by back-projecting the scintigraphic projections onto that half

of the image plane which is nearest the scanning probe. Thus the scintigraphic projections are related to those parts of the cross-section from which the measured photons are most likely to have originated. Their other method, called double sector addition (DSA), averages the scintigraphic projections from opposing views (c.f. eqn 8.2). The layergrams produced by these methods are treated as the final reconstructed images, and no further processing is suggested.

8.5 Phantom Study

8.5.1 Experimental Procedure and Data Processing

A phantom study, to test the feasibility of the procedures described above, was performed using a gamma camera to record the scintigraphic projections, and a small computer to process the data. A perspex phantom of dimensions 20 cm x 20 cm x 10 cm (fig. 8.3) was constructed so that it could be rotated about its longitudinal axis in a step-wise fashion. Four 2.5 cm diameter hollow plastic balls attached to an axial rod were each filled with 400μCi of ^{99m}Tc in water to simulate hot lesions. 1% of this concentration was introduced into the surrounding water to act as a background level.

The gamma camera which was used (at the Nuclear Medicine Department of Christchurch Hospital) is normally interfaced to a PDP-8 computer which has 8K 12-bit words of magnetic core memory, and magnetic tape facilities. The possibility was considered of using this machine for processing the data, but the author's lack of familiarity with its assembly language, combined with the machine's lack of fast arithmetic facilities, made it advantageous to perform the image processing on the

EAI-640 computer in the Electrical Engineering department of the University of Canterbury. The EAI-640 is a larger machine (16K, 16 bit words plus disk storage and hardware integer multiply/divide facilities) than the PDP-8, but is of a comparable size and computing power to many computers presently installed in hospitals.

Views of the phantom made at 20^{o} intervals throughout the range $0 \leqslant \phi < 2\pi$ were recorded by the gamma camera under the control of the PDP-8 computer. Opposing views were averaged and punched onto paper tape for transfer to the EAI-640, each view being represented digitally as a 32 x 32 element matrix. A flood field measurement, made on the same day as the phantom measurements, was used to correct each image for the effects caused by the non-uniform sensitivity of the camera across its aperture. The recording time for each successive frame was increased fractionally over that for the previous one to ensure that the number of counts detected was not affected by the decay of the isotope.

The rho-filtered layergram method was used to reconstruct the isotope distribution from the measured scintigraphic projections. The nine 32 x 32 element images were reorganised into 32 sets of 32 element projections for each of the 9 orientations of the phantom, and each set of data was used to reconstruct a different layer of the object. The reconstruction programs were written partly in Fortran and partly in 640-Assembly language, and the FFT routine was employed to compute the Fourier transforms of the projections. Provision was made to introduce a variable frequency cut-off data window into the rho-filtering operation in order to reduce artefacts

due to noise and angular aliasing (see chapter 5). However, for this particular experiment, satisfactory reconstructed images were obtained without the use of such a cut-off.

The computing time required for reconstructing an image of each section was approximately two minutes, although by writing the routines entirely in assembly language, and using integer arithmetic throughout, this time could be reduced typically by a factor of 10.

8.5.2 Results

Of the 32 distinct sections of the phantom capable of being reconstructed using the technique described above, only 20 of these sections intersect the simulated lesions. The reconstructed images of these sections were displayed on a storage oscilloscope as shown in fig. 8.4. This set of images may be thought of as being a reconstruction, sampled on a three-dimensional lattice, of that part of the phantom containing the radioactivity. A more realistic representation of the reconstructed volume may be obtained by printing the reconstructed sections onto transparencies, and stacking the serial sections in the correct order to give the illusion of a three-dimensional distribution as outlined in chapter 2.

Four of the sections shown in fig. 8.4 are also displayed in fig. 8.5 as (unfiltered) discrete layergrams. These images are equivalent to the DSA method of Kuhl and Edwards (1968). Comparison of the two sets of reconstructed images illustrates the increased resolution that can be obtained using Fourier transform processing techniques in gamma camera tomography.

8.6 Discussion

The procedure described in section 8.5 has yet to be tested clinically. There are two possible ways of using the gamma camera to record a set of scintigraphic projections of brain tumours. The first is to modify the mechanical positioning apparatus of the conventional gamma camera to enable the camera to be stationed at arbitrary positions relative to the patient's head. An alternative method is to maintain the camera in a fixed position while the patient is made to sit in a rotating chair. The former is the more satisfactory method of the two since the patient is not always conscious, and it may prove difficult to maintain him in a rigid upright position for the duration of the tomographic examination.

By using the processing methods discussed in chapters 3-5, it would be relatively inexpensive to convert an existing gamma-camera installation into a system with tomographic capabilities. Provided a computer is already part of the system, the only modification required is a means of positioning the camera relative to the patient in a satisfactory manner.

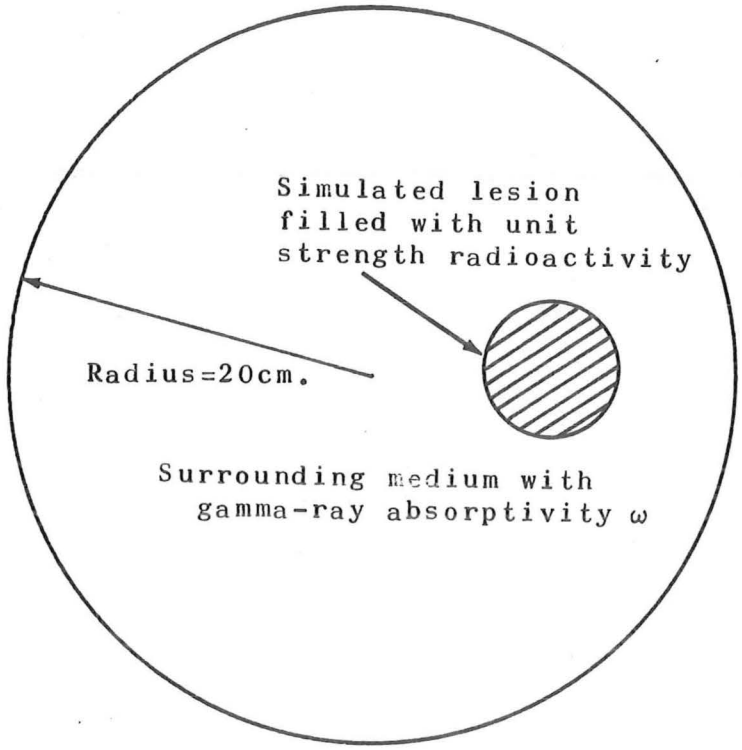

Fig. 8.1. Model of lesion surrounded by gamma-ray absorbing medium.

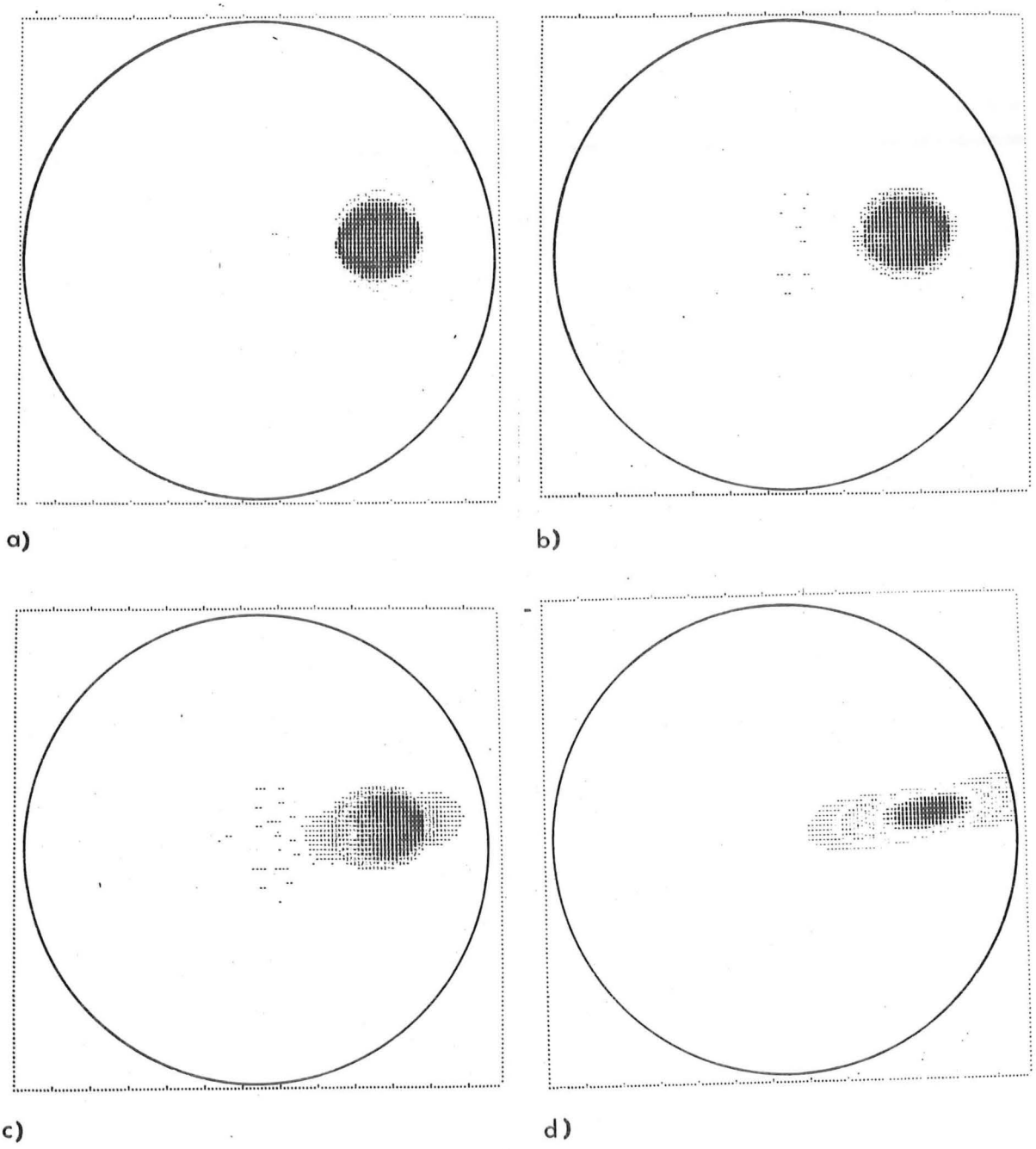

Fig. 8.2. Reconstructed images of lesion in fig. 8.1 with

a) $\omega = 0.$

b) $\omega = .3 cm^{-1}$

c) $\omega = .6 cm^{-1}$

d) $\omega = 3. cm^{-1}$.

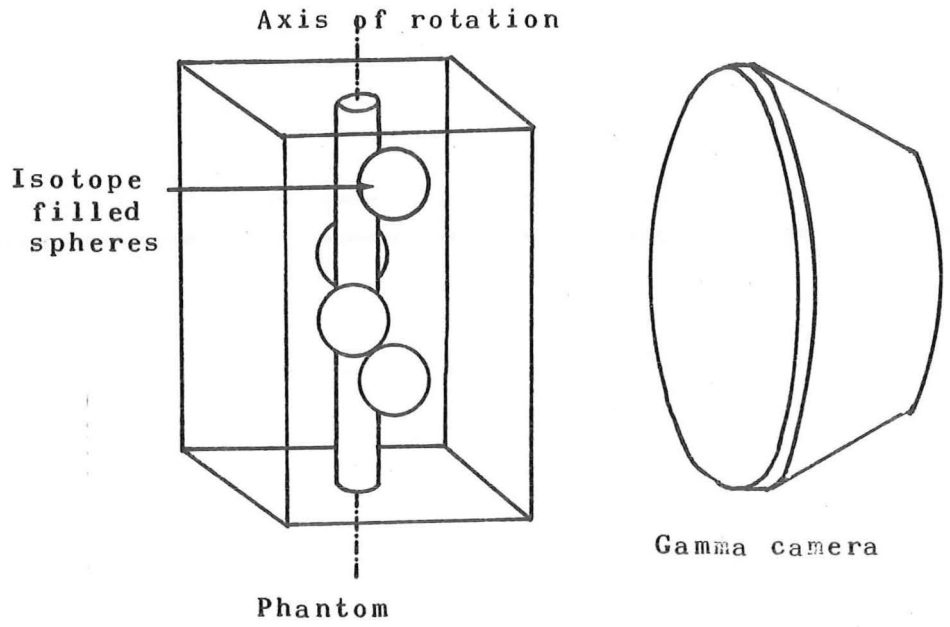

Fig.8.3. Gamma camera and experimental phantom.

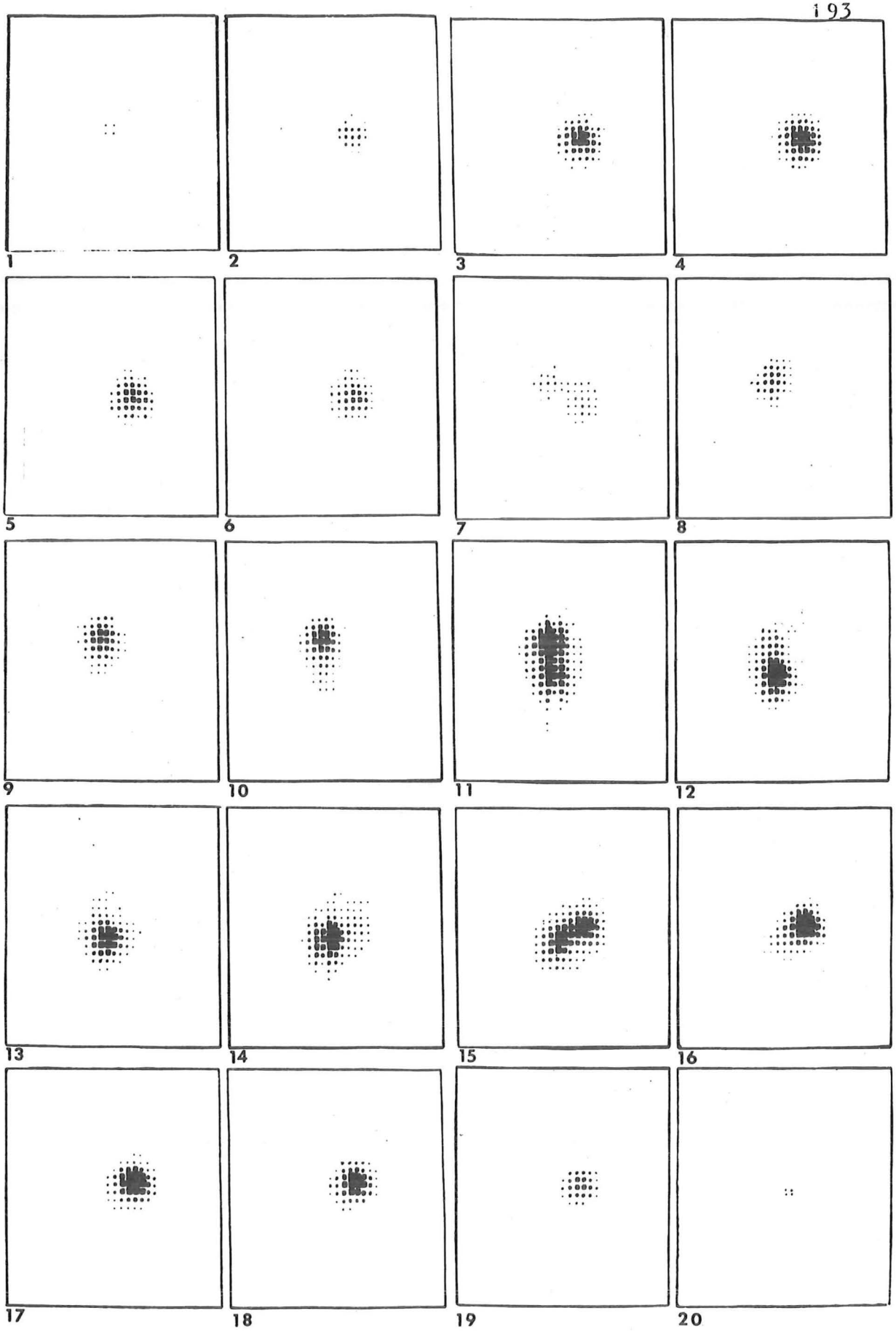

Fig. 8.4. Reconstructed images of 20 serial sections of the phantom using rho-filtered layergram processing.

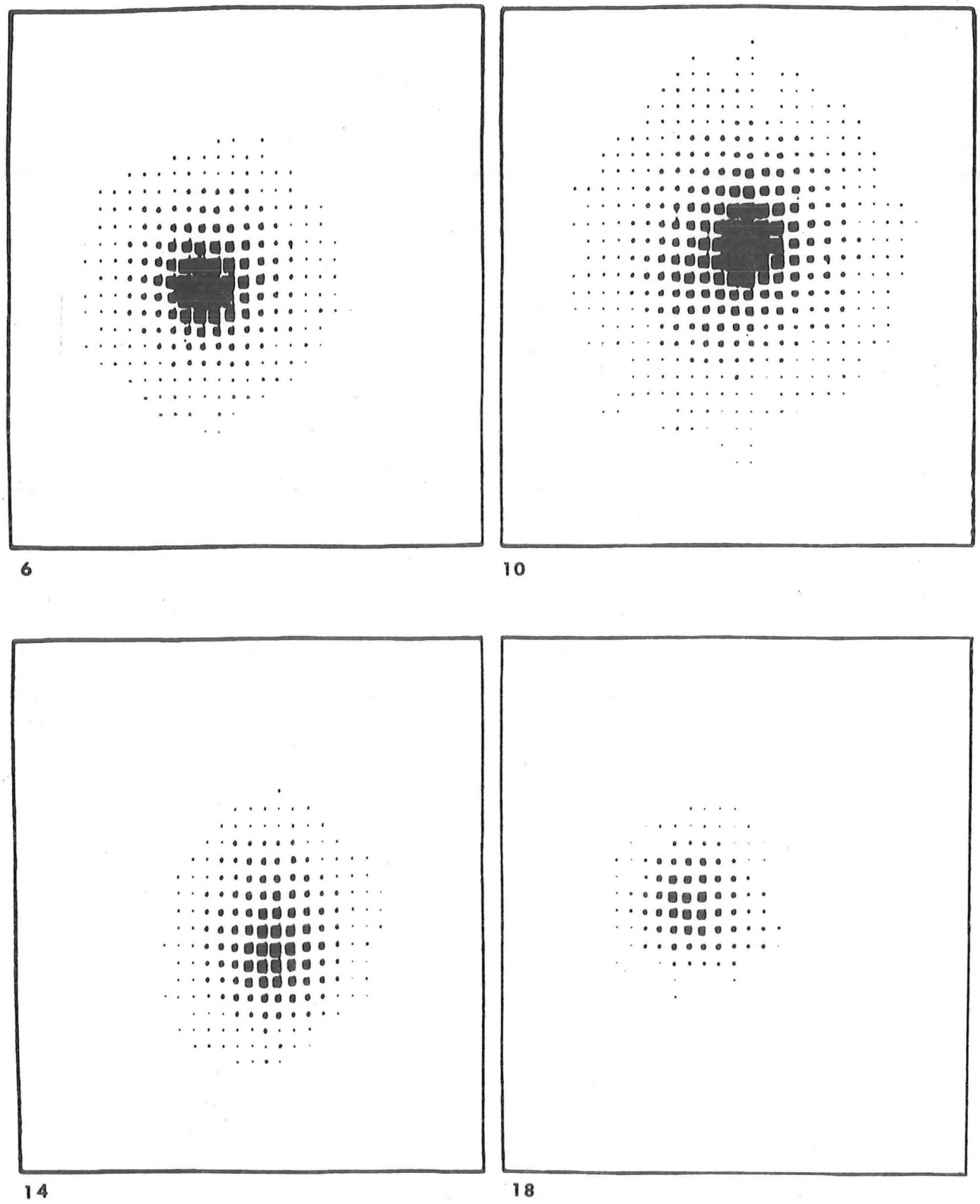

Fig. 8.5. Four of the sections displayed in fig.8.4. reconstructed using the (unfiltered) layergram technique. These images are equivalent to those obtained by the DSA method of Kuhl and Edwards (1968).

CHAPTER 9

COMPUTATIONAL CONSIDERATIONS

In this chapter, some comments are made regarding the computation and manipulation of Fourier transforms as applied to the work reported in this thesis. Two algorithms which are vital to the efficiency of the reconstruction techniques are discussed in detail.

9.1 Computation of Fourier Transforms

Most of the numerical reconstruction techniques reported in this thesis require digital computation of Fourier transforms of one- or two-dimensional arrays. Using the fast Fourier transform algorithm (FFT) (Cooley and Tukey 1965) such transforms may be computed very efficiently. Both before and since its formal introduction in 1965, the FFT has found applications in a wide variety of scientific and engineering problems (Bergland 1969, IEEE 1967, IEEE 1969). The FFT actually computes a discrete Fourier series, but may be used to approximate a continuous Fourier integral using sampled data. It has been shown (Hunt 1971) that the discrete Fourier transform of sampled data, as computed by the FFT, is equivalent to a trapezoidal approximation to the Fourier integral, and that the Fourier transform computed in this manner is more accurate than that evaluated using a higher order interpolation scheme on the data, provided that there is no aliasing (Bates et al. 1970).

The formula for the discrete Fourier transform is given in chapter 5 (eqns 5.1 and 5.2). It is convenient to re-express this formula in a slightly modified form for which some new notation is necessary. The members of the set $\{X_{m,n}\}$ represent MN samples of a two-dimensional function. The members of the set $\{a_{k,\ell}\}$ denote MN samples of the discrete Fourier transform of the $X_{m,n}$. $W_N^{\ell m}$ denotes $\exp(j2\pi\ell m/N)$. The discrete Fourier transform formula relating the $a_{k,\ell}$ to the $X_{m,n}$ is then

$$a_{k,\ell} = \sum_{n=0}^{N-1} \sum_{m=0}^{M-1} X_{m,n} W_N^{kn} W_M^{m\ell}. \tag{9.1}$$

The samples $X_{m,n}$ are found from the Fourier coefficients $a_{k,\ell}$ by

$$X_{m,n} = \frac{1}{MN} \sum_{k=0}^{N-1} \sum_{\ell=0}^{M-1} a_{k,\ell} W_N^{-kn} W_M^{-\ell m}. \tag{9.2}$$

For the usual version of the FFT algorithm, M and N are restricted to be some power of two. While procedures exist to allow transforms to be computed using data records of arbitrary length, the radix-two algorithm is the most compact.

Some practical aspects of the use of the FFT are given below.

9.1.1 Sampling of Data

When using the FFT algorithm to compute Fourier transforms, the most important requirement is that the data be sampled sufficiently finely. The sampling theorem specifies that the data must be sampled at a rate greater than or equal to twice its maximum spatial frequency component. Thus if a function $f(\xi)$ has negligible frequency components for $|\rho| > \hat{\rho}$, then

$f(\xi)$ must be sampled at intervals of not less than $(2\hat{\rho})^{-1}$. If $f(\xi)$ is sampled at N values of ξ in the range (-a,a), then N Fourier components spaced by $(2a)^{-1}$ in spatial frequency are obtained when the FFT is used.

The effect of aliasing has already been mentioned (chapter 5) with regard to angular interpolation. This phenomenon always occurs when the data being transformed is sampled too coarsely. If the sampling interval of the data is greater than $(2\hat{\rho})^{-1}$, (say $[2\rho_s]^{-1}$), then frequency components for $|\rho| > \rho_s$ become folded back into the range $|\rho| < \rho_s$. So, not only is the maximum spatial frequency, for which the transform is computed, reduced from $\hat{\rho}$ to ρ_s, but the values of the Fourier transform computed for $(2\hat{\rho}-\rho_s) \leqslant |\rho| \leqslant \rho_s$ are incorrect.

9.1.2 Data Windows

Sometimes when a one-dimensional or two-dimensional Fourier transform of measured data is computed, it is found that the Fourier components above a particular frequency $\hat{\rho}$ are unreliable estimates of the true values because of noise introduced by the recording process. This is particularly so after 'rho-filtering' a spectrum. It is therefore necessary to truncate the transform at some value $\hat{\rho}$, by multiplying the sequence of Fourier transform samples by a data window. However, from the convolution theorem for Fourier transforms, multiplication in the frequency domain is equivalent to convolution in the domain of the data. Thus, setting the spectrum of the data to zero for $|\rho| > \hat{\rho}$ (fig. 9.1a), which is equivalent to multiplying the spectrum by rect $(\frac{\rho}{2\hat{\rho}})$, has the effect of convolving the data with $2\hat{\rho}\ \mathrm{sinc}(2\hat{\rho}\xi)$, (fig. 9.1b). This convolution causes ripples (Gibbs' phenomenon) to appear

in $f(\xi)$ near regions of discontinuity. To overcome this difficulty, many authors have suggested using modified data windows which taper gradually to zero, rather than those which cut off abruptly. Away from their main peaks the Fourier transforms of such window functions are found to have lower amplitude ripples than the sinc function. Suitable windows include the Dolph-Chebyshev function (Helms 1967) and Tukey's 'interim' data window (Tukey 1967). This latter window consists of a raised cosine applied to the first and last ε% of the data. This window with $\varepsilon = 25\%$, and its Fourier transform, are shown in figs 9.1c,d. Since the 'interim' data window is simple and rapidly computed, it is used in this thesis for introducing cut-off frequencies in both rho-filtering and Fourier transform interpolation procedures. This window was originally suggested by Tukey as a one-dimensional function, but may be used equally effectively as a two-dimensional radially symmetric window (Huang 1972).

9.1.3 Conjugate Symmetry in Fourier Transforms of Real Data

Most of the Fourier transform operations described in this thesis compute the spectra of real functions, or conversely, compute real functions from their spectra. It is known (Bracewell 1965, p.14) that the Fourier transform of a real function is conjugate symmetric. This means that if

$$\Lambda(\rho,\phi) = \mathfrak{F}_2\{\lambda(r,\theta)\}, \tag{9.3}$$

then

$$\Lambda(\rho,\phi) = \Lambda^*(\rho,\phi+\pi). \tag{9.4}$$

Now the conventional FFT algorithm computes a set of complex Fourier coefficients from a set of complex data points. If the input happens to be entirely real, the imaginary values of

the input record are simply set to zero, so that half of the computer memory being used to store this data is effectively wasted. Also, since $\Lambda(\rho,\phi)$ is computed for ϕ in the range $0 < \phi < 2\pi$, half of the computed values are redundant since they may be determined from eqn (9.4).

This limitation was found to be particularly restrictive, since the core memory capacity of the computer used by the author (IBM 360/44) was only 32k words. Using the library FFT subroutine HARM (IBM 1968), the maximum size of complex square array able to be transformed is of 64 x 64 points. Arrays of 128 x 128 complex points just fail to be accommodated. An alternative algorithm which stores the data on disk and transfers sections of it to core memory for processing (Brenner 1968), proved to be inefficient because of the time taken to perform the numerous disk transfer operations.

To overcome these problems, an algorithm (R2FORT) was developed for use with a standard FFT program, to enable only half the spectrum of a real data record to be computed. This algorithm, which is described in the next section, not only permits a 128 x 128 point image to be transformed in core memory of the IBM 360/44 computer, but also reduces the computation time by a factor of two over that for the equivalent sized complex array.

9.2 R2FORT Algorithm

Cooley et al. (1969) show that it is possible to evaluate the transforms of two real functions simultaneously, by considering the samples of one sequence to be real data, and the other to be imaginary. The composite data record so

obtained is treated as a complex array, and is transformed using a conventional FFT algorithm. The transform of this composite sequence is then 'unscrambled' to obtain the Fourier transforms of the two original functions. This principle is used in R2FORT as explained below.

The real two-dimensional sequence $X_{m,n}$ comprises $2M \times N$ data points. By grouping the members of $\{X_{m,n}\}$ into MN ordered pairs of numbers $(X_{2m,n}, X_{2m+1,n})$ and considering each pair as the complex number $(X_{2m,n} + jX_{2m+1,n})$, a conventional FFT may be performed on the derived $M \times N$ point complex sequence;

$$a_{i,k} = \sum_{n=0}^{N-1} \sum_{m=0}^{M-1} (X_{2m,n} + jX_{2m+1,n})\, W_M^{im}\, W_N^{kn}. \qquad (9.5)$$

Similarly,

$$a_{M-i,N-k} = \sum_{n=0}^{N-1} \sum_{m=0}^{M-1} (X_{2m,n} + jX_{2m+1,n}) W_M^{m(M-i)} W_N^{n(N-k)} \qquad (9.6)$$

$$= \sum_{n=0}^{N-1} \sum_{m=0}^{M-1} (X_{2m,n} + jX_{2m+1,n}) W_M^{-im} W_N^{-kn}. \qquad (9.7)$$

Thus

$$\tfrac{1}{2}(a_{i,k}+a_{M-i,N-k}) = \sum_{n=0}^{N-1} \sum_{m=0}^{M-1} (X_{2m,n} + jX_{2m+1,n}) \cos 2\pi(im+kn)$$

$$= \alpha_{i,k} + j\beta_{i,k} \qquad (9.8)$$

and

$$\tfrac{1}{2}(a_{i,k}-a_{M-i,N-k}) = j \sum_{n=0}^{N-1} \sum_{m=0}^{M-1} (X_{2m,n}+jX_{2m+1,n}) \sin 2\pi(im+kn)$$

$$= \gamma_{i,k} + j\delta_{i,k} \qquad (9.9)$$

where $\alpha_{i,k}$ and $\gamma_{i,k}$ are the real parts, and $\beta_{i,k}$ and $\delta_{i,k}$ are the imaginary parts of eqns (9.8) and (9.9) respectively.

The symbols $B_{i,k}$, $C_{i,k}$ and $D_{i,k}$ are defined by the following expressions:

$$C_{i,k} = \alpha_{i,k} + \beta_{i,k} \cos \frac{\pi k}{M} + \gamma_{i,k} \sin \frac{\pi k}{M} , \qquad (9.10)$$

$$D_{i,k} = \delta_{i,k} + \beta_{i,k} \sin \frac{\pi k}{M} - \gamma_{i,k} \cos \frac{\pi k}{M} , \qquad (9.11)$$

and

$$\begin{aligned} B_{i,k} = C_{i,k} + jD_{i,k} = & \sum_{n=0}^{N-1} \sum_{m=0}^{M-1} \left[X_{2m,n} \cos 2\pi \left(\frac{im}{M} + \frac{kn}{N}\right) \right. \\ & \left. + X_{2m+1,n} \cos 2\pi \left(\frac{i(m+1)}{M} + \frac{kn}{N}\right) \right] \\ & + j \sum_{n=0}^{N-1} \sum_{m=0}^{M-1} \left[X_{2m,n} \sin 2\pi \left(\frac{im}{M} + \frac{kn}{N}\right) \right. \\ & \left. + X_{2m+1,n} \sin 2\pi \left(\frac{i(m+1)}{M} + \frac{kn}{N}\right) \right], \qquad (9.12) \\ = & \sum_{n=0}^{N-1} \sum_{m=0}^{2M-1} X_{m,n} W_M^{im} W_N^{kn}; \quad \begin{matrix} 0 \leqslant i \leqslant M-1 \\ 0 \leqslant k \leqslant N-1 \end{matrix} \\ & \qquad (9.13) \end{aligned}$$

The terms $B_{i,k}$ are recognised as being the semi-spectrum of the discrete Fourier transform of the sequence $\{X_{m,n}\}$. Since the values $B_{M-i,N-k}$ may be computed simultaneously with the values $B_{i,k}$, the algorithm may be executed without the need for any additional 'work areas' of storage to be provided. The inverse procedure for regaining a real function from its complex semi-spectrum is similar to that described above and is performed using the same sequence of operations.

This algorithm ('R2FORT') is programmed in Fortran and used whenever Fourier transforms or inverse Fourier transforms are required to be computed for real data or their spectra respectively.

While similar algorithms for transforming one-dimensional data are well known (c.f. Singleton 1969), the literature does not appear to contain any accounts of such an algorithm for transforming two-dimensional data.

9.3 FTFSI Algorithm

The assignment of values to points on a Fourier transform grid, by Fourier series interpolation of samples existing along radial lines in the Fourier transform domain, may appear at first to be a formidable computational task. However, a number of short-cuts have been noticed which enable the algorithm to be programmed in such a manner that it takes only twice as long to run as a simple linear interpolation scheme. The expression describing the FTFSI method is

$$\Lambda(\rho,\phi) = \sum_{n=-N}^{N} a_n(\rho)\, \exp(jn\phi) \tag{9.14}$$

where the $a_n(\rho)$ are radially dependent angular Fourier series coefficients computed from the transforms of the measured projections. However, it is required to compute the transform on points of a two-dimensional grid, and so the Cartesian coordinate representation of the Fourier transform of the cross-section is more convenient, i.e.

$$\Omega(\alpha_k,\beta_\ell) = \sum_{n=-N}^{N} a_n[(\alpha_k^2+\beta_\ell^2)^{\frac{1}{2}}]\exp\left[jn \arctan\left(\frac{\beta_\ell}{\alpha_k}\right)\right], \tag{9.15}$$

where (α_k,β_ℓ) are the coordinates of the sample points in the two-dimensional Fourier transform space.

Before describing the procedure used for implementing the FTFSI algorithm, it is necessary to derive a property of a certain class of Fourier series. When $\lambda(r,\theta)$ is real, at any radius ρ in the Fourier transform plane, $\Lambda(\rho,\phi)$ and $\Lambda(\rho,\phi+\pi)$ are related by

$$\Lambda(\rho,\phi) = \Lambda^*(\rho,\phi+\pi) = \Lambda_R(\rho,\phi) + j\Lambda_I(\rho,\phi) \tag{9.16}$$

(where the subscripts R and I denote real and imaginary parts respectively) by virtue of the conjugate symmetry which exists between opposing half planes in two-dimensional Fourier space. Recalling that $\Lambda(\rho,\phi)$ is determined from the transforms of the projections only for $\phi = \pm \frac{n\pi}{N}$, it may be expanded in terms of an angular Fourier series:

$$\Lambda(\rho,\phi) = \sum_{m=-N}^{N} a_m(\rho) \exp(-jm\phi), \tag{9.17}$$

where

$$a_m(\rho) = \frac{1}{2N+1} \sum_{n=-N}^{N} \Lambda(\rho,\phi_n) \exp(jm\phi_n) \tag{9.18}$$

$$= \frac{1}{2N+1} \sum_{n=0}^{N} \varepsilon_n \{\Lambda(\rho,\phi_n) \exp(jm\phi_n) + \Lambda^*(\rho,\phi_n) \exp(jm\phi_n+\pi)\} \tag{9.19}$$

$$= \frac{1}{2N+1} \sum_{n=0}^{N} \varepsilon_n \{\Lambda(\rho,\phi_n) + (-1)^m \Lambda^*(\rho,\phi_n)\} \exp(jm\phi_n) \tag{9.20}$$

$$= \begin{cases} \frac{1}{2N+1} \sum_{n=0}^{N} \varepsilon_n \Lambda_R(\rho,\phi_n) \exp(jm\phi_n) ; & m \text{ even} \\ \frac{-j}{2N+1} \sum_{n=0}^{N} \varepsilon_n \Lambda_I(\rho,\phi_n) \exp(jm\phi_n) ; & m \text{ odd.} \end{cases} \tag{9.21}$$

where ε_n is the Neumann factor as defined in the glossary. Notice also that

$$a_{-m}(\rho) = (-1)^m a_m^*(\rho). \qquad (9.22)$$

By using expressions (9.21) and (9.22) to compute the set ot coefficients $\{a_m(\rho)\}$, the saving in the number of computational operations required, results in an increase in speed of greater than 400% over that required for evaluation of expression (9.17) directly. FFT methods are not used to compute the angular Fourier series, since N is never large, and is often not an integer power of 2.

Another consequence of the conjugate symmetry of the Fourier transform is that it is necessary only to interpolate values from the transforms of the projections, onto half of the Fourier transform plane. This half-plane may be divided into four octants as shown in fig. 9.2, noting that for each point with coordinates (ρ,ϕ) in octant 1, there exist 'mirror-image' points with coordinates $(\rho,\frac{\pi}{2}-\phi)$, $(\rho,\frac{\pi}{2}+\phi)$, $(\rho,\pi-\phi)$ in octants 2, 3 and 4 respectively.

The procedure for reconstructing a cross-section from a set of projections using the FTFSI method is as follows.

a) Compute the Fourier transform of each individual projection $f(\xi,\phi_n)$ for $1 \leqslant n \leqslant N$, using the FFT algorithm in conjunction with the R2FORT algorithm, to form $\Lambda(\rho_m,\phi_n)$.

b) Using the algorithm described by eqn (9.21) above, evaluate $\{a_n(\rho_m)\}$ for positive n and store in the locations originally occupied by $\Lambda(\rho_m,\phi_n)$.

c) Apply a data window to $\{a_n(\rho_m)\}$ and/or set the insignificant and/or the ambiguous coefficients (as defined in chapter 4) to zero if required.

d) Scan the points (α_k, β_ℓ) in octant 1, computing the radial coordinates (ρ,ϕ) of each point, where

$$\rho = (\alpha_k^{\,2} + \beta_\ell^{\,2})^{\frac{1}{2}} ;$$

$$\phi = \arctan\left[\frac{\alpha_k}{\beta_\ell}\right] .$$

e) Linearly interpolate from the set of coefficients $\{a_n(\rho_m)\}$, a set of angular coefficients $\{a_n(\rho)\}$.

f) Compute the Fourier series interpolation at the points (ρ,ϕ), $(\rho,\frac{\pi}{2}-\phi)$, $(\rho,\frac{\pi}{2}+\phi)$ and $(\rho,\pi-\phi)$ in octants 1, 2, 3 and 4 simultaneously, using eqn (9.15). Note that the trigonometric functions needed to interpolate the point (ρ,ϕ), may also be used to interpolate the three 'mirror-image' points.

g) Repeat steps d-f for all points lying in octant 1, performing the interpolations at the 'mirror-image' points simultaneously.

h) Compute the inverse Fourier transform using the FFT in conjunction with R2FORT to obtain the reconstructed image.

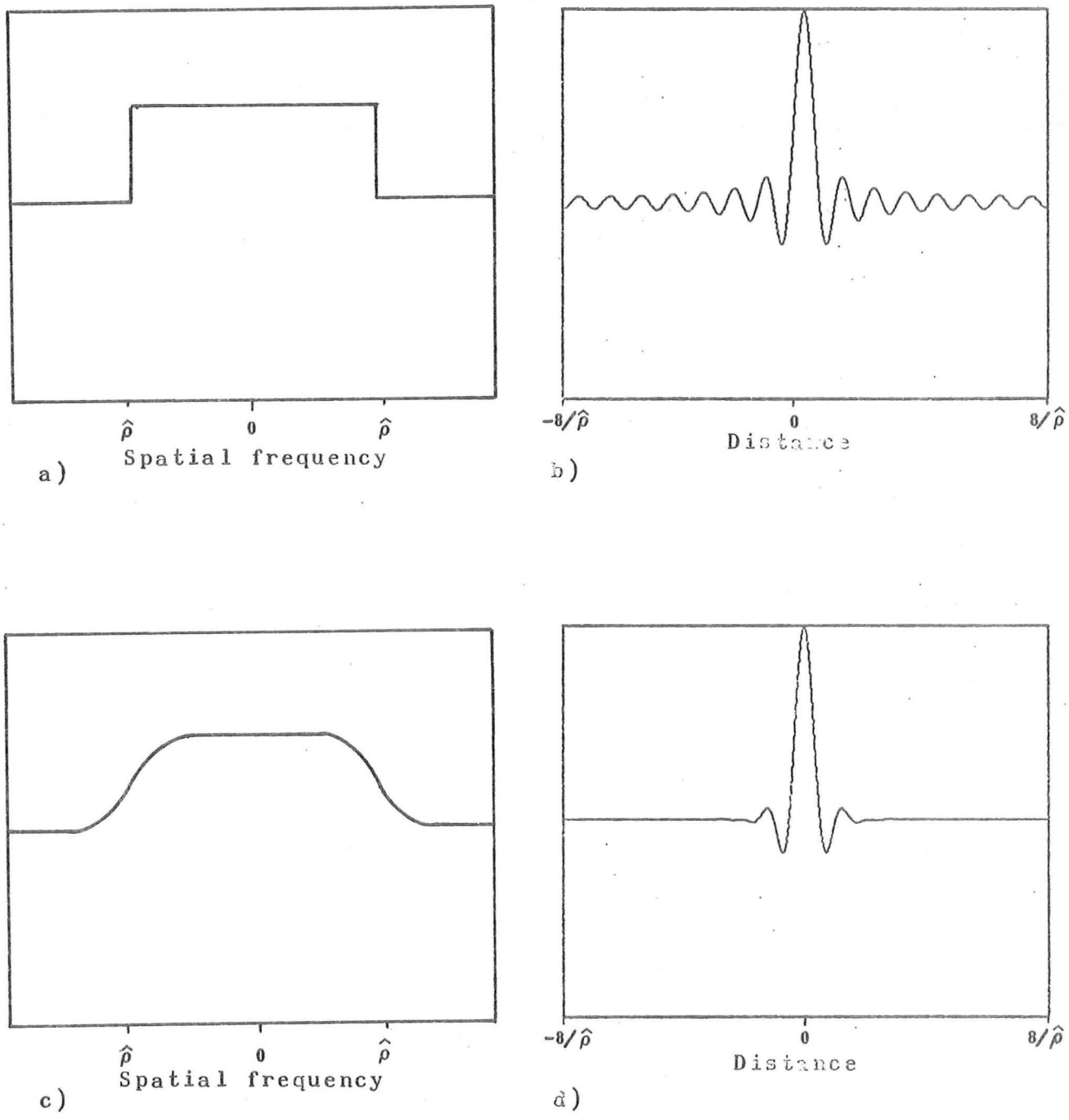

Fig. 9.1. Data windows.

a) Rectangular data window.

b) Fourier transform of rectangular data window.

c) Tukey's interim data window.

d) Fourier transform of interim data window.

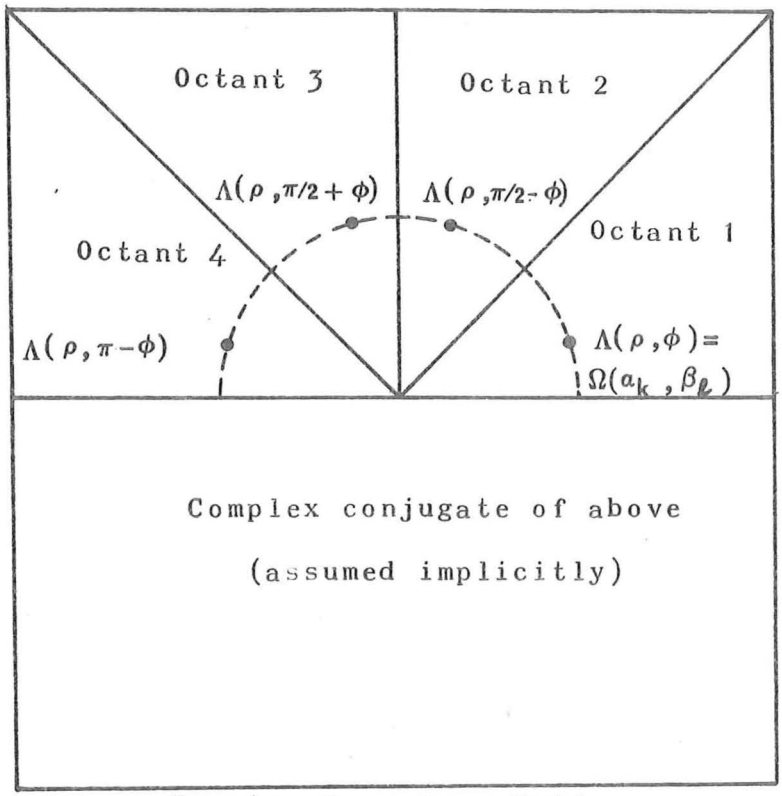

Fourier Transform Grid

Fig. 9.2. Organization of Fourier transform grid for FTFSI algorithm.

CHAPTER 10

CONCLUDING REMARKS

This thesis has demonstrated the usefulness of Fourier transform processing techniques for obtaining images of cross-sections of objects from their projections. Particular emphasis has been placed upon the use of these techniques in the field of medical image processing. It is considered that the methods presented here have potential use in computer-aided radiographic tomographic devices such as the 'EMI-SCANNER' (Ambrise and Hounsfield 1973), in gamma camera tomography and in conventional radiographic transverse tomography.

10.1 Suggestions for Further Research on Image Reconstruction from Finite Numbers of Projections

The medical area in which it appears that image reconstruction techniques are of the most value is in radiotherapy treatment planning. It is common for radiotherapy departments to employ devices which rotate an X-ray source and a detector (e.g. a radiotherapy simulator c.f. Takahashi 1965) about a human body with a planetary motion. Such a device is also required to enable projections of the anatomy to be measured at various angles. It would therefore be of interest to investigate means of adapting existing systems to enable them to be used for computerised tomography. The relative merits of various recording media (e.g. scintillation counters and photographic film) should also be investigated. It is possible that computerised tomography could be integrated with radiotherapy treatment planning, using a computer with inter-

active facilities, to produce a treatment plan automatically.

It may soon become standard practice to obtain images of soft organs using ultrasonic transmission-time measurements (c.f. Le Croissette and Heyser, 1972). If the ultrasonic refractive index of an organ relative to that of water is sufficiently close to unity, then ultrasonic transmission-time images may be interpreted as projections of the 'acoustic density' of the organ (Bates and Dunlop 1973). Using acoustic transmission-time projections as data, the image reconstruction methods described in this thesis could be used to obtain two- or three-dimensional images of soft organs. Since small changes in density of soft tissues could be displayed in this way, an acoustic transmission-time tomographic system would be a useful complement to conventional radiographic and ultrasonic diagnostic methods.

10.2 Suggestions for Further Research on Rho-Filtered Layergrams

The most important factor affecting the quality of the rho-filtered layergram as described in chapter 7, is the non-linearity introduced by the film. Therefore the most pressing area for further research is to evaluate the characteristics of available photographic materials in order to obtain a system with maximum linearity. Since the resolution of the system is limited by the resolution of the fluorescent screen, the development of a more suitable screen would enable the layergraphic system to produce images containing more detail than those displayed by the experimental results of chapter 7. For use in a practical situation when the divergence of the X-ray

beam is significant, a suitable conical lens would have to be designed or simulated to back-project the projections onto the film in the correct manner. The overall optics of the layergraph could also be significantly improved to increase the light gathering power of the system and to provide a miniature image (35 mm size) of the layergram. This would help to reduce the radiation dosage administered to the patient.

It is also worth investigating the use of Xero-radiography (Roach 1970) in transverse tomography. When a selenium plate is exposed to X-radiation, a latent image is produced on the surface of the plate as a pattern of electric charge. When this plate is coated with some suitable powder, the electric charge pattern is rendered visible. Xero-radiography has the property of enhancing high spatial frequencies in an image, and so it may be found that a tomogram produced in this way sufficiently resembles a rho-filtered layergram that there is no need for any further processing.

APPENDIX A

CLUTTER ASSOCIATED WITH THE RHO-FILTERED DISCRETE LAYERGRAM OF A GAUSSIAN DENSITY DISTRIBUTION

Because the rho-filtering operation is position invariant, the clutter (due to N being finite) associated with a particular feature is a function only of the radius vector from an appropriately chosen origin in the feature. Consequently, when analysing the rho-filtered discrete layergram of the Gaussian blob introduced in eqn (5.42), it is sufficient to centre the blob at the origin of coordinates of fig. 3.1a. Thus,

$$\lambda(r,\theta) = \exp(-r^2/2\ W^2) \tag{A.1}$$

of which the projected density is

$$f(\xi,\phi) = (2\pi)^{\frac{1}{2}}\ W \exp(-\xi^2/2W^2) \tag{A.2}$$

which gives, using eqn (3.4) and formula 11.4.29 of Abramowitz and Stegun (1965),

$$\Lambda(\rho,\phi) = 2\pi W^2 \exp(-2\pi^2 W^2 \rho^2). \tag{A.3}$$

Multiplying eqn (A.3) by $\mathrm{Star}_N(\rho,\phi)$ (eqn 4.1), rho-filtering, and inverting the transform (eqn 3.24), the rho-filtered layergram is

$$\bar{\lambda}_N(r,\theta) = \frac{4\pi^2 W^2}{N} \sum_{n=1}^{2N} \int_0^{\infty}\int_0^{2\pi} \delta(\phi-(n\pi/N))\ \exp(-2\pi^2 W^2 \rho^2)$$

$$.\exp(-i2\pi r\rho\ \cos(\phi-\theta))\,\rho\,d\phi\,d\rho \tag{A.4}$$

when ϕ_n is given by (4.5). Expressing the complex exponential

in (A.4) as a trigonometrical Fourier series (c.f. formulae 9.1.44 and 9.1.45 Abramowitz and Stegun 1965), integrating with respect to ϕ, summing over n and writing $t = 2^{\frac{1}{2}}\pi W\rho$ gives

$$\bar{\lambda}_N(r,\theta) = 4 \sum_{m=0}^{\infty} \varepsilon_m (-1)^{mN} \cos(2mN\theta) \int_0^{\infty} J_{2mN}(2^{\frac{1}{2}} rt/W) \exp(-t^2)\, t\, dt \tag{A.5}$$

where ε_m is the usual Neumann factor. The term for m = 0 in eqn (A.5) is $\lambda(r,\theta)$, as given by (A.1). The remaining terms can be evaluated by integrating by parts, which replaces $t\, J_{2mN}(2^{\frac{1}{2}} rt/W)$ in the integrand by a constant multiplied to the derivative of the Bessel function, and then using the second recurrence relation in formula 9.1.27 of Abramowitz and Stegun (1965). The resulting integrals can be expressed in terms of modified Bessel functions using eqn (5), p.394, of Watson (1966). So, the clutter introduced by there being only N given projections can be written as

$$\bar{\lambda}_N(r,\theta) - \lambda(r,\theta) =$$

$$\frac{\pi^{\frac{1}{2}} r}{2^{\frac{1}{2}} W} \exp(-r^2/4W^2) \sum_{m=1}^{\infty} \left[I_{mN-\frac{1}{2}} \left(\frac{r^2}{4W^2} \right) - I_{mN+\frac{1}{2}} \left(\frac{r^2}{4W^2} \right) \right] \cos(2mN\theta). \tag{A.6}$$

APPENDIX B

IMAGE RECONSTRUCTION FROM A SINGLE 'PROJECTION'

Consider a rectangular image, of dimensions A by B, divided into MxMy rectangular cells, where Mx and My are positive integers. Fig. B.1 shows the geometry. The density is constant within each cell.

$$\omega(x,y) = \omega_{m,n}; \quad m \leqslant x + Mx/2 + 1 \leqslant m+1, \qquad (B.1)$$

$$n \leqslant My/2 - y + 1 \leqslant n+1,$$

$$1 \leqslant m \leqslant Mx, \quad 1 \leqslant n \leqslant My.$$

The image is projected onto the ξ-axis which is oriented at an angle to the x-axis of θ, which is given by

$$\theta = \tan^{-1}(1/My). \qquad (B.2)$$

The resulting pseudo projection is then sampled at points ξ_k, where

$$\xi_{k-1} - \xi_k = A/(MxMy \cos\theta); \qquad (B.3)$$

$$\xi_1 = -\tfrac{1}{2}[A\sec\theta + (B - A\tan\theta - 2B/My)\sin\theta] \qquad (B.4)$$

as shown in fig. B.1. $f(\xi_k,\theta)$ is then given by

$$f(\xi_k,\theta) = \alpha\{\sum_{i=1+1}^{My} \delta_m \omega_{i,m} + \sum_{i=1}^{1} \omega_{i,m+1}\}; \qquad (B.5)$$

$$1 = k \pmod{My};$$

$$m = (k-1)/My;$$

$$\delta_m = 0, \quad m = 0$$

$$= 1, \quad m \neq 0;$$

$$\alpha = (B \sec \theta)/My.$$

α is a constant of proportionality made necessary by the path of integration through each cell. If one is given the MxMy values of $f(\xi_n, \theta)$, then each member of $\{\omega_{m,n}\}$ can be obtained iteratively starting with

$$\omega_{1,1} = \alpha f(\xi_1, \theta) \tag{B.6}$$

which can be substituted into (B.5) to give $\omega_{1,2}$. This process may be continued until eventually all the $\omega_{m,n}$ are obtained. Note that the given data is equivalent to a single projection given at MxMy values of ω.

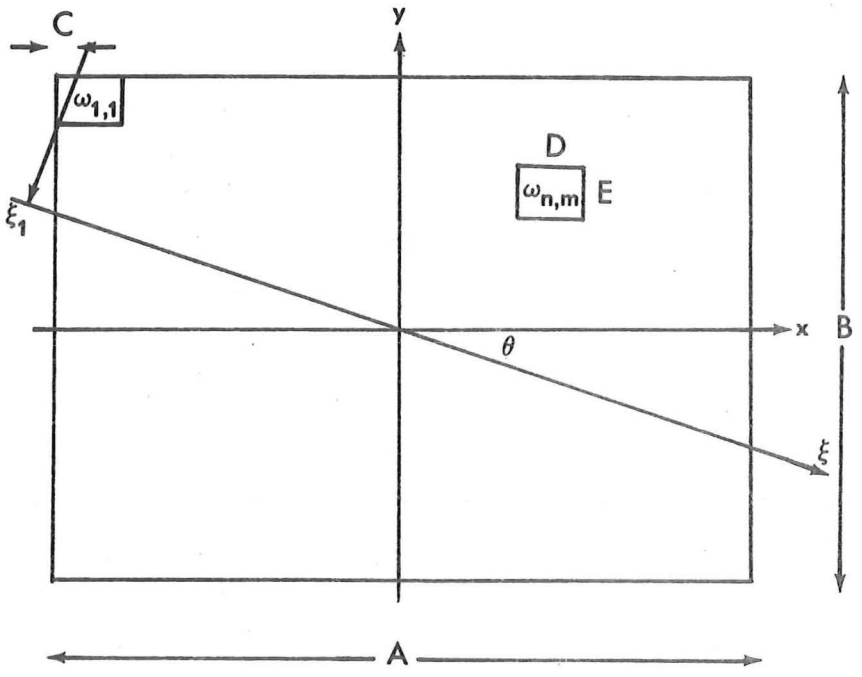

Fig. B.1. Geometry of grid for constructing pseudo-projection.

A,B Overall dimensions of grid.

C Spacing on x axis between adjacent projection samples = $A/(M_x.M_y)$.

D,E Cell dimensions.

APPENDIX C

HIGH QUALITY IMAGE RECORDING AND DISPLAY USING A SMALL HYBRID COMPUTER

C.1 Introduction

To enable the various image recording and display requirements of this project to be fulfilled, an inexpensive image-processing station consisting of an image scanner and a facsimile machine was interfaced to the Electrical Engineering Department's EAI-590 computer. The image scanner was built specifically for the project, while a standard facsimile (wire-photo) machine was adapted for computer use. This appendix describes the operation of this system and presents results which demonstrate its capabilities.

The main requirement of the system was that it should be capable of digitizing and reproducing images with a high degree of fidelity. The Hybrid Computer was used because it is a source of high quality analogue and digital hardware which would otherwise have to be either assembled from commercially available units, or constructed specifically for the task in hand. This computer exercises direct control of an image scanner, to digitize pictures, and a facsimile recorder to produce permanent records of processed pictures.

C.2 System Configuration

The configuration of the system was dictated mainly by the facilities already available within the university. The hybrid computer comprises a medium sized digital machine (EAI-640) with 16K, 16 bit words of magnetic core memory and

additional disk storage, a small analogue computer (EAI-580) and a hybrid interface between the two units. The combination of these three units is known as the EAI-590 Hybrid computer system. Two-way communication between the digital and analogue machines is provided by four logic sense lines, four logic control lines, two interrupt lines, 16 analogue to digital converter (ADC) channels, and six digital to analogue multiplier (DAM) channels. The output of this latter device is a voltage which is proportional to the digital input signal multiplied by an analogue reference signal.

Without the hybrid link, the only input/output facilities available on the digital computer are paper tape, teletype, and interactive graphics.

C.3 Image Scanner

The specifications for the scanner were that it should be able to digitize transparencies ranging in size from 35 mm to 4"x5" plates, with a spatial resolution of at least 128 x 128 picture elements (pixels) and a grey scale resolution of at least 64 brightness levels. Flying spot scanning systems (Ledley et al. 1965) and drum systems (Jessup and Wallace 1968) were considered,but the system eventually adopted was a scanning densitometer using a digitally controlled translation table. A simple optical system directs a suitably apertured beam of light onto the transparency, and the transmitted light is detected with a selenium photo-electric cell. Driving circuits for the stepper motors, which drive the translation table, are such that they may be operated directly from pulses supplied by the computer control lines. However, appropriate logic circuitry is inserted between the control lines and the

motor controllers to enable manual operation of the scanner if desired. Micro-switches provide protection against the stepping motors overdriving the limits of the imaging area.

A schematic of the scanner and circuitry is shown in fig. C.1, while the scanner itself is shown in fig. C.3. Light from a stabilised DC incandescent light source is focussed by a condensing lens onto an aperture which is reprojected onto the transparency with a microscope objective lens. The size of the sampling aperture at the transparency may be varied by changing either the aperture size itself or the magnification of the optical system. A further microscope objective lens focusses the light transmitted through the film onto the selenium photo-electric cell housed at the upper end of the microscope barrel. The output current from this cell is fed directly into the summing junction of one of the operational amplifiers which forms part of the analogue computer hardware. Gain and contrast are provided by further amplifier and potentiometer circuits, and the output voltage of the system is finally transferred to the digital computer via an ADC channel.

The scanning of the translation table and sampling of the ADC are controlled exclusively by the digital computer. Parameters entered by the user determine the size and resolution of the picture frame to be scanned, and the positioning of this frame relative to the edges of the transparency. While the image may be sampled as the table traverses in both the forward and reverse directions, effects of mechanical backlash in the system are minimised if the picture is sampled only when the table is moving in the forward direction.

Successive samples are stored in computer memory until the end of a raster line is reached, at which time the digital record is written onto a disk file.

This system is capable of scanning a picture and digitally recording the optical density of the image with a repeatable accuracy of better than 1%. The output of the system may be calibrated against the density of the transparency by scanning a standard photographic density tablet and performing the appropriate rescaling in the digital computer. The image is built up on a storate oscilloscope as the scanning operation proceeds to enable its progress to be monitored.

C.4 Facsimile Machine

For effective evaluation of the results of computer image processing experiments the picture display device must have a wide dynamic range, a well defined relationship between the density of the image and the numerical values representing that image, and adequate spatial resolution. Much ingenuity has been used (McLeod 1970) in adapting a standard line-printer to fill this role but, because a line-printer is not specifically designed for this purpose, the images obtained in this manner are only of limited value. In contrast, a facsimile machine, commonly known as a wire-photo machine, is designed for image reproduction and will typically display a 20 cm x 20 cm image with a resolution of 800 x 800 elements, and a continuous grey scale range of 32 db. The picture quality is in fact far superior to that attainable using a television system.

Many variations of facsimile machines have been developed, but the best quality units for picture reproduction use photographic paper as the recording medium. The paper is wrapped around a drum which rotates at constant speed. A modulated light source traverses the length of the drum to build an image as a spiral on the photographic paper. In the unit (Muirhead D700S) used here, the drum rotates at 240 r.p.m. giving a scan rate of 4 lines per second. A full 20 cm x 20 cm picture is reproduced in 200 seconds. The film drum is housed in a light tight cassette, and the light source, focussing optics, motor drive and electronics are contained in a light-proof box. The facsimile machine used is shown in fig. C.4.

Facsimile machines are generally designed to be driven via a standard communication channel, usually a telephone line, and require the specific control and data signals described in the following paragraphs, in which numerical values apply to the Muirhead D700S.

All picture information is amplitude modulated on a 2.5 Khz carrier. Picture reproduction begins with 3 seconds of start tone (300 Hz) which initialises the recorder. During the next five seconds a series of pulses synchronises the facsimile machine with the incoming signal and an automatic attenuator adjusts to the signal level. Throughout the period of picture transmission which follows, the demodulated signal is applied to the light source. The correct drum speed is maintained by feeding the hysteresis motor with a signal of appropriate frequency derived either from the internal tuning fork oscillator at 1200 Hz, or from an external local source. At the completion of the transmission, the operator changes

the cassette and rewinds the frame carriage in readiness for the next picture.

To adapt the facsimile machine to computer use, either its internal electronics must be modified, or an interface supplying amplitude modulated information and control signals must be provided. With the hybrid computer available, the interface is readily assembled from standard computing components as shown in fig. C.2. Since its operating speed may not be varied at will, the facsimile acts as a 'master' via the interrupt facilities of the hybrid system. Using the line and element interrupt signals (fig. C.2) as a time base, the CPU transmits the 300 Hz start tone and the phasing sequence. Data is then assembled from disk and printed line by line under interrupt control. If the number of picture elements to be displayed is less than the resolution capability of the facsimile machine (and because of the 640,000 pixels possible this would normally be the case), interpolation between elements is performed within the CPU so that a picture of reasonable size is printed. Because of the time taken to read a line of the digital image from disk, and the time taken to perform the interpolation, only 512 of the possible 800 elements per line are used. Since the normal digital picture record is 128 x 128 elements, this image is easily interpolated to fill the 512 x 512 element facsimile field.

C.5 Results

A 35 mm transparency (fig. C.5a) was digitized into a record of 128 x 128 pixels using the image scanner. The same image formed by the line-printer character overprints using the method of McLeod (1970) is shown in fig. C.5b. The image is quantised into 21 distinct 'grey' levels by this process, although it is debatable how many of these are discerned as such by the eye.

Fig. C.5c displays the same image as it appears on the face of a storage oscilloscope. As this oscilloscope is essentially a binary imaging device, the 'density' of each image point is represented by filling a small square matrix on the screen with a number of dots proportional to the square of the value of the pixel being displayed. On the oscilloscope used (Tektronix 611) it is possible to display an image of 128 x 128 elements with only a 3 bit (8 level) grey scale. However, the device is very useful for initial scrutiny of the image prior to printing on the facsimile. This oscilloscope also has a hard-copy unit (Tektronix 4601) attached, making it an extremely useful device, in spite of its limited number of effective grey levels.

Fig. C.5d shows the image reproduced by the facsimile machine. The loss of information in the images shown in figs C.5b and C.5c is readily apparent.

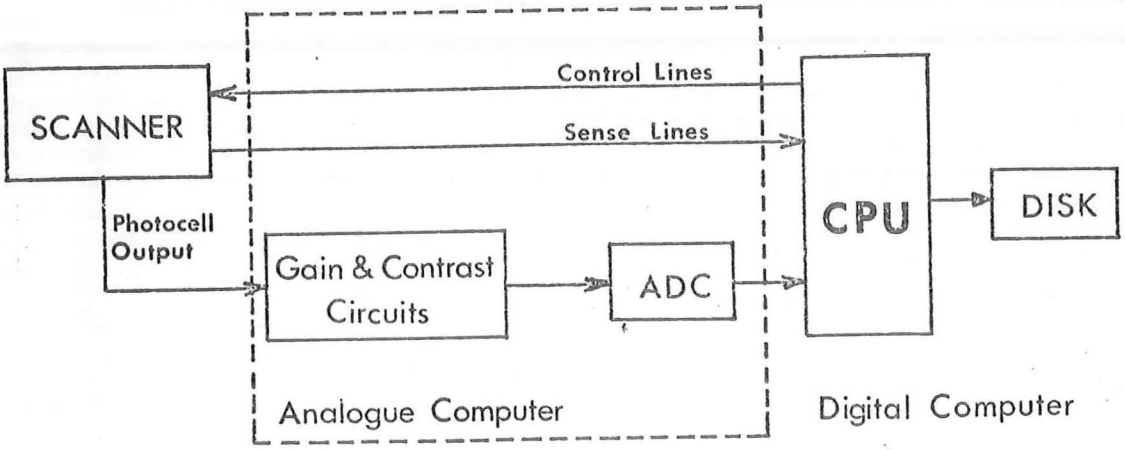

Fig. C.1. Block diagram of scanner circuitry.

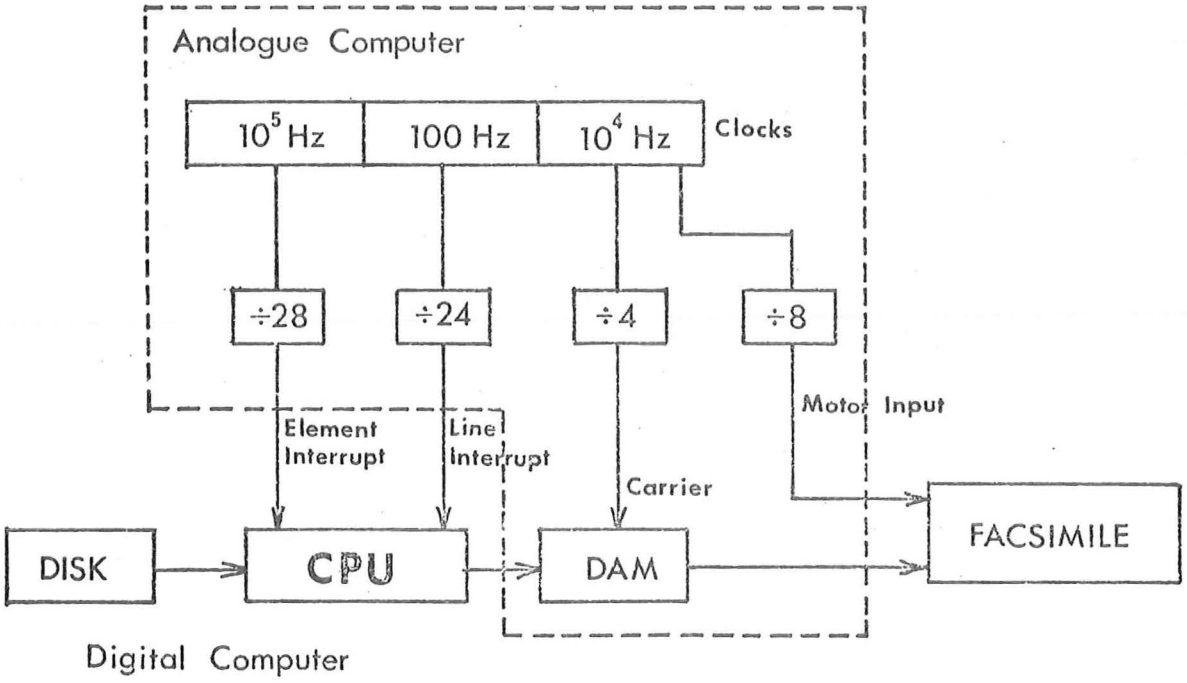

Fig. C.2. Block diagram of facsimile machine circuitry.

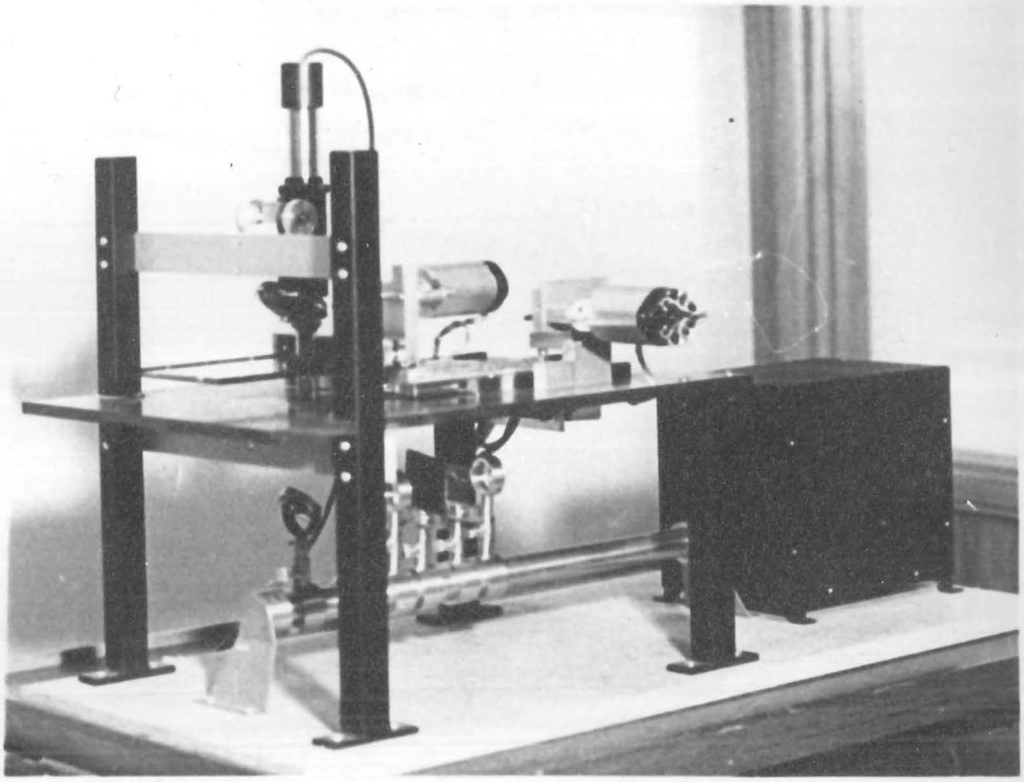

Fig. C.3. Image scanner.

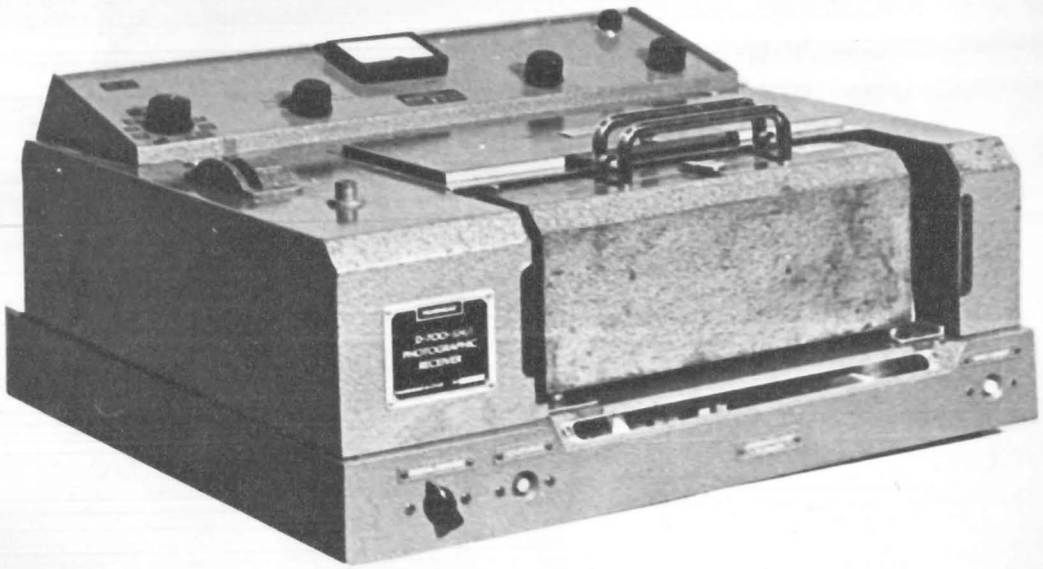

Fig. C.4. Facsimile machine.

a)

b)

c)

d)

FIG.C.5. RESULTS USING SCANNER AND FACSIMILE MACHINE

a) ORIGINAL PHOTOGRAPH

b) OUTPUT USING LINE-PRINTER

c) OUTPUT USING STORAGE OSCILLOSCOPE

d) OUTPUT USING FACSIMILE MACHINE

REFERENCES

Abramowitz M. and Stegun I.A. 1965 Handbook of Mathematical Functions, Dover, N.Y.

Ambrose J. and Hounsfield G. 1973 New techniques for diagnostic radiology. Brit. J. Radiol. 46, 148-149.

Amisano P. 1955 Three dimensional stratigraphic examination - Axial transverse stratigraphy. Part II. Am. J. Roent. Rad. Ther. Nucl. Med., 74, 777-789.

Andrews J.R. 1936 Planigraphy, I. Introduction and history. Am. J. Roent. Rad. Ther. 36, 575-587.

Andrews J.R. and Stava R.J. 1937 Planigraphy II. Mathematical analysis of the methods, description of the apparatus and experimental proof. Am. J. Roent. Rad. Ther. 38, 145-151.

Anger H.O. 1968 Tomographic gamma-ray scanner with simultaneous read-out of several planes. In Fundamental Problems in Scanning. Gottschalk A. and Beck R.N. (eds) C.C. Thomas, Ill. 195-211.

Anger H.O., Price D.C. and Yost P.E. 1967 Transverse-section tomography with the scintillation camera. J. Nucl. Med. 8, 314-315.

Baily N.A., Lasser E.C. and Crepeau R.L. 1971 Holographic image reconstruction from planigraphic sections. Invest. Radiol. 6, 221-224.

Barnes C.W. 1966 Object restoration in a diffraction-limited system. J. Opt. Soc. Am. 56, 575-578.

Bates R.H.T. and Dunlop G.R. 1973 Simplified approach to acoustic transmission tomography. In preparation.

Bates R.H.T., Napier P.J. and Chang Y.P. 1970 Square wave Fourier transform. Electron. Letts 6, 741-742.

Bates R.H.T. and Peters T.M. 1971 Towards improvements in tomography. N.Z. J. Sci. 14, 883-896.

Baum G. and Greenwood J. 1961 Orbital lesion localization by three-dimensional ultrasonography. N.Y. State J. Med. 61, 4149-4157.

Bellman S.H., Bender R., Gordon R. and Rowe J.E. 1971 ART is science, being a defence of algebraic reconstruction techniques for three-dimensional electron microscopy. J. Theor. Biol. 32, 205-216.

Bergland G.D. 1969 A guided tour of the fast Fourier transform. IEEE Spectrum, 41-52

Berry M.V. and Gibbs D.F. 1970 The interpretation of optical projections. Proc. Roy. Soc. Lond. A 314, 143-152.

Biraud Y. 1969 A new approach for increasing the resolving power by data processing. Astron. and Astrophys. 1, 124-127.

Blanch G. 1964 Numerical evaluation of continued fractions. S.I.A.M. Review 6, 383-421.

Bocage A.E.M. 1922 French Patent No. 536464.

Bracewell R.N. 1956 Strip integration in radio astronomy. Aust. J. Phys. 9, 198-217.

Bracewell R.N. and Riddle A.C. 1967 Inversion of fan-beam scans in radio astronomy. Astrophys. J. 150, 427-34.

Bracewell R.N. 1965 The Fourier Transform and its Applications. McGraw-Hill, N.Y.

Brenner N.M. 1969 Fast Fourier transform of externally stored data. IEEE Trans. Audio Electro. AU-17, 128-132.

Burns W.R. and Yao S.S. 1970 A new approach to aperture synthesis processing. Astron. and Astrophys. 6, 481-485.

Byrd P.F. and Friedman M.D. 1962 Handbook of Elliptic Integrals for Engineers and Physicists. Lange, Maxwell and Springer, Lond.

Cartwright P.H. 1971 Modulation transfer function basic principles. National Radiation Laboratory publication NRL T33, Department of Health, N.Z.

Chang S.K. 1971 The reconstruction of binary patterns from their projections. Comm. A.C.M. 14, 21-25.

Chang S.K. and Chow C.K. 1973 The reconstruction of three-dimensional objects from two orthogonal projections and its application to cardiac cineangiography. IEEE Trans. Comput. C-22, 18-28.

Chang S.K. and Shelton G.L. 1971 Two algorithms for multiple view binary pattern reconstruction. IEEE Trans. Syst. Man. Cyber. 1, 90-94.

Chau H.H. 1971 Three-dimensional reproduction of shadowgrams. Optics Commun. 4, 1-4.

Cooley J.W., Lewis P.A.W. and Welch P.D. 1969 The finite Fourier transform. IEEE Trans. Audio and Electroac., AU-17, 77-85.

Cooley J.W. and Tukey J.W. 1965 An algorithm for the machine generation of complex Fourier series. Math. Comp. 19, 297-301.

Cormack A.M. 1963 Representation of a function by its line integrals, with some radiological applications, I. J. Appl. Phys. 34, 2722-2728.

Cormack A.M. 1964 Representation of a function by its line integrals, with some radiological applications, II. J. Appl. Phys. 35, 2908-2912.

Crowther R.A. 1971 Procedures for three-dimensional reconstruction of spherical viruses by Fourier synthesis from electron micrographs. Phil. Trans. Roy. Soc. Lond. B 261, 221-230.

Crowther R.A., De Rosier D.J. and Klug A. 1970 The reconstruction of a three-dimensional structure from projections and its application to electron microscopy. Proc. Roy. Soc. Lond. A 317, 319-340.

Crowther R.A. and Klug A. 1971 ART or science, or, Conditions for 3-D reconstructions from electron microscope images. J. Theor. Biol. 32, 199-203.

Cutrona L.J., Leith E.N., Porcello L.J. and Vivian W.E. 1966 On the application of coherent optical processing techniques to synthetic aperture radar. Proc. IEEE 54, 1026-1032.

De Rosier D.J. and Klug A. 1968 Reconstruction of three-dimensional structures from electron micrographs. Nature 217, 130-134.

De Rosier D.J. and Moore P.B. 1970 Reconstruction of three-dimensional images from electron micrographs of structures with helical symmetry. J. Mol. Biol. 52, 355-369.

Edholm P. 1960 The tomogram. Its information and content. Acta Radiol. Suppl. 193.

Edholm P. and Quiding L. 1970 Elimination of blur in linear tomography. Acta Radiol. [Diag.] (Stockholm), 10, 441-447.

EMI Ltd, 1972 The EMI-Scanner. Trade brochure.

Etter L.E. (ed.), 1965 The Science of Ionizing Radiation C.C. Thomas, Springfield, Ill.

Farmer F.T. and Collins M.P. 1971 A new approach to the determination of anatomical cross-sections of the body by Compton-scattering of gamma rays. Phys. Med. Biol. 16, 577-586.

Freedman, G.S. 1972 Gamma camera tomography. Theory and preliminary clinical experience. Radiology 102, 365-369.

Frieder G. and Herman G.T. 1971 Resolution in reconstructing objects from electron micrographs. J. Theor. Biol. 33, 189-211.

Frieden B.R. 1972 Restoring with maximum likelihood and maximum entropy. J. Opt. Soc. Am. 62, 511-518.

Frieden B.R. and Burke J.J. 1972 Restoring with maximum entropy, II. Superresolution of photographs of diffraction-blurred impulses. J. Opt. Soc. Am. 62, 1202-1210.

Gilbert P.F.C. 1972a. The reconstruction of three-dimensional structure from projections and its application to electron microscopy. II. Direct methods. Proc. Roy. Soc. Lond. B 182, 89-102.

Gilbert P.F.C. 1972b Iterative methods for the reconstruction of three-dimensional objects from projections. J. Theor. Biol. 36, 105-117.

Goitein M. 1972 Three dimensional density reconstructions from a series of two-dimensional projections. Nucl. Inst. and Methods 101, 509-518.

Goodman J.W. 1968 Introduction to Fourier Optics. McGraw-Hill (N.Y.).

Gordon R., Bender R. and Herman G.T. 1970 Algebraic reconstruction techniques (ART) for three-dimensional electron microscopy and X-ray photography. J. Theor. Biol. 29, 471-481.

Gordon R. and Herman G.T. 1971 Reconstruction of pictures from their projections. Comm. A.C.M. 14, 759-768.

Gori F. and Guattari 1971. Non-uniform sampling in optical processing. Optica Acta 18, 903-911.

Gough P.T. and Bates R.H.T. 1972 Computer generated holograms for processing radiographic data. Computers and Biomed. Res. 5, 700-708.

Grant D.G. 1972 Tomosynthesis: A three-dimensional radiographic imaging technique. IEEE Trans. Biomed. Eng. BME-19, 20-28.

Groh G. and Kock M. 1970 3-D display of X-ray images by means of holography. Applied Optics 9, 775-777.

Grossman G. 1935 Practical considerations of tomography. Fortschr. a.d. Geb. D. Röntgenstrahlen 52, 44.

Harris J.L. 1964 Diffraction and resolving power. J. Opt. Soc. Am. 54, 931-936.

Hartwell J.W. 1971 A procedure for implementing the fast Fourier transform on small computers. IBM J. Res. Dev. 355-363.

Helstrom C.W. 1967 Image restoration by method of least squares. J. Opt. Soc. Am. 57, 297-303.

Hendee W.R. 1970 Medical Radiation Physics. Year Book Medical Publishers, Chicago, Ill.

Herman G.T. 1972 Two direct methods for reconstructing pictures from the projections. A comparative study. Spring Joint Computer Conf., 971-984.

Herman G.T. and Rowland S. 1971 Resolution in ART. An experimental verification of the resolving power of an algebraic picture reconstruction technique. J. Theor. Biol. 33, 213-223.

Hildebrand F.B. 1956 Introduction to Numerical Analysis. McGraw-Hill, N.Y.

Hildebrand B.P. 1962 A discussion of the Fourier transform properties of lenses. Report 3663-5-T, Radar Laboratory, Institute of Science and Technology, University of Michigan.

Hounsfield G. 1972 Private communication.

Huang T.S. 1972 Two dimensional windows. IEEE Trans. Audio Electroac. AU-20, 88-89.

Hunt B.R. 1971 Spectral effects in the use of Newton-Cotes approximations for computing discrete Fourier transforms. IEEE Trans. Comp. C-20, 942-943.

Hunt B.R., Janney D.H. and Zeigler R.K. 1970 Introduction to the restoration and enhancement of radiographic images. Los Alamos Scientific Lab. Rept LA-4305.

IBM 1968 System/360 Scientific Subroutine Package (360A-CM-03X) Version III Programmer's Manual, IBM Technical Publications Dept (N.Y.).

IEEE, 1967 Special issue on the fast Fourier transform and its application to digital filtering and spectral analysis. IEEE Trans. Audio and Electroac. AU-15, 43-117.

IEEE, 1969 Special issue on the fast Fourier transform. IEEE Trans. Audio Electroac. AU-17, 66-170.

James T.H. and Higgins G.C. 1948 Fundamentals of Photographic Theory. Wiley, N.Y.

Jessup A.M. and Wallace C.S. 1968 A cheap graphic input device. Austral. Comp. J. 1, 95-97.

John F. 1955 Plane Waves and Spherical Means applied to Partial Differential Equations. Interscience, N.Y.

Kennedy W.K. and Peters T.M. 1973 High quality image recording and display using a small hybrid computer. Submitted for publication in Aust. Computer J.

Kieffer J. 1938 The laminagraph and its variations, applications and implications of the planigraphic principles. Am. J. Roentgenol. 39, 560.

Klug A. and Crowther R.A. 1972 Three-dimensional image reconstruction from the viewpoint of information theory. Nature 238, 435-440.

Klug A., Crick F.H.C. and Wykoff H.W. 1958 Diffraction of helical structures. Acta Crystallografica 11, 199.

Kotoulas K. and Sinis G. 1970 Theoretische untersuchung der projektionsbewegungsbedingungen der transversalen tomographie. Röntgenblatter 23, 15-19.

Kuhl D.E. 1968 The current status of tomographic section scanning. In Fundamental Problems in Scanning. Gottschalk A and Beck R.N. eds. C.C. Thomas, Ill. 179-190.

Kuhl D.E. and Edwards R.Q. 1968 Reorganizing data from transverse section scans of the brain using digital processing. Radiology 91, 975-983.

Kuhl D.E. and Edwards R.Q. 1970 The Mark III scanner. A compact device for multiple-view and section scanning of the brain. Radiology 96, 563-570.

Kuhl D.E., Edwards R.Q., Ricci A.R. and Reivich M. 1972 Quantitative section scanning. Proc. Symp. Med. Radioisotope Scin. IAEA/SM-164/157. Monte Carlo, Monaco, 23-28 Oct. 1972.

LeCroissette D.H. and Heyser R.C. 1972 Transmission ultrasonic soft tissue visualization. In Digest of 3rd Int. Conf. on Medical Physics Including Medical Engineering. Gothenburg, Sweden, 30 July - 4 Aug. 1972. 35.4.

Ledley R.S., Rotolo L.S., Golab T.J., Jacobsen J.D., Ginsberg M.D. and Wilson J.B. 1965 Fidac: Film input to digital automatic computer and associated syntax-directed pattern recognition programming system. In Tippet J.T. et al. (Eds), Optical and Electro-Optical Information Processing MIT Press, Cambridge Mass. 591-693.

Lipson S.G. and Lipson H. 1969 Optical Physics. C.U.P.

Majkowski R.F. and Gara A.D. 1972 Accuracy of holographic images. Applied Optics 11, 1867-1869.

McLeod I.D.G. 1970 Pictorial output from a line-printer. IEEE Trans. on Computers C-19, 160-162.

McLeod J.H. 1954 The axicon: A new type of optical element. J. Opt. Soc. Am. 44, 592-597.

Miller E.R., McCurry E.M. and Hruska B. 1971 An infinite number of laminagrams from a finite number of radiographs. Radiology 98, 249-255.

Muehllehner G. and Wetzel R.A. 1971 Section imaging by computer calculation. J. Nucl. Med. 12, 76-84.

NASA 1968 Evaluation of Motion Degraded Images. Proc. of seminar held in Cambridge, Mass. Dec. 3-5 1968. NASA SP-193.

Offner A. 1968 Optical system simulating a conical lens. U.S.A. Patent 3,402,978.

Papoulas A. 1962 The Fourier Integral and its Applications. McGraw-Hill, N.Y.

Papoulas A. 1968 The Fourier Transform and its Application in Optics. McGraw-Hill, N.Y.

Peters T.M. 1972 Improvements to transverse body-section radiography using computerprocessing. Proc. 5th Hawaii Internat. Conf. on Syst. Sciences, HICSS-5. Jan. 12-14 1972, 238-240.

Peters T.M. 1973 Spatial filtering to improve transverse tomography. Submitted for publication in IEEE Trans. Biomed. Eng.

Peters T.M., Rogers T.G.H. and Glasgow G.M. 1973 Fourier transforms in gamma camera tomography. Submitted for publication in Phys. Med. Biol.

Peters T.M., Smith P.R. and Gibson R.D. 1973 Computer aided body-section radiography. Brit. J. Radiol. 46, 314-317.

Radon J. 1917 Über die bestimmung von funktionen ducrh ihre integralwerte längs gewisser Mannigfultigkieten. Ber. Verh. Süchs. Akad. 69, 262-278.

Ramachandran G.N. and Lakshminarayanan A.V. 1971a Three-dimensional reconstruction from radiographs and electron micrographs: Application of convolutions instead of Fourier transforms. Proc. Nat. Acad. Sci. USA, 68, 2236-2240.

Ramachandran G.N. and Lakshminarayanan A.V. 1971b Three-dimensional reconstruction from radiographs and electron micrographs. Part III. Description and application of the convolution method. Indian J. Pure Appl. Phys. 9, 997-1003.

Rao G.U.V. 1971 A new method to determine the focal spot size of x-ray tubes. Am. J. Roent., Rad. Ther. and Nucl. Med. 111, 628-633.

Rawson E.G. 1969 Vibrating varifocal mirrors for 3-D imaging. IEEE Spectrum 37-43.

Redman J.D., Wolton W.D. and Shuttleworth E. 1968 Uses of holography to make truly three-dimensional X-ray images. Nature 220, 58.

Reichmann S. 1972a Modified theory of the development of tomographic blurring. Acta Radiologica (Diag.) 12, 457-468.

Reichmann S. 1972b Development of spurious contours of spherical and cylindrical objects in tomography. Acta Radiological (Diag.) 12, 317-334.

Rider K.L., Rudin S. and Hart H.E. 1972 Resolution characteristics of tomographic rotating collimator systems. IEEE Trans. Biomed. Eng. BME-19, 186-193.

Roach J.F. 1970 Xeroradiography. Radiol. Clin. N. Am. 8, 271-275.

Robinson D.E. 1972 Display of three-dimensional ultrasonic data for medical diagnosis. J. Acoust. Soc. Am. 52, 673-687.

Rowland S.W. 1972 SNARK - A picture reconstruction framework. M.Sc. Report, Dept of Computer Science, State University of New York at Buffalo, N.Y.

Schack R.V. and Swindell W. 1968 An analogue image processor. In Evaluation of Motion Degraded Images. Proc. Seminar held in Cambridge Mass., Dec. 3-5 1968. NASA SP-193, 175-178.

Schechter M.M., Hoppenstein R., Hayes R.A. and Fouquart J.J. 1971 Four-dimensional time sequence radiography. Radiology 99, 551-558.

Scheuer P.A.G. 1962 On the use of lunar occultations for investigating the angular structure of radio sources. Aust. J. Phys. 15, 333-343.

Semler R.A. and Moler R.B. 1967 X-ray laminography for the testing of multilayer printed circuit boards. Proc. Fall 1967 Tech. Seminar, Inst. of Printed Circuits.

Shapiro R. 1972 Information loss and compensation in linear interpolation. J. Comp. Phys. 10, 65-84.

Shulman A.R. 1970 Optical data processing. Wiley, N.Y.

Singleton R.C. 1969 An algorithm for computing the mixed radix fast Fourier transform. IEEE Trans. Audio Electroac, AU-17, 93-103.

Slepian D. 1967 Restoration of photographs blurred by image motion. Bell Syst. Tech. J. 2353-2359.

Slepian D. and Pollak H.O. 1961 Prolate spheroidal wave functions, Fourier analysis and uncertainty. Bell. Syst. Tech. J. 40, 43-84.

Smith P.R., Peters T.M. and Bates R.H.T. 1973 Image reconstruction from a finite number of projections. J. Phys. A 6, 361-382.

Som S.C. 1971 Analysis of the effect of linear smear on photographic images. J. Opt. Soc. Am. 61, 859-864.

Stauffer H., Henny G. and Blackstone A. 1962 Stereoscopic televised fluoroscopy. Radiology 79, 30.

Stieve F.E. 1972 Uber den bildanfban in der Tomographie bei ein-und Mehrdimensionaler Verwischung. Fortschr. Röntgenst. 116, 253-273.

Stroke G.W. 1973 Optical Computing. IEEE Spectrum, Dec. 24-41.

Swindell W. 1970 A non-coherent optical analog image processor. Appl. Opt. 9, 2459-2469.

Takahashi S. 1965 Conformation radiotherapy. Rotation techniques as applied to radiography and radiotherapy of cancer. Acta. Radiol. Suppl. 242.

Taylor J.H. 1967 Two-dimensional brightness distribution observations of radio sources from lunar occultation observations. Astrophys. J. 150, 421-426.

Temes G.C., Barcilon V. and Marshall F.C. 1973 The optimization of band-limited systems. Proc. IEEE 61, 196-234.

Toraldi di Francia G. 1955 Resolving power and information. J. Opt. Soc. Am. 45, 497-501.

Toraldo di Francia G. 1969 Degrees of freedom in an image. J. Opt. Soc. Am. 59, 799-604.

Tretiak O.J., Eden M, and Simon W. 1969 Internal structure from X-ray images. Proc. 8th Int. Conf. on Med. Biol. Eng. Chicago Ill., Jul. 20-25 1969.

Tukey J.W. 1967 An introduction to the calculation of numerical spectral analysis. In Spectral Analysis of Time Series, Bernard Harris (Ed.). Wiley, N.Y.

Vainshtein B.K. 1971a. Finding the structure of objects from projections. Soviet Physics - Crystallography 15, 781-787. Translated from Kristallografiya 15, 894-902 (1970).

Vainshtein B.K. 1971b The Synthesis of projecting functions. Doklady Akademii Nauk SSSR 196, 1072-1075.

Vallebona A. 1930 A modified technique of roentgenographic dissociation of shadows applied to the study of the skull. Radiol. Med. 17, 1090-1097.

Vallebona A. 1947 Nouvelle méthode roentgenstratigraphique. Radiol. Clin. 47.

Vallebona A. 1955 Three-dimensional stratigraphic scintigraphic examination. Axial transverse stratigraphy. Part I. Am. J. Roent. Rad. Ther. Nucl. Med. 74, 769-776.

von Bieren K. 1971 Lens design for optical Fourier transform systems. Appl. Optics 10, 2739-2742.

Watson G.N. 1966 A Treatise on the Theory of Bessel Functions C.U.P.

Whittaker E.T. and Watson G.N. 1952 A Course of Modern Analysis, C.U.P.

Ziedes des Plantes B.G. 1932 A new method of differentiation in roentgenography (planigraphy). Acta Radiol. 13, 182-191.

Ziedes des Plantes B.G. 1971 Body-section radiography: History, image formation, various techniques and results. Australasian Radiology 15, 57-64.

Helms H.D. 1967 Non recursive digital filters: design methods for achieving specifications on frequency response. IEEE Trans. Audio Electroac. AU-16, 336-342